Mimicking Photosystem II With Synthetic Manganese Complexes

Author: Wen-Feng Lo

Boston College

The Graduate School of Arts and Sciences

Department of Chemistry

MIMICKING PHOTOSYSTEM II WITH SYNTHETIC MANGANESE COMPLEXES

a dissertation

by

WEN-FENG LO

submitted in partial fulfillment of the requirements

for the degree of

Doctor of Philosophy

Mimicking Photosystem II With Synthetic Manganese Complexes

Wen-Feng (Wayne) Lo

Dissertation Advisor: William H. Armstrong

Abstract

The Oxygen-Evolving Complex (OEC) of Photosystem II (PSII) utilizes a Mn_4Ca cluster to catalyze the conversion of water to dioxygen within plant chloroplasts. The active site of the water oxidase is found on the lumenal side of the thylakoid membrane. For many years, the nature of this convoluted system, including the unresolved structural arrangement of the OEC manganese-oxo aggregate, stimulated on-going research projects in a diverse set of scientific fields. A tetranuclear oxo-bridged manganese complex associated with calcium [Ca] and chloride [Cl], along with a redox active tyrosine (Tyr), is thought to be the center of this remarkable and unique biological machinery. An illustrious catalytic cycle, known as the Kok cycle, progresses through a series of five intermediate states (S_i, i = 0-4) to conduct water oxidation and dioxygen evolution. A tentative structural proposal based on the single crystal X-ray diffraction (XRD) crystallographic measurements introduced a $CaMn_3$ cubane cluster and an appended fourth manganese atom. It was proposed that water binds between the "dangling" Mn atom and the Ca atom, and that is where the O-O bond formation is proposed to occur, followed by O_2 release without structural rearrangement of the cubane core. The plausible manganyl (Mn^V=O) species was also suggested as an intermediate in the S_4 state for the O-O bond formation and release O_2.

We have examined plausible reactive manganyl species as are proposed to exist at the OEC S_4 state. The existence of manganyl in synthetic model systems will be presented in Chapter 2. In this study, we utilized stopped-flow UV-vis spectroscopy and mass spectrometry to investigate the formation and the nature of the intermediate in the reaction between mononuclear Schiff base manganese complexes and a reagent that is often used for O atom transfer reactions. Chapter 3 involves establishment of a logical synthetic method to prepare the related complexes, $Mn_2O_2(bpy/dmb)_2(Ar^RCOO)_2$ [R = 2,6-diphenyl, 2,6-ditolyl]. The dimanganese-oxo center is considered as a basic unit on the path toward the construction of higher nuclearity of Mn aggregates, preferably Mn_4 clusters to be used for OEC catalytic cycle mimicry. Controlled ligand exchange synthesis of this type of carboxylate-rich/bridged $\{Mn_2O_2\}$ dimers will provide an alternate pathway toward obtaining the Mn aggregates that are not attainable by direct 'self-assembly' synthetic methods. In Chapter 4, we will describe a novel mixed-ligand tetranuclear Mn cluster of the adamantane core type, $[Mn_4(\mu\text{-}O_6)(bpy)_4(py)_4](ClO_4)_4$. This cluster was synthesized by using a simple reaction and its spectroscopic characterization will be discussed. We will also demonstrate chromatographic behavior of the Mn clusters that we encountered in this work (see Appendix A).

Acknowledgements

It is once said in a movie that “we have no way of knowing what lays ahead of us in the future. All we can do is use the information at hand to make the best decision possible”. The years that I spent here at Boston College, it has been a great adventure for the unusual situation and ultimate challenges since day 1 all the way to the end. During my graduate study life, there are many people to whom I am deeply indebted and an enormous gratitude should contribute to them in particular from the very bottom of my heart. First of all, Professor Bill Armstrong is a truthfully grand scientific scholar whose profound insights and knowledge of chemistry, especially enthusiasm for science, have long been the key factor to influence on the research works presented here. His endless excellence in conducting creative and original works sets a trademark on me in all the aspects. For which, I am sincerely thankful to Bill to offer such a precious gift throughout everything to me and make me become a close-to-scholar scientist, that is priceless nowadays in such a Chemistry world. After all, I would love to say to my wonderful advisor: “Sir, it’s a great honor and pleasure to work with you and I believe more will and can be done, no matter what~~”.

For these endless challenges with regard to my research works, I wholeheartedly cherish all the lessons what I got from the members of the Armstrong research group, Dr. Christopher Dubé, Dr. Sumitra Mukhopadhyay, Dr. Sumit Bhaduri, Dr. Richard Chang and Dr. Henry Mok. They found precious time from their busy schedules to help and teach me to learn all the techniques that are needed for my research works. I am truly grateful for their supportiveness and assistance. Mr. Marek Domin, to whom, I owe very

much for his tremendous helps in mass spectrometry. He is really my best friend at Boston College for the past years and without his kindness and expertise, I probably cannot get things done in an efficient way. I would also love to express my thankfulness to Mark for his forever friendship.

Professor Richard H. Holm at Harvard University is a great person, who is kind enough to allow me to be part of his research group for learning many things from his postdoctoral fellows and be able to operate the instrumentations in his laboratory. For this, I am grateful to him for the opportunity to work with experienced chemists, which made me feel not alone in the lab at all. Dr. Richard Staples, Dr. Jian-Feng Jiang, and Dr. Christian Tessier are the three teachers who taught me every detail with regard to small molecule X-ray crystallography. I am indebted to them for all the helps and skills learned from each meeting in solving the crystal structures. That will be my long-lasting assets. Dr. Jun-Jieh Wang, Dr. Taichi Miyaji are two chemists who helped to show me the detailed UV-vis and NMR spectroscopic measurements. I am grateful to both of them for every small things that they were kind enough to teach me.

Extraordinarily thankful to Professor Elena V. Rybak-Akimova and Dr. Ivan V. Korendovych at Tufts University for the incredible experimental runs with regard to the stopped-flow UV-vis kinetic studies. Dr. Ralph T. Weber (Bruker Bio-Spin EPR, Billerica, MA) is extremely thankful for his great guidance for the EPR measurements. Dr. Peter Müller at MIT is also appreciative for his friendly discussions and grand helps with resolving difficult crystal structures, especially disorder and twinning ones. Dr. Shaoyan Chu and Mr. Patrick Boisvert at MIT CMSE center deserve special thanks for their fabulous helps with magnetism measurements on the SQUID magnetometer. We

are particularly grateful for Dr. Chu for his in-depth assistance with magnetism experimental design, data calculations and training for data fittings. I owe a special thank to them for introducing me to the related material science works in depth. Dr. John Boylan and Dr. Shaw Huang are thankful for the NMR training and valuable spectroscopic studies and 2D experimental design. I am grateful for Professor Steven J. Lippard and his group at MIT for the hospitality every time when I visited them for experiment questions.

Dr. Shivaiah Vaddypally and all the members of the Armstrong research group are appreciative. Patrick Cappilion and Dr. John Miecznikowski from the Caradonna group at Boston University are like my close brothers, I thank them for the friendships. Professor Paul Leavis at Boston Biomedical Research Institute (BBRI) in Watertown deserves a grateful thank for his kindness to teach me the peptide synthesis techniques.

Many people enrich my lonely life at Boston College, the Armstrong family: Nancy, Billy, Edward, and Allison; the Domin Family: Michelle, Hayley, and Mark, they always gave me the warmest greeting under any circumstances. Miss Sally Wyman, the liberian, Paul Madden and Hank, the plumbers, Bob, the electrician, Jose, the BC security guard, and Mr. Richard Pijar, that I, personally indebt for their generosity of teaching me all the facility works and electronic engineering. Hong Troung, Erik Tometti, Allen Weng and Jason Chiang are thankful for the computer knowledge and skills that I learned from them, which will be part of me forever. Foremost, I have to give my sincere gratefulness to my family, my parents, Mr. Chin-Tsai Lo, Mrs. Li-Shueh Lu, my younger sister Yun-Yao Lo, my grandparents and relatives. Finally to my love wife Vivian Lo without their continuing supports I cannot make through all the rough paths in past years.

Table of Contents

List of Complexes

Complex Formula	Complex No.
$[Mn^{III}(N\text{-methyl-Sal})_2](Cl)$	**1**
$[Mn^{III}(N\text{-ethyl-Sal})_2](Cl)$	**2**
$[Mn^{III}(N\text{-}n\text{-propyl-Sal})_2](Cl)$	**3**
$[Mn^{III}(N\text{-}n\text{-butyl-Sal})_2](Cl)$	**4**
$[Mn^{III}(\text{N-methyl-3-}NO_2\text{-Sal})_2](CH_3COO)$	**5**
$[Mn^{III}(\text{N-ethyl-3-}NO_2\text{-Sal})_2](CH_3COO)$	**6**
$[Mn^{III}(\text{N-}n\text{-propyl-3-}NO_2\text{-Sal})_2](CH_3COO)$	**7**
$[Mn^{III}(\text{N-}n\text{-butyl-3-}NO_2\text{-Sal})_2](CH_3COO)$	**8**
$[Mn^{III}(\text{N-isobutyl-3-}NO_2\text{-Sal})_2](CH_3COO)$	**9**
$[Mn^{III,III}{}_2(\mu\text{-O})(\mu\text{-OMe})(\mu\text{-OAc})(N\text{-}n\text{-}Bu\text{-3-}NO_2\text{-Sal})_2]_2$	**10**
$[Mn^{III,III}{}_2(\mu\text{-O})(\mu\text{-OMe})(\mu\text{-OAc})(N\text{-}Et\text{-3-}NO_2\text{-Sal})_2]_2$	**11**
$[Mn^{III}(\text{N-H-3-}NO_2\text{-Sal})_2](Cl)$	**12**
$[Mn^{III}(\text{N-methyl-3-}NO_2\text{-Sal})_2](Cl)$	**13**
$[Mn^{III}(\text{N-ethyl-3-}NO_2\text{-Sal})_2](Cl)$	**14**
$Mn^{III}(N\text{-ethyl-3-}NO_2\text{-Sal})_3$	**14a**
$[Mn^{III}(\text{N-}n\text{-propyl-3-}NO_2\text{-Sal})_2](Cl)$	**15**
$[Mn^{III}(\text{N-}n\text{-butyl-3-}NO_2\text{-Sal})_2](Cl)$	**16**
$[Mn^{III}(\text{N-isobutyl-3-}NO_2\text{-Sal})_2](Cl)$	**17**
$[Mn_2O_2(bpy)_4](ClO_4)_3$	**19**
$[Mn_2O_2(dmb)_4](ClO_4)_3$	**20**
$[Mn_2O_2(bpy)_2(Ar^{Ph}CO_2)_2](ClO_4)$	**21**
$[Mn_2O_2(bpy)_2(Ar^{Tol}CO_2)_2](ClO_4)$	**22**
$[Mn_2O_2(bpy)_2(Ar^{2,4,6\text{-}Tri\text{-}iPr}CO_2)_2](ClO_4)$	**23**
$[Mn_6(\mu\text{-O})_4(\mu_3\text{-O})_4(bpy)_6(Ar^{2,4,6\text{-}Tri\text{-}iPr}CO_2)_2](ClO_4)_4$	**24**
$[Mn_6(\mu\text{-O})_4(\mu_3\text{-O})_4(dmb)_6(OAc)_2](OTf)_4$	**25**
$[Mn_4O_2(bpy)_6(Ar^{3,5\text{-}CF_3}CO_2)_7](ClO_4)$	**26**
$[Mn(bpy)_3](X)_2$ (where X = ClO_4, OTf)	**27**
$[Mn_2(\mu\text{-O})_2(bpy)_2(Ar^{Ph}CO_2)_3]$	**28**
$[Mn_2(bpy)_4(Ar^{2,4,6\text{-}trimethyl}CO_2)](ClO_4)_2$	**29**
$[Mn_2O_2(phen)_4](X)_3$ (where X = ClO_4, OTf)	**30**
$[Mn_2O_2(bpy)_3(py\text{-}d_5)_2](X)_3$ (where X = ClO_4, OTf)	**31**

List of Ligands

Ligand(s)	Abbreviation
Salicylaldehyde	Sal
2,2'-bipyridine	bpy
4,4'-dimethyl-2,2'-bipyridine	dmb
2,6-Di-phenylbenzoic Acid	$Ar^{Ph}COOH$
2,6-Di-tolylbenzoic Acid	$Ar^{Tol}COOH$
2,4,6-Tri-*i*-propylbenzoic Acid	$Ar^{2,4,6\text{-Tri-}i\text{-Pr}}COOH$
3,5-bis-trifluoromethylbenzoic Acid	$Ar^{3,5\text{-}CF_3}COOH$
N,*N*-bis(2-pyridylmethyl)methylamine	bpma
N,*N*-bis(2-pyridylmethyl)ethylamine	bpea
1,1,1-tris(aminomethyl)ethane	tame
1,4,7-triazacyclononane	tacn
Methyliminodiacetate	mida
Diethylenetriamine	dien
N,*N*-dimethylformamide	dmf
Pyridine	py

Other Chemical Abbreviations

Compound	Abbreviation
N,*N'*-bis(salicylidene)-1,3-diaminoethane	SALEN
N,*N'*-bis(salicylidene)-1,3-diaminopropane	SALPN
Tetrabutylammonium perchlorate	TBAP
Ferrocene	$Fe(Cp)_2$
Tetraethylammonium perchlorate	TEAP
2,4-pentanedione	acac

List of Figures

Chapter 1. Introduction

Chapter 2. Spectroscopic and Kinetic Study of a Model of the Photosystem II S_4 State Using Schiff Base Complexes

Chapter 4. Synthesis, Structure, Spectroscopic and Electrochemical Study of a Novel Mixed-Ligand Manganese Cluster: $[Mn_4(\mu\text{-}O_6)(bpy)_4(py)_4](ClO_4)_4$

List of Schemes and Tables

Chapter 1

Introduction

1.1. General Background

Solar energy is the original energy source for nearly all organisms on Earth. Through the process of photosynthesis, green plants capture light energy from the Sun and transform this energy into chemical energy in the form of nutrients, which are consumed by many life forms.[1] The overall process occurs in four stages: 1) Light energy is captured by antenna chlorophyll; 2) in light-dependent reactions, electrons are produced on the so-called donor side; 3) the sequential events of electron transportation and ATP synthesis take place; 4) carbon fixation and the final phase in generating carbohydrates, such as sucrose or glucose. The first three stages are light-dependent reactions and take place in the thylakoid membranes (Figure 1).[2]

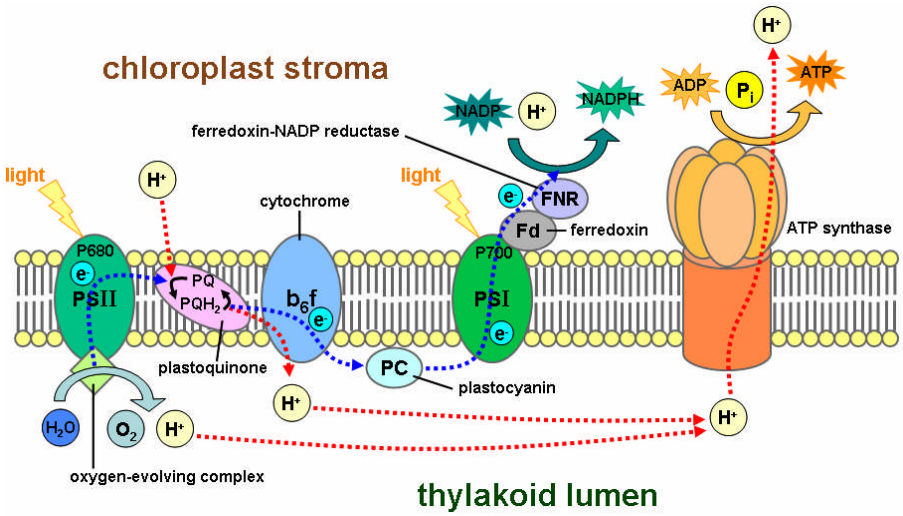

Figure 1.1. Light-dependent reactions of photosynthesis.[2]

The fourth stage involves light-independent reactions (dark reactions) that proceed within the stroma. These reactions are referred to as the Calvin-Benson Cycle.

Solar radiation is used to drive the thermodynamically 'uphill'[3] process that converts water and carbon dioxide to carbohydrates and molecular oxygen.[4] The overall reaction carried out in photosynthesis is shown in Equation 1.1.[5]

$$12H_2O + 6CO_2 + \text{light} \rightarrow C_6H_{12}O_6 \text{ (glucose)} + 6O_2 + 6H_2O \qquad (1.1)$$

Standard Free Energy ($\triangle G^{\ddagger}$) = +2.870 kJ/mole[6]

This process can also be viewed as a pair of the two half reactions shown in Equation 1.2 and 1.3

$$\text{Oxidation: } 2H_2O \rightarrow O_2 + 4e^- + 4H^+ \qquad (1.2)$$

$$\text{Reduction: } CO_2 + 4H^+ + 4e^- \rightarrow CH_2O \text{ (carbohydrate)} + H_2O \qquad (1.3)$$

The light-dependant reactions are known to involve two of the enzyme cofactors, P680 (absorption spectrum peak at 680 nm; Photosystem II, or PSII) and P700 (absorption spectrum peak at 700 nm; Photosystem I, or PSI). In Photosystem II, the electrons are transferred from water, shuttled to a quinone terminal electron acceptor and then ultimately to Photosystem I. In PS I, the ferredoxin-like iron-sulfur clusters function as terminal electron acceptors and subsequently generate reducing power in the form of NADPH, which along with ATP is utilized in the Calvin-Benson Cycle, which converts CO_2 into the carbohydrates of life.[1,3]

1.2. Photosystem II Water Oxidase

As mentioned earlier, the two systems of light-dependent photosynthetic reactions reside within the chloroplast thylakoid membranes and these "light-harvesting" reactions have been summarized as a zig-zag, or Z, pathway (Figure 2).

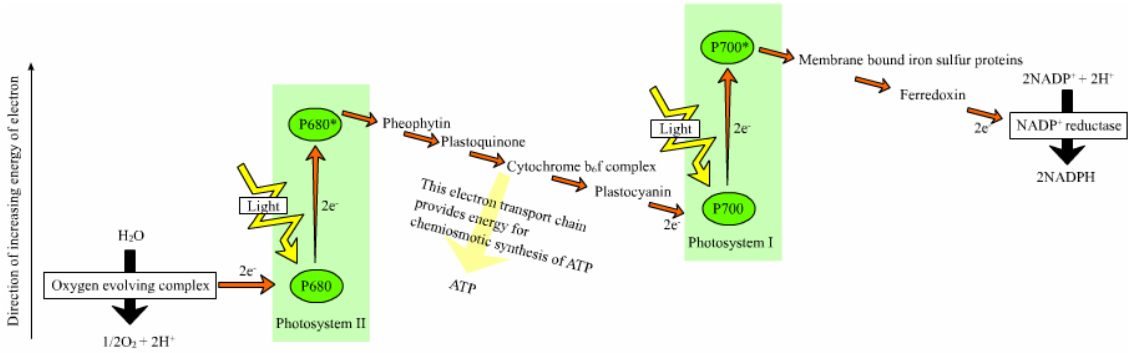

Figure 1.2. The Z-scheme.[7]

In our research we mainly concentrate on studying artificially synthesized molecules that mimic certain aspects of the Photosystem II (PSII) – P680 reaction center.[8] In PSII, water splits into molecular oxygen, protons and electrons, a process also referred to as photooxidation. The active site of the water oxidase, commonly referred to as the Oxygen Evolving Complex or OEC, is found on the lumenal side of the thylakoid membrane, which is a proton reservoir as well (Figure 3).[8,9]

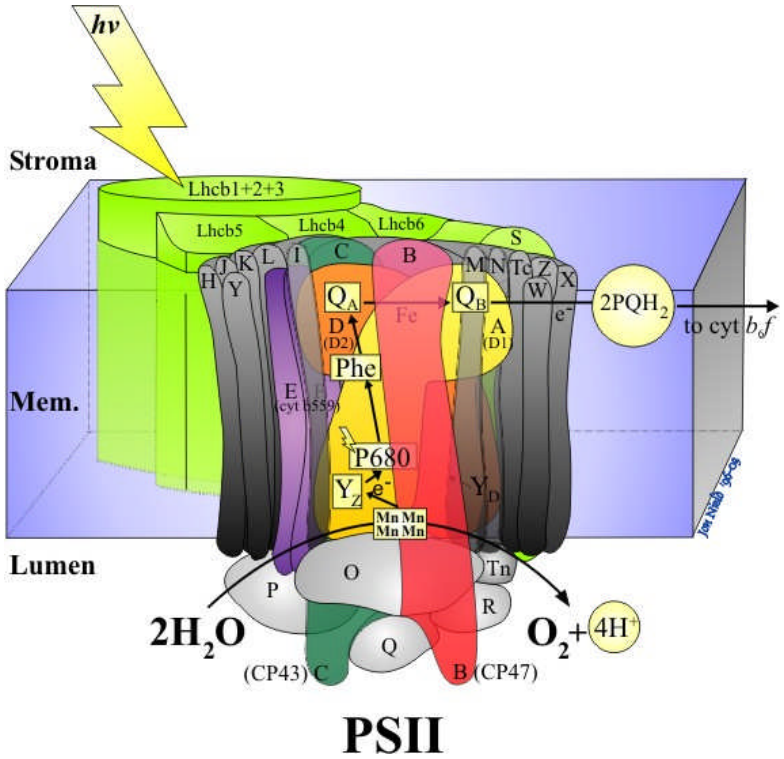

Figure 1.3. Photosystem II complex. Copyright Wolfson Laboratories, Department of Biological Sciences, Imperial College London, 2003.

There are more than 22 polypeptides associated with PSII,[10] and the core complex consists of D1, D2, cytochrome *b559*, CP47, CP43; three extrinsic proteins to stabilize the Mn-oxo cluster, Ca^{2+} and Cl^- cofactors, and low molecular weight subunits and antenna subunits.[11] For many years, the nature of this convoluted system, including the unresolved crystal structure of the OEC manganese-oxo aggregate, stimulated on-going research projects in a diverse set of scientific fields. For example, PSII photophysics and how it is related to proton-coupled electron transfer (PCET), mechanistic studies of the water oxidase catalytic cycle, and the structural/functional modeling by utilizing synthetic complexes.[12]

In the 1970's, several pioneering results altered the direction of research into photosynthetic water oxidation. Originally, it was thought that PSII reaction centers generate diffusible oxidants to split water at a remote center that was independent of the site of charge separation.[13] A key measurement carried out by Joliot and coworkers showed that the oxygen evolved from dark-adapted spinach chloroplasts or Chlorella when successive illuminations of short (~ 10μsec), intense pulses of visible light were applied. Initially, dioxygen evolved after the first three flashes, thereafter resulting in a remarkable oscillation pattern with a period of a four for O_2 evolution *vs.* flash number. Later, Kok et al. reproduced these results and interpreted the data to devise a new illustrious scheme, now known as the Kok cycle or the 'S-state' cycle, where S stands for storage (Figure 4). The catalytic cycle progresses through a series of five intermediate states (S_i, i = 0-4). At the S_4 state, four oxidizing equivalents are stored in the OEC tetramanganese oxo-bridged cluster, after which the four-electron water oxidation occurs and the enzyme returns to the S_0 state. It is generally believed that the manganese-oxo

complex, along with cofactors Ca^{2+} and Cl^{-} and stabilizing polypeptides are at the center of this remarkable and unique biological machinery. Within the OEC system, a redox active tyrosine (Tyr) is thought to be the initial receptor in the electron transport chain.

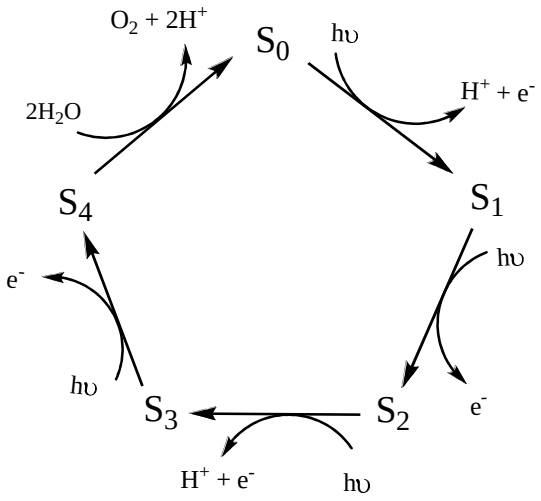

Figure 1.4. The proposed Kok Cycle.

An accurate structure determination of the PSII OEC is desirable in order that the research in this area advance to the next stage. Electron microscopy and synchrotron radiation X-ray diffractometry have long been applied in the protein structural determinations. The first three dimensional PSII structure studies were done by using electron microscopy, which is limited to low resolution. The PSII structure was reported at 30 Å[14] and 8 Å[15] – in 1993 and 1998, respectively. While these studies were useful in visualizing the enzyme subunits and their relative orientation to each other, higher resolution information was essential to gain a greater understanding of the system. Benefiting from newer technology, such as high intensity synchrotron radiation X-ray sources and highly sensitive detectors to collect better crystallographic data more quickly, and the emerging high-speed computer era, crystal structure determination has been greatly enhanced by allowing better phase selection, data integration, and result refinement. This advancement has made it possible to study successfully the single

crystal X-ray diffraction (XRD) structure of PSII at higher resolution levels of 3.7 Å in 2003[16], 3.5 Å in 2004[17] and 3.0 Å in 2005[18] (Figure 5).

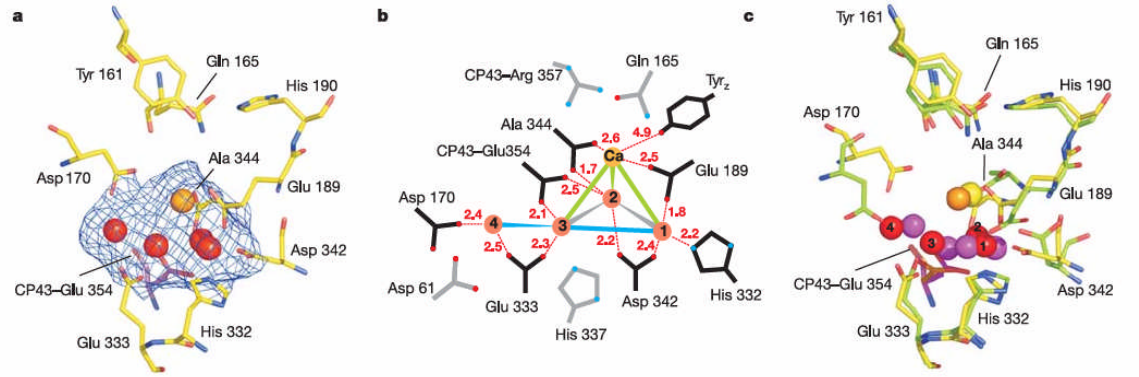

Figure 1.5. Single crystal X-ray diffraction structure of PSII OEC – at 3.0 Å resolution. (a) crystal structure data; (b) representative diagram of assigned atoms for electron densities; (c) comparison diagram between different resolution structures, 3.5 Å in purple and 3.0 Å resolution in red.

These tantalizing results for the single crystal structure of PSII were greatly lauded when they were first reported, but later on X-ray absorption spectroscopy (XAS) studies produced results that contradicted the tetramanganese complex structural proposals based on XRD. The Mn X-ray absorption near-edge spectroscopy (XANES) study showed that the geometry of the OEC Mn_4Ca cluster changes owing to the photoreduction caused by the XRD X-ray source.[19] It was demonstrated that the PSII active site in the dark stable S_1 state was structurally damaged, and such a conclusion was based on the XANES Mn K-edge shift result by using high doses of X-ray irradiation in the single-crystal measurement. This behavior was confirmed by a XANES study of synthetic Mn_4 (III_3,IV) and Mn_4 (III_2,IV_2) complexes, which one can consider to be clusters related to the OEC.[20] The III, IV oxidation state of manganese centers were shown to undergo rapid reduction to Mn^{II} in both the PSII enzyme and inorganic complexes (Figure 6).

This phenomenon greatly hinders one's ability to determine the structure of the OEC enzyme manganese cluster in its native, catalytic form. [21]

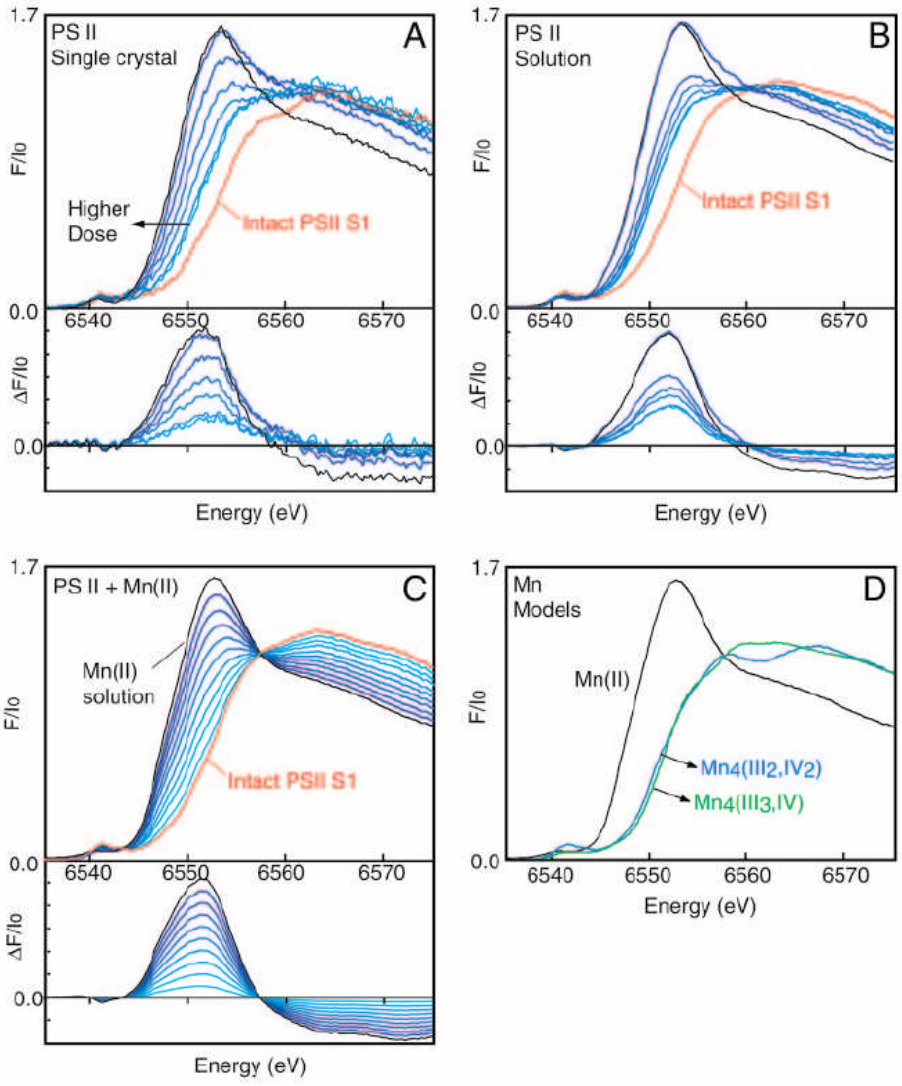

Figure 1.6. Mn XANES spectra of PSII *versus* X-ray dose (A), (B) and (C) and XANES spectrum of inorganic model complexes (D).[19,22]

As broadly described above, the Mn K-edge XAS studies, including extended X-ray absorption fine structure spectroscopy (EXAFS) to determine the Mn-Mn distances and X-ray absorption near-edge spectroscopy (XANES) for oxidation states of complexes, have long been applied to examine the Mn-Mn and Mn-Ca distances within the PSII OEC

cofactor. The following diagram adapted from ref. 13 shows the possible structural arrangements for $Mn_4(Ca)$ cofactors based on the EXAFS results.[23]

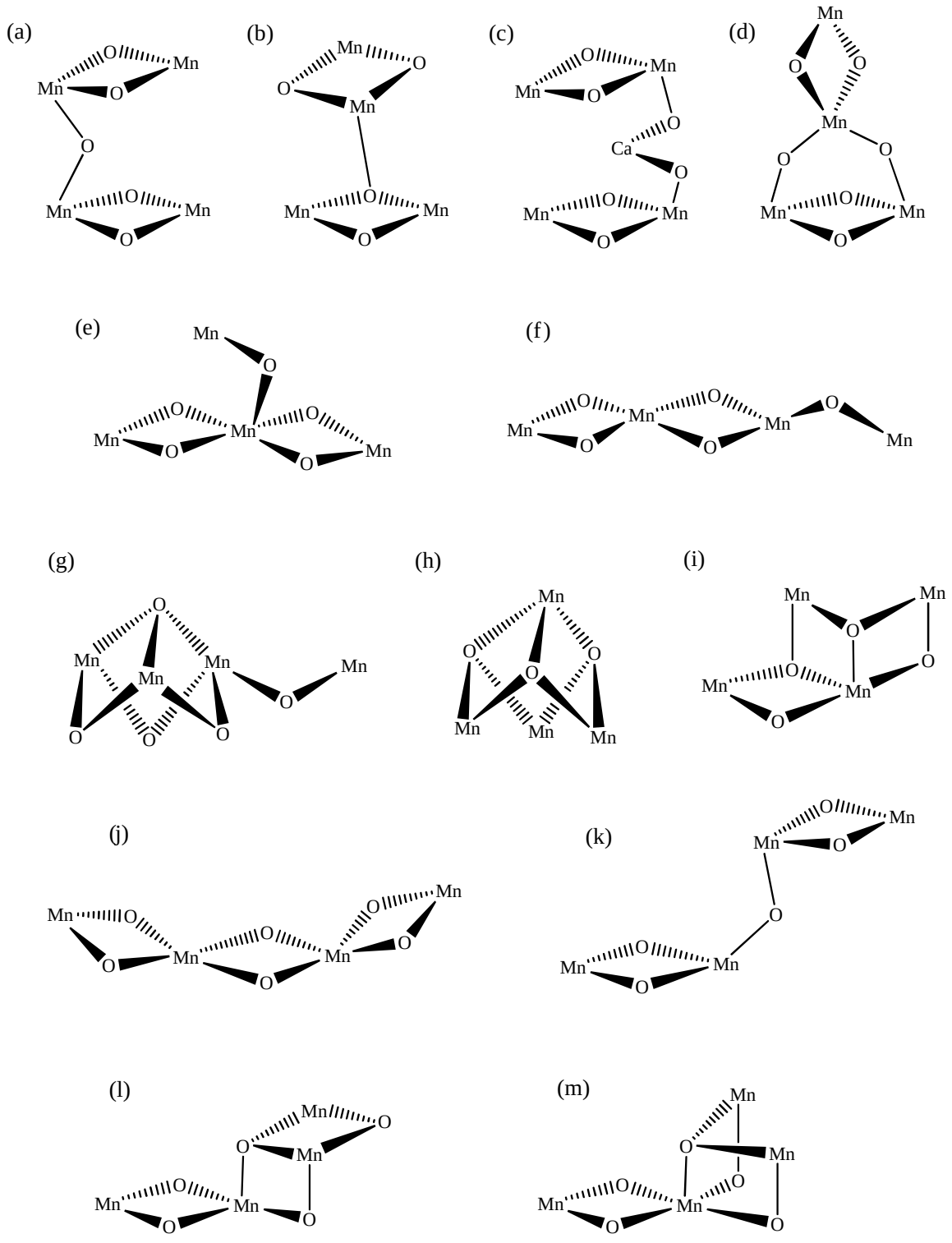

Figure 1.7. Possible Mn_4 structural arrangements in the PSII based on EXAFS studies.

None of the proposed structures for the WOC cofactor shown in Figure 7 should be ruled out without further detailed investigation. In addition to the XAS and XRD studies, 'indirect' physical methods such as electron paramagnetic resonance (EPR) spectroscopy, vibrational spectroscopy (Raman, resonance Raman, infrared, especially FTIR) and mass spectroscopy (MS) also have been used to probe the PSII enzyme. The EPR/ESR (electron spin resonance) spectroscopy is the method, complimentary to XRD and XAS, which provides a way to explore the electronic structure of the OEC Mn_4Ca.[24] ESR spectroscopy encompasses several different techniques, including continuous wave electron paramagnetic resonance (CW-EPR), pulsed electron nuclear double resonance (ENDOR), and electron spin-echo envelope resonance (ESEEM) spectroscopy. Since the OEC consists of a paramagnetic tetramanganese cluster, these methods are useful for the analysis of its electronic properties. These studies provide valuable information with regard to the OEC Mn cluster oxidation states as well as its intracluster magnetic coupling. EPR spectra for the OEC states S_0, S_1, S_2 and S_2-$Y_z^{\bullet}$ have been measured (Figure 8).[25] Furthermore, the comparisons between the spectra of the OEC and synthetic model compounds promise to provide information that has not yet come from X-ray crystallography. In addition, the EPR techniques have been used to detect water molecule binding as well as the electron transfer processes. ESEEM, ENDOR methods have been used to investigate the former, specifically whether water binds to the OEC in S_2 or S_3 state while EPR spectroscopy was used to study the latter, namely the issue of the involvement of interactions between manganese cluster and the tyrosine radical.[26]

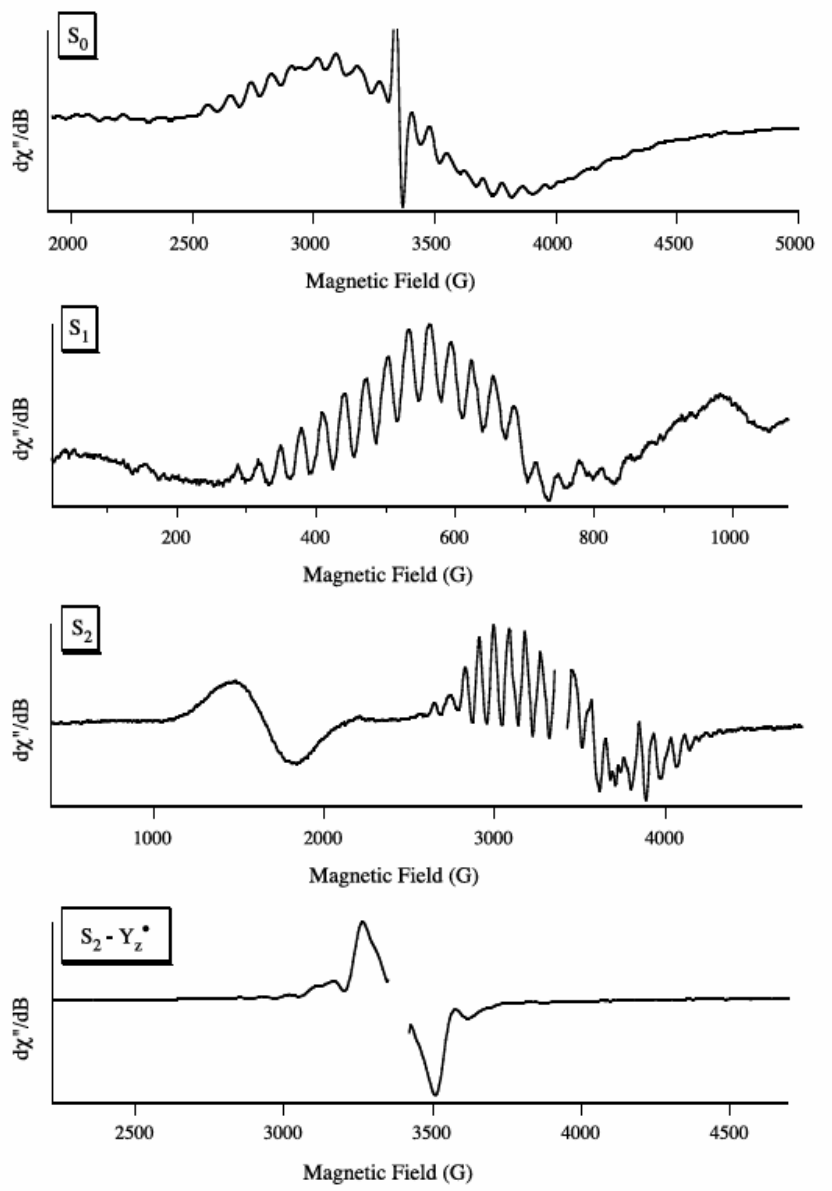

Figure 1.8. CW-EPR Signals associated with the S_0, S_1, S_2, S_2-$Y_z^{\bullet}$ states of PSII OEC.

The vibrational spectroscopic methods FTIR[27,28] and Raman[29], have been used to probe the aforementioned features of the PSII enzyme study as well. Several IR and Raman bands are associated with the OEC and synthetic model complexes can aid in vibrational assignments as characteristic markers. These methods also have been used for the purpose of monitoring the mechanistic process including product formation.[30] Mass

spectrometry has been used as well to elucidate certain aspects of the water oxidation mechanism such as the timing of water binding. The principal application of mass spectrometric methods has been to detect the O_2 evolution from water oxidation.[31]

The analytical methods described above have been employed extensively in studying the active site of PSII WO enzyme with regard to its cofactor structure and related water oxidation activities. A comparison between spectral characteristics of the enzyme and well characterized synthetic complexes provides insight into the structure and function of the OEC that would not be possible without the latter.

1.3. Manganese Complexes for Modeling PSII Catalytic Cycle

In one aspect of bioinorganic chemistry, researchers study spectroscopic, redox and chemical properties of metal complexes in order to better understand and ultimately to mimic the active sites of metalloenzymes.[32] As a result of studies of PSII OEC, several proposals have been suggested to rationalize the oxygen evolution catalytic cycle. In the absence of a defined structure of the OEC, these postulations may or may not accurately represent the actual catalytic cycle. However, the preliminary hypotheses are quite useful in designing further experiments. In the following diagrams, proposed catalytic cycles are presented, each based on different structural motifs. The synthetic models were derived in order to match Mn oxidation states and Mn-Mn distances from the reported EXAFS, EPR and other spectroscopic results. To illustrate possible O_2 evolution mechanisms, these proposals incorporated the ideas of structural rearrangement, a plausible S_4 state intermediate and/or Ca^{2+}, Cl^{-} cofactors into the mechanism along with requisite successive 1 e^{-} oxidation and deprotonation. Even though speculated structures

from some of the proposals have been ruled out, we think there is still much important information from these proposed mechanisms with regard to ligand configuration designs, plausible high oxidation state intermediates and structural rearrangement that can be used to drive our own research.

The first proposal we examine here was suggested by Babcock and coworkers. They utilized an open dimer-of-dimers Mn-oxo aggregate bridged through carboxylates as the structural model with the tyrosine radical $Y_z^{\bullet}$ playing an important role in the mechanism (Figure 9).[33] In this proposal, they suggested the formation of a plausible intermediate manganyl species [Mn=O] before the O-O bond formation and release of O_2. This suggested that a manganyl intermediate is of considerable interest and identification of such a reactive species has also been emphasized by several research groups including ours.

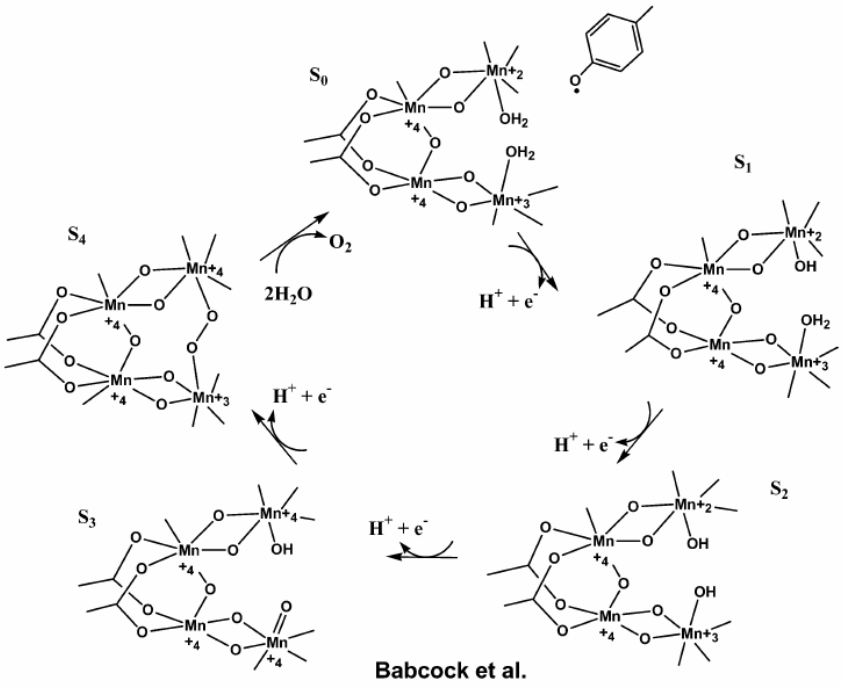

Figure 1.9. CW-EPR Signals associated with the S_0, S_1, S_2, S_2-$Y_z^{\bullet}$ states of PSII OEC.[33]

The second proposal was suggested by Siegbahn.[34] In this mechanism, a "C-shaped" Mn-oxo cluster was used as the template for a hypothetical O-O bond formation caused by the interaction between an oxyl radical and a μ-oxo atom (Figure 10). The incorporated Ca^{2+} was included as a bridging metal ion to assist in the formation of an oxyl radical between the S_2 and S_3 states of the OEC cycle.

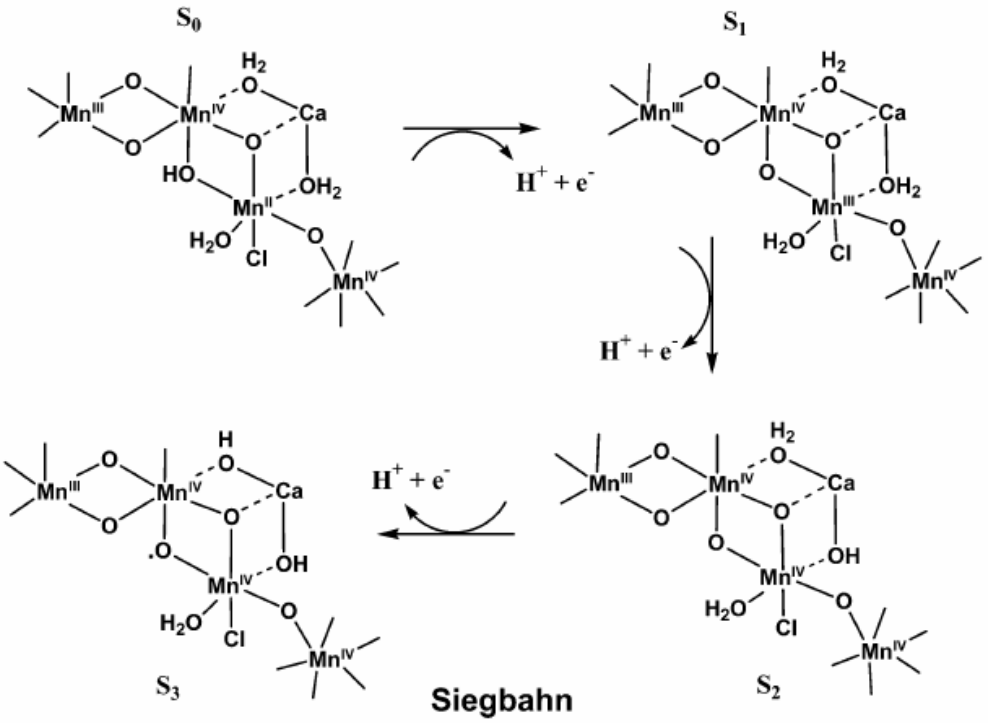

Figure 1.10. Partial water oxidation cycle proposed by Siegbahn based on a "C-shaped" Mn-oxo cluster.[34]

A third scheme proposed for water oxidation and dioxygen evolution was made on the basis of the X-ray absorption (EXAFS) and EPR spectroscopy data (Figure 11).[35] The Mn-oxo complex is an open dimer-of-dimers model as well, which is also known as the 'Berkeley model'. Yachandra et al. suggested that in the model, which consists of a single oxo-bridge between the two $\{Mn_2O_2\}$ units, the intermediate oxyl radical species was utilized for the O-O bond formation preceding O_2 evolution. Even though the exact

structure of the S_4 state remains in dispute, the biophysical data for the PSII enzyme study have established several aspects of the OEC structure in the S_0 to S_3 states.

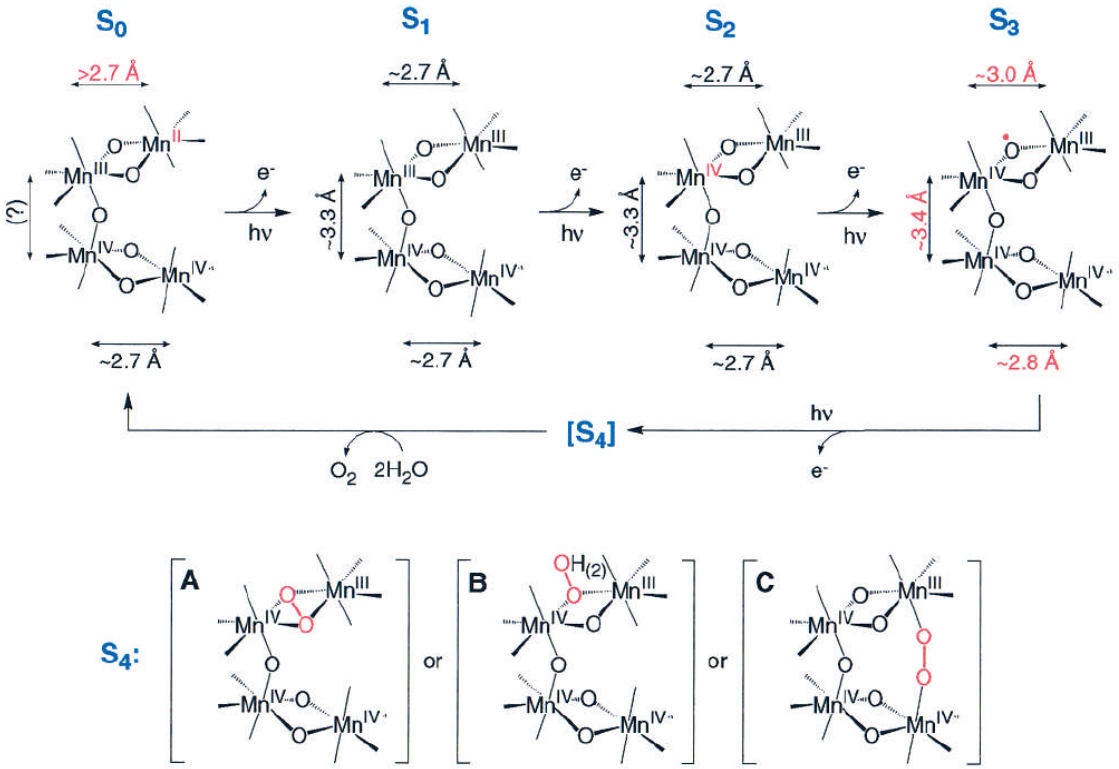

Figure 1.11. A catalytic cycle proposed by Yachandra et al. incorporating an open dimer-of-dimer structural model.

Brudvig and Crabtree proposed a cycle that incorporated cubane- and adamantane-shaped Mn-oxo cores in the catalytic cycles (Figure 12).[36] During the course of the catalytic cycle, the Mn-oxo cluster undergoes a structural rearrangement from cubane to adamantane at $S_2 \rightarrow S_3$ state and, after releasing O_2, the cluster would transform back to the original cubane conformation. They suggested that this type of structural rearrangement would facilitate the water molecules binding to the active site of the OEC cluster, and the structural transition would help in the releasing of O_2.

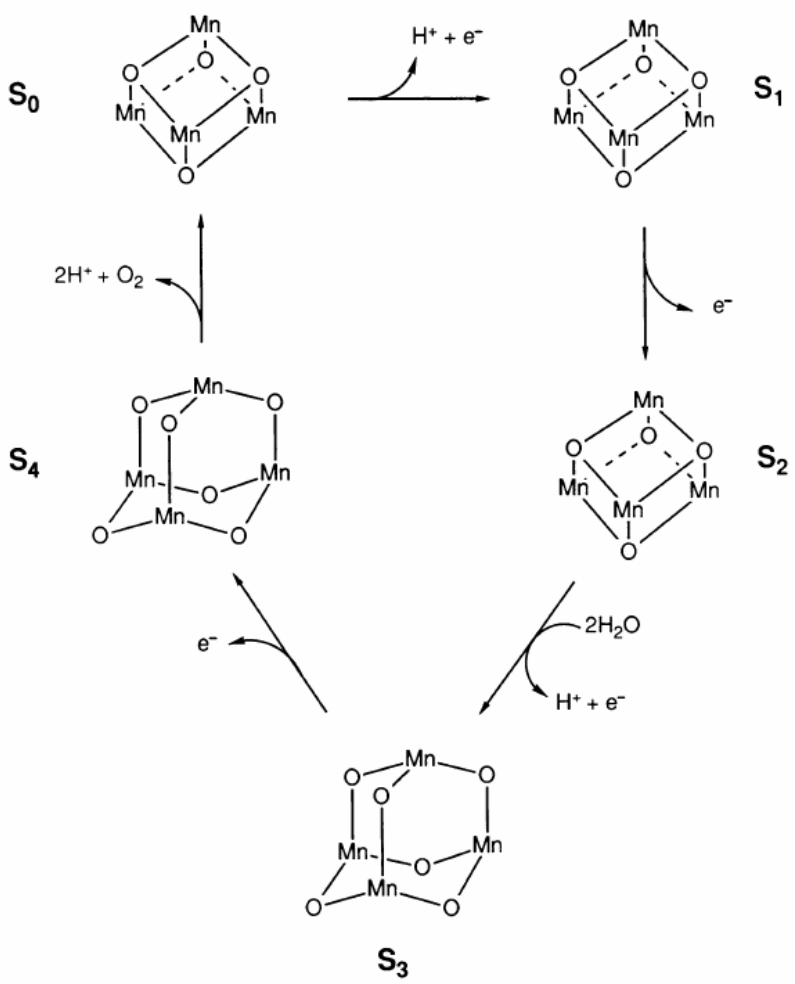

Figure 1.12. The catalytic cycle proposed by Brudvig and Crabtree, which involved cubane to adamantane and the reverse structural rearrangements.

One of the most recent proposals was put forth by Messinger et al. (Figure 13).[37] It is based on the XRD crystallographic structure at 3.5 Å resolution (shown in Fig. 5 (c) in purple), which introduces a proposed structure incorporating a $CaMn_3$ cubane cluster and an appended fourth manganese atom. Note that the position of chloride is also indicated. It was proposed that water binds between the "dangling" Mn atom and the Ca atom, and that is where the O-O bond formation is proposed to occur, followed by O_2 release without structural rearrangement of the cubane core. The plausible manganyl (Mn^{V}=O)

species was also suggested as an intermediate in the S_4 state responsible for the O-O bond formation and O_2 release.

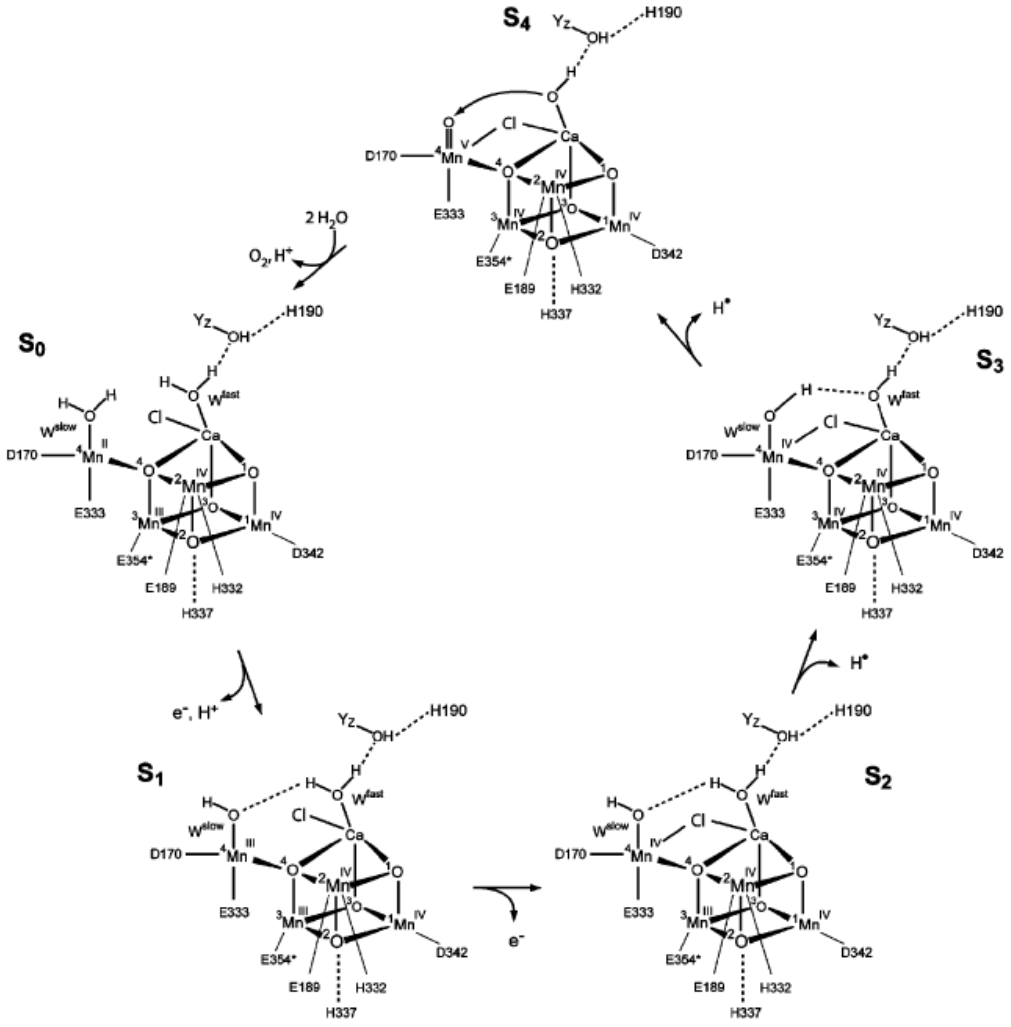

Figure 1.13. The recently proposed catalytic cycle by Messinger based on the XRD crystallographic structure reported by Barber et al.

Lastly, there are more recent proposals similar to the one shown in Figure 13. The mechanisms for each of these are based on the different hypothetical structures and they should also be considered equally possible. Researches such as Dau, Dismukes, Christou, Pecoraro, Wieghardt and Armstrong all have proposed catalytic cycles or key steps based on their own synthetic cluster systems. These additional ideas could be

incorporated while refining proposed mechanisms for PSII OEC water oxidation and dioxygen evolution. We believe that synthesis and characterization of the tetramanganese-oxo-bridged structures such as those with cubane, adamantane, butterfly, dimer-of-dimers, semi-cubane, linear and bent Mn_4O_6 cores will not only greatly enhance the study of high valent manganese coordination chemistry but also the study of them and new ones to come will eventually lead to a detailed understanding of the PSII OEC catalytic cycle.

We have long been involved in studying the theory of some of the proposed catalytic cycles that were mentioned above. We have examined plausible manganyl species of the intermediate type as proposed to exist at the OEC S_4 state. The existence of manganyl in synthetic model system will be presented in Chapter 2. In this study, we utilized stopped-flow UV-vis spectroscopy and mass spectrometry to investigate the formation and the nature of the intermediate in the reaction between mononuclear Schiff base manganese complexes and a reagent that is often used for O atom transfer reactions. Chapter 3 involves establishment of a logical synthetic method to prepare the related complexes, $Mn_2O_2(bpy/dmb)_2(Ar^RCOO)_2$ [R = 2,6-diphenyl, 2,6-ditolyl]. The dimanganese-oxo center was considered as a basic unit on the path toward the construction of high nuclearity Mn aggregates, preferably Mn_4 clusters to be used for OEC catalytic cycle mimicry. Controlled ligand exchange synthesis of this type of carboxylate-rich/bridged $\{Mn_2O_2\}$ dimers will provide an alternate pathway toward obtaining the Mn aggregates that are not attainable by direct 'self-assembly' synthetic methods. In Chapter 4, we will describe a novel mixed-ligand tetranuclear Mn cluster of the adamantane core type, $[Mn_4(\mu\text{-}O_6)(bpy)_4(py)_4](ClO_4)_4$. This cluster was synthesized by using a simple reaction

and its spectroscopic characterization will be discussed. We will also demonstrate the possible chromatographic separation for the Mn clusters which we encountered in this work (see Appendix A).

1.4. References

1. Hill, R. *Proc. Roy. Soc. London. Series B, Biol. Sci.* **1939**, *127(847)*, 192-210.
2. (a) Taiz, L.; Zeiger, E. *Plant Physiology 4th Ed.*, **2006**.
   (b) Bryant, D. A.; Frigaard, N.-U. *Trends Microbiol.* **2006**, *14(11)*, 488-496.
3. Govindjee, Govindjee, R. *Bioenergetics of Photosynthesis*, *Academic Press*, **1975**, pp. 27; Demeter, S.; Govindjee *Physiologia Plantarum*, **1989**, *Vol. 75*, 121-130.
4. Shriver, D. F.; Atkins, P.; Lanford, C. H. *Inorganic Chemistry 2nd Edition*, **1994**, *Chapter 19*, pp. 813.
5. Clavin, M. *Nobel Lecture, Dec. 11, 1961, Chemistry 1942-1962*, Elsevier Publishing Company, Amsterdam, **1964**.
6. Singhal, G. S.; Renger, G.; Sopory, S. K.; Irrgang, K. D. *Concepts in Photobiology: Photosynthesis and Photomorphogenesis* **1999**, pp. 13.
7. Hill, R.; Bendall, F. *Nature* **1960**, *186*, 136-137.
8. Barber, J. *Q. Rev. Biophys.*, **2003**, *36*, 71-89.
9. Bricker, T. M.; Ghanotakis, D. F. in *Oxygenic Photosynthesis: The Light Reactions*; Ort, D. R.; Yocum, C. F., Eds.; Kluwer Academic Publishers: Dordrecht, **1996**; pp. 113-136.
10. Masojikek, J.; Droppa, M.; Horvath, G. *Eur. J. Biochem.* **1987**, *169*, 283-288.

11. Tsiotis, G.; Walz, T.; Spyridake, A.; Lustig, A.; Engel, A.; Ghanotakis, D. *J. Mol. Biol.* **1996**, *259*, 241-248.

12. (a) Meyer, T. J.; Huynh, M. H. V.; Thorp, H. H. *Angew. Chem. Int. Ed.* **2007**, *46*, 5284-5304.

(b) Mayer, J. M.; Rhile, I. J.; Larsen, F. B.; Mader, E. A.; Markle, T. F.; DiPasquale, A. G. *Photosynth. Res.* **2006**, *87*, 3-20.

(c) Tommos, C.; Babcock, G. T. *Acc. Chem. Res.* **1998**, *31(1)*, 18-25.

13. Britt, R. D. in *Oxygenic Photosynthesis: The Light Reactions*; Ort, D. R.; Yocum, C. F., Eds.; Kluwer Academic Publishers: Dordrecht, **1996**; pp. 137-164.

14. Holzenburg, A.; Bewley, M. C.; Wilson, F. H.; Nicholson, W. V.; Ford, R. C. *Nature* **1993**, *363*, 470-472.

15. Rhee, K.-H.; Morris, E. P.; Barber, J.; Kühlbrandt, W. *Nature* **1998**, *396*, 283-286.

16. Kamiya, N.; Shen, J.-R. *Proc. Natl. Acad. Sci. U.S.A.* **2003**, *100*, 98-103.

17. Ferreira, K. N.; Iverson, T. M.; Maghlaoui, K.; Barber, J.; Iwata, S. *Science*, **2004**, *19*, 1831-1838.

18. Loll, B.; Kern, J.; Saenger, W.; Zouni, A.; Beisiadka, J. *Nature*, **2005**, *438*, 1040-1044.

19. Yano, J.; Kern, J.; Irrgang, K.-D.; Latimer, M. J.; Bergmann, U.; Glatzel, P.; Pushkar, Y.; Biesiadka, J.; Loll, B.; Sauer, K.; Messinger, J.; Zouni, A.; Yachandra V. K. *Proc. Natl. Acad. Sci. U.S.A.* **2005**, *102*, 12047-12052.

20. (a) Wemple, M. W.; Adams, D. M.; Folting, K.; Hendrickson, D. N.; Christou, G. *J. Am. Chem. Soc.* **1995**, *117*, 7275-7276.

(b) Cinco, R. M.; Rompel, A.; Visser, H.; Aromí, G.; Christou, G.; Sauer, K.; Klein, M. P.; Yachandra, V. K. *Inorg. Chem.* **1999**, *38*, 5988-5998.

(c) Chan, M. K.; Armstrong, W. H. *J. Am. Chem. Soc.* **1991**, *113*, 5055-5057.

(d) Chan, M. K. *Ph. D thesis*, University of California, Berkeley, **1986**.

21. Grabolle, M.; Haumann, M.; Müller, C.; Liebisch, P.; Dau, H. *J. Biol. Chem.* **2006**, *281(8)*, 4580-4588.
22. Dubois, L.; Jacquamet. L.; Pécaut, J.; Latour, J.-M. *Chem. Comm.* **2006**, *43*, 4521-4523.
23. (a) Yachandra, V. K. *Philos. Trans. R. Soc. London. Ser. B: Biol. Sci.* **2002**, *357*, 1347-1358.

(b) Sauer, K.; Yachandra, V. K. *Proc. Natl. Acad. Sci. U.S.A.* **2002**, *99*, 8631-8636.

(c) Britt, R. D.; Peloquin, J. M.; Campbell, K. A. *Annu. Rev. Biophys. Biomol. Struct.* **2000**, *29*, 463-495.

24. Mamedov, F.; Danielsson, R.; Gadjieva, R.; Albertsson, P.-Å.; Styring, S. *Biochemistry* **2008**, *47*, 3883-3891.
25. Britt, R. D.; Campbell, K. A.; Peloquin, J. M.; Gilchrist M. L.; Aznar, C. P.; Dicus, M. M.; Robblee, J.; Messinger, J. *Biochim. Biophy. Acta* **2004**, *1655*, 158-171.
26. Tang, X.-S.; Randall, D. W.; Force, D. A.; Diner, B. A.; Britt, R. D. *J. Am. Chem. Soc.*, **1996**, *118(32)*, 7638-7639.
27. Chu, H.-A.; Hillier, W.; Law, N. A.; Sackett, H.; Haymond, S.; Babcock, G. T. *Biochim. Biophy. Acta.* **2000**, *1459*, 528-532.
28. Visser, H.; Dubé, C. E.; Armstrong, W. H.; Sauer, K.; Yachandra, V. K. *J. Am. Chem. Soc.* **2002**, *124*, 11088-11017.

29. Cua, A.; Stewart, D. H.; Reifler, M. J.; Brudvig, G. W.; Bocian, D. F. *J. Am. Chem. Soc.* **2000**, *122*, 2069-2077.

30. Eilers, G.; Zettersten, C.; Nyholm, L.; Hammarström, L.; Lomoth, R. *Dalton Trans.*, **2005**, *6*, 1033-1041.

31. Burda, K.; Bader, K.; Schmid, G. H. *Biochim. Biophy. Acta* **2003**, *1557*, 77-82.

32. Lippard, S. J.; Berg, J. M. *Principles of Bioinorganic Chemistry*; University Science Books, **1994**.

33. Tommos, C.; Babcock, G. T. *Acc. Chem. Res.* **1998**, *31*, 18-25.

34. Siegbahn, P. E. M. *Inorg. Chem.* **2000**, *39*, 2923-2925.

35. Messinger, J.; Robblee, J. H.; Bergmann, U.; Fernandez, C.; Glatzel, P.; Visser, H.; Cinco, R. M.; McFarlane, K. L.; Bellacchio, E., Pizarro, S. A.; Pizarro, S. A.; Cramer, S. P.; Sauer, K.; Klein, M. P.; Vachandra, V. K. *J. Am. Chem. Soc.* **2001**, *123*, 7804-7820.

36. Brudvig, G. W.; Crabtree, R. H. *Proc. Natl. Acad. Sci. USA* **1986**, *Vol. 83*, 4586-4588.

37. (a) Messenger, J. *Phys. Chem. Chem. Phys.* **2004**, *6*, 4764-4771.

(b) Vrettos, J. S.; Limburg, J.; Brudvig, G. W. *Biochim. Biophys. Acta* **2001**, *1503*, 229-245.

Chapter 2

Spectroscopic and Kinetic Study of a Model of the Photosystem II S_4 State Using Schiff Base Complexes

2.1. Background

In photosynthesis, water is the ultimate source of electrons required for CO_2 reduction.[1] In turn, the $4e^-$ oxidation of water results in the formation of dioxygen. It is thought that the substrate water molecules bind to the OEC active site tetramanganese-oxo cluster active site as the first step in oxygen production, however, the actual detailed mechanism is still poorly understood (Chapter 1). Several hypothetical mechanisms for enzymatic water oxidation invoke a reactive manganyl (Mn=O) intermediate (Figure 1); generally it is accepted as Mn^{V}=O but disputably also proposed as Mn^{IV}≡O by some researchers.[2]

Hypothesis:

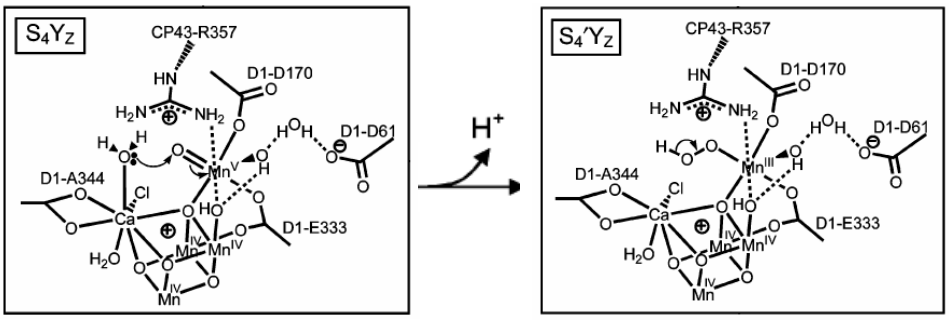

Figure 2.1. The proposed mechanism for the OEC catalytic cycle at S_4 state based on the crystal structure reported by Barber and coworkers.[3,4]

Among synthetic compounds, there are few examples of complexes with manganese in the +5 oxidation state. Even though the direct structural evidence for the existence of reactive Mn^{V}=O complexes is still under investigation, this postulated manganyl intermediate has long been proposed as a critical intermediate in various areas of

chemistry. In organometallic chemistry, catalysis applications, such as the Kochi-Katsuki-Jacobsen epoxidation, treat the formation of a manganyl complex as the essential first step in the catalytic cycle.[5] The manganyl species has also been invoked as a hypothetical intermediate in manganese metalloenzymes structural modeling studies. For instance, the proposed OEC catalytic cycles of water oxidase as described above,[6] Mn-porphyrin complexes in biological systems[7] and Mn-catalase[8] (Mn-CAT). In these systems it has been proposed that at the enzyme active site Mn centers, the manganyl intermediate was postulated to be either the precursor of O-O bond formation[9] or the product formed after O-O bond cleavage. Most recently in an OEC catalytic cycle investigation, a German group studied the PSII protein by exploiting time-resolved X-ray absorption spectroscopy (XAS) to monitor the redox behavior of the Mn cluster.[10] They concluded that a short life-time intermediate, possibly a manganyl species, is present in the S_4/S_4' state of the photosynthetic water oxidation cycle. To our knowledge, several well characterized manganyl complexes have been reported, yet they are relatively stable and have not been shown to oxidize water.[11,12] This prompted us to search for a system that would generate a manganyl intermediate and possibly lead to O_2 evolution afterwards. We have chosen a system that retains such required characteristics according to the reported observations.[13] Within this system, mononuclear Mn Schiff-base complexes incorporating two bidentate ligands were found to react with water to produce O_2. This behavior has not been mentioned for the other related synthetic complexes such as Mn-SALEN or Mn-SALPN. Therefore, in order to scrutinize the manganyl mechanistic hypothesis, we have engaged in using the bis-bidentate model system to attempt to generate well defined manganyl species and subsequently to characterize their

characteristic spectral reactivity behavior. Here, we are examining the reactions between a strong oxygen atom transfer reagent and L_2MnX species, where, as mentioned above, L is a bidentate Schiff base ligand and X is an anion such as chloride, nitrate, or acetate. Below are described the results of stopped-flow kinetics experiments that were followed by UV-vis spectroscopy and mass spectrometry. A reactive intermediate whose properties are consistent with formulation of a manganyl species has been discovered. Analytical methods that we used for the study were all performed at room temperature. Under such conditions, the observed intermediate was found to have a short half-life (*ca.* 2 seconds). The simplified O-atom transfer reaction is shown in Equation 2.1 and a proposed reaction mechanism of the process will be provided (Scheme 2.1).

$$L_2Mn^{III}X + YO \rightarrow L_2Mn^{V}(O)X + Y \qquad (2.1)$$

However, we were neither able to isolate this detected manganyl species for structural analysis nor to obtain FTIR or resonance Raman spectroscopic data in order to make a comparison to the vibrational properties reported for the stable manganyl complexes.[11] Importantly, by altering the ligands in L_2MnX, one may tune physical properties of interest, which include Mn redox potentials and the steric environment around the metal center. The ligand alterations involve changing the nitrogen and aromatic ring substituents of the coordinated bidentate Schiff-base ligands. Success with the tunable systems described here has encouraged us to continue to employ them in our efforts to mimic key aspects of the reactivity of the PSII water oxidase active site manganese cluster.

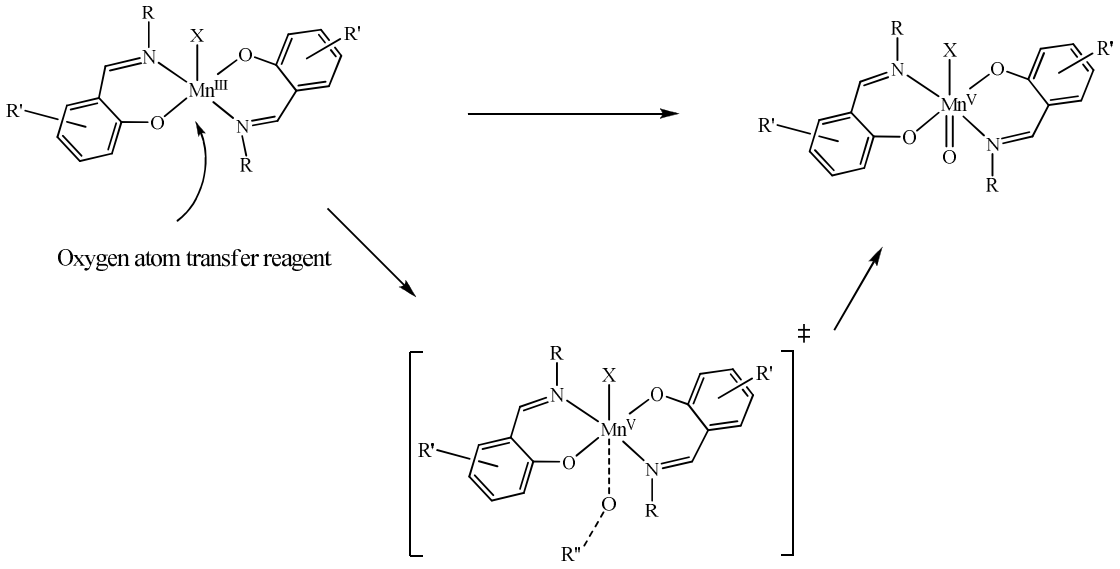

Scheme 2.1. The proposed reaction mechanism of oxygen atom transfer process.

2.2. Experimental Section

2.2.1. Materials. Methanol was distilled from magnesium turnings under nitrogen and stored over 4 Å molecular sieves prior to use. Acetonitrile used for synthesis and spectroscopic studies was distilled over CaH_2 under nitrogen and stored over 3 Å molecular sieves prior to use. Deuterated acetonitrile (Cambridge Isotope Laboratories, Inc.) was dried in oven-dried glassware over activated 3 Å molecular sieves. All other reagents were purchased from commercial sources and used as received. The solvents used for UV-vis spectroscopy measurements were anhydrous, CHROMASOLV® Plus grade (≥ 99.9%) and used as received. Paratone-N oil was obtained from Hampton Research Corp. All chemicals used in this work were reagent grade.

2.2.2. Physical Methods. ^{1}H NMR spectra data were collected on Varian Unity 300 MHz and 400 MHz spectrometers with a 60-100 kHz sweep width. A first-order correction function provided with the spectrometer software was used for baseline

correction wherever needed. Chemical shifts are quoted on the δ scale with downfield shifts assigned as having positive signs. Values for chemical shifts (ppm) are the observed shifts referenced to resonances for residual protons in the various deuterated solvents: CHD_2CN, 1.94 ppm; $CHCl_3$, 7.26 ppm; and $CHDCl_2$, 5.32 ppm. Electrospray ionization mass spectrometry (ESI-MS) was performed in the Boston College Mass Spectrometry Facility and recorded by using a Waters LCT classic instrument (Milford, MA). All samples were dissolved in LC/MS CHROMASOLV® grade solvents (≥ 99.9 %) such as acetonitrile, methanol and filtered through filter paper prior to analysis. Mass spectra were measured for 10-100 μM sample solutions in positive ion mode, and samples were infused into the spectrometer using a Harvard syringe pump operating at a flow rate of 10μL per minute. Typical instrument conditions: 3.5 kV nebulizer voltage, 5 V cone voltage, desolvation temperature at 120 °C, data were recorded using the electrospray method. Electronic spectra were collected by using a Hewlett Packard 8453 diode array spectrophotometer and a Varian Cary 50 Bio spectrophotometer. Infrared spectra were recorded by using a Nicolet 380 FTIR spectrometer on samples prepared as either KBr pellets or acetonitrile solutions or in some cases untreated when using diamond ATR analysis. Elemental analyses were obtained from Robertson Microlit Laboratories, Inc. Madison, NJ.

2.2.3. Stopped-Flow UV-vis Spectroscopy and Data Analysis. The system used was a Hi-Tech Scientific (Salisbury, Wilshire, UK) SF-43 Multi-Mixing Cryogenic Stopped-Flow instrument in the diode array mode at Tufts University, courtesy of Professor Elena Rybak-Akimova. The instrument was equipped with stainless steel plumbing, a stainless steel mixing chamber with sapphire windows, and an anaerobic gas-flushing kit. The

temperature in the mixing cell (1 cm) was maintained at 25 ± 0.1 °C, and the mixing time was 2-3 ms. Experiments were performed in the single-mixing mode. Fits of kinetic data to appropriate models was performed using nonlinear least-squares fitting methods contained in *Specfit/32* version 3.0.36.[14]

2.2.4. X-ray Crystallography. Data were collected by using a Bruker SMART CCD (charge coupled device) based diffractometer equipped with an LT-3 low-temperature apparatus operating at 193K or 100K. Suitable single crystals were chosen and mounted on a glass fiber or glass loop by using APIEZON-T grease mixed with Paratone-N oil. Data were measured using omega scans of 0.3° per frame for 20 or 30 seconds, such that a hemisphere was collected. A total of 1271 frames at the sample-detector distance of 5.00 cm or 2412 frames at 6.00 cm were collected to a maximum resolution of 0.75 Å. The first 50 frames were recollected at the end of data collection to monitor for decay. All of the crystals used for the X-ray diffraction studies showed no decomposition during the data collection. Cell parameters were determined by using the SMART software[15] and data reduction was performed and refined by using the SAINT software[16], which corrects for Lp and decay on all observed reflections. Absorption corrections were performed with the program SADABS[17] as supplied by George Sheldrick. The structures were solved by the direct or Patterson method using the program SHELXS-97 program[18] and refined by least squares methods on F^2 in SHELXL-97, incorporated in SHELXTL-PC V 5.10[19]. All non-hydrogen atoms were refined with anisotropic thermal parameters. Hydrogen atom positions were calculated by geometrical methods and refined by using a riding model. All ORTEP drawings are made using 50% probability thermal ellipsoids.

2.2.5. Preparation of Compounds.

Ligand Synthesis. The ligands were prepared by the same condensation method[20] as described below.

2-((R-imino)methyl)phenol [*N*-R-salicylideneamine] (R = H, methyl, ethyl, *n*-propyl, *n*-butyl, isobutyl). Mixing salicylaldehyde (1.0 mL, 10 mmole) with 1 equivalent of various amines (2.0M ammonia in EtOH, 0.22 mL; 33 wt% methylamine in absolute EtOH, 1.2 mL; 2.0M ethylamine in MeOH, 5.0 mL; *n*-propylamine, 0.82 mL; *n*-butylamine, 0.99 mL; isobutylamine, 0.99 mL) in 10 mL of methanol. A bright yellow solution was formed after adding each of the amines. The resulting solutions were refluxed with continuous stirring for 20 min and then evaporated to dryness by using a rotary evaporator. Not surprisingly, crude yields of the products were approximately quantitative (ammonia, 1.16 g; methylamine, 1.20 g; ethylamine, 1.44 g; *n*-propylamine, 1.58 g; *n*-butylamine, 1.73 g; isobutylamine, 1.88 g). The oil-like products were used for further synthesis without purification. The purity of these ligands was verified by ^{1}H NMR and mass spectra. Examples of the analytical results are provided in Appendix B and D.

2-((R'-imino)methyl)-6-nitro-phenol [*N*-R'-3-nitro-salicylideneamine] (R' = H, methyl, ethyl, *n*-propyl, *n*-butyl). One equivalent of various amines (2.0M ammonia in EtOH, 21.7 µL; 33 wt% methylamine in absolute EtOH, 0.12 mL; 2.0M ethylamine in MeOH, 5.0 mL; *n*-propylamine, 82.2 µL; *n*-butylamine, 99.2 µL) were mixed with 2-hydroxy-3-nitro-benzaldehyde (0.167 g, 1 mmole) in 10 mL of methanol. For each reaction, a bright yellow, slightly orange solution formed after addition of the amines. The resulting solutions were refluxed with continuous stirring for 20 min and evaporated

to dryness by using a rotary evaporator. Crude yields of the products were approximately quantitative (ammonia, 0.18 g; methylamine, 0.18 g; ethylamine, 0.20 g; *n*-propylamine, 0.22 g; *n*-butylamine, 0.25 g). The products were used for the syntheses of manganese complexes without further purification. The purity of these ligands was verified by ^{1}H NMR and mass spectra. Examples of the analytical results are provided in Appendix B and D.

2-((R'-imino)methyl)-4-nitro-phenol [*N*-R'-5-nitro-salicylideneamine] (R' = H, methyl, ethyl, *n*-propyl, *n*-butyl, isobutyl). Mixing 2-hydroxy-5-nitro-benzaldehyde (33.42 mg, 2 mmole) with 1 equivalent of various amines (2.0M ammonia in EtOH, 1.0 mL; 33 wt% methylamine in absolute EtOH, 0.25 mL; 2.0M ethylamine in MeOH, 1.0 mL; *n*-propylamine, 0.16 mL; *n*-butylamine, 0.198 mL; isobutylamine, 0.198 mL) in 10 mL of methanol resulted in the formation of a bright yellow, slightly orange solution. The resulting solution was refluxed with continuous stirring for 20 min and evaporated to dryness by using a rotary evaporator. Crude yields of the products were approximately quantitative (ammonia, 0.36 g; methylamine, 0.38 g; ethylamine, 0.396 g; *n*-propylamine, 0.42 g; *n*-butylamine, 0.44 g; isobutylamine, 0.47 g). The products were used for the synthesis of manganese complexes without further purification. The purity of these ligands was verified by ^{1}H NMR and mass spectra. Examples of the analytical results are provided in Appendix B and D.

Synthesis of Manganese Complexes.

[Mn^{III}(*N*-R-Sal)$_2$](Cl) (where R = methyl [**1**], ethyl [**2**], *n*-propyl [**3**], *n*-butyl [**4**])**.**

Method (A). The complexes were synthesized by using a published method.[21] A quantity of 1 mmole of each Schiff-base ligand (**1**, 0.18 g; **2**, 0.20 g; **3**, 0.22 g; **4**, 0.23 g)

was dissolved in 25 mL of EtOH to give a bight yellow, slightly orange colored solution. Immediately, 0.5 equivalent of solid $Mn(OAc)_3 \cdot 2H_2O$ (0.14 g, 0.5 mmole) was added and a dark green colored solution was formed after mixing well. The resulting solution was refluxed for 1 h and then 1.5 equivalents of solid LiCl (31.8 mg, 0.75 mmole) were added into the solution. The LiCl was not fully dissolved in solution - some residue was observed floating on the surface. The solution was refluxed once again for another 1 h and the undissolved LiCl gradually disappeared. The solvent was removed by using a rotary evaporator to give a dark greenish crude product. The crude product was dissolved in a small amount of MeOH (*ca.* 10 mL), filtered, and the filtrate was layered with 200 mL of diethyl ether (Et_2O) in a 250 mL round-bottom flask. The mixture was kept at –20 °C for 1 d. Dark green crystalline product was obtained and collected by filtration. Yield: **1**, 79.15 mg (4.82%); **2**, 0.27 g (34.91%); **3**, 0.28 g (18.02%); **4**, 0.25 g (15.22%). The purity of the complexes was confirmed by ^{1}H NMR and mass spectra.

Method (B). A 10 mmole quantity of each bidentate Schiff-base ligand (**1**, 1.49 g; **2**, 1.53 g; **3**, 1.61 g; **4**, 1.79 g) was dissolved in 10mL of MeOH to form a bright yellow solution. To this yellow methanol solution, an ethanolic solution (*ca.* 7 mL) of 0.5 equivalent of $MnCl_2 \cdot 4H_2O$ (1.01 g, 5.0 mmole) was added slowly and a dark green color developed. The resulting solution was refluxed for 2 h with continuous stirring. The solution was then evaporated to dryness by using a rotary evaporator to give a dark brownish green crude product. The crude product was redissolved in a minimum amount of MeOH (*ca.* 6 mL), filtered, and the filtrate was layered with 200 mL of diethyl ether (Et_2O) in a 250 mL round-bottom flask. The mixture was kept at –20 °C for 1 d. Dark green crystalline product was obtained and collected by filtration. Yield: **1**, 1.11 g

(56.2%); **2**, 0.587 g (31.03%); **3**, 1.003 g (49.04%); **4**, 0.787 g (35.19%). The purity of the complexes was confirmed by ^{1}H NMR and mass spectra.

Targeted Complex: [Mn^{III}(N-R-3-NO_2-Sal)$_2$](CH_3COO) (where R = methyl [**5**], ethyl [**6**], *n*-propyl [**7**], *n*-butyl [**8**], isobutyl [**9**]).

One mmole of each bidentate Schiff-base ligand (**5**, 0.18 g; **6**, 0.19 g; **7**, 0.20 g; **8**, 0.22 g; **9**, 0.22 g) was dissolved in 10 mL of MeOH to give a yellowish colored solution. Immediately, 0.5 equivalents of $Mn(OAc)_3{\cdot}2H_2O$ (0.14 g, 0.5 mmole) was added and a dark greenish color solution was formed. The resulting solution was stirred for 5-10 min at room temperature open to the air. The solution was evaporated to dryness by using a rotary evaporator. The crude products were examined by mass spectrometry and the desired species were observed, however impurities were presented as well. In addition, for ligands **5**, **6**, **7** and **8** we found unexpected MS results (Appendix D), which revealed a set of m/z signals corresponding to a putative high nuclearity manganese aggregate. The actual structure of this complex is still unclear.[22] The crude product was then redissolved in a minimum amount of MeOH (*ca.* 8 mL), filtered, and the filtrate was layered with 150 mL of diethyl ether (Et_2O) in a 200 mL round-bottom flask. The mixture was kept at –20 °C for 1 d. We did not observe the targeted mononuclear manganese complexes in the recrystallized products but instead tetramanganese aggregates {[$Mn^{III,III}_2$(μ-O)(μ-OMe)(μ-OAc)(*N*-*n*-*Bu*-3-NO_2-Sal)$_2$]$_2$} [**10**] and {[$Mn^{III,III}_2$(μ-O)(μ-OMe)(μ-OAc)(*N*-*Et*-3-NO_2-Sal)$_2$]$_2$} [**11**] were isolated and structurally characterized. See Section 2.3.1 for further discussion.

[Mn^{III}(N-R-3-NO_2-Sal)$_2$](Cl) (where R = H [**12**], methyl [**13**], ethyl [**14**], *n*-propyl [**15**], *n*-butyl [**16**], isobutyl [**17**]).

The synthetic procedure described above as Method A was followed. The reactions were carried out on a 1 mmole scale of the bidentate Schiff-base ligand. The various amines (**12**, 0.18 g; **13**, 0.19 g; **14**, 0.20 g; **15**, 0.22 g; **16**, 0.23 g; **17**, 0.23 g) were dissolved in a mixture of 10mL of CH_2Cl_2 and 10 mL of MeOH to give a bight yellow, slightly orange solution. Then 0.5 equivalent of solid $Mn(OAc)_3 \cdot 2H_2O$ (0.15 g, 0.5 mmole) was added into this solution. The solution color changed from light yellowish orange to dark green, brown. The resulting solution was stirred at room temperature for 2-3 min, and then 1.5 – 2 equivalents of LiCl (35.7 – 49.6 mg, 0.84 – 1.17 mmole) were added but it did not fully dissolve. The solution was then refluxed for 1 h during which time the remaining LiCl dissolved. The solvent was removed by using a rotary evaporator to give a dark green crude product. This material was dissolved in a minimum amount of MeOH (*ca.* 10 mL), filtered, and the filtrate was layered with 200 mL of diethyl ether (Et_2O). The mixture was kept at –20 °C for 1 d. Dark green crystalline product was obtained and collected by filtration. Yield: **12**, 0.118 g (51.67 %); **13**, 0.2195 g (97.92%); **14**, 0.167 g (68.3%); **15**, 22.8 mg (8.55%); **16**, 75.2 mg (25.1%); **17**, 0.113 g (36.32%). The purity of the complexes was assessed by ^{1}H NMR and mass spectra.

2.3. Results and Discussion

2.3.1. Synthesis. In this work, a series of mononuclear Mn Schiff-base complexes were prepared either according to the literature procedure[13] or by using an alternative synthetic method developed by us (Section 2.2.5). For the purpose of carrying out a comparative study, we have altered the substituents on the aromatic ring as well as at the imino

nitrogen (*N*-) position. We also varied the counterions coordinated to the manganese center. This ligand diversity allows us to probe the feasibility of transferring an oxygen atom from a donor to a given manganese center ideally to form a detectable manganyl intermediate. Use of an assorted ligand type that allows us to vary systematically electronic and steric properties was deemed to be highly desirable. For the bidentate Schiff-base ligands without substituents on the aromatic ring, we were able to obtain relatively pure MnL_2X (where X = Cl) monomeric complexes, which were characterized spectroscopically. The corresponding X-ray crystal structures for two of these complexes are shown in Section 2.3.2. In a second Schiff-base ligand series with each member having a NO_2 substituent at the 3-position of the aromatic ring, the products of reactions between manganese starting material, $Mn(OAc)_3{\cdot}2H_2O$, and these ligands resulted in a more diverse set of complex types, which were structurally characterized as well. The first type of unexpectedly formed species was a dimer-of-dimer aggregate, which formed during the attempted preparation of MnL_2X (where X = acetate). Crystal structures are presented in Figure 2 and 3 for $\{[Mn^{III,III}{}_2(\mu\text{-}O)(\mu\text{-}OMe)(\mu\text{-}OAc)(N\text{-}n\text{-}Bu\text{-}3\text{-}NO_2\text{-}Sal)_2]_2\}$ [**10**] and $\{[Mn^{III,III}{}_2(\mu\text{-}O)(\mu\text{-}OMe)(\mu\text{-}OAc)(N\text{-}Et\text{-}3\text{-}NO_2\text{-}Sal)_2]_2\}$ [**11**] respectively. Within these aggregates, the Mn oxidation states remained at 3+ and methoxy anions are bridging between three metal centers. We decided not to carry out O-atom transfer reactions with these tetranuclear aggregates and instead to focus on mononuclear systems, which was our original intention. A second type of unusual complex we discovered while working with the nitro-substituted ligands was $[ML_2$(L-dealkylated-*N*-R)], a tris-bidentate mononuclear Mn(III) complex with one abnormal Schiff-base ligand that was apparently the result of *N*-dealkylation. The X-ray crystal structure of such a

species is presented in Figure 4 below. Since the complexes described above were found only in the 3-NO_2 substituted Schiff-base ligand system, we have speculated that the formation of these clusters is correlated to the strong electron withdrawing character of this aromatic ring substituent. Even though we encountered unexpected products from the synthetic procedures, we kept our focus on using the MnL_2X with 3-NO_2 substituted Schiff-base ligand system as O atom acceptors, mainly due to the reported ability of these species to oxidize water with the release of dioxygen.[21] A key aspect of our work was to detect reaction intermediates and to see if there was any evidence of manganyl complex ($L_2Mn=O$) formation. We postulated that the likelihood of producing reactive manganyl complexes was greater with the ligands we chose compared to the polyanionic ligands employed by others, where stable Mn=O species were obtained.[11,12] Additionally, the Mn complexes of tetradentate Schiff-base ligands SALEN/SALPN, which are effective as epoxidation catalysts, are thought to convert to manganyl complexes under O-atom transfer conditions; however, dioxygen evolution has not been reported in these cases. Therefore, we have directed most of our attention on the synthetic Mn complexes obtained by using the *N*-ethyl 3-NO_2 Schiff-base ligands as the first system to carry out related examinations for the purpose of testing our postulation (Section 2.3.4 and 2.3.5). In this system, we observed both MnL_2X (where X = Cl) and ML_3 as a mixture for the resulting product, which unfortunately co-crystallized such that we were not able to achieve isolation of $[Mn^{III}(N\text{-Et-3-}NO_2\text{-Sal})_2](Cl)$ [**14**] by itself. Several synthetic procedures, alternative to the one described above in Section 2.2.6, were used in order to attempt to prevent the occurrence of the ML_3 species [**14a**] and to obtain pure MnL_2X, which is complex needed for further kinetics study. For example, we tried 1) slow-

addition of ligand to a solution of the manganese starting material, 2) low-temperature reaction conditions and 3) sequential ligand substitution using $Mn(acac)_3$ as the starting material [$Mn(acac)_3$ + n L $\rightarrow$ product, where n = 1, 2, 3, and 4]. While these methods have not been successful, we continue to investigate systems with various ligand types that have different *N*- as well as aromatic substituents. It is worth noting that in the $Mn(acac)_3$ case, the reaction could be followed by NMR spectroscopy and interesting spectra consistent with ligand exchange products were observed. The resulting ^{1}H NMR spectrum of the reaction between one equivalent of $Mn(acac)_3$ and two equivalents of ligand is shown in Appendix B. We believe that this method is particularly worthy of further investigation. For our initial O-atom transfer studies presented below, the co-cyrstallized product [**14**] + [**14a**] was used since no alternative systems were available. We presume that the ML_3 [**14a**] species is innocent under our reaction conditions because it does not have an open or rapidly exchangeable coordination site, which is most likely required in order for it to function as an O-atom transfer acceptor. Additionally, when we carried out a reaction using the stoichiometric ratio of 1 $Mn(OAc)_3{\cdot}2H_2O$: 4 L, overnight stirring at room temperature and then heating at 50 °C for 3 h, an interesting ^{1}H NMR spectral result, which is also included in Appendix B, was observed. The spectrum revealed a simple pattern of isotropic shifts, showing six prominent resonances in the paramagnetic region between –30 to +100 ppm[23] and approximately eight resonances were also observed in the diamagnetic region between 0 to +12 ppm.

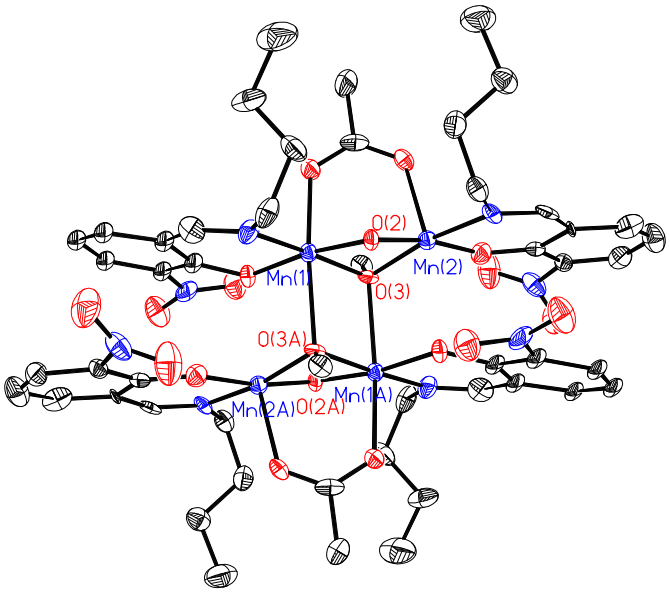

Figure 2.2. ORTEP drawing of {[$Mn^{III,III}_2$(μ-O)(μ-OMe)(μ-OAc)(*N-n-Bu*-3-NO_2-Sal)$_2$]$_2$} [**10**] showing 50% probability thermal ellipsoids and all the hydrogen atoms omitted for clarity.

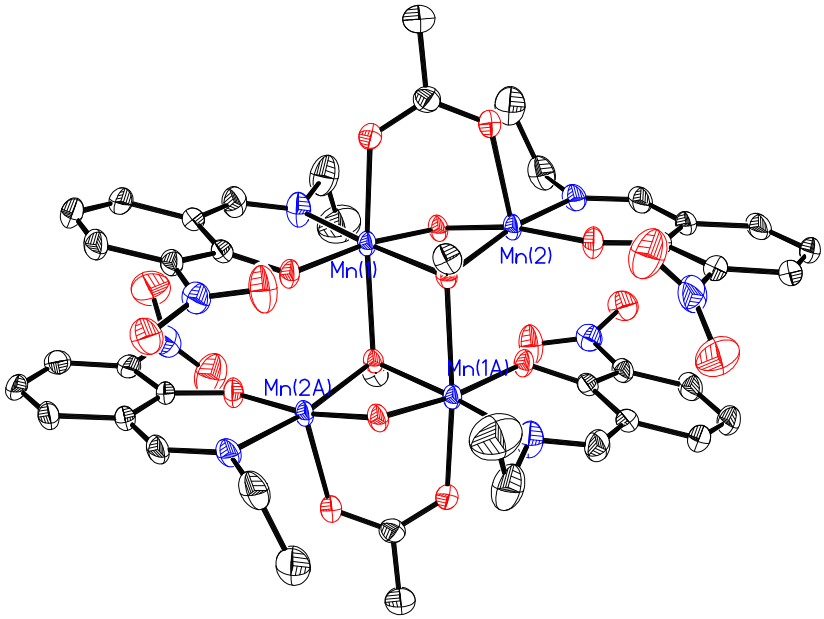

Figure 2.3. ORTEP diagram of crystal structure of {[$Mn^{III,III}_2$(μ-O)(μ-OMe)(μ-OAc)(*N-Et*-3-NO_2-Sal)$_2$]$_2$} [**11**], showing 50% probability thermal ellipsoids and all the hydrogen atoms are omitted for clarity.

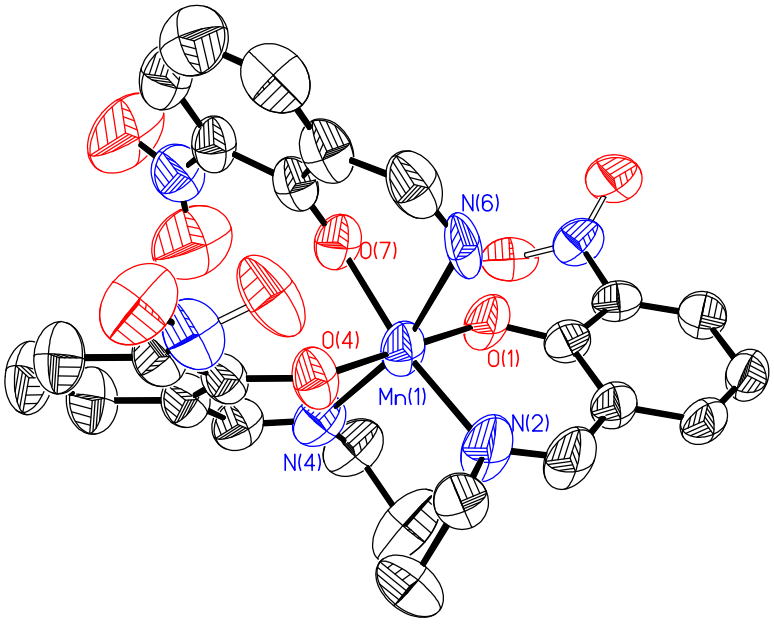

Figure 2.4. ORTEP diagram Mn^{III}(*N*-Et-3-NO_2-Sal)$_2$(3-NO_2-salicylaldehyde) showing 50% probability thermal ellipsoids and all the hydrogen atoms are omitted for clarity.

2.3.2. Crystal Structures. The X-ray crystal structures shown in this section represent the two systems that we prepared for subsequent spectroscopic studies. Mn^{III}(*N*-n-propyl-Sal)$_2$Cl and Mn^{III}(*N*-n-butyl-Sal)$_2$Cl are examples of manganese complexes of the Schiff-base ligands with unsubstituted aromatic ring and are shown in Figures 5 and 6, respectively. For manganese complexes of the Schiff-base ligand with a 3-NO_2 substituent on the aromatic ring, we obtained a co-crystallized product of MnL_2Cl with ML_3, which are shown in Figures 7 and 8, respectively. The ORTEP diagrams presented here are displayed in separate figures for the purpose of clarity. These two molecules were located in the same unit cell and the final refinement gave a relatively high R value (R = ~ 18 %) because the crystal was inherently twinned. Nonetheless, the overall structure and the connectivity for both of molecular Mn complexes were identified

without ambiguity. In the MnL_2X (X = Cl) crystal structures presented here, the bidentate Schiff-base ligands were observed ligating in a *trans* configuration with respect to each other. The manganese coordination sphere has N atoms from one ligand trans to the oxygen atoms of the other ligand. This is in contrast to the manganese coordination environment in Mn SALEN/SPLEN complexes, where N atoms are in a *cis* orientation with respect to each other as are the O atoms. The molecular shape of the MnL_2Cl complexes is observed to be square pyramidal. It is noteworthy that these Mn(III) mononuclear complexes have longer Mn-Cl bond lengths compared to those of the MnL_2Cl_2 complexes in which manganese is in the +4 oxidation state.[24] The MnL_2Cl_2 molecules have two *trans* chloride ligands and surprisingly, the bond distances between Mn-N and Mn-O were found to be nearly identical. For complexes [**3**], [**4**] and [**14**], Mn-Cl bond lengths are 2.398 Å [**3**], 2.406 Å [**4**] and 2.406 Å [**14**]. On the other hand, for the Mn(IV) species, MnL_2Cl_2, Mn-Cl bond lengths are between 2.243 – 2.272 Å. However, the Mn-N and Mn-O bond distances in both the +3 and +4 oxidation states complexes, Mn-N bonds are all observed between 2.024 – 2.039 Å and Mn-O bonds between 1.849-1.853 Å. The only exception for Mn-N and Mn-O bond lengths was [**14**], for which Mn-O bonds are 1.858 and 1.883 Å and Mn-N bonds are 2.068 and 2.076 Å. We think the reason for the observed exceptional bond lengths is mainly because of the strong electron withdrawing character of the nitro substituent on the aromatic ring (3-NO_2), which affected the related metal to ligand bonds. Additionally, since the dichloromanganese (IV) complexes were reported with chloride ligands coordinated in a *trans* configuration, we conjecture that the putative manganyl intermediate has the oxo group trans to chloride.

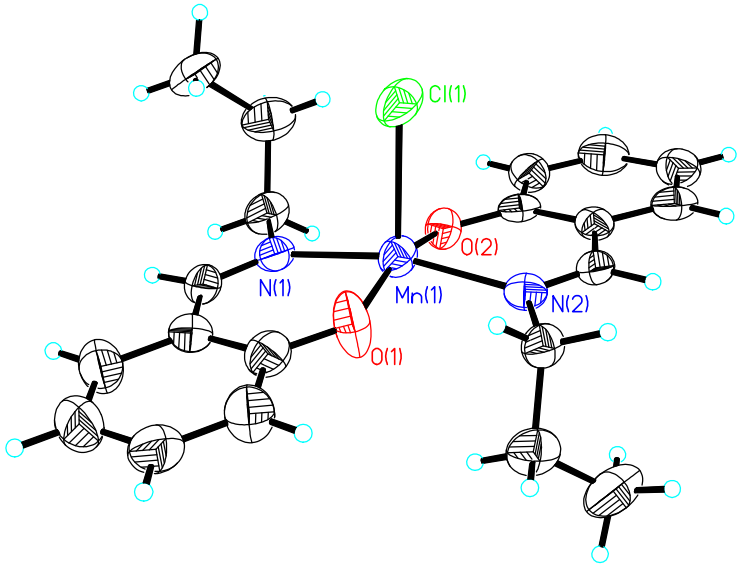

Figure 2.5. ORTEP diagram of Mn^{III}(*N*-n-Pr-Sal)$_2$Cl [**3**] showing 50% probability thermal ellipsoids.

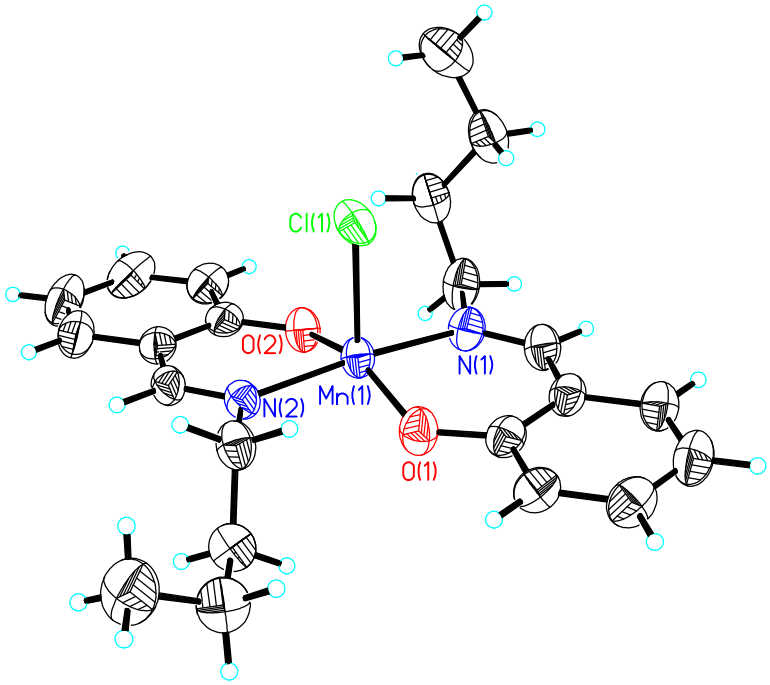

Figure 2.6. ORTEP diagram of Mn^{III}(*N*-n-Bu-Sal)$_2$Cl [**4**] showing 50% probability thermal ellipsoids

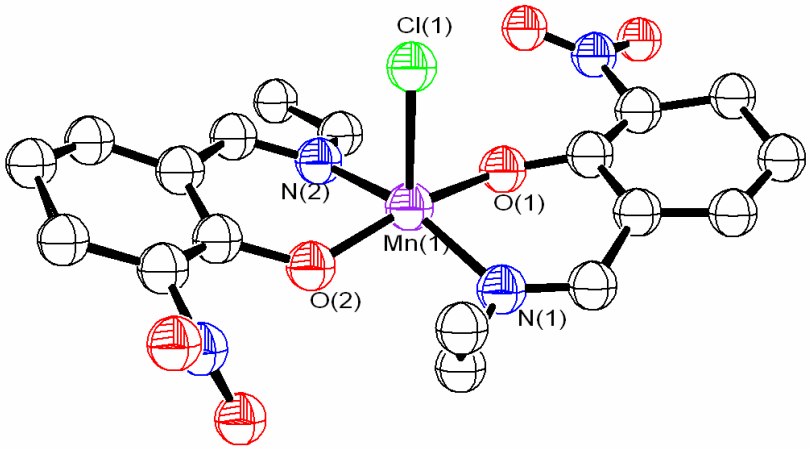

Figure 2.7. ORTEP diagram of Mn^{III}(*N*-Et-3-NO_2-Sal)$_2$Cl [**14**], all the hydrogen atoms are omitted for clarity.

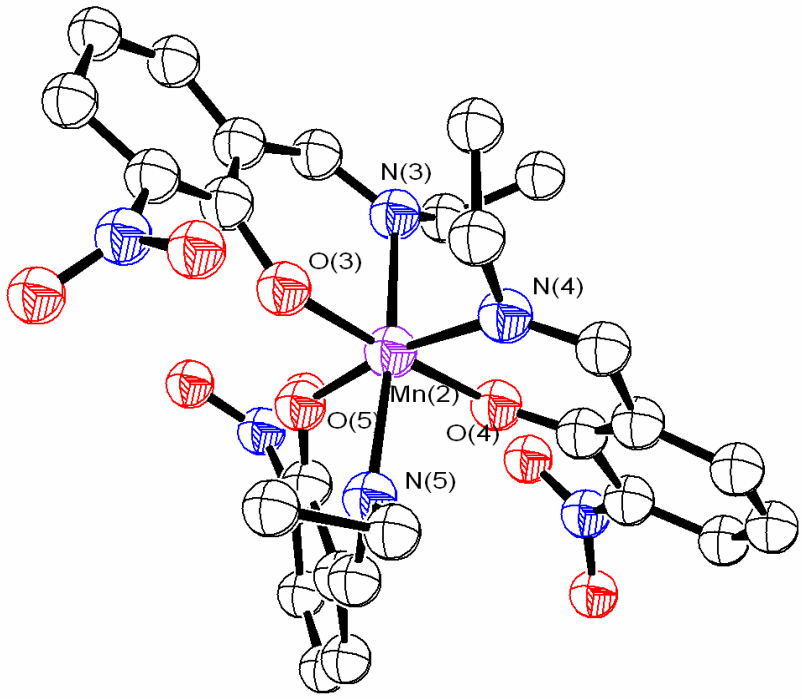

Figure 2.8. ORTEP diagram of Mn^{III}(*N*-Et-3-NO_2-Sal)$_3$ [**14a**], all the hydrogen atoms are omitted for clarity.

2.3.3. NMR Spectroscopic Study. Besides utilizing X-ray crystallography to determine the structures of synthetic products, we have used NMR spectroscopy to examine these complexes in the solution phase. For the two types of systems studied, as described in the previous section, we were able to obtain ^{1}H NMR spectra, which are shown below (Figures 9 and 10). First, for the examples of mononuclear Mn complexes which contain unsubstituted aromatic ring Schiff-base ligands, four ^{1}H NMR spectra are presented in Figure 9. Two of these complexes were structurally identified by X-ray diffraction methods, as described above in Section 2.3.2. In addition, the mass spectroscopic results have shown that there is no evidence of mixtures of ML_2X and ML_3 in these systems, but a possible dimeric Mn complex with a single chloride bridge formulation was observed in the mass spectra. Secondly, in the system with the 3-NO_2 aromatic ring substituted Schiff-base ligands, the analogous ^{1}H NMR spectra were obtained. The results are shown in Figure 10, where the signature peaks between –15 and –25 ppm region correspond to the ones between –20 and –30 ppm shown in Figure 9. The close correspondence of these upfield signals led us to the conclusion that they are indicative of the presence of the ML_2X species in solution. Moreover, according to the reported ^{1}H NMR results for $[Mn^{III}(SALPN)(CH_3OH)^{25}/(H_2O)^{26}](ClO_4)$ [**9**], it was concluded that the peaks at $\{-21.1\text{and } -24.5\}^{25}/\{-22.6 \text{ and } -25.5\}^{26}$ ppm found in the ^{1}H NMR spectra were assigned as the 4- (21 – 22 ppm) and 5- (24 – 25 ppm) position protons of the phenolate ring in the mononuclear Mn complex. These ^{1}H NMR assignments support the conclusion that we made above for the observed spectral results from ML_2X species. Furthermore, the X-ray crystal structure of [**14**] was found to have a very similar structural topology as compared to the structures of mononuclear Mn

complexes that we obtained and discussed in the previous section. Such a structural correlation solidifies the conclusion made based on ^{1}H NMR spectral results. Even though there is still uncertainty according to co-crystallized mixtures like [**14**] and [**14a**] that appeared in some cases,[27] we are inclined to conclude the signature ^{1}H NMR peaks in the range of –20 to –30 ppm shown in Fig. 10 (a) are associated with mononuclear MnL_2X complexes and the peaks between +6 to +18 ppm possibly correspond to MnL_3 species.[28] Before performing the kinetics experiments described below, several attempts, as discussed in Section 2.3.1, were made to separate [**14**] and [**14a**] but none of them proved to be successful. In the future, we will explore the use of size exclusion HPLC methods to separate [**14**] and [**14a**] as discussed in Appendix A.

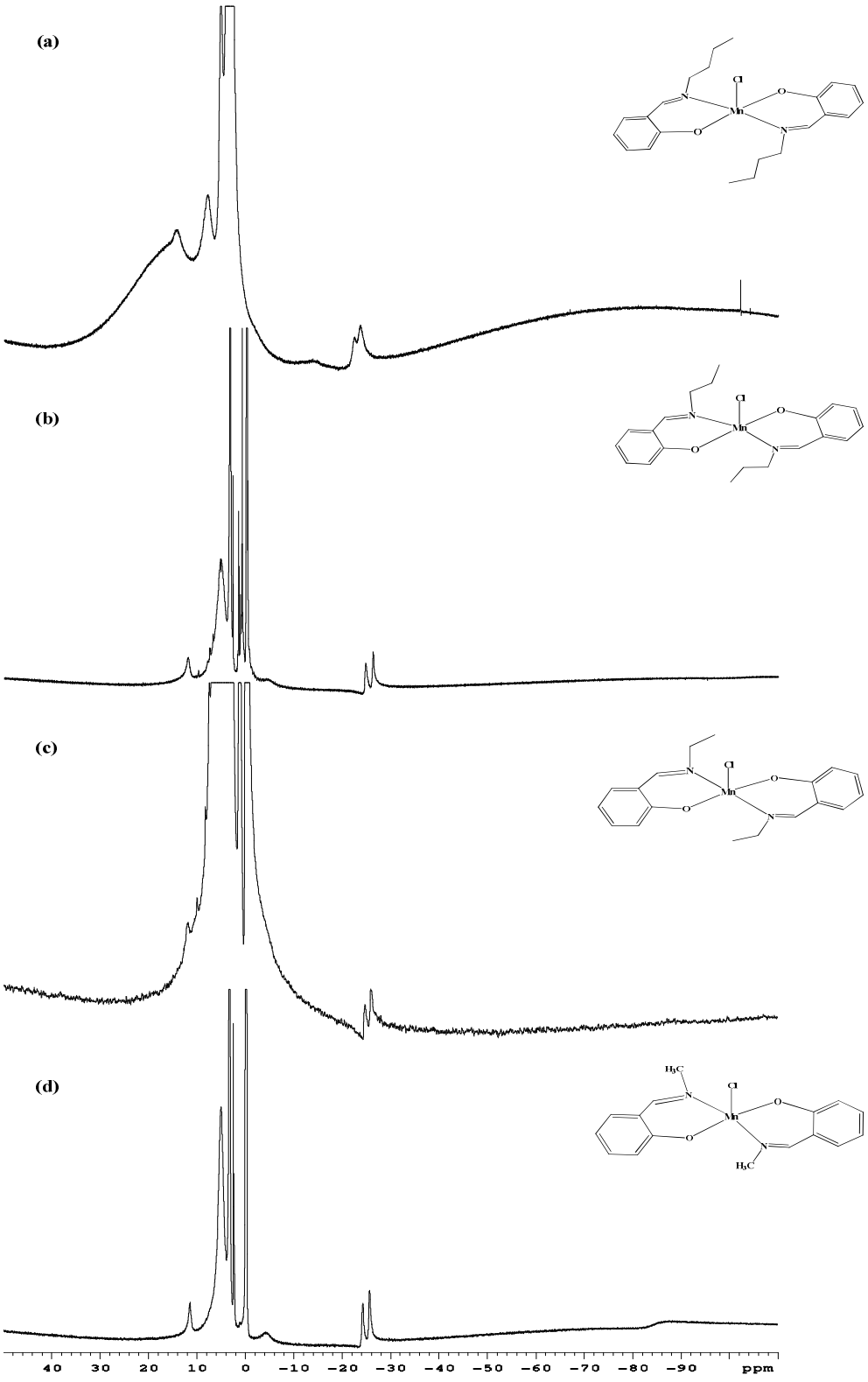

Figure 2.9. ^{1}H NMR spectra of (a) Mn^{III}(*N*-n-Bu-Sal)$_2$Cl [**4**]; (b) Mn^{III}(*N*-n-Pr-Sal)$_2$Cl [**3**]; (c) Mn^{III}(*N*-Et-Sal)$_2$Cl [**2**]; (d) Mn^{III}(*N*-Me-Sal)$_2$Cl [**1**].

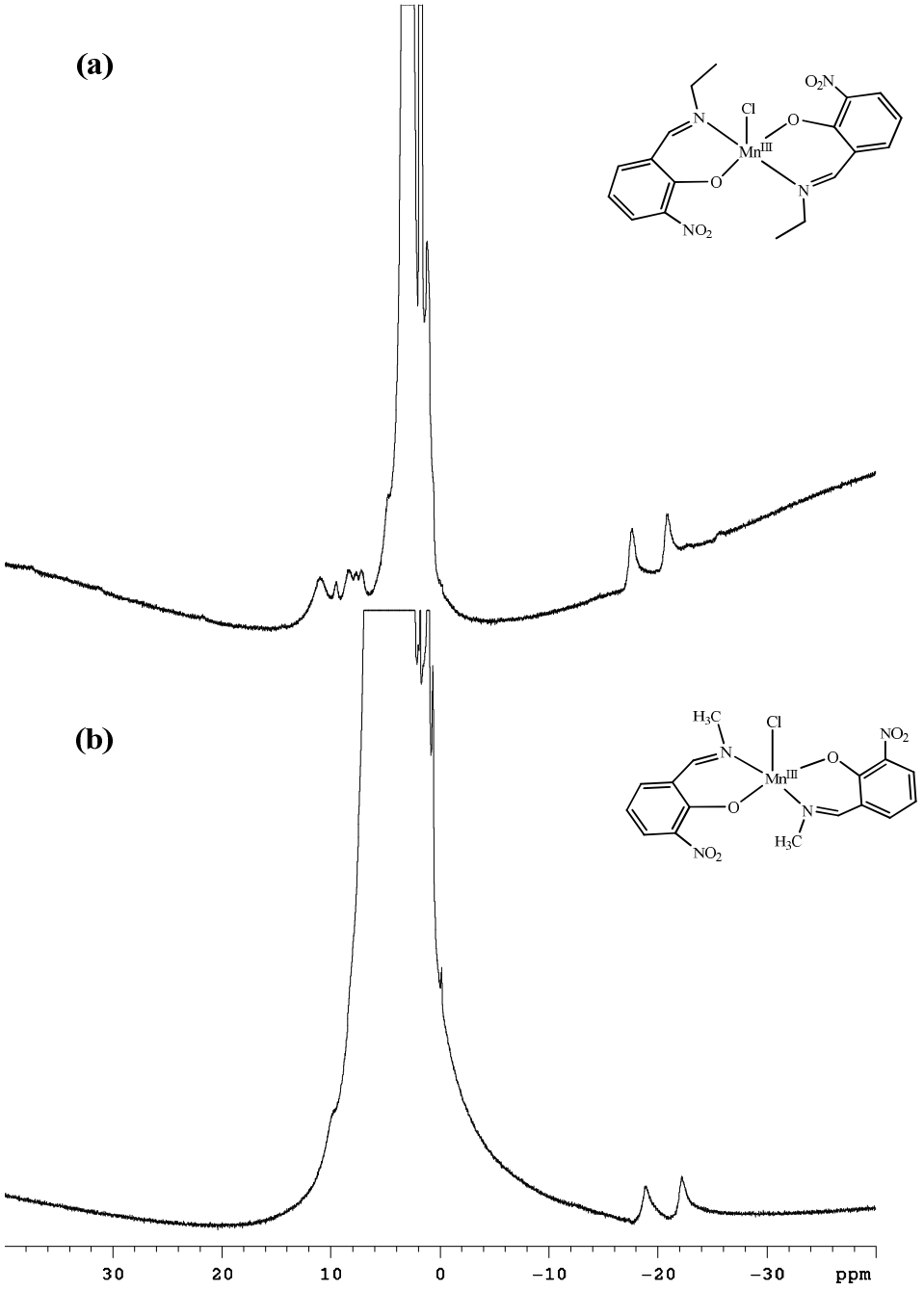

Figure 2.10. ^{1}H NMR spectra of (a) Mn^{III}(*N*-Et-3-NO_2-Sal)$_2$Cl [**14**]; (b) Mn^{III}(*N*-Me-3-NO_2-Sal)$_2$Cl [**13**].

2.3.4. **UV-vis Spectroscopic Oxygen Atom Transfer Study.** The O-atom transfer[29] reactions were carried out in acetonitrile solution and monitored by the UV-vis spectroscopy. In our studies, the mononuclear manganese complexes discussed in the

previous sections were selected as the oxygen atom acceptors and *n*-$Bu_4N{\cdot}HSO_5$ was employed as the O-atom donor.[30] We postulate that for the co-crystallized product of MnL_2Cl [**14**] and MnL_3 [**14a**], the MnL_3 complex is not an efficient O-atom acceptor based on its lack of an open coordination site and thus will not compete with [**14**] during the O-atom transfer reactions. In the work performed here, we first attempted to examine reactions between HSO_5^- and the Mn Schiff-base complexes which have unsubstituted phenolate ring on coordinated ligands. Reactions were carried out at room temperature with 1:1 stoichiometric ratio and for both reactants, the concentrations were 500 μM. The overall experimental time span was 5 min. The color of manganese solutions changed from dark green to light yellow and in the UV-vis spectral results, we observed changes in both the UV and visible regions and no prominent isosbestic points were obtained. Then we investigated the same type of reaction for the Mn Schiff-base complexes having 3-NO_2 substituted phenolate ring on the ligands, which gave the more promising results shown in Figure 11 and 12. One interpretation for both spectra (Fig. 11 and 12) is that O-atom transfer does indeed take place and that, upon close inspection, a reactive intermediate is observed. Determining the nature of this intermediate was of special interest to us and will be addressed in Section 2.3.5. In a less sterically crowded Mn Schiff-base complex, [**13**], the ligands in which have *N*-methyl substituents, the UV-vis study showed that the O-atom transfer reaction follows a complicated mechanistic pathway. The behavior of the absorbance maximum at 441 nm shown in Fig. 11 depicts a complexity indicating that there were various mechanism steps, at least two were observed in Fig. 11. The red curve in Fig. 11 shows the initial stage of the reaction mechanism and at 441 nm its intensity first decreased as shown by the dashed arrow, then

it increases to the same intensity level comparable to the initial stage and level off but afterwards, it continues to increase and reaches another level-off stage as shown by the solid arrow. The changes observed in the final phase of the reaction presumably occur after the formation of the intermediate, perhaps corresponding to either a dimerization or polymerization step, which are illustrated in Scheme 2.2.

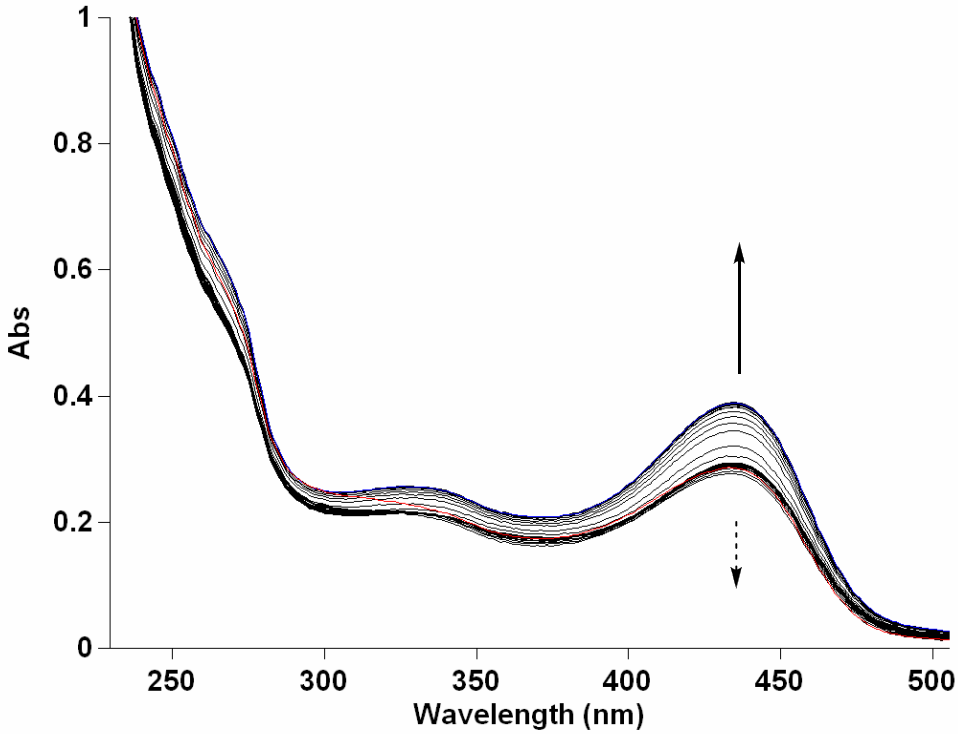

Figure 2.11. UV-vis spectrum of kinetic study at room temperature, 500 µM of Mn complex, [**13**], mixing with 500 µM Bu_4NHSO_5, the first scan shown in red color the final scan in blue. There were 40 scans within overall time interval of 600 seconds and each scan time span was 15 seconds between 200 to 800 nm.

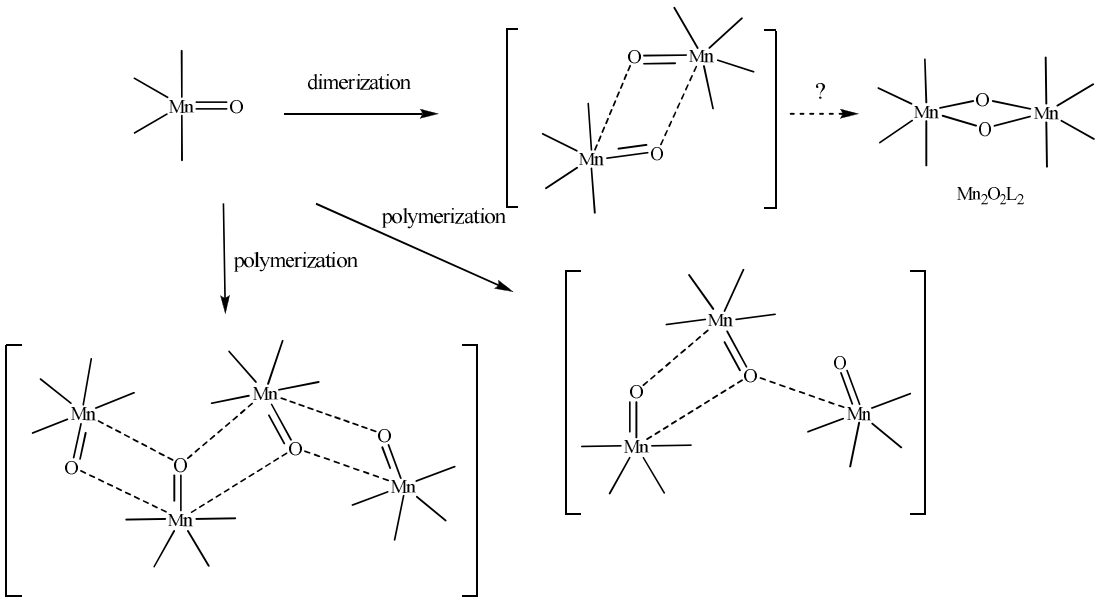

Scheme 2.2. The proposed reaction process for probable dimerization and polymerization mechanisms for the manganyl intermediate.

Parallel studies were carried out for the Mn Schiff-base complex, [**14**], which has the *N*-ethyl substituent ligand system. In this case, the O-atom transfer reaction is expected to be slower, which we attribute to a difference in steric crowding of N-ethyl substituents. The result is shown in Figure 12, in which the isosbestic points at 295 and 331 nm demonstrate that a clean reaction takes place, possibly indicating the formation of a manganyl species. On the other hand, if manganyl species is very short lived, we may be observing a subsequent process such as dimer formation. According to the results from both Fig. 11 and Fig. 12, we propose that the steric effect from the ligand substituents influences the O-atom transfer rate. Based on the data in Fig. 12, we predicted that there may be a reactive intermediate formed on a shorter time scale. This speculation was invoked while comparing the spectral result in Fig. 12 with the reported spectrum in a manganese porphyrin system.[31] In the Mn-porphyrin study by Groves and coworkers, they showed that the oxomanganese$^{(V)}$ porphyrin was generated and could be monitored

by using time-resolved UV-vis spectroscopy. They demonstrated that $Mn^{(V)}$=O species was formed within 120 ms and with a fast rate constant, 3.8×10^5 $M^{-1}s^{-1}$. In our work, the corresponding absorbance at 441 nm shown in Fig. 12 decreased over time within 300 s. Therefore, with this comparison in mind, we proposed the existence of a more reactive preceding intermediate formed before the experimental UV-vis measurements. To our knowledge with respect to the reported related systems, the formation of a manganyl intermediate was known to be very unstable with short life-time and not able to be detected from the general spectroscopic studies at room temperature. In the systems that we studied, a precursor is believed to exist for a relatively short period of time as well. In order to find evidence for the existence of a short-lived reactive manganyl species, we decided to utilize stopped-flow UV-vis spectroscopy.

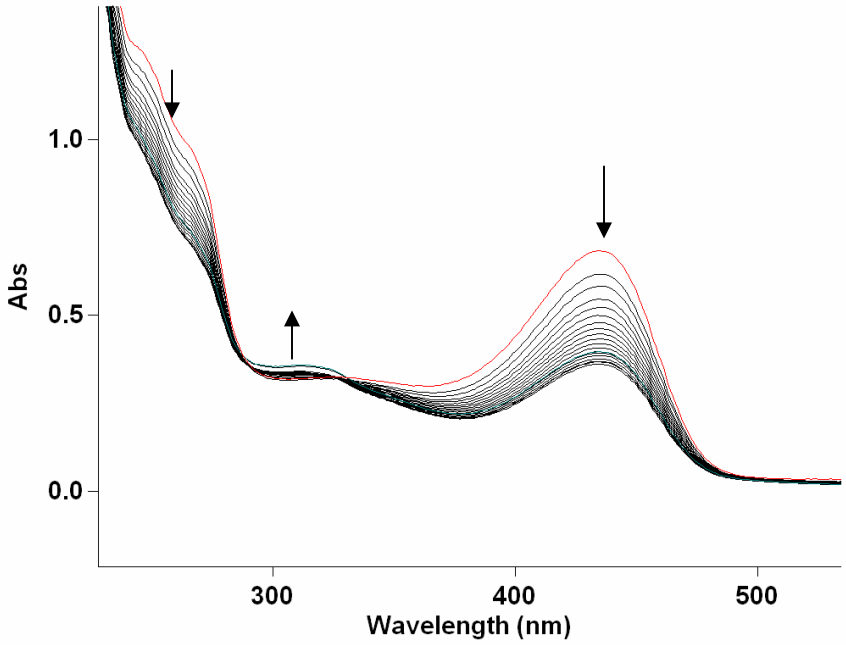

Figure 2.12. UV-vis spectrum of kinetic study at room temperature, 500 µM of Mn complex, co-crystal of [**14**] + [**14a**], mixing with 500 µM Bu_4NHSO_5, the first scan shown in red color the final scan in blue. There were 20 scans within overall time interval of 300 seconds and each scan time span was 15 seconds between 200 to 800 nm.

In order to test the hypothesis regarding the formation of a reactive intermediate with a short life-time that we could not detect as described above in the Mn-porphyrin study, we turned to stopped-flow methods on the seconds timescale in collaboration with the Rybak-Akimova group at Tufts University. We were indeed able to find solid evidence for the formation of the proposed reactive intermediate. The corresponding spectroscopic results are shown in Figures 13 and 14. The spectra revealed that a new species forms within 2 seconds after which a slower second process occurs. The latter was found in the corresponding spectral results shown in Fig. 12. The proposed reaction scheme is shown in Scheme 2.3.

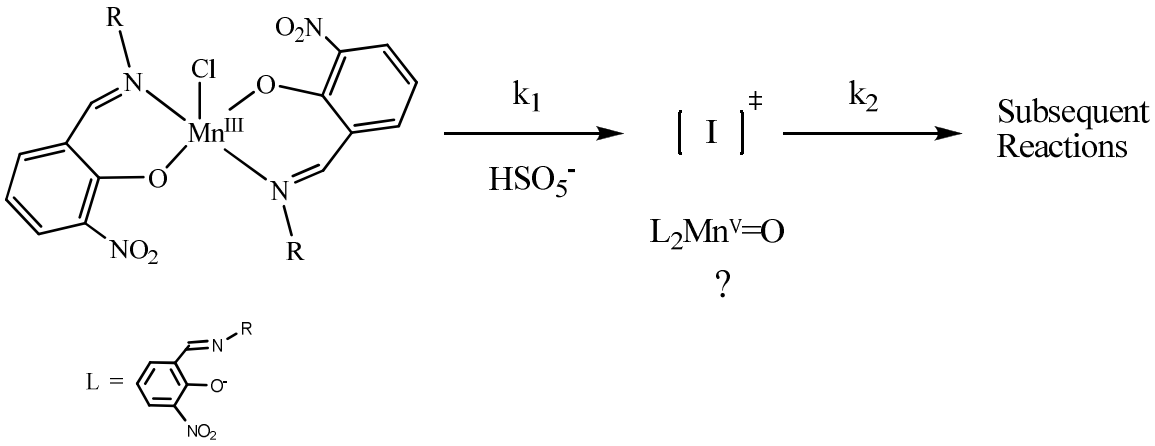

Scheme 2.3. The proposed the O-atom transfer reaction scheme.

In Figure 13, the absorbance at 434 nm gradually increases and reaches a plateau in an overall time range of 9.6 seconds. The isosbestic point at 393 nm implies that only two manganese species are present in this time frame, implying an A→B type reaction mechanism. It is noteworthy that the increasing absorbance in the time range of 9.6 second is completely different from the decreasing one observed in Figure 12. Therefore, this experimental observation strongly suggested the occurrence of a first step in

formation of the intermediate which is shown in Scheme 2.2. We have also performed a second stopped-flow experiment over a longer time span of 96 seconds, the results of which are shown in Figure 14. These data are presented as plots of absorbance *vs.* time, which were used to calculate the kinetic rate constants for the reactions examined. The extracted rate constants from the data analysis confirm that the reaction goes by the mechanism shown in Scheme 2.2, with k_1 = 1.281 sec/μM (Rate = $k_1[L_2MnCl]$) and k_2 = $5.431*10^{-2}$ sec/μM (Rate = k_2 [I]). From these two constants, we can conclude that an intermediate is readily formed in the early stages of the reaction, existing for around 2 seconds and then in the following step of the reaction, which has a rate about 24-fold slower, then a second species is formed. Additionally in Figures 15 and 16, the observed plateaus from these two spectral results indicate the formation of the reactive intermediate is presented for both experimental time-scales.

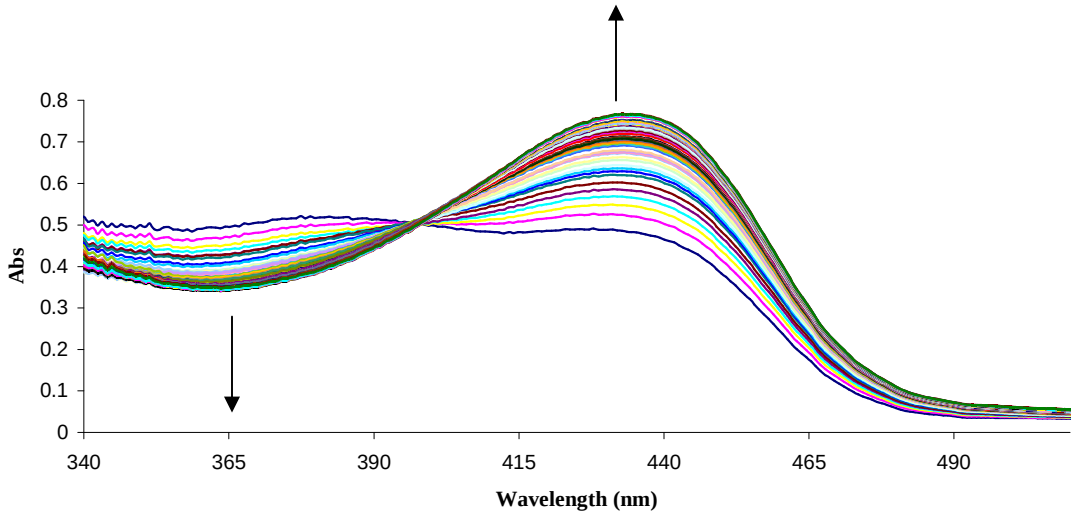

Figure 2.13. Stopped-flow UV-vis spectrum Experimental condition: Temperature, 25 °C; 100 μM Mn Complex of [**14**] and 500 μM Bu_4NHSO_5. There were 96 scans within overall time interval of 9.6 seconds and each scan time span was 0.1 seconds between 319 to 700 nm.

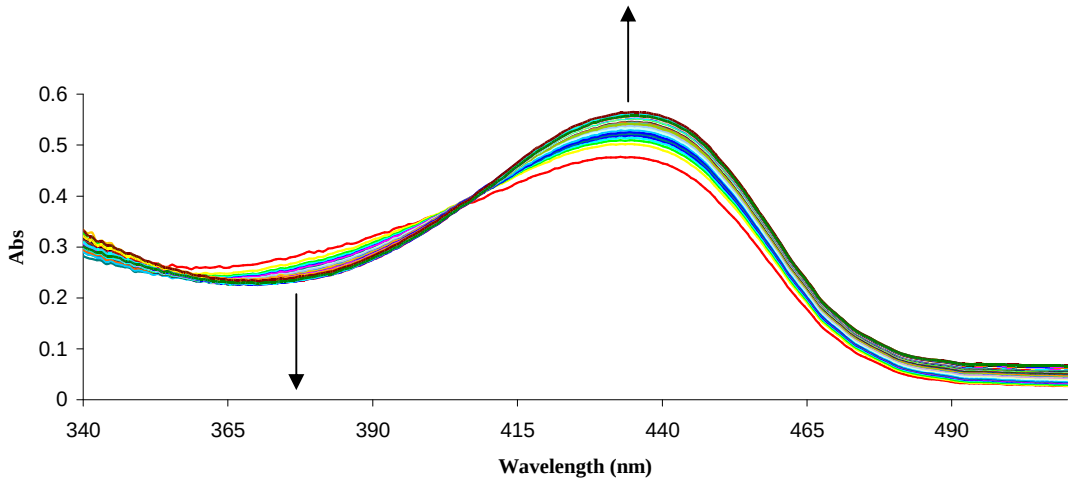

Figure 2.14. Stopped-flow UV-vis spectrum Experimental condition: 100 µM Mn Complex of [**14**] and 500 µM Bu_4NHSO_5; There were 96 scans within overall time interval of 96 seconds and each scan time span was 1 seconds between 319 to 700 nm.

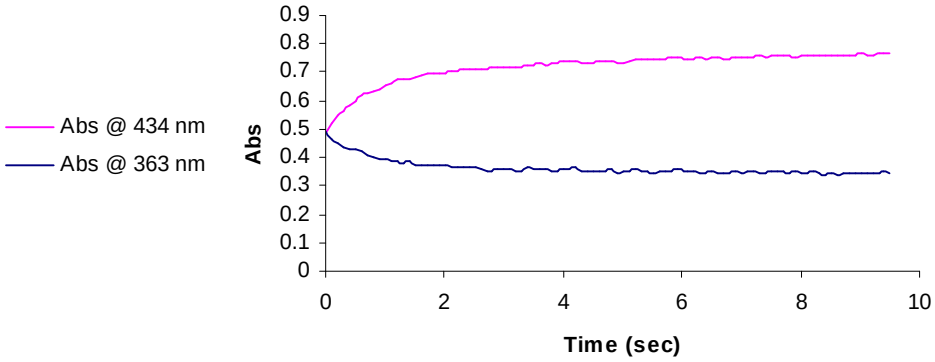

Figure 2.15. First step overall time period 9.6 seconds.

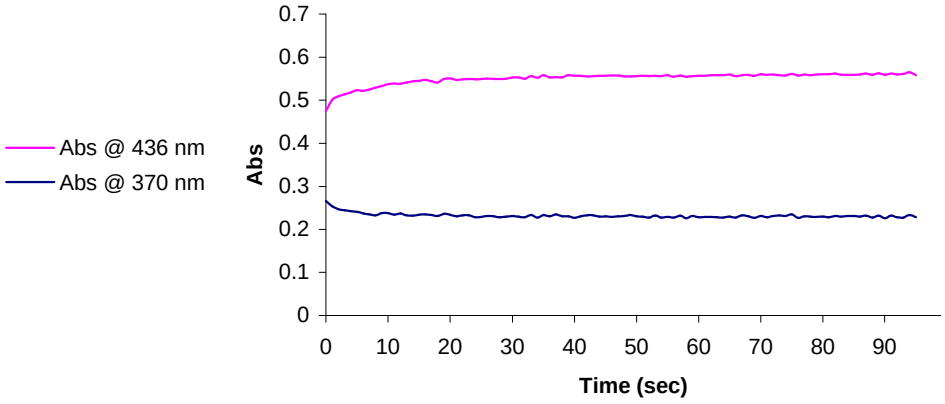

Figure 2.16. Second step overall time period 96 seconds.

2.3.5. Mass Spectroscopic Study. Above, we speculated the kinetic intermediate is a reactive manganyl species. However, we cannot conclude from the UV-vis spectral results alone that this is correct. Other possibilities for the reactive intermediate include a direct O atom oxidation on the Mn center to form an $Mn^{(IV)}$ complex or a ligand oxidation reaction. We sought to use a more definitive spectral method to resolve this issue. We chose to employ a stopped-flow method using electrospray ionization mass spectrometer (ESI-MS) as a detection tool, and the conceptual setup is shown in Figure 17.[32] ESI-MS is very desirable because of its sensitivity with regard to the compounds involved in the study and we anticipated it would be useful to determine the formulation of the reactive intermediate. The experimental setup involved the use of two separate syringes, one of which contained an acetonitrile solution of the Mn Schiff-base complex and the other had an acetonitrile solution of *n*-$Bu_4N{\cdot}HSO_5$. The molar concentration for both reactants was set at 100 μM, which is selected in order to attain suitable signal to noise in the ESI-MS data. Samples were introduced by using a dual syringe pump (Harvard Apparatus) and different quantities for both solutions were used in order to monitor consequential dissimilar signals (Fig. 18).[33] We also used a low dead volume mixing T for the purpose of shortening the flow time before reaching the mass spectrometer. In this way, we thought we could observe the O-atom transfer reaction intermediate prior to any subsequent process, as described above for the UV-vis experimental results. Another advantage of using ESI-MS to monitor the time-resolved reaction process is that we can focus on the region of molecular ion peaks of interest. The experimental data are shown in Figure 18, which illustrates the raw signal of total ion current *vs.* time as obtained from the mass spectrometer. The magnitude of total ion

current on the y axis in the diagram represents for the actual ion intensity to reach MS detector. In real time as shown in Fig. 18, the data reveal several different plateaus after each sample injection and for each of these time periods, the ion current was then converted into the spectroscopic form mass over charge (m/z) ratio. The resulting mass spectra for each time period are shown in Figure 19. Our observations show that formation of a manganyl complex undeniably takes place. The MS signal (m/z) *vs.* time plot also showed that after the mixing period, a final plateau was reached, which is similar to the corresponding phenomenon observed in the experiments monitored by UV-vis. The MS ion peak position that matched to a formulation of $Mn^{V}L_2(O)$ was observed and its isotope pattern, shown in Figure 20, is consistent with this formulation as well. It is noteworthy that we also found a related species that we formulate as either $[Mn^{V}L_2(O)(Cl)]$ or $[Mn^{IV}L_2(O)(Cl)]$ but there is no conclusive structural assignment for this complex yet. We cannot rule out another possibility for such a species as $[Mn^{IV/V}L_2(OCl)]$ as well since only the mass, not structure, is determined. Further studies are still in progress.

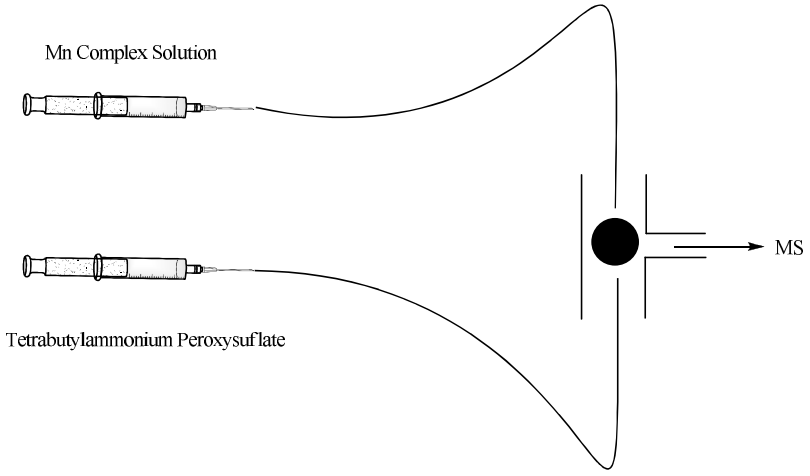

Figure 2.17. Setup for the stopped-flow mass spectrometer detection.

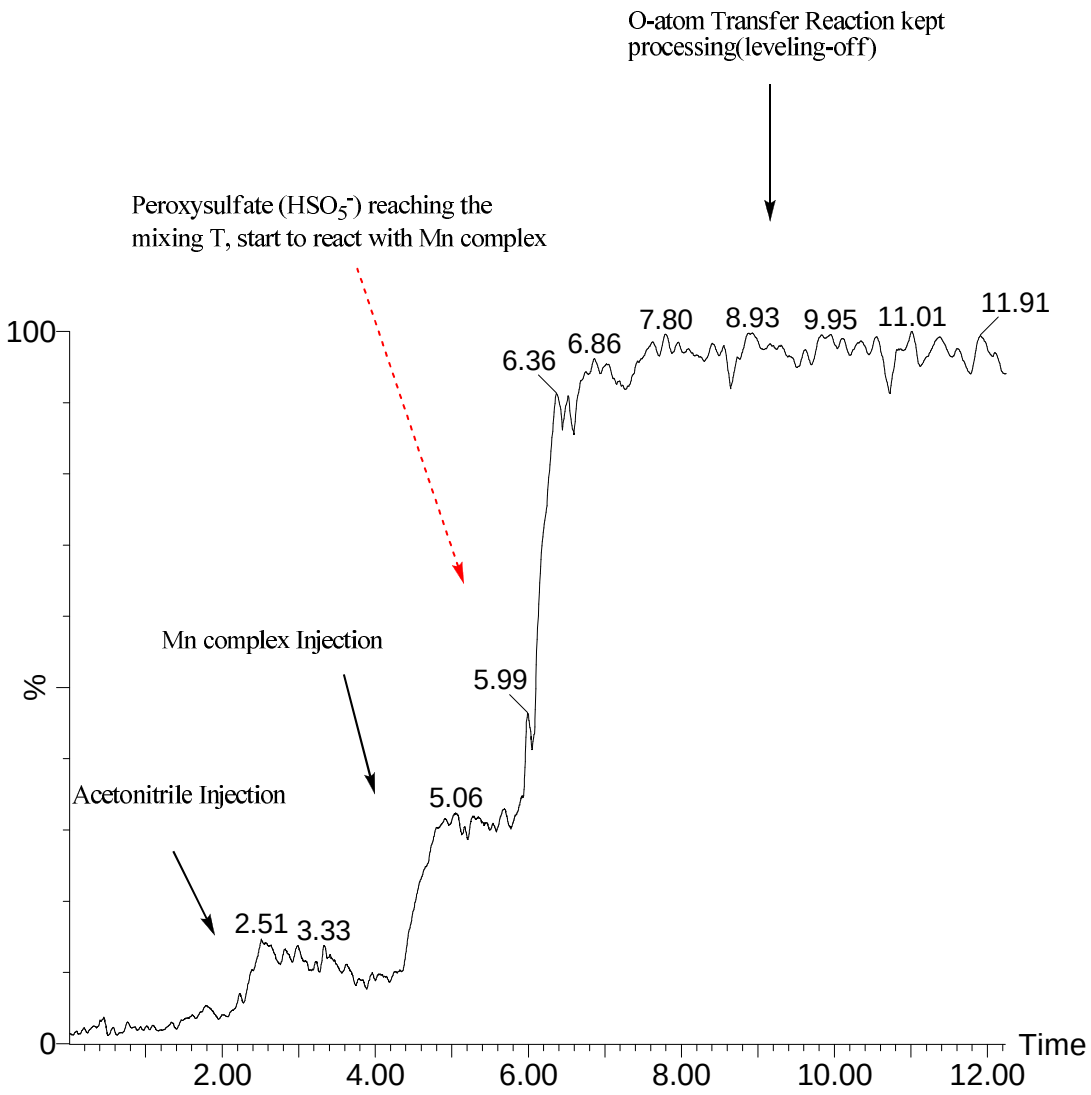

Figure 2.18. Corresponding raw mass spectroscopic signal of total ion current *vs*. time (in minutes) diagram.

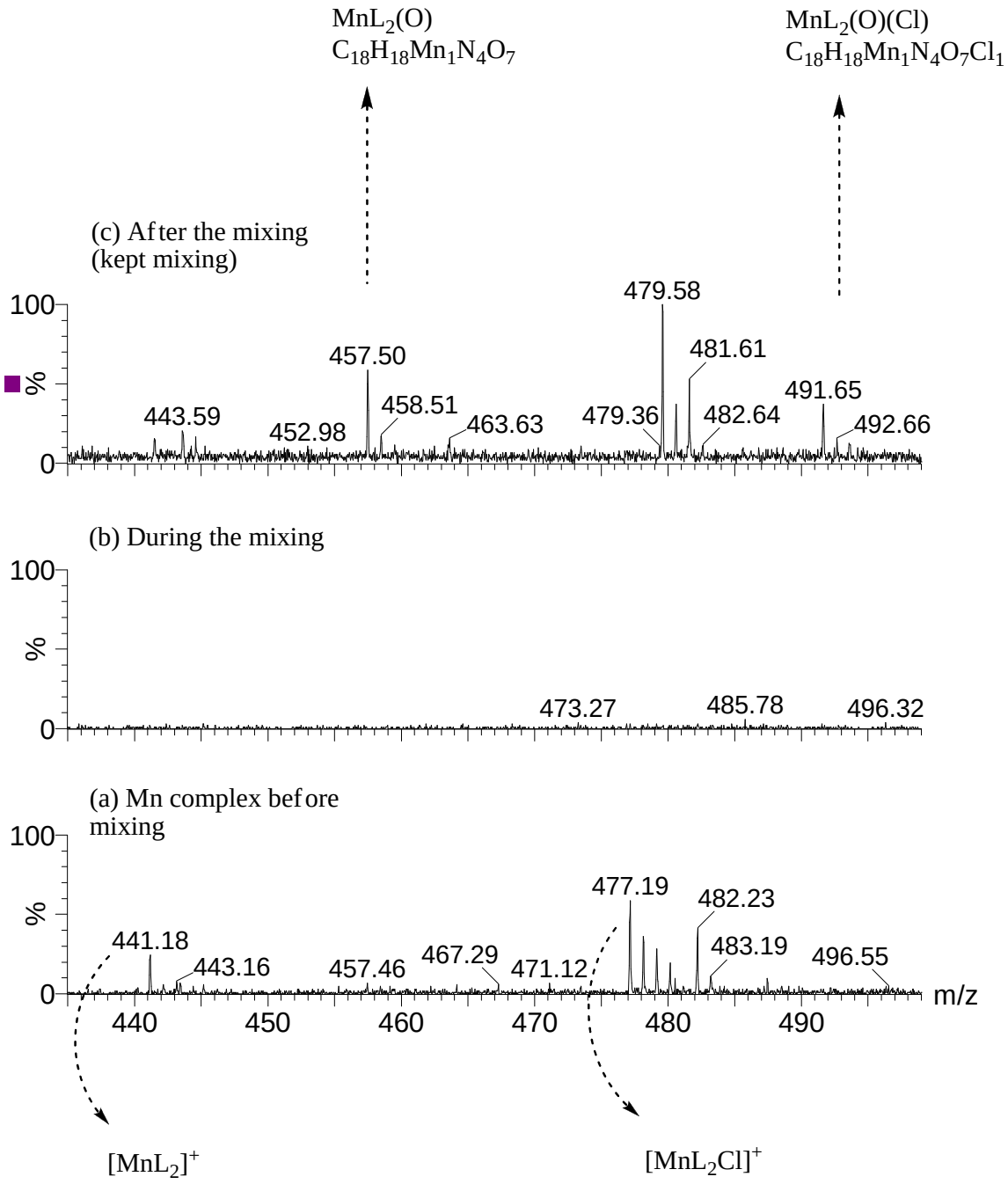

Figure 2.19. Time-resolved mass spectra results. (a) before mixing (b) during mixing (c) after mixing periods.

Top: Expermental Result

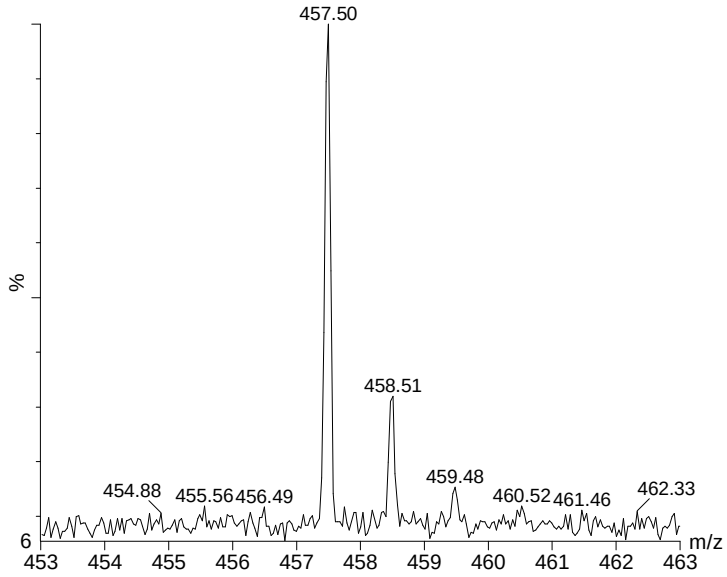

Suspected Structure:

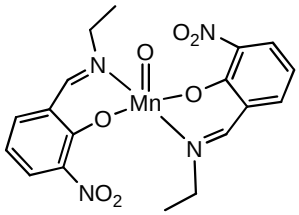

Bottom: Theoretical

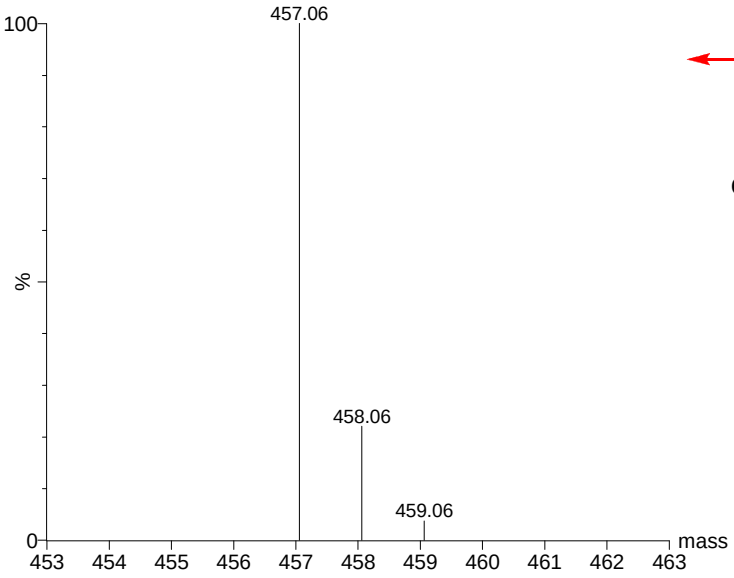

Mass Simulation of $L_2Mn(O)$

Chemical Formula: $C_{18}H_{18}MnN_4O_7$
Exact Mass: 457.06

Figure 2.20. Isotopic patterns and the corresponding structural formula of the speculated species of $L_2Mn(O)$ observed at m/z 457.50.

Top: Expermental Result

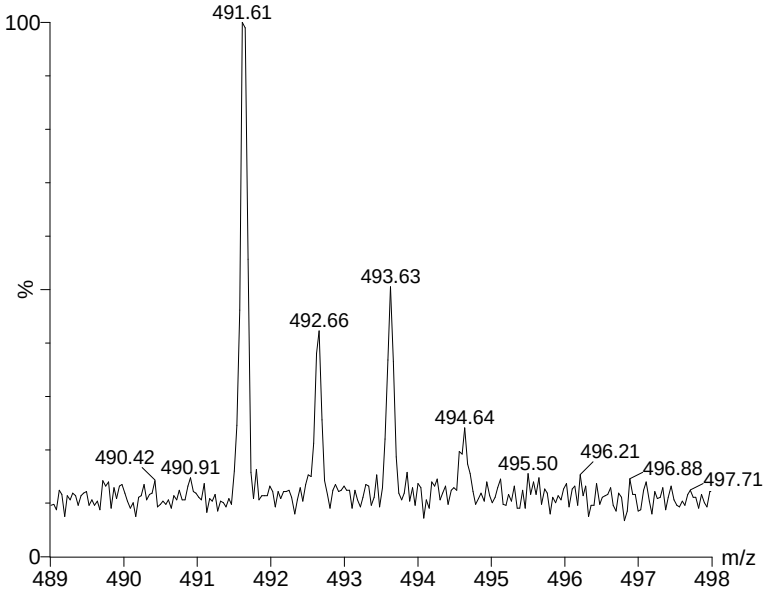

Suspected Structure:

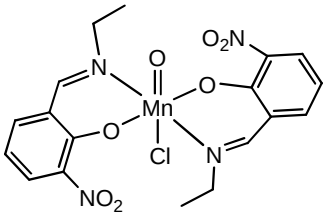

OR

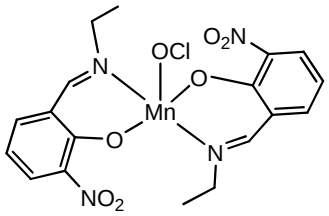

Bottom: Theoretical

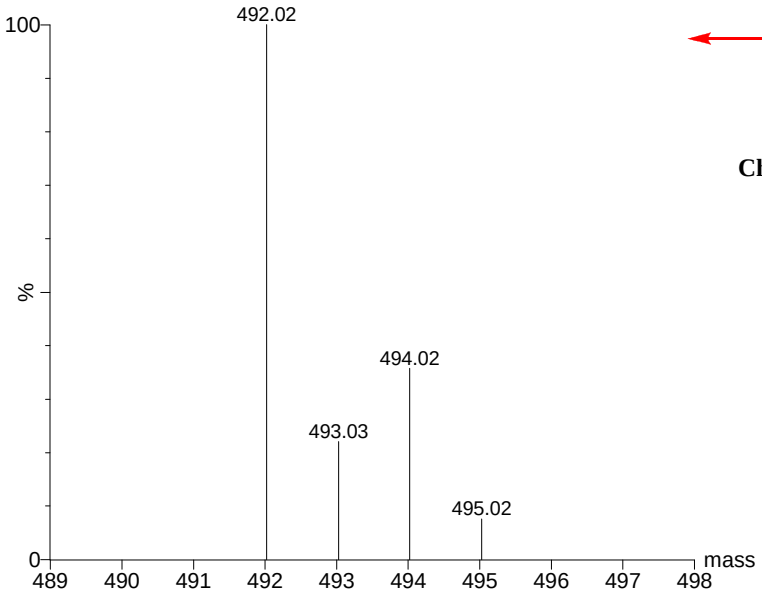

Mass Simulation of $L_2Mn(O)(Cl)$

Chemical Formula: $C_{18}H_{18}ClMnN_4O_7$
Exact Mass: 492.02

Figure 2.21. Isotopic patterns and the corresponding structural formula of the speculated species of $L_2Mn(O)(Cl)$ at m/z 491.61.

2.4. Conclusion

In this study, we have demonstrated the existence of a species that is plausibly assigned as a manganyl complex by utilizing stopped-flow UV-vis spectroscopy and ESI-MS spectrometry. We believe this is the reactive intermediate designated as $Mn^{V}L_2(O)$ species in Scheme 2.3. Meanwhile we have attempted to obtain the FTIR and Raman spectra of this reactive manganyl species but have not had success to date. To our knowledge, with exception of the porphyrin complex studied by Groves and coworkers and the Kochi-Katsuki-Jacobsen epoxidation system that utilizes a $Mn^{(V)}$=O species[34] as the catalytically active complex, this is the first time that the formation and loss of a reactive manganyl complex has been characterized kinetically. In the system that we studied, related complexes were reported to be able to oxidize water and release O_2. We believe that the manganyl species observed here will be important in our ongoing effort to understand the PSII water oxidase. This reactive intermediate can play the crucial role as the precursor in the O-O bond formation by reacting with a water molecule, followed by release of dioxygen.[35] Such a proposition is valid, since we know that the O_2 evolution was reported by Matsushita and coworkers. Even though we do not know for a fact that the work presented by Matsushita et al. involves a reactive manganyl intermediate for O_2 formation, the study conducted by us which is illustrated here suggests such a species does exist and that it probably retains an intrinsic behavior like the aforementioned precursor in the O-O bond formation due to the observed instability. Furthermore, investigations with regard to the related water isotope labeling in formation of the dioxygen and the potential role of cofactor Cl^- in this system are underway.[36]

2.5. Acknowledgement

Special thank goes to Mr. Marek Domin for his great guidance setting up the stopped-flow Mass spectrometry experiments. We also thank Dr. Richard J. Staples for the pivotal role he played in solving crystal structures. And Professor Richard H. Holm and Dr. Jun-Jieh Wang at Harvard University for their tremendous help with UV-vis spectroscopy experiments. Extraordinarily thankful to Professor Elena V. Rybak-Akimova and Dr. Ivan V. Korendovych at Tufts University for the incredible experimental runs with regard to the stopped-flow UV-vis kinetic studies.

2.6. References

1. Calvin, M. *Science* **1974**, *184*, 375-381.
2. (a) Hoganson, C. W.; Babcock, G. T. *Science* **1997**, *277*, 1953-1956. (b) Mullins, C.; Pecoraro, V. L. *Coord. Chem. Rev.* **2008**, *252*, 416-443.
3. McEvoy, J. P.; Gascon, E. P.; Batista, V. S.; Brudvig, G. W. *Photochem. Photobiol. Sci.* **2005**, *4*, 940-949.
4. Ferreira, K. N.; Iverson, T. M.; Maghlaoui, K.; Barber, J.; Iwata, S. *Science* **2004**, *303*, 1831-1838.
5. (a) Srinivasan, K.; Michaud, P.; Kochi, J. K. *J. Am. Chem. Soc.* **1986**, *108*, 2309-2320.
   (b) Chang, S.; Galvin, J. M.; Jacobsen, E. N. *ibid.* **1994**, *116*, 6937-6938.
6. Weng, T.-C.; Hsieh, W.-Y.; Uffelman, E. S.; Gordon-Wylie, S. W.; Collins, T. J.; Pecoraro, V. L.; Penner-Hahn, J. E. *J. Am. Chem. Soc.* **2004**, *126*, 8070-8071.

7. (a) Stern, M. K.; Groves, J. T. In *Manganese Redox Enzymes*; Pecoraro, V. L., Ed.; VCH Publishers, Inc.: New York, **1992**, pp. 233-259.

(b) Marla, S. S.; Lee, J.; Groves, J. T. *Proc. Natl. Acad. Sci. USA* **1997**, *94*, 14243-14248.

8. Okawa, H.; Sakiyama, H. *Pure & Appl. Chem.* **1995**, *67(2)*, 273-280.

9. (a) Siegbahn, P. E. M.; Crabtree, R. H. *J. Am. Chem. Soc.* **1999**, *121*, 117-127.

(b) Limburg, J.; Vrettos, J. S.; Liable-Sands, L. M.; Rheingold, A. L.; Crabtree, R. H.; Brudvig, G. W. *Science* **1999**, *283*, 1524-1527.

(c) Limburg, J.; Vrettos, J. S.; Chen, H.; De Paula, J. C.; Crabtree, R. H.; Brudvig, G. W. *J. Am. Chem. Soc.* **2001**, *123*, 423-430.

10. Haumann, M.; Liebisch, P.; Müller, C.; Barra, M.; Grabolle, M.; Dau, H. *Science* **2005**, *310*, 1019-1021.

11. (a) Collins, T. J.; Gordon-Wylie, S. W. *J. Am. Chem. Soc.* **1989**, *111*, 4511-4513.

(b) Workman, J. M.; Powell, R. D.; Procyk, A. D.; Collins, T. J.; Bocian, D. F. *Inorg. Chem.* **1992**, *31*, 1550-1551.

(c) Miller, C. G.; Gordon-Wylie, S. W.; Horwitz, C. P.; Strazisar, S. A.; Peraino, D. K.; Clark, G. R.; Weintraub, S. T.; Collins, T. J. *J. Am. Chem. Soc.* **1998**, *120*, 11540-11541.

12. MacDonnell, F. M.; Fackler, N. L. P.; Stern, C.; O'Halloran, T. V. *J. Am. Chem. Soc.* **1994**, *116*, 7431-7432.

13. Fujiwara, M.; Matsushita, T.; Shono, T. *Polyhedron*, **1985**, *4(11)*, 1895-1900.

14. Binstead, R. A.; Zuberbühler, A. D.; Jung, B. *Specfit/32 Global Analysis System*, version 3.0.36; Spectrum Software Associates; Chapel Hill, N.C., **2004**.

15. SMART V 5.050 (NT) Software for the CCD Detector System: Bruker Analytical X-ray Systems, Madison, WI (**1998**).
16. SAINT V 5.01 (NT) Software for the CCD Detector System Bruker Analytical X-ray Systems, Madison, WI (**1998**).
17. SADABS. Program for absorption corrections using a Siemens CCD detector based on the method reported by Robert Blessing; Blessing, R. H. *Acta Cryst.* **1995**, *A51*, 33-38.
18. Sheldrick, G. M. SHELXL-97, *Program for the Solution of Crystal Structure*, University of Göttingen, Germany, **1997**.
19. SHELXTL 5.10 (PC-Version), Program library for Structure Solution and Molecular Graphics; Bruker Analytical X-ray Systems, Madison, WI (**1998**).
20. Harrison, G. C.; Diehl, H. *Chem. Abstr.* **1948**, *42*, 1240-1241.
21. Matsushita, T.; Kono, H.; Shono, T. *Bull. Chem. Soc. Jpn.*, **1981**, *54*, 2646-2651.
22. For all of the four mass spectra results**1**, **2**, **3** and **4**, the high mass unit region was found to have a set of m/z peaks: m/z: 1223, 1307, 1391, 1475. Each peak was separated by a unit of 84.
23. These prominent isotropic shifts were observed at +61.4, +47.8, +17.2, –7.5, –18.1, and –19.3 ppm. There were two broad resonances also observed at +81.8 and +90.6 ppm.
24. Asada, H.; Fujiwara, M. Matsushita, T. *Polyhedron*, **2000**, *19*, 2039-2048.
25. Larson, E. J.; Pecoraro, V. L. *J. Am. Chem. Soc.* **1991**, *113*, 3810-3818.
26. Gohdes, J. W.; Armstrong, W. H. *Inorg. Chem.* **1992**, *31*, 368-373.

27. We only obtained one product which cocrystallized in a mixture, the structure in solid state of co-crystal [**14**] and [**14a**] was determined by X-ray crystallography but in some the other systems, we also observed the analogous products formed according to the obtained mass spectral results. The corresponding m/z signals revealed that ML_2X and ML_3 species were co-existed within the products based on the structural formulations.

28. Bonadies, J. A.; Maroney, M. J.; Pecoraro, V. L. *Inorg. Chem.* **1989**, *28*, 2044-2051.

29. (a) Holm, R. H.; Donahue, J. P. *Polyhedron* **1993**, *12(6)*, 571-589.

(b) Holm, R. H.; Kennepohl, P.; Solomon, E. I. *Chem. Rev.* **1996**, *96*, 2239-2314.

30. (a) Borhan, B.; Travis, B. R.; Schomaker, J. M. *U. S. Pat. Appl. Publ.* **2003**, 40 pp. US 2003149299 A120030807.

(b) Travis, B. R.; Sivakumar, M.; Hollist, G. O.; Borhan, B. *Eur. J. Org. Chem.* **2002**, *20*, 3429-3434.

(c) Hsieh, W.-Y.; Pecoraro, V. L. *Inorg. Chim. Acta* **2002**, *341*, 113-117.

31. Jin, N.; Bourassa, J. L.; Tizio, S. C.; Groves, J. T. *Angew. Chem. Int. Ed.* **2000**, *39(21)*, 3849-3851.

32. (a) Sam, J. W.; Tang, X. –J.; Peisach, J. *J. Am. Chem. Soc.* **1994**, *116*, 5250-5256.

(b) Kim, J.; Dong, Y.; Larka, E.; Que, L. Jr. *Inorg. Chem.* **1996**, *35*, 2369-2372.

(c) Santos, L. S.; Knaack, L.; Metzger, J. O. *International J. Mass Spec.* **2005**, *246*, 84-104.

33. The volume quantity of Mn complex was 6 mL, and for *n*-$Bu_4N{\cdot}HSO_5$, we used 4.5 mL, so the corresponding signals revealed each injection with plateaus appearing while reaching equilibrium.

34. Feichtinger, D.; Plattner, D. A. *Chem. Eur. J.* **2001**, *7(3)*, 591-599.

35. Kurz, P.; Berggren, G.; Anderlund, M. F.; Styring, S. *Dalton Trans.* **2007**, 4258-2461.

36. Pizarro, S. A.; Visser, H.; Cinco, R. M.; Robblee, J. H.; Pal, S.; Mukhopadhyay, S.; Mok, H. J.; Sauer, K.; Wieghardt, K.; Armstrong, W. H.; Yachandra, V. K. *J. Biol. Inorg. Chem.* **2004**, *9*, 247-255.

Chapter 3

Synthesis and Characterization of a Series of Manganese Dimers with the $[Mn_2(\mu\text{-}O)_2(\mu\text{-}CO_2Ar)_2]^+$ Core and the Unexpected Formation of Hexamers with the $\{Mn_6O_8\}^{4+}$ Core

3.1. Background

The element manganese plays a crucial role in the active site of many enzymes.[1] (For examples, see Chapter 2.1) It is relatively abundant among the metals in nature, constituting about 0.085% of the earth's crust.[2] Mn in the form of oxides is also important in material science because of its presence in octahedral molecular sieve catalysts[3] as well as in substances that display colossal magnetoresistance (CMR) in, for example, rare-earth perovskite magnetite systems $Ln_{1-x}A_xMnO_3$ (Ln = La, Pr, Nd and A = Ca, Sr).[4] Also, Christou and coworkers and others have reported the synthesis and magnetic properties of many interesting polynuclear manganese-oxo aggregates, a number of which behave as single molecule magnets (SMM).[5] In addition, manganese is roughly similar to Fe in its physical and chemical properties;[6] therefore, the research concepts applied in Fe chemistry may be used as a guide while studying Mn chemistry. The Oxygen-Evolving Complex (OEC) of Photosystem II (PSII) utilizes a Mn_4Ca cluster to catalyze the conversion of water to dioxygen within plant chloroplasts. We have engaged in exploring potential structural candidates as the models for the OEC cluster. The synthetic approach which we employ incorporates carboxylate and pyridyl ligands that are taken to resemble peptide side-chain donors of the amino acid residues known to bind the PSII Mn_4Ca cluster, namely aspartate (Asp), glutamate (Glu), and histidine (His) into the synthetic model complexes.[7] Generally, smaller carboxylate ligands, such as

acetate and benzoate, are coordinated to manganese in attempts to mimic the PSII active site. However, often with such ligands rather large aggregates are observed. For example, complexes which contain from six to 84 or even higher numbers of manganese atoms have been structurally characterized.[8] These sizable aggregates are of course not particularly useful for modeling the OEC active site. Nonetheless, in many cases their magnetic properties have been studied in detail in the search for SMM applications. We have demonstrated that by using sterically bulkier carboxylate ligands the cluster nuclearity may be limited to some degree, which is desirable when modeling the OEC $CaMn_4$ center. We conjecture that a useful pathway to tetramanganese complexes is to make new binuclear complexes and then to dimerize them to form a dimer-of-dimers or another type of tetranuclear aggregate.[9] With such an approach, the synthetic products may be predicted and the number of manganese atoms of the resulting clusters is expected to be controllable. Ligand exchange syntheses, a route that helps control aggregate size, are highlighted in this work. There are two types of carboxylates in the complexes that we present here – sterically hindered benzoate derivatives [2,6-Di(*p*-tolyl)-benzoate, 2,6-Di(phenyl)-benzoate and 2,4,6-tri-*i*-propyl-benzoate] and less sterically crowding benzoates [2,4,6-trimethyl-benzoate, 3,5-bis-trifluoromethyl-benzoate and unsubstituted benzoate]. Ligand-exchange synthetic methods provide an alternative pathway in the preparation of various novel complexes that likely could not be prepared by direct self-assembly methods.[10] We prepared several new polynuclear aggregates, which are identified by X-ray diffraction, and characterized by NMR, EPR, mass spectroscopy, FTIR, UV-Vis and elemental analysis. We have also investigated the magnetic properties of two of the bulky carboxylate ligand system products.

3.2. Experimental Section

3.2.1. Materials. Acetonitrile used for synthesis and spectroscopic studies was distilled from CaH_2 under nitrogen and stored over 3 Å molecular sieves prior to use. Deuterated acetonitrile (Cambridge Isotope Laboratories, Inc.) was dried in oven-dried glassware over activated 3 Å molecular sieves. All other reagents were purchased from commercial sources and used as received. The supporting electrolytes TBAP, tetrabutylammonium perchlorate, and TEAP, tetraethylammonium perchlorate, were electrochemical grade (≥ 99%) and used as received. Paratone-N oil was obtained from Hampton Research Corp. All chemicals used in this work were reagent grade.

3.2.2. Physical Methods. ^{1}H NMR spectra data were collected on Varian Unity 300 MHz and 400 MHz spectrometers with a 60-100 kHz sweep width. A first-order correction function provided with the spectrometer software was used for baseline correction wherever needed. Chemical shifts are quoted on the δ scale with shifts downfield being positive. Values for chemical shifts (ppm) are the observed shifts referenced to resonances for residual protons in the various deuterated solvents: CHD_2CN, 1.94 ppm; $CHCl_3$, 7.26 ppm; and $CHDCl_2$, 5.32 ppm. Electrospray ionization mass spectrometry (ESI-MS) was performed in the Boston College Mass Spectrometry Facility and recorded by using a Waters LCT classic instrument (Milford, MA). All samples were dissolved in LC/MS CHROMASOLV® grade solvents (≥ 99.9%) such as acetonitrile, methanol and filtered through filter paper prior to analysis. Mass spectra were measured for 10-100 μM sample solutions in positive ion mode, and samples were infused into the spectrometer using a Harvard syringe pump operating at a flow rate of 10μL per minute. Typical instrument conditions: 3.5 kV capillary voltage, 5 V cone

voltage, and desolvation temperature at 120 °C, data were recorded using the electrospray method. Electronic spectra were collected by using a Hewlett Packard 8453 diode array spectrophotometer and a Varian Cary 50 Bio spectrophotometer. Infrared spectra were recorded by using a Nicolet 380 FTIR spectrometer on samples prepared as either KBr pellets or as acetonitrile solutions or in some cases untreated when using diamond ATR analysis. Elemental analyses were performed by Robertson Microlit Laboratories, Inc. Madison, NJ.

3.2.3. Magnetic Susceptibility Study. Solid state magnetic susceptibility measurements were performed on a Quantum Design AC and DC Magnetic Property Measurement System (MPMS®, Model C280) magnetometer at the MIT Center for Materials Science and Engineering (CMSE). A Superconducting Quantum Interference Device (SQUID) instrument was used for the experimental measurements. The microcrystalline samples were measured in the temperature range of 2 K - 300 K with a constant applied magnetic field (*H*) of 1 kG (0.1 T). The following setup for the measurements was employed. The microcrystalline sample was placed in tightly-wrapped polyethylene protective filter paper (PPP) and that was sealed within a plastic straw. The straw was carefully chosen for its qualitative feature in order to eliminate the background noise. Contamination from manual handling was avoided, and the sample was placed into the magnetometer then vented the system until it reached the pressure-steady status for the measurement. A background correction term was included into the equation used for data analysis. Magnetization (*M*) measurements were performed in the 2 - 300 K temperature range. A zero-field cooling (ZFC) process[11] took place first and that was followed by a subsequent magnetic field application of H = 0.1 T at 2 K. The

macroscopic magnetization was recorded as a function of time in a constant applied magnetic field of 0.1 T. The magnetic moment data were collected in 0.2 degree increments from 2 – 4 K and 2 degree increments from 4 – 300 K

3.2.4. EPR Spectroscopic Study. X-band EPR spectra were collected with a Bruker 500 CW-EPR spectrometer of the ELEXSYS series at Bruker Instruments, Inc., Billerica, MA in the temperature range 4 – 77 K with an Oxford Instruments ESR 900 continuous-flow cryostat interfaced with an Oxford Instruments ITC4 temperature controller.

3.2.5. Electrochemistry. A BAS-100A Electrochemical Analyzer was used for electrochemical measurements. A conventional three-electrode cell was used for the study employing a platinum disk working electrode, a platinum wire auxiliary electrode and $Ag/AgClO_4$ was used as the reference electrode. The measurements were performed in distilled acetonitrile solution in the presence of supporting electrolyte (generally 0.1 M TBAP or 0.1 M TEAP) and under a dry, purified argon atmosphere. Under these conditions the $E_{1/2}$ value for the Fc/Fc^+ couple was +79 mV. Potentials are reported versus the Fc/Fc^+ couple.[12] The potentials reported in this work were uncorrected for a junction contribution.

3.2.6. X-ray Crystallography. Data were collected by using a Bruker SMART CCD (charge coupled device) based diffractometer equipped with an LT-3 low-temperature apparatus operating at 193K or 100K. Suitable single crystals were chosen and mounted on a glass fiber or glass loop by using APIEZON-T grease mixed with Paratone-N oil. Data were measured using omega scans of 0.3° per frame for 20 or 30 seconds, such that a hemisphere was collected. A total of 1271 frames at the sample-detector distance of 5.00 cm or 2412 frames at 6.00 cm were collected to a maximum resolution of 0.75 Å.

The first 50 frames were recollected at the end of data acquisition to monitor for decay. All of the crystals used for the X-ray diffraction studies showed no decomposition during the data collection. Cell parameters were determined by using SMART software and data reduction was performed and refined by using SAINT software, which corrects for Lp and decay on all observed reflections. Absorption corrections were performed with the program SADABS as supplied by George Sheldick. The structures were solved by the direct or Patterson method using the SHELXS-97 program and refined by least squares methods on F^2 in SHELXL-97, incorporated in SHELXTL-PC V 5.10. All non-hydrogen atoms were refined with anisotropic thermal parameters. Hydrogen atom positions were calculated by geometrical methods and refined by using a riding model. All ORTEP drawings are made using 50% probability thermal ellipsoids.

3.2.7. Preparation of Compounds.

Ligand Synthesis. The ligands were synthesized on a 10 mmole scale according to literature procedures.[13] Purification was performed via recrystallization and the corresponding X-ray crystal structures were obtained and they are shown in Appendix E. During the synthesis, we also isolated the impurities from products, which were found to be intermediates in the synthesis and were structurally determined. The X-ray crystal structures of these impurities are provided in Appendix E as well.

2,6-Di(R)benzoic Acid (Ar^RCOOH) (where, R = phenyl, *p*-tolyl, 4-*tert*-butylphenyl). To a stirred solution of 1,3-dichlorobenzene (1.14 mL, 10 mmole) in 20 mL of tetrahydrofuran (THF) at –70 °C ($CHCl_3$/dry ice slush) was added a 1.6 M hexane solution of BuLi (6.3 mL, 10 mmole) slowly over 20 minutes via a cannula transfer line under an N_2 atmosphere. The reaction mixture was stirred at –70 °C for 1.5 hrs, after

which the resulting solution was cooled to –84 °C (EtOAc/liq. N_2 slush). To this stirred solution a THF solution of 1.0 M phenylmagnesium bromide (20 mL, 20 mmole) was added slowly dropwise by using a cannula transfer line under an N_2 atmosphere. The reaction mixture was allowed to warm up to room temperature and refluxed under N_2 overnight. 'Bone-dry' CO_2 gas was bubbled through the solution for an hour and the solution was then acidified with 25 mL of 10% aqueous HCl. The aqueous layer was extracted with 30 mL of CH_2Cl_2 several times. The combined organic layers were washed with water and dried over anhydrous $MgSO_4$ for 4 hrs. The light yellow solution was filtered and the filtrate was evaporated to dryness by using a rotary evaporator. The crude product was purified by dissolving it in hot hexane/EtOAc and then cooling to –20 °C, after which a white precipitate deposited. Purity of the products was assessed by using ^{1}H NMR and mass spectrometry. The yields of the products were 1.17g (phenyl, 42.8%); 0.72g (*p*-tolyl, 23.7%); 0.11g (*tert*-butyl-phenyl, 2.7%).

Sodium 2,6-Di(R)benzoate (Ar^RCOONa) (where, R = phenyl, *p*-tolyl, 4-*tert*-butylphenyl). Two synthetic pathways were used to prepare sodium salts of the ligands.

Method A. To a white suspension of the acid (Ar^RCOOH, 0.2 mmole) in 10 mL of MeOH was added one equivalent of NaOH and the mixture was stirred for 20 minutes to give a clear colorless solution. The resulting solution was then evaporated to dryness to give white powder. Purity of the products was confirmed by ^{1}H NMR and mass spectrometry. The yields of products were 0.59 g (phenyl, 99.6%); 0.62g (*p*-tolyl, 95.6%); 0.77 g (*tert*-butyl-phenyl, 94.2%).

Method B. This method is analogous to Method A but sodium methoxide (NaOMe) was used instead of NaOH. To a white suspension of the acid (Ar^RCOOH, 0.2 mmole) in

10 mL of MeOH was added one equivalent of NaOMe and the mixture was stirred for 8 h to give a clear colorless solution. The resulting solution was then evaporated to dryness to give white powder. Purity of the products was confirmed by ^{1}H NMR and mass spectrometry. The yields of the products were similar to the ones reported in Method A.

Synthesis of Complexes.

$[Mn_2O_2(L)_4](ClO_4)_3$ (where, L = bpy [**19**] and dmb [**20**])**.** The Mn_2O_2 (III,IV) dimer with bpy ligands was synthesized according to the literature procedure, which is described in Method A below.[10a] Alternatively both the bpy and dmb complexes can be obtained by a synthetic method that was developed by our group, in which *tert*-butyl-hydroperoxide (*t*-BuOOH) is used as the oxidant.[14]

Method A. $Mn(OAc)_2 \cdot 4H_2O$ (17.5 mmole, 4.3 g) was allowed to react with 2,2'-bipyridine (52.5 mmole, 8.2 g) in approximately 100 mL of a H_2O/acetone solvent mixture. After adding 80 mL of 1M pH 4.5 acetate buffer, the resulting solution was then cooled to 0 °C and 30 mL of an aqueous solution of the oxidant $KMnO_4$ (7.5 mmole, 1.18 g) was added dropwise over 20 min with continuous stirring, which continued for 15 min after the addition was completed. An aqueous solution of concentrated sodium perchlorate was added causing precipitation of a greenish product, which was filtered on a medium frit and washed with cold ethanol and diethyl ether and dried under vacuum. The purity of the product was assessed by using ^{1}H NMR and mass spectrometry. The yield was 9.57 g (68.4%).

Method B. To a clear acetonitrile solution (20 mL) of $Mn(ClO_4)_2 \cdot 6H_2O$ (0.200 g, 0.552 mmole) was added 2,2'-bipyridine (0.174 g, 1.113 mmole) or 4,4'-dimethyl-2,2'-bipyridine (dmb, 0.205g, 1.113 mmole) to give a light yellow solution. Then 3.86 mL of

70% *t*-BuOOH was added dropwise over 15 min to the resulting yellow solution with continuous stirring and the solution color immediately turned to dark green along with the evolution of oxygen gas during the addition. The solution was then stirred for an additional 30 min, filtered, and evaporated to dryness. The crude product was washed with diethyl ether (Et_2O) and redissolved in acetonitrile, filtered, and kept for recrystallization by ACN/Et_2O vapor diffusion at –20 °C. A dark green crystalline product was deposited after 1d and the crystals were collected by filtration, washed with diethyl ether and dried under vacuum. Purity of the products was assessed by ^{1}H NMR and mass spectrometry. Yield: 95.7 mg (bpy, 32.6 %); 216.8 mg (dmb, 66.7%).

$[Mn_2O_2(bpy)_2(Ar^RCO_2)_2](ClO_4)$ (where *R* = di-phenyl [**21**], di-*p*-Tolyl [**22**], 2,4,6-tri-*i*-propyl [**23**]). To a stirred green acetonitrile (40 mL) solution of $[Mn_2O_2(bpy)_4](ClO_4)_3$ [**19**] (106.4 mg, 0.1 mmole) was added 2 equivalent of solid Ar^RCO_2Na (0.2 mmole, **21**, 59.26 mg; **22**, 64.87 mg; **23**, 54.07 mg). The dark green solution with a white suspension was stirred at room temperature for 6 h under ambient conditions. The solution color changed from dark green to dark reddish brown and all of the white carboxylate solid dissolved. The solvent was evaporated to dryness under reduced pressure. The residue was washed several time with small portions of diethyl ether in order to remove the uncoordinated 2,2'-bipyridine from the reaction product. The solid residue was extracted with 25 mL of CH_2Cl_2, filtered, and the filtrate was then concentrated to 5 mL by slow evaporation under ambient conditions to afford microcrystalline solid. The product was collected by filtration, then washed with Et_2O and dried under vacuum. The yields: **21**, 32.6 mg (40 %); **22**, 34.2 mg (50%). We were not able to determine the yield of the 2,4,6-tri-*i*-propyl benzoate reaction product. The

mass spectrum of material from the CH_2Cl_2 extraction in this case revealed a mixture of dinuclear (Mn_2O_2) and hexanuclear (Mn_6O_8) species along with the Mn(II) complex $[Mn(bpy)_2(Ar^RCO_2)]^+$. Recrystallization of this mixture provided crystals of only $[Mn_6(\mu\text{-}O)_4(\mu_3\text{-}O)_4(bpy)_6(Ar^{2,4,6\text{-tri-}i\text{Pr}}CO_2)_2](ClO_4)_4$, which is described below.

$[Mn_6(\mu\text{-}O)_4(\mu_3\text{-}O)_4(L)_6(Ar^RCO_2)_2](ClO_4)_4$ [**24**] (where, L = bpy and *R* = 2,4,6-tri-*i*-propyl). These hexanuclear complexes were synthesized by using two different methods, both of which were modifications of a procedure reported before by our group.[14, 15] The related discussion was in Section 3.2.5.

Method A: To a stirred green acetonitrile (40 mL) solution of $[Mn_2O_2(bpy)_4](ClO_4)_3$ [**19**] (106.4 mg, 0.1 mmole) was added 2 equivalents of solid Ar^RCO_2Na (54.1 mg, 0.2 mmole). The dark green solution with a white suspension was stirred at room temperature for 6 h under ambient conditions and the color changed from dark green to dark reddish brown, with all of the carboxylate having dissolved. The solvent was evaporated to dryness under reduced pressure then the resulting solid was washed with small portions of diethyl ether several times in order to remove the reaction product 2,2'-bipyridine. The solid residue was extracted with 25 mL of CH_2Cl_2. The filtrate was then concentrated to 5 mL by slow evaporation under ambient conditions to afford a microcrystalline solid. The product was collected by filtration, then washed with Et_2O and dried under vacuum. As describe above, the product contained dinuclear (Mn_2O_2), hexanuclear (Mn_6O_8) and mononuclear $[Mn(bpy)_2(Ar^RCO_2)]^+$ species. The yield was 0.13 g for the mixture. This mixture was redissolved in acetonitrile, filtered, and kept for recrystallization by ACN/Et_2O vapor diffusion at –20 °C. A dark green, brownish crystalline product was obtained after 2d and the crystals were collected by filtration,

washed with diethyl ether and dried under vacuum. The recrystallized product was structurally identified by X-ray crystallography (Fig. 4) and also characterized by the mass spectrometry (Fig. 14), showing that the compound has the formulation $[Mn_6(\mu\text{-}O)_4(\mu_3\text{-}O)_4(bpy)_6(Ar^{2,4,6\text{-tri-}i\text{Pr}}CO_2)_2](ClO_4)_4$ [**24**]. Yield: 57.6 mg (75.5%, based on Mn).

$[Mn_6(\mu\text{-}O)_4(\mu_3\text{-}O)_4(L)_6(OAc)_2](OTf)_4$ [**25**] (where, L = dmb).

Method B: This method was developed by following the procedures described by Dr. Sumitra Mukhopadhyay for the purpose of investigating the unknown compound which was generated during the preparation of $[Mn_4(\mu\text{-}O)_5(dmb)_4(dmbO)_2](OTf)_4$.[14] To a blackish-blue acetonitrile solution of $[Mn_2O(OAc)_2(dmb)_2(OTf)_2]$ (0.109 g, 0.115 mmole) was added a light yellow solid of the O atom donor 2-*tert*-butyl-sulfoxide-iodosobenzene (0.04 g, 0.118 mmole). The heterogeneous reaction mixture was stirred under ambient conditions overnight. In contrast to the previous work, we did not observe the product $[Mn_4(\mu\text{-}O)_5(dmb)_4(dmbO)_2]^{4+}$. Instead, the ESI-MS data shown in Fig. 15 revealed that a product with the formulation of $[Mn_6(\mu\text{-}O)_4(\mu_3\text{-}O)_4(dmb)_6(OAc)_2](OTf)_4$ [**25**] was obtained. Yield: 37.2 mg (42.6%, based on Mn).

$[Mn_4O_2(bpy)_6(Ar^RCO_2)_7](ClO_4)$ (*R* = 3,5-bis-trifluoromethyl [**26**]). An acetonitrile (40 mL) solution of $[Mn_2O_2(bpy)_4](ClO_4)_3$ [**19**] (106.4 mg, 0.1 mmole) was added 2 equivalents Ar^RCO_2Na (56.0 mg, 0.2 mmole) as a solid. The carboxylate did not dissolve immediately. This mixture was stirred at room temperature for 6 h under ambient conditions and the color changed from dark green to dark reddish brown, during which time the carboxylate salt fully dissolved. The solvent was evaporated to dryness under reduced pressure. The resulting residue was washed with small portions of diethyl ether several times in order to remove the reaction product 2,2'-bipyridine. The solid residue

was extracted with 25 mL of CH_2Cl_2 and the filtrate was then concentrated to 5 mL by slow evaporation under ambient conditions to afford a microcrystalline solid. The product was collected by filtration, then washed with Et_2O and dried under vacuum. Mass spectrometry analysis of this compound indicated the presence of $[Mn_4O_2(bpy)_6(Ar^RCO_2)_7](ClO_4)$ [**26**], the peak for which indicated that it was the major product.

$[Mn(bpy)_3](X)_2$ ([**27**]$(X)_2$, where X = ClO_4, OTf). These complexes were prepared according to a reported procedure.[14] To an acetonitrile solution (20 mL) of $Mn(ClO_4)_2 \cdot 6H_2O$ (0.200 g, 0.552 mmole) or $Mn(OTf)_2 \cdot 2CH_3CN$ (0.240 g, 0.552 mmole) was added 3 equivalents of 2,2'-bipyridine (bpy) (0.258 g, 1.656 mmole) to give a light yellow solution. The resulting solution was stirred for 10 min and evaporated to dryness. Recrystallization was accomplished by using diethyl ether vapor diffusion into an acetonitrile solution at –20 °C. The products were structurally identified by X-ray crystallography and the purity of the products was confirmed by mass spectrometry. The yields were [**27**]$(ClO_4)_2$, 36.1 mg (63.7%); [**27**]$(OTf)_2$, 22.9 mg (34.4%).

3.3. Results and Discussion

3.3.1. Synthesis. A survey of products obtained from reactions between [**19**] or [**20**] and a series of carboxylates (Scheme 3.1), which were carried out with the initial purpose of finding ligands for which the exchange reactions provide products that have an intact dinuclear core rather than larger aggregates. The results of this survey, shown in Scheme 3.1, led us to propose a correlation between the reaction product type and variables such as pK_a and ligand steric properties. In 2003, we reported a dinuclear cluster, $[Mn_2^{(III,IV)}O_2(bpy)_2(Ar^{p\text{-}tolyl}CO_2)_2](ClO_4)$, [**22**], in which the bulky carboxylate ligand, 2,6-

di(tolyl)benzoate, was used as the bridging ligand between the two manganese centers.[16] Based on the X-ray crystal structure of the complex, we originally postulated that the space between bipyridine rings and two of the tolyl groups from benzoate was not particularly sterically crowded, allowing the formation of this Mn_2O_2 cluster. A related higher nuclearity Mn aggregate, $[Mn_6O_8(dmb)_6(Ar^{p\text{-}tolyl}CO_2)_2](ClO_4)_4$ [**25**], was obtained with the ligand combination of dmb and 2,6-di(tolyl)benzoate.[15] We thought for this ligand arrangement, if an analogous Mn_2O_2 cluster similar to [**22**] was formed, a significant steric clash between methyl groups of dmb and $Ar^{p\text{-}tolyl}CO_2$ would destabilize the dinuclear conformation and trigger further aggregation to form [**25**]. That was the original idea proposed tentatively for the observation of various resulting clusters – the steric clash was suggested as a factor that correlates with the formation of products. The work presented here was initiated mainly to test this idea. First, we decided to use a sterically smaller substituent on the benzoate ring, such as phenyl and isopropyl groups, as compared to the tolyl group that was used previously. Based on the original hypothesis, we reasoned that these carboxylates would provide a dinuclear structure like the one for the 2,6-di(tolyl)benzoate ligand. Also, we thought that this set of benzoic acids have pKa values close enough to each other such this parameter was being held essentially constant. In all, we have examined six carboxylates and the results are summarized in Scheme 3.1. Our observations from screening of the chemistry for these carboxylates have led us to revise the original hypothesis. In the tolyl system, the "structural clash" hypothesis was not valid with regard to the observation of a resulting hexanuclear complex, $[Mn_6O_8(bpy)_6(Ar^{p\text{-tolyl}}CO_2)_2]^{4+}$, which retained a less sterically crowded space between bipyridine and $Ar^{p\text{-}tolyl}CO_2$ in the postulated binuclear precursor.

However, we were not able to obtain a single crystal of the hexanuclear complex for X-ray structure determination, but instead, in the 2,4,6-tri-*i*-propyl benzoate ligand system, the structure of an analogous hexanuclear complex, $[Mn_6O_8(bpy)_6(Ar^{2,4,6\text{-tri-}^{i\text{Pr}}}CO_2)_2](ClO_4)_4$ [**24**], was obtained. Meanwhile, dimanganese complexes similar to [**22**] were also found with less sterically crowded ligands, such as 2,6-di(phenyl), 2,4,6-tri-methyl and 2,4,6-tri-*i*-propyl systems. At first, we thought only multinuclear manganese aggregates such as the Mn_4O_2 butterfly-type complex or Mn_6O_8 aggregate or even a cluster with a much larger number of Mn atoms would be generated as the product for these less sterically crowded ligands since the original hypothesis suggested that a certain level of steric crowdedness helps to stabilize the Mn_2O_2 dicarboxylate-bridged complexes, but the results showed the opposite – dinuclear complexes were also formed in these systems. Moreover, the dimanganese complexes were not the only reaction products observed in the systems we studied according to the mass spectroscopic results. We routinely employ mass spectroscopy to examine reaction systems at each stage and our initial assumption is that the relative quantity of a species formed can be determined by MS signal intensities. The mass spectral data indicate that multinuclear Mn aggregates were formed in addition to the dinuclear ones. One of the dimanganese complexes was isolated and structurally determined, [**21**], as shown in Figure 1. The multinuclear, Mn_6O_8 and Mn_4O_2 type of clusters, which were products from various ligand systems, were identified by both X-ray crystallography and ^{1}H NMR spectroscopy. These will be discussed in the following sections. Reactions using the much less sterically hindered carboxylates such as benzoate, were found to yield a mixture of the products $[Mn_4O_2(bpy)_6(OPh)_7]^{4+}$ and $[Mn^{III,III}{}_2O(bpy)_2(OPh)_2(H_2O)_2]^{2+}$ as detected by mass

spectroscopy. For the reaction involving 3,5-bis-trifluoromethyl benzoate, we found that $[Mn_4O_2(bpy)_6(Ar^{3,5\text{-}CF_3}CO_2)_7](ClO_4)_4$ [**26**] was the major product, the structure of which is shown in Figure 5. Additionally, a lesser amount of $[Mn^{III,III}_2O(bpy)_2(Ar^{3,5\text{-}CF_3}CO_2)_2(H_2O)_2]^{2+}$ was generated but we have not confirmed this assignment by X-ray crystallography yet. For the purpose of examining the correlation between ligand physical properties and reaction products in our studies, we used ligand steric properties and pKa values as two variables for investigation. Variations of the former parameter were described above and 3,5-bis-trifluoromethyl benzoate is a well-defined example for the latter. In the 3,5-bis-trifluoromethyl benzoate ligand system, which led to the formation of the Mn_4O_2 butterfly type cluster as the major product. We suggest that a possible reason for this is that the corresponding carboxylic acid has a lower pK_a due to the electron-withdrawing CF_3 substituents, which favors the formulation of the Mn_4O_2 reaction product. Moreover, we believe that these much less sterically hindered carboxylates such as benzoate and 3,5-bis-trifluoromethyl benzoate do not hold the dinuclear core intact but rather undergo further aggregation. There were examples of many high nuclearity clusters reported by others for much less sterically hindered carboxylates.[17] But the sterically larger *ortho*-substituted benzoate ligand systems tend to provide the desired low nuclearity dimanganese species. These "*ortho*-position-heavy-substituents" are prone to block aggregation, thus helping to retain the Mn_2O_2 core unless another steric clash occurs within the structure. As shown in Scheme 3.2, we propose a possible ligand-exchange reaction mechanism in detail but there are no intermediates isolated or structurally characterized to verify this proposal to date. A noteworthy aspect of this proposal is the existence of a plausible reaction product based on the crystal

structure shown in Figure 2, for which there is one bridged and two terminal carboxylates coordinated to the Mn_2O_2 core. The discovery of this interesting binuclear complex leads to a possible design for further aggregation. We think that a dimanganese (III,IV) complex with this type of ligand arrangement is a potential candidate as a precursor for subsequent structural designs with regard to constructing novel synthetic complexes. Furthermore, the possibility of intermolecular conversion in the solution from Mn_2 to Mn_6 clusters should also be evaluated. This work shows that steric effects as well as pK_as probably influence the type of product formed. This information may allow one to make predictions for the outcome of related ligand exchange reaction in the future. Advanced investigations to test the ideas presented here are in progress.

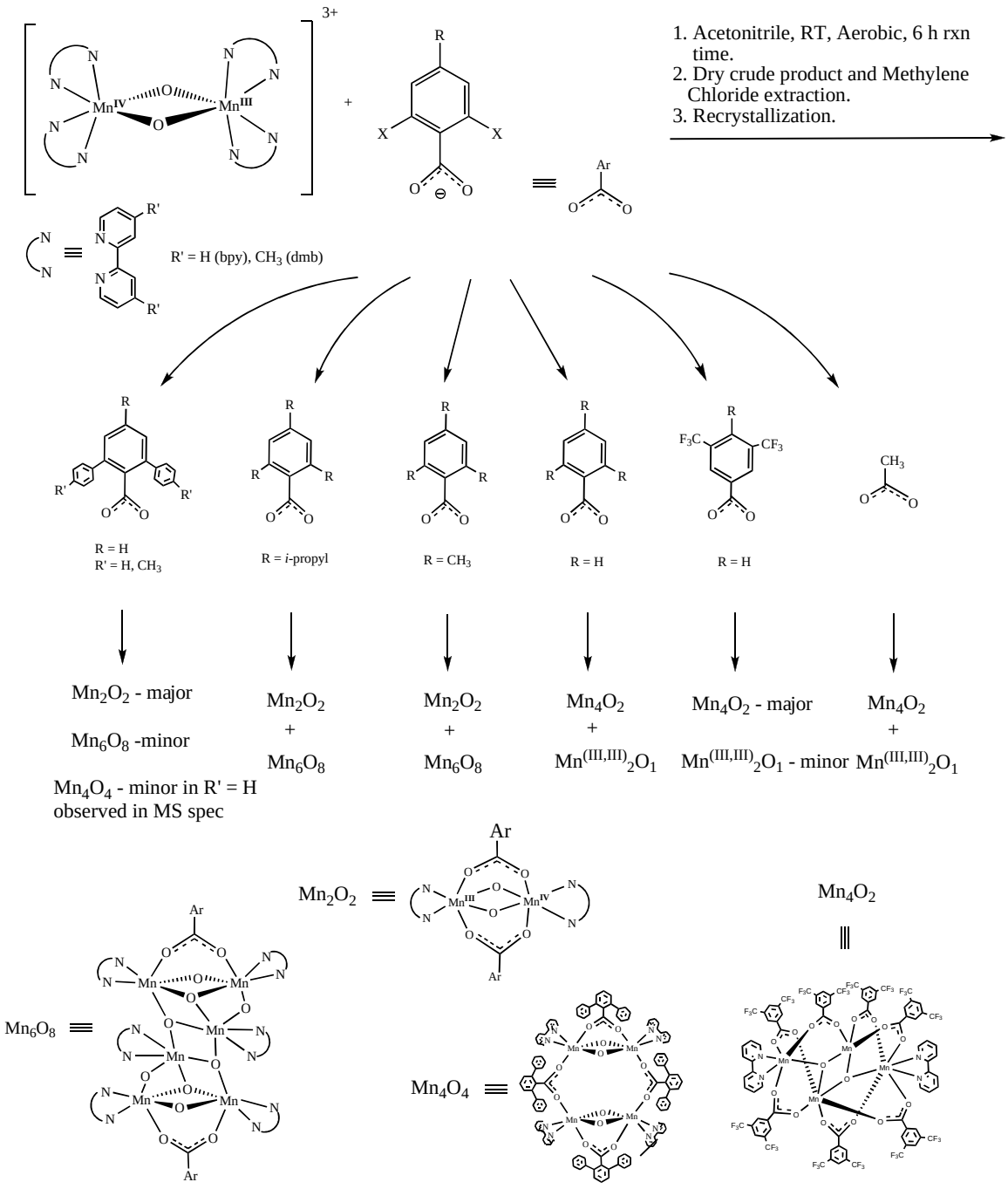

Scheme 3.1. Summary of the synthetic results performed in this work via ligand exchange method. Structures are abbreviated according to the Mn core formulation.

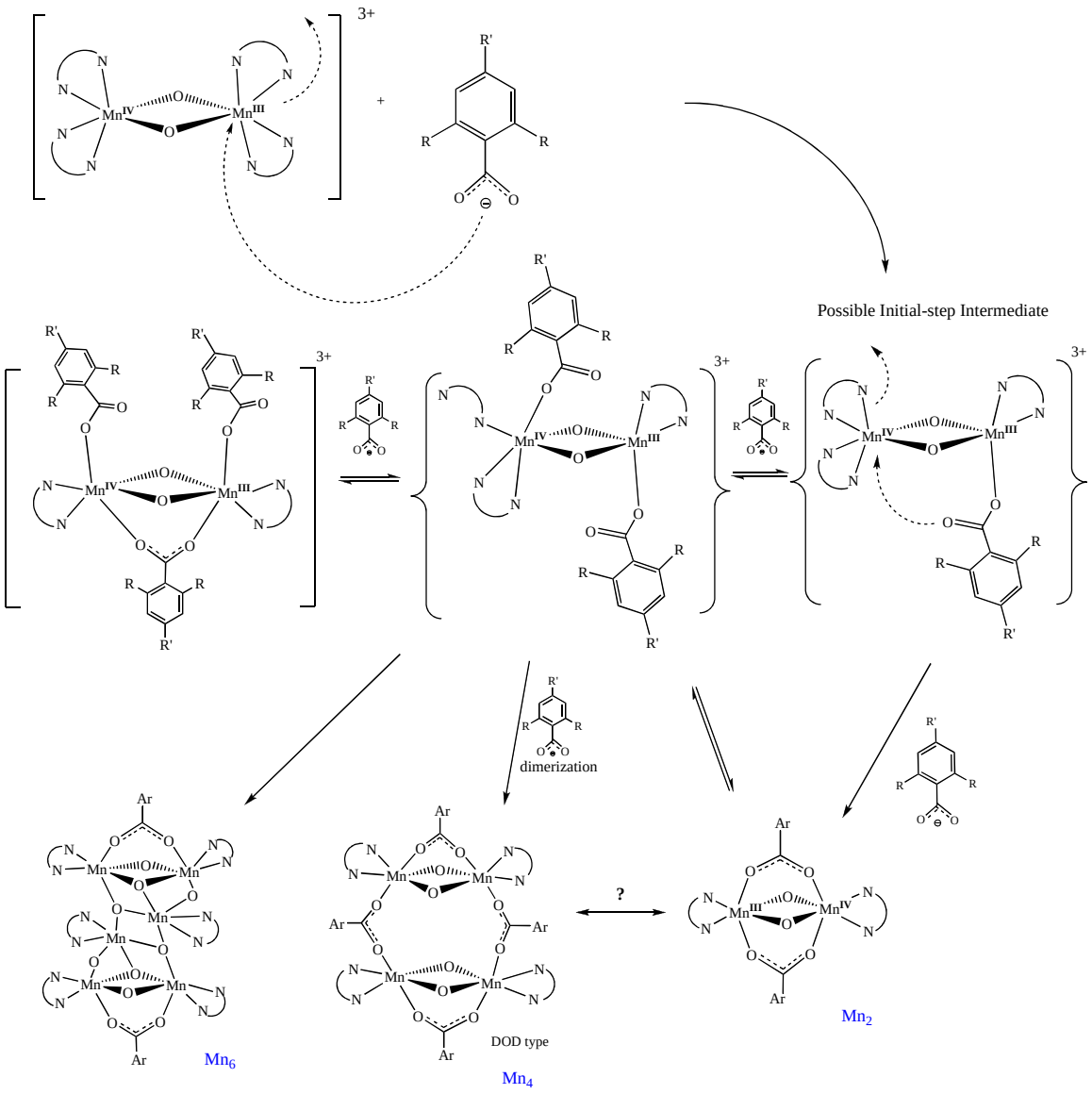

Scheme 3.2. Proposed mechanistic scheme for the benzoate-type ligand substitution in the formation of products observed.

3.3.2. Crystal Structure. Some aspects of the reactions discussed in the previous section were based on solid state structures established by single crystal X-ray diffraction methods. Structural features of the products are presented in this section. In [**21**], Mn(1) and Mn(2) are assigned as +4 and +3 ions, respectively, based on Mn(1) having shorter bond distances between the manganese center and oxo bridging ligands as well as for the

O atoms from bridging carboxylates: Mn(1)-O(1), Mn(1)-O(2) [*average*, 1.76 Å] and Mn(1)-O(3), Mn(1)-O(5) [*average*, 1.96 Å]. The +3 formal oxidation state of Mn(2) induces the Jahn-Teller distortion effects which elongate the bonds around the metal center as compared to the bonds observed at Mn(1) center: Mn(2)-O(1), Mn(2)-O(2) [*average*, 1.82 Å] and Mn(2)-O(4), Mn(2)-O(6) [*average*, 2.24 Å]. As expected, a comparison between [**21**] and [**22**] (ORTEP diagram shown in Appendix E) reveals a close correspondence in bond distances and angles as illustrated in Table 3.1.

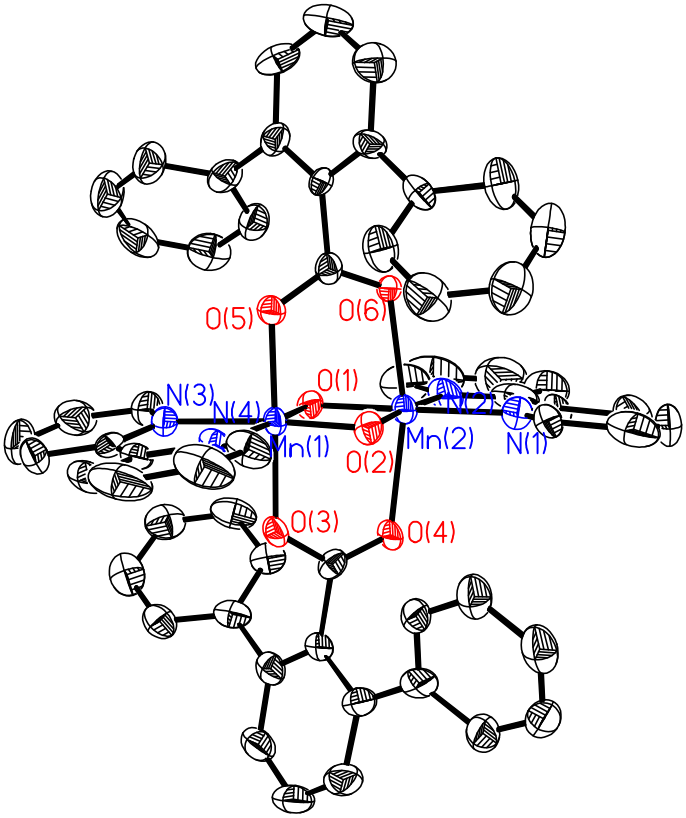

Figure 3.1. ORTEP diagram of $[Mn_2(\mu\text{-}O)_2(bpy)_2(Ar^{Ph}CO_2)](ClO_4)$ [**21**] showing 50 % probability ellipsoids and atom labeling scheme. The H atoms, perchlorate counterion and CH_2Cl_2 molecules are omitted for clarity.

Table 3.1. Selected bond distances (Å)and angles (°) of [**21**] and [**22**].

	[**21**]	[**22**]
Mn(1)-O(1)	1.758(5)	1.764(3)
Mn(1)-O(2)	1.767(6)	1.768(3)
Mn(1)-O(4)	1.962(6)	1.808(4)
Mn(1)-O(6)	1.955(6)	1.831(3)
Mn(2)-O(1)	1.810(6)	1.942(4)
Mn(2)-O(2)	1.827(6)	1.948(4)
Mn(2)-O(3)	2.278(6)	2.310(4)
Mn(2)-O(5)	2.203(6)	2.326(4)
Mn(1)-Mn(2)	2.5062(19)	2.5058(11)
O(1)-Mn(1)-O(2)	93.0(3)	93.07(16)
O(1)-Mn(1)-O(6)	91.3(3)	91.70(16)
O(2)-Mn(1)-O(6)	91.0(3)	91.03(16)
O(1)-Mn(1)-O(4)	89.9(3)	90.48(16)
O(6)-Mn(1)-O(4)	178.1(3)	174.78(14)
O(1)-Mn(2)-O(2)	89.4(3)	89.59(15)
O(1)-Mn(2)-O(5)	85.6(2)	85.35(15)
O(2)-Mn(2)-O(5)	84.4(2)	83.99(14)
O(5)-Mn(2)-O(3)	164.7(2)	162.62(12)
Mn(1)-O(1)-Mn(2)	89.2(2)	89.08(15)
Mn(1)-O(2)-Mn(2)	88.4(2)	88.25(15)

Of special interest is a novel complex, [**28**], which was obtained from recrystallization of the crude reaction product of [**21**] via vapor diffusion of diethyl ether (Et_2O) into an acetonitrile solution. The crystal structure of [**28**] is shown in Figure 2. We invoked this dimanganese complex as a possible reaction product as shown in the proposed reaction mechanism, which is displayed in Scheme 3.2. Based on the crystal structure data for [**28**], the dinuclear $\{Mn_2O_2\}$ core is still in the (III,IV) oxidation state, judging from the bond lengths around manganese centers. The observed bond distances between Mn and μ-oxo bridged ligands indicate the assigned oxidation states for Mn(1) and Mn(2) are +4

and +3 ions, respectively: Mn(1)-O(1), Mn(1)-O(2) [1.758 and 1.803 Å respectively] are shorter than Mn(2)-O(1), Mn(2)-O(2) [1.809 and 1.851 Å respectively]. Also, between manganese and the bridging carboxylate ligand, the Mn-O bond lengths behave similarly: Mn(1)-O(3) [2.052 Å] is slightly shorter than Mn(2)-O(4) [2.107 Å]. Making a comparison between a single carboxylate bridge complex, [**21**], and doubly-carboxylate-bridged complex, [**28**], we have observed an interesting phenomenon for the bond distances between Mn and μ-oxo bridged ligands around the two different oxidation state manganese centers, which in [**28**], Mn(1)-O(2) [1.803 Å] is longer than the corresponding Mn(1)-O(1) [1.758 Å]. However, in [**21**] the Mn-O bond distances at $Mn^{(IV)}$ are found to be equal; Mn(1)-O(1), Mn(1)-O(2) [*average*, 1.76 Å]. At $Mn^{(III)}$ site, Mn(2)-O(2) [1.851 Å] is longer than Mn(2)-O(1) [1.809 Å] in [**28**] but is the same in [**21**]. We think that the *trans* effects caused by the terminally coordinated carboxylates at the Mn centers are the main reason for the aforementioned bond distance variations. The carboxylate O atom donors are harder than the N atoms of bpy ligands; therefore, according to HSAB rules, the doubly-bridged carboxylates in [**21**] reveal that the $Mn^{(IV)}$ center has shorter Mn-O bonds than $Mn^{(III)}$ and so as for the μ-oxo atoms, given that +3 oxidation state of Mn is a softer than +4. But in complex [**28**], the Mn-O bonds are dramatically different as compared to [**21**]. When there is only one carboxylate anion bridging between manganese atoms, the *trans* positions at Mn for the O-donors from the bridging carboxylate are occupied by the N atom donors from the bipyridine, but in [**21**], those positions are occupied by the O atoms from another bridging carboxylate ligand (see the crystal structure shown in Fig. 1). Therefore, in [**28**] the Mn-O bond distance between Mn and μ-oxo ligand which is *trans* to the terminal carboxylate reveals a shorter bond

length for the higher oxidation state of +4 compared to the one which is *trans* to the N atom from bpy. In other words, the $Mn^{(IV)}$ center retains more positive polarity to draw the bridging carboxylate O atom closer with the *trans* effect from O atom of terminal carboxylate. In contrast, at the lower oxidation state +3 Mn center in [**28**], the *trans* COO^{-} competes for the electrostatic charge of the bound manganese atom, an effect which leads to elongation of the Mn-O bond between manganese and μ-oxo bridge ligand. That also produces a shorter Mn-O bond for the terminally coordinated COO^{-} ligand due to the corresponding distorted Jahn-Teller distortion at the $Mn^{(III)}$ center. Additionally, the Mn-O bonds between manganese and the bridging COO^{-} ligand in [**28**] are shorter than the ones observed in [**21**]: in [**28**], Mn(1)-O(5) and Mn(2)-O(7) [2.036 Å and 1.919 Å respectively] are shorter than the ones observed in [**21**], Mn(1)-O(3) and Mn(2)-O(4) [2.052 Å and 2.107 Å respectively]. One more thing to be noted here is that the Mn····Mn distances are different for both complexes, Mn(1)-Mn(2) is 2.644 Å in [**28**] and 2.506 Å in [**21**]. The detailed *average* bond distances for [**21**] and [**28**] are depicted in Figure 3. This observation has led us to think more about the related structural geometry of $\{Mn_2O_2\}$ motif, since in complex [**21**] and [**22**], the Mn_2O_2 geometry was found to be planar while in [**28**], the Mn_2O_2 core was observed to be slightly puckered. We have examined several comparable dimeric manganese-oxo analogues reported in the literature. Selected bond lengths and angles for the complexes studied are shown in Table 3.2. At one stage we thought there could be an important correlation between structural parameters and the magnetic coupling interaction between the manganese atoms in the dinuclear complexes. First, we speculated that the planar geometry of $\{Mn_2O_2\}$ in complex [**21**], which retains a shorter Mn····Mn distance, would increase the

magnetic coupling constant, *J*, between the manganese centers. However, experimental results (Section 3.3.7) revealed that the magnetic coupling constants for both complexes [**21**] and [**22**] are close to the ones found in complexes with puckered $\{Mn_2O_2\}$ cores. Therefore, such observations caused us to revise our initial concepts regarding these doubly carboxylates bridged complexes because the planar structural arrangement of Mn_2O_2 and shorter Mn···Mn distances seem not to be a main factor in determining magnetic coupling between manganese centers in dinuclear complexes, whereas the Mn-O bond distances of the $\{Mn_2O_2\}$ core are more responsible for differences in magnetic couplings.[18] Complex [**28**] shows an interesting set of Mn-O bond lengths in its Mn_2O_2 core with respect to a Mn_2O_2 (III,IV) dimeric complexes and thus we believe it is a good candidate for magnetic measurements in the future. In addition, in [**28**], the *anti*-configuration of the coordinated terminal carboxylate ligands can also be seen as related to various other $Mn_2O_2(O_2CR)X_2$ species.[19] In all, based on the described structural details of complex [**28**], we think that provides a potential perspective for the designs of novel synthetic complexes, especially with the possible coordination sites at those terminal monodentate carboxylate ligands that can be utilized as the starting material for the further aggregation purpose, such as generating highly-ordered/arrayed manganese complexes for nano-material applications or framework structural constructions.[20]

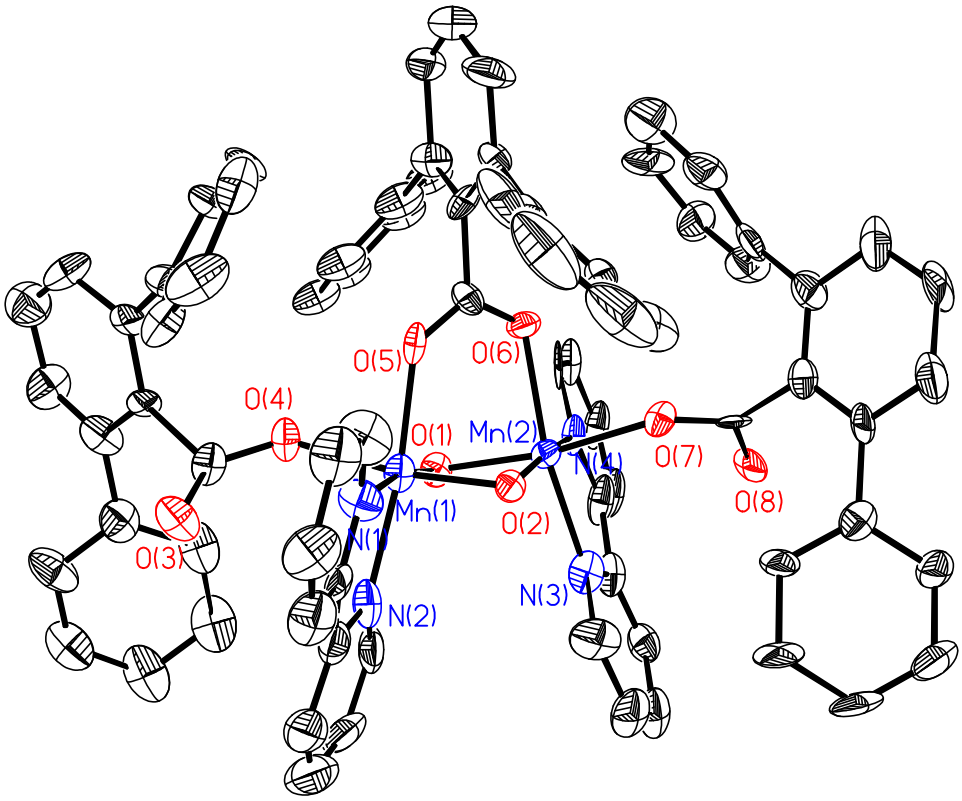

Figure 3.2. ORTEP diagram of $[Mn_2(\mu\text{-}O)_2(bpy)_2(Ar^{Ph}CO_2)_3]$ [**28**] showing 50 % probability ellipsoids and atom labeling scheme. The H atoms and acetonitrile molecules are omitted for clarity.

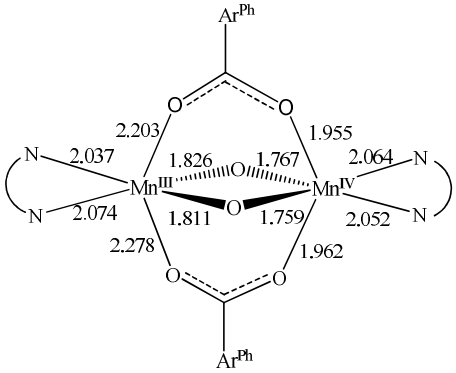

$[Mn_2(\mu\text{-}O)_2(bpy)_2(Ar^{Ph}CO_2)](ClO_4)$

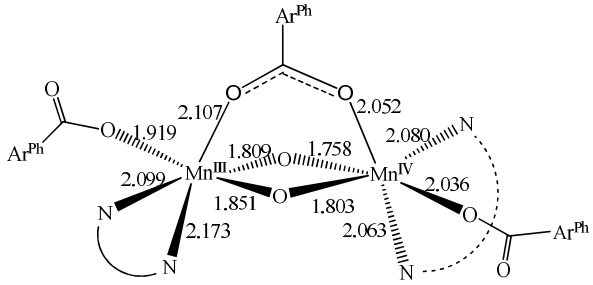

$[Mn_2(\mu\text{-}O)_2(bpy)_2(Ar^{Ph}CO_2)_3]$

Figure 3.3. The depiction of detailed bond distances for [**21**] and [**28**].

In the 2,4,6-tri-*i*-propyl benzoate system, we were only able to isolate the Mn_6O_8-core complex [**24**] but not the dicarboxylate-bridged $\{Mn_2O_2\}$ core complex, both of which were identified as reaction products by ESI-MS spectroscopy (see Section 3.3.1, 3.1 above). The crystal structure of [**24**] is shown in Figure 3. The bond distances and angels are in good agreement with $[Mn_6(\mu\text{-}O)_8(dmb)_2(Ar^{Tol}CO_2)_2]^{4+}$ complex, which was prepared by addition of 2,6-di-tolyl benzoate to $[Mn_2O_2(dmb)_4]^{3+}$ [**20**].[15] For [**24**], it was obtained by an analogous method as described in Section 3.2.7. The corresponding ^1H NMR spectrum of [**24**] is presented in the next section.

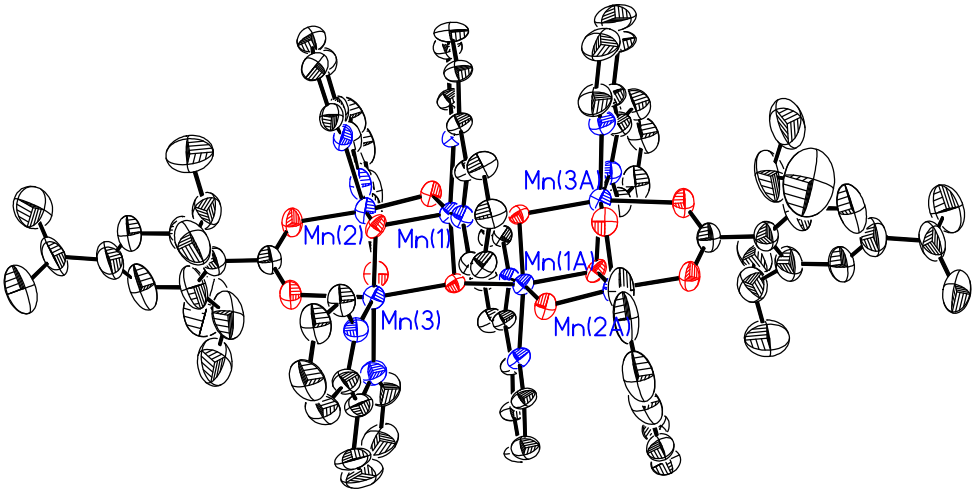

Figure 3.4. ORTEP diagram of $[Mn_6(\mu\text{-}O)_8(bpy)_2(Ar^{2,4,6\text{-tri-}i\text{Pr}}CO_2)_2](ClO_4)_4$ [**24**] showing 50 % probability ellipsoids and atom labeling scheme. Hydrogen atoms, perchlorate counterions and CH_2Cl_2 solvent molecules are omitted for clarity.

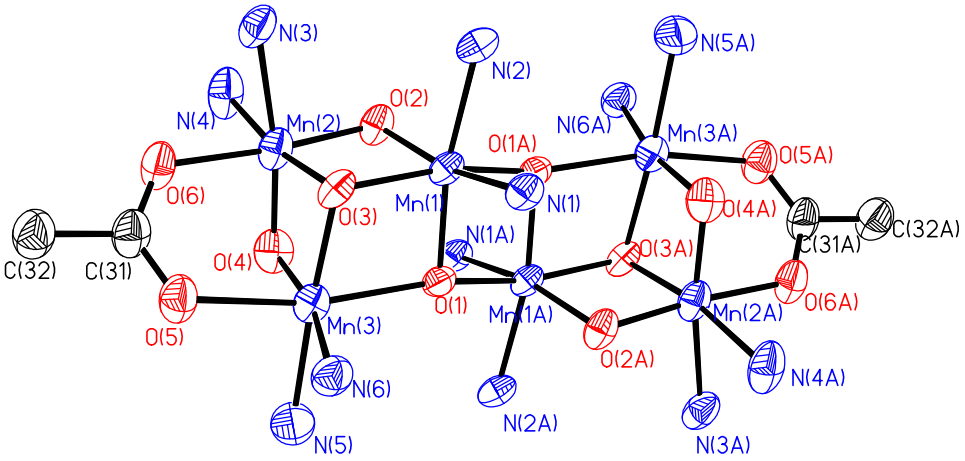

Figure 3.5. An ORTEP diagram of [**24**] presenting only the $\{Mn_6O_8\}$ core and remaining coordinated donor atoms.

As mentioned before, in the 3,5-trifluoromethyl benzoate ligand system, the Mn_4O_2 butterfly type cluster was obtained as the major product. Figure 5 shows the ORTEP diagram of $[Mn_4O_2(bpy)_6(Ar^{3,5\text{-}CF_3}CO_2)_7](ClO_4)$ [**26**], which retains a tetramanganese oxidation state of (III,III,III,III).

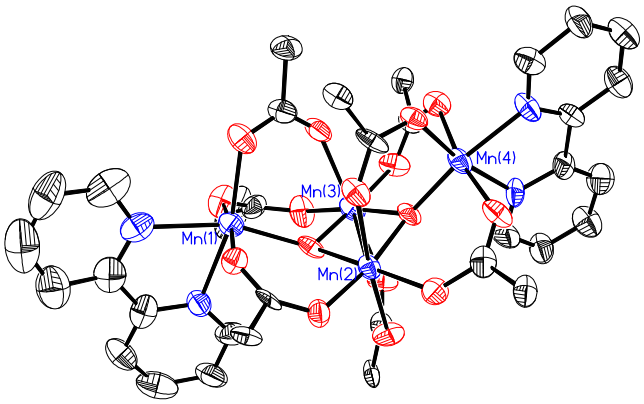

Figure 3.6. An ORTEP diagram of [**26**] presenting only the $\{Mn_4O_2\}$ core and remaining coordinated acetate and bpy donors. All the hydrogen atoms, benzoate aromatic rings and CF_3 substituents are omitted for clarity.

In one of the reaction mixtures that contained a less sterically crowded carboxylate ligand, namely, 2,4,6-trimethyl benzoate, we found an interesting Mn_2(II,II) complex as a minor product. The crystal structure of this dinuclear complex, [**29**], is displayed in Figure 6 and selected bond distances and angles are listed in Table 3.3. The observed structure conformation of this complex is a dimerized version of the mononuclear Mn complex $[Mn(dmb)_2(Ar^XCO_2)(OH_2)]^+$, which was reported by our group and utilized as the starting material for synthesis of oxo-bridged aggregates.[15] In the reported $[Mn(dmb)_2(Ar^XCO_2)(OH_2)]^+$ (where x = 2,6-di(*p*-tolyl)benzoate and 2,6-di(4-*tert*-butylphenyl)benzoate), the bulky carboxylate anion was coordinated to the manganese atom in a monodentate non-bridging mode and water molecule was found coordinated to the Mn center as well. However, in [**29**], the less sterically hindered carboxylate ligands bridge between two manganese ions, leaving no room for water molecules. We think that whether a monomer or dimer forms depends on the steric bulk of the carboxylate ligand. We speculate that there could be two possible synthetic pathways that explain the formation of [**29**]. One is the direct coordination between carboxylate ligands and an impurity $[Mn(bpy)_2]^{2+}$ species followed by dimerization. Another possible formation pathway is from the disproportionation of the high oxidation state Mn aggregates, such as $\{Mn_2O_2\}$ (IV,IV) dimer which is believed to be a unstable species and possibly involved with the formation of $\{Mn_6O_8\}$ or a putative $\{Mn_8O_{10}\}$ type cluster observed in the mass spectrum as shown in Section 3.3.4. Additionally, the dinuclear Mn_2O_2 (III,IV) complex and hexanuclear cluster of interest for this 2,4,6-trimethyl benzoate ligand system were both observed in mass spectrum (Appendix D), however, we were unable to isolate them or to obtain single crystals suitable for structure determinations.

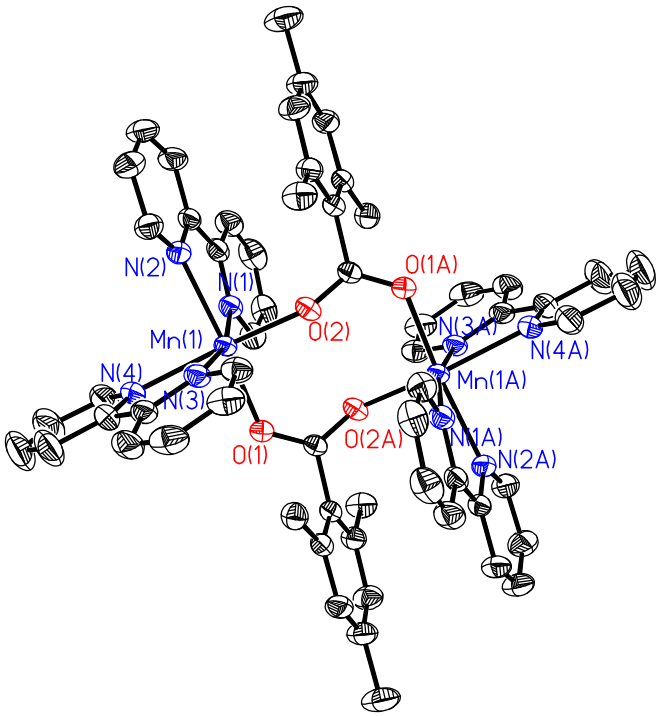

Figure 3.7. ORTEP diagram of $[Mn_2(bpy)_4(Ar^{2,4,6\text{-trimethyl}}CO_2)](ClO_4)_2$ [**29**] showing 50 % probability ellipsoids and atom labeling scheme. The H atoms, perchlorate counterion and acetonitrile molecules are omitted for clarity.

Based on the information provided by the crystal structures shown above, we have proposed a reaction mechanism as illustrated in Scheme 3.2. There is still a need for additional supporting evidence with regard to the mechanistic proposal in Scheme 3.2, such as structural identification of the crucial intermediate which is speculated to be an initial product leading to further ligand substitution and aggregation. Meanwhile, purification of the observed complex of [**29**] will be critical for the further characterization by magnetic measurement as discussed above. Of course, this suggested reaction mechanism is tentative and as more species are detected or isolated with respect to the proposed intermediates, this hypothetical mechanism will be further modified.

Lastly, the more complicated reaction mechanism involving the disproportionation of higher nuclearity clusters should not be ignored for this type of ligand exchange reaction because various reaction products observed from mass spectrometry and ^{1}H NMR spectroscopy are still not structurally identified and they could play a significant role.

3.3.3. ^{1}H NMR Spectroscopy. The ^{1}H NMR spectra of [**24**] and [**25**] are shown in Figure 6(a) and 6(b), respectively. The identity of both complexes was established by using ESI-MS and X-ray crystallography. The corresponding ^{1}H NMR isotropic shifts for [**24**] are observed between –5 to +50 ppm (Figure 6(a)), and for [**25**], the resonances are between –66 to +55 ppm (Figure 6(b)). Our attention has been particularly drawn to these remarkable ^{1}H NMR chemical shifts patterns. In general, the reported binuclear $\{Mn_2O_2\}^{3+}$ core complexes such as $[Mn_2O_2(bpy)_4]^{3+}$ are known to have strong antiferromagnetic coupling between the two Mn centers and as such the ^{1}H NMR isotropic shifts are relatively small so that the resonances are not far outside of the diamagnetic region (details see Chapter 4, Section 4.3.2). However, in sharp contrast, the $\{Mn_2O_2\}$ core of the doubly carboxylate bridged (III,IV) type of complexes such as [**21**] and [**22**] do not have prominent peaks in the paramagnetic region. We propose that these ^{1}H NMR spectral isotropic shifts are a result of the intrinsic high molecular symmetry, like $[(Mn_2O_2)_2(tphpn)_2]^{4+}$ dimer-of-dimer (DOD) type cluster, which leads to the corresponding ^{1}H NMR resonances broadened and difficult to observe. For the hexanuclear complexes like [**24**] and [**25**], the molecular symmetry was found to be lower than [**21**] or [**22**], which makes the resulting ^{1}H NMR spectra consist of a more complicated set of isotropically shifted resonances as displayed in Fig. 6. In previous

work,[15] our group obtained two analogous manganese hexanuclear clusters and the ^{1}H NMR results revealed a similar pattern of isotropically shifted resonances as shown in Fig. 6(a), except for several different chemical shifts which we believe were mainly due to different carboxylate ligand types used. Between [**24**] and [**25**], we used different bidentate ligands, dmb and bpy, which are differentiated by methyl groups in the 4-position for dmb. Complex [**25**] has several peaks in the upfield region shown in Fig. 6(b), whereas, [**24**] has no upfield peaks. Therefore, the bpy 4.4'-proton resonances fall in the upfield region and we believe the dmb 4,4' methyl groups are in the downfield region or the diamagnetic region. Moreover, even though we cannot explicitly describe that the solution state structure is the same as the solid state one, the NMR and mass spectral data support our contention that it is.

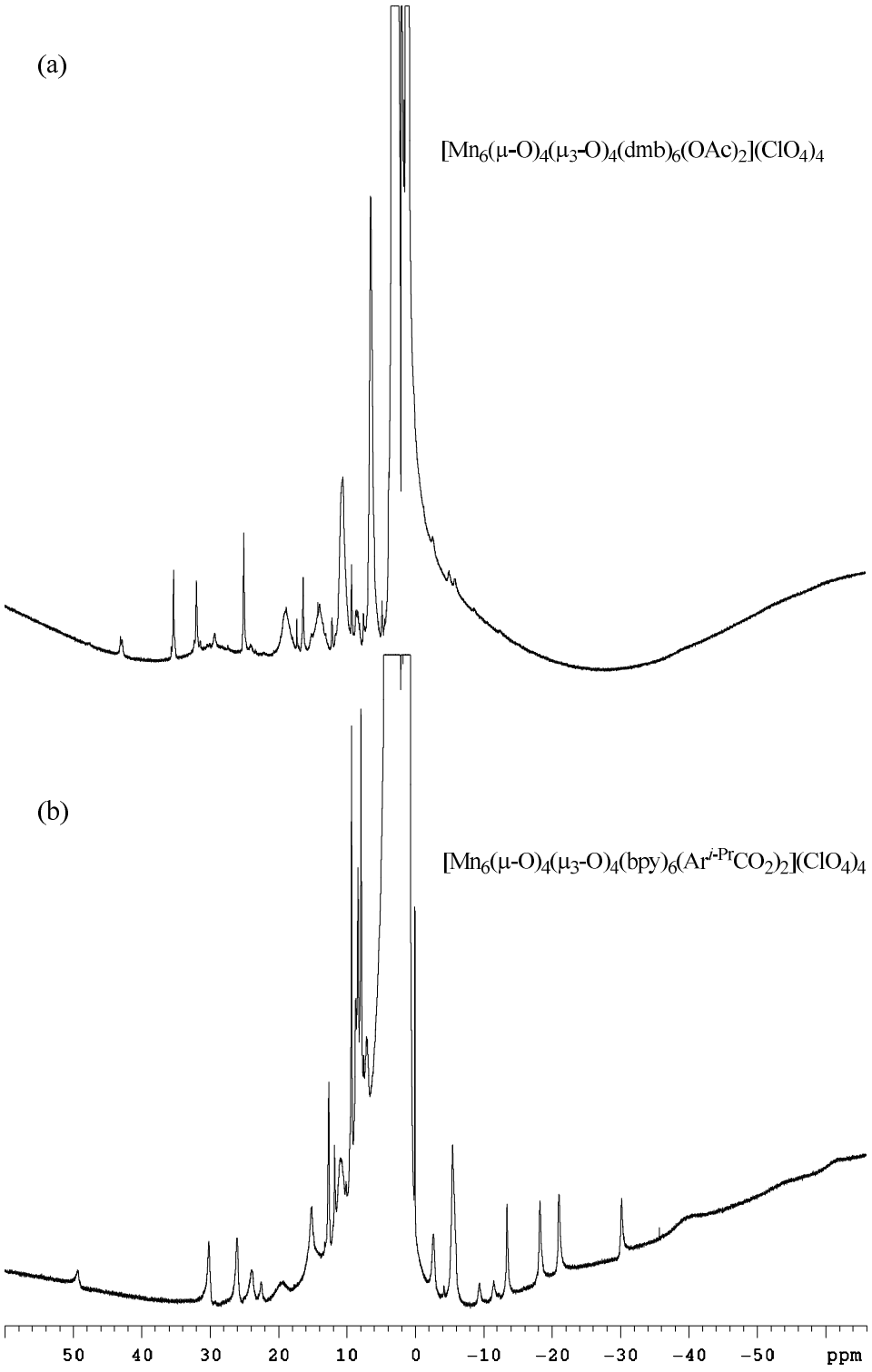

Figure 3.8. NMR spectrum of (a) $[Mn_6(\mu\text{-}O)_4(\mu_3\text{-}O)_4(bpy)_6(OAc)_2](ClO_4)_4$ [**25**] and (b) $[Mn_6(\mu\text{-}O)_4(\mu_3\text{-}O)_4(dmb)_6(Ar^{i\text{-}Pr}CO_2)_2](OTf)_4$ [**24**].

3.3.4. Mass Spectroscopy. Our group utilizes electrospray ionization mass spectrometry (ESI-MS) as an analytical tool which is complementary to NMR spectroscopy, for routine identification of reaction products. We believe this is a powerful way to identify all products of a reaction even if some of them are not structurally characterized or if they are later removed during a purification process. Most of the compounds studied in our work are positively charged and therefore carry anions. We think this character facilitates the use of the ESI-MS technique because loss of a fairly loosely bound counterion is a relatively low energy process. After extensive examination of our ESI-MS results for various types of reactions presented in this thesis, we do indeed find that ESI-MS can be used to identify major and even very minor products that would be virtually impossible to detect by any other method. Often, the mass spectral data we obtain will set us in search of interesting heretofore unknown clusters.[21] In this section, the positive mode ESI-MS spectral results for [**21**], [**22**], [**23**], [**25**] and [**26**] are shown in the figures 9, 12, 14, 15 and 16, respectively. The simulated isotope patterns for each product are also shown. Complex [**21**] is shown in Fig. 9. We assign the m/z 1000.27 signal as $[M - ClO_4]^+$ for [**21**] (Fig. 9) and one unknown species with +3 charge was also found at m/z = 929.17 (Fig. 10). The unknown species is tentatively assigned with a postulated formulation of $[Mn_8O_{12}(O_2CAr^{Ph})_2(bpy)_9](ClO_4)_5]$ (molecule weight = 3081.01 g/mole), the oxidation state of which would be (IV,IV,IV,IV,IV,IV,IV,III) and further investigation is in progress. The analogous complex [**22**] was found to behave in a similar manner as is shown in Fig. 10 with m/z 1056.23 for the $[M - ClO_4]^+$ species.

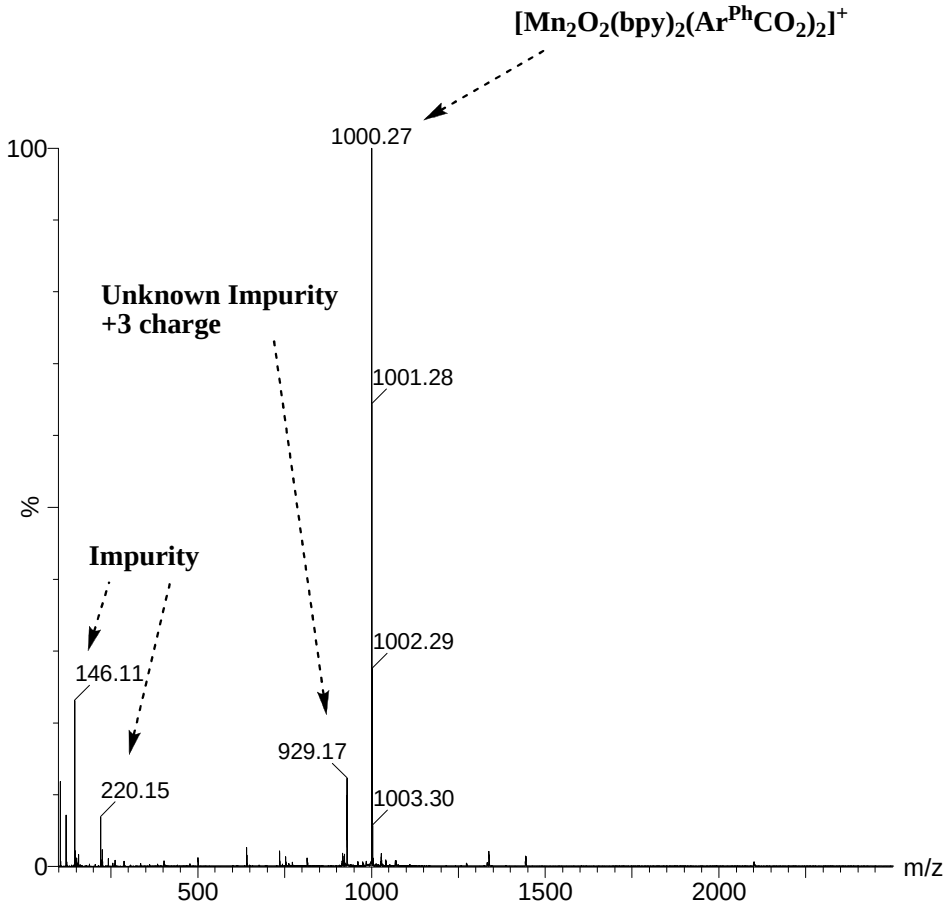

Figure 3.9. Positive ion electrospray ionization mass spectrum of [**21**] in acetonitrile.

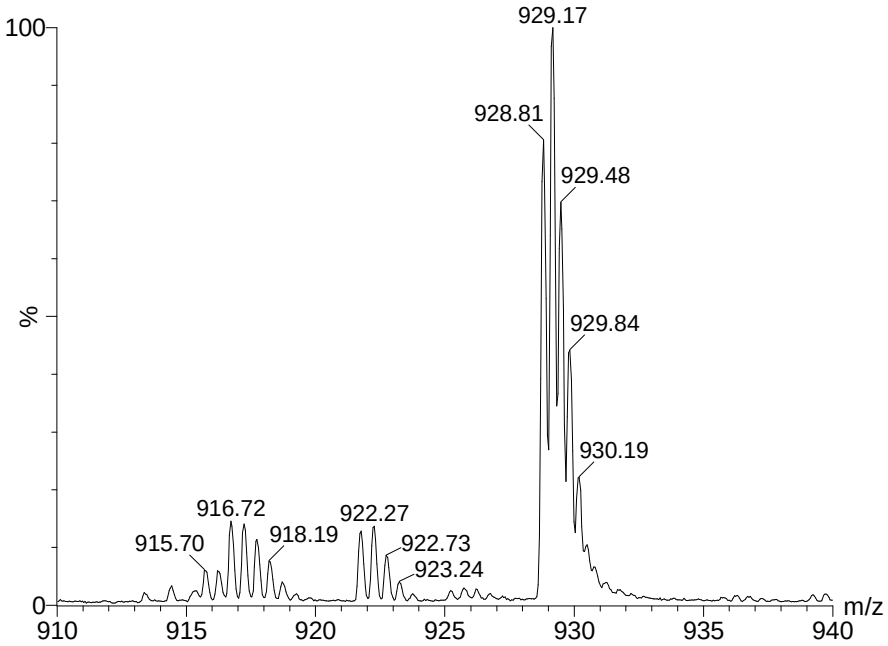

Figure 3.10. Unknown Impurity with +3 charge in an expanded mass spectrum.

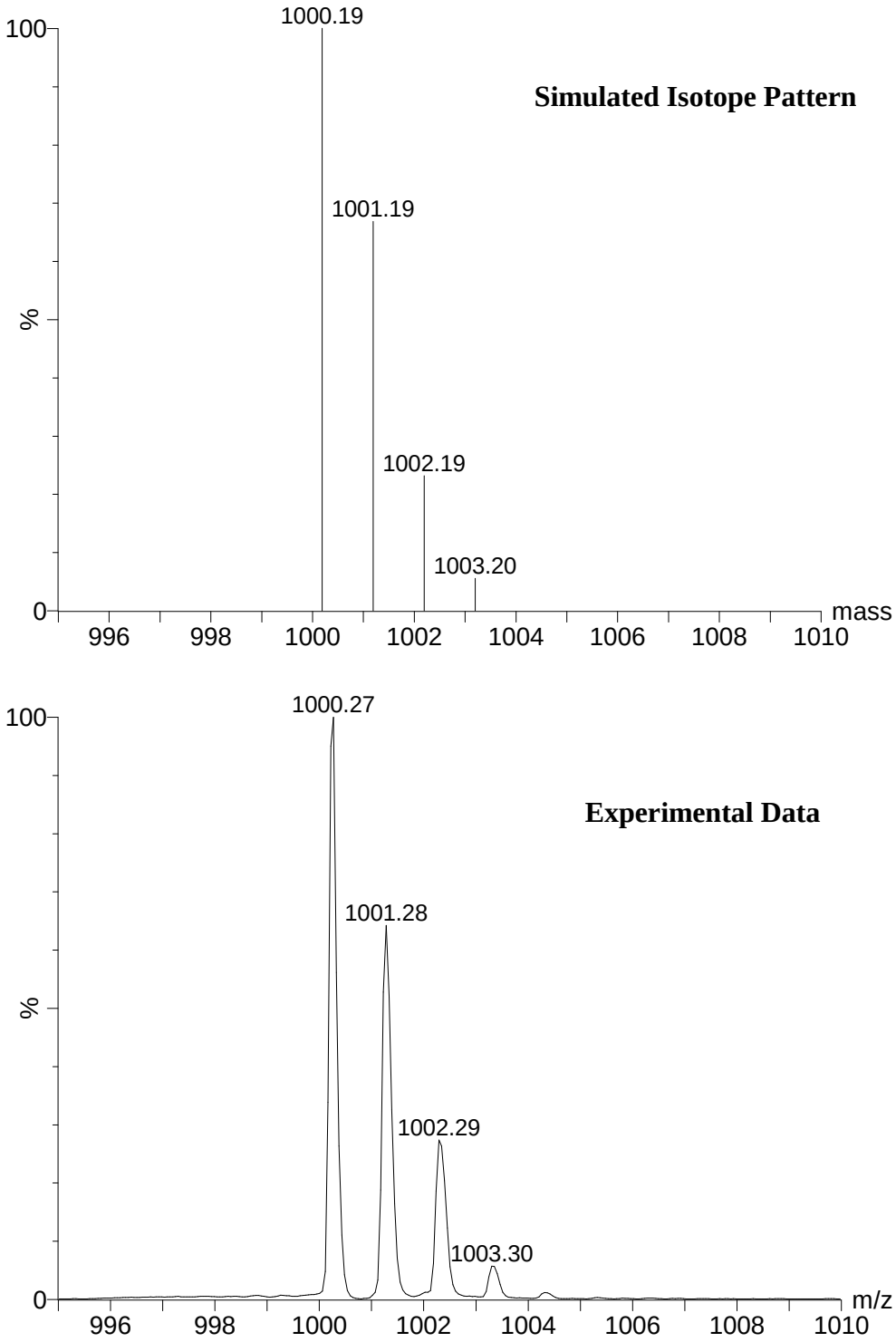

Figure 3.11. Positive ion ESI-MS spectra of a simulated isotope pattern (upper) and an experimental molecular ion signal (lower) of [**21**].

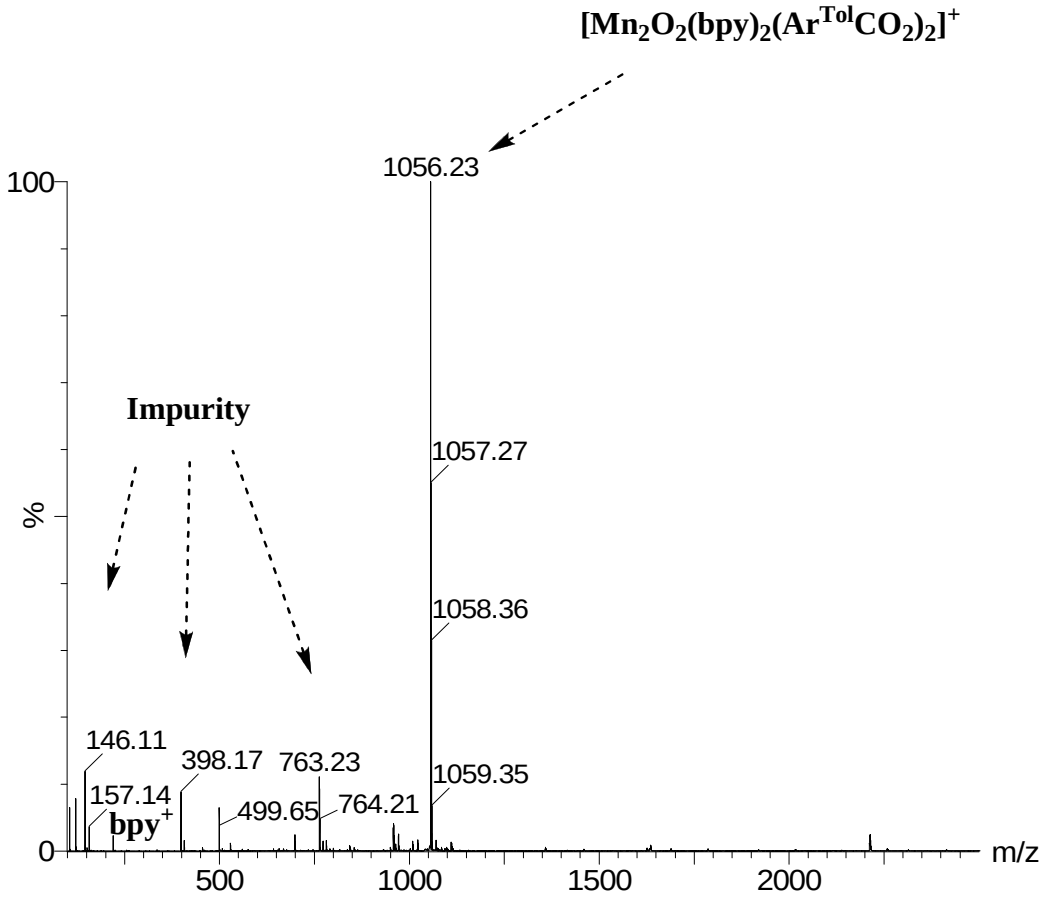

Figure 3.12. Positive ion electrospray ionization mass spectrum of [**22**] in acetonitrile.

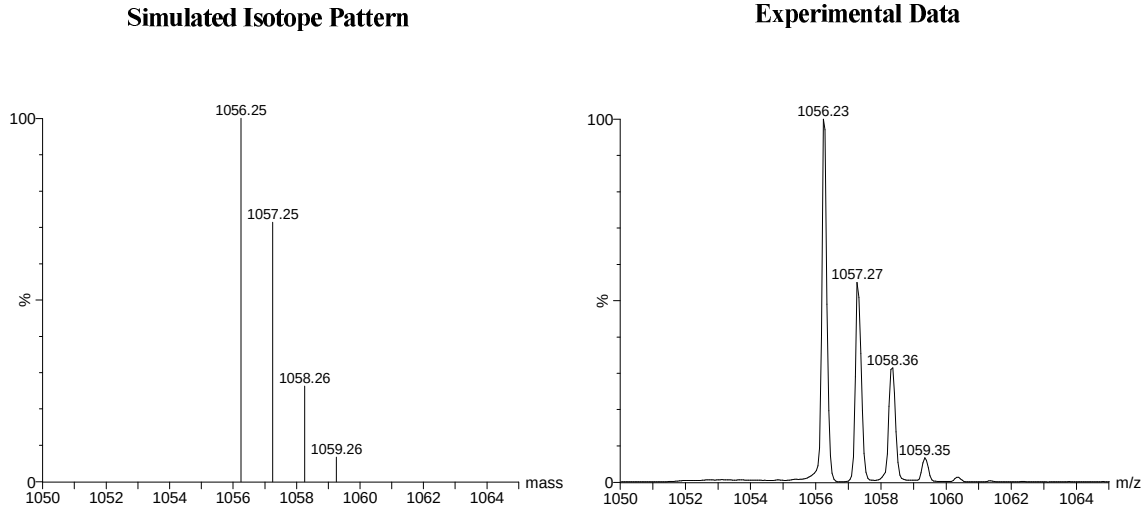

Figure 3.13. Positive ion ESI-MS spectra of a simulated isotope pattern (left) and an experimental molecular ion signal (right) of [**22**].

In Figure 14, the indicated m/z fragments support the formulation $[Mn_6(\mu\text{-}O)_4(\mu_3\text{-}O)_4(bpy)_6(Ar^{i\text{-}Pr}CO_2)_2](ClO_4)_4$, [**24**]. The molecular ion signals were found as follows: m/z 2186.49 is assigned as $[\mathbf{24} - ClO_4]^+$; m/z 1042.67 is $[\mathbf{24} - 2ClO_4]^{2+}$; m/z 662.11 is $[\mathbf{24} - 3ClO_4]^{3+}$; m/z 471.86 is $[\mathbf{24} - 4ClO_4]^{4+}$. Each of these fragments is consistent with the chemical formulation for the solid state structure, as determined by X-ray crystallography (Section 3.3.2). The simulated isotope patterns of each individual signal were found to match well with the experimental ones.

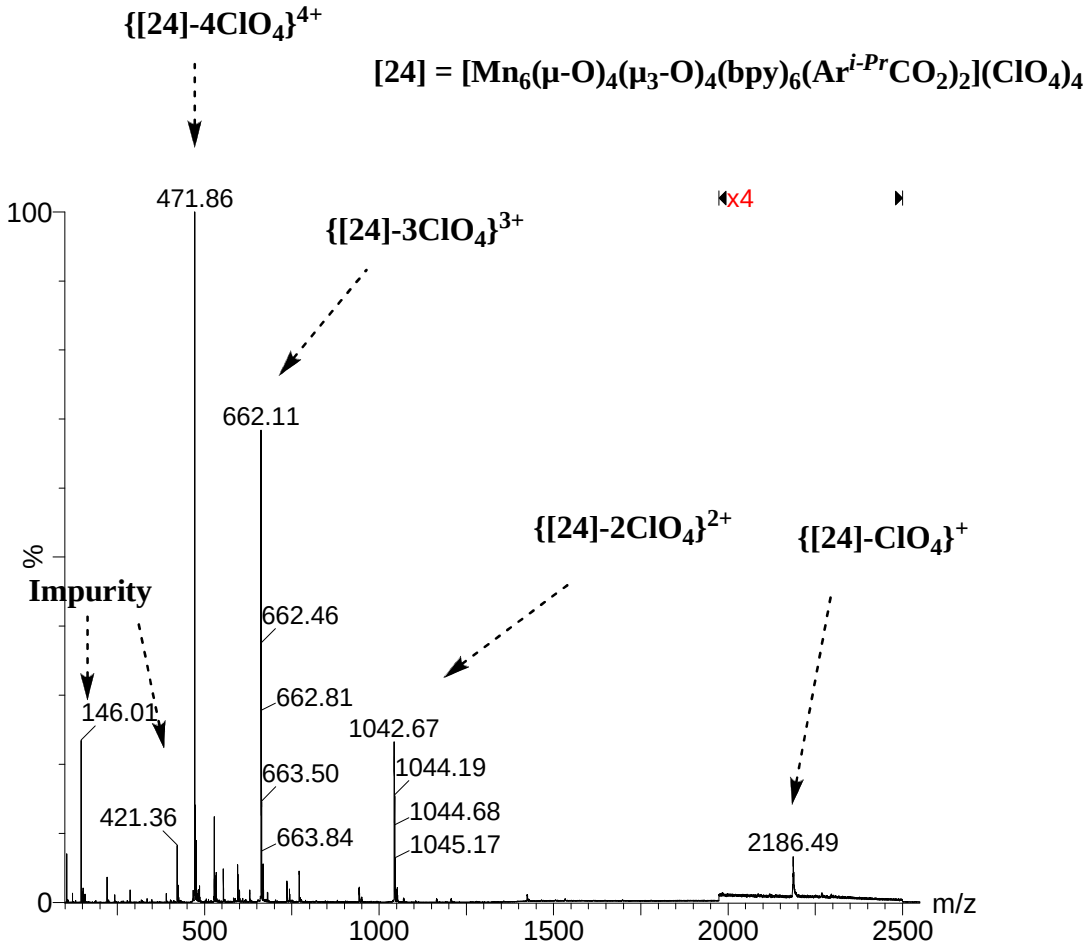

Figure 3.14. Positive ion electrospray ionization mass spectrum of [**24**] in acetonitrile.

In Fig. 15, the positive ion ESI mass spectrum shows that the observed ion fragments match with the formulation $[Mn_6(\mu\text{-}O)_4(\mu_3\text{-}O)_4(dmb)_6(OAc)_2](OTf)_4$, [**25**]. Even though the X-ray crystal structure of this complex was not determined, we still can readily conclude with a high level of confidence that is has the indicated hexanuclear structure. The molecular ion fragments were found as following: m/z 2129.81 is assigned as [**25** – $OTf]^+$; m/z 989.77 is [**25** – $2OTf]^{2+}$; m/z 610.15 is [**25** – $3OTf]^{3+}$; m/z 420.36 is [**25** – $4ClO_4]^{4+}$. The simulated isotope patters for both of these hexanuclear complexes [**24**] and [**25**] are shown in Fig. 16; here we simply present the spectra for +1 charged fragment.

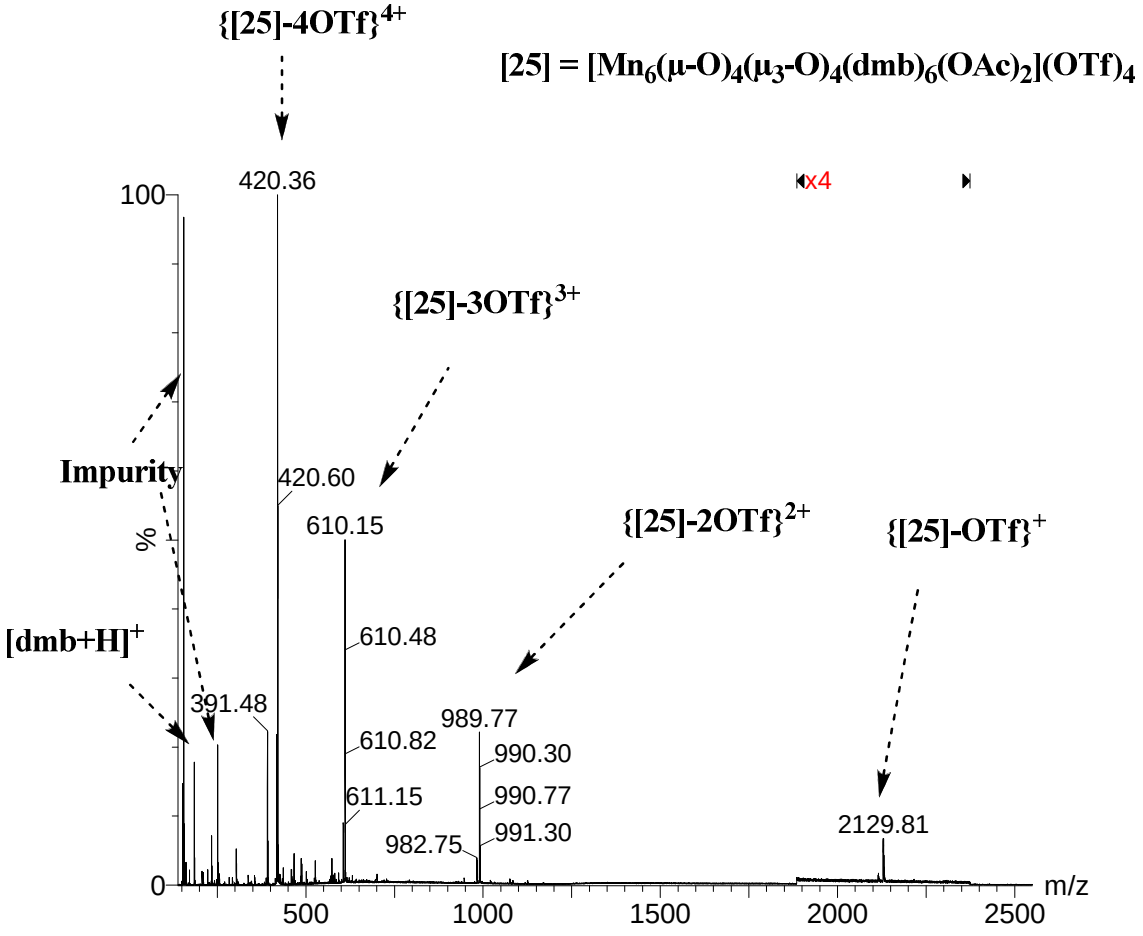

Figure 3.15. Positive ion electrospray ionization mass spectrum of [**25**] in acetonitrile.

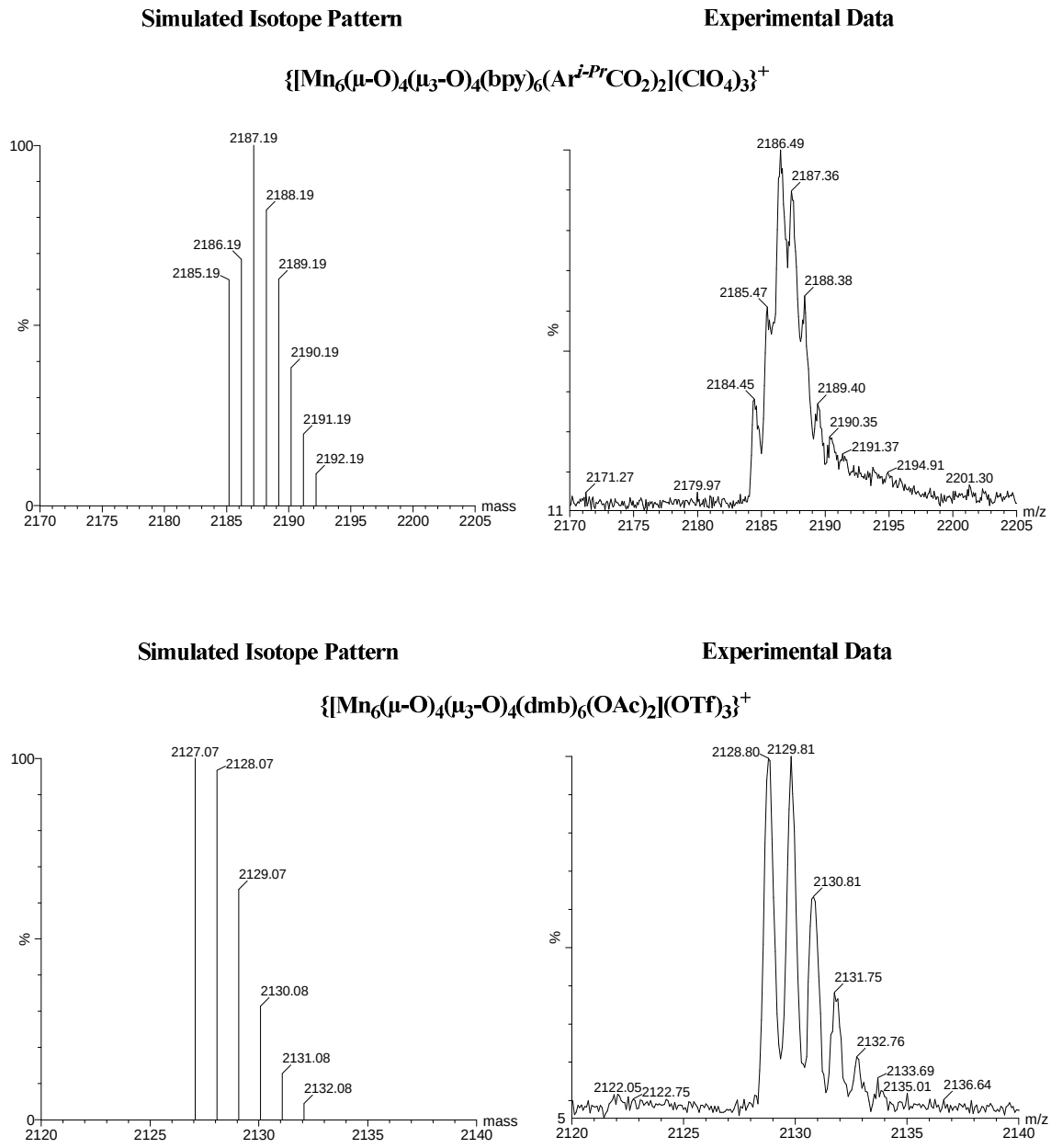

Figure 3.16. Positive ion ESI-MS spectra of simulated isotope patterns compared with experimental molecular ion fragments (+1 charge signals). [**24**] (top) and [**25**] (bottom).

3.3.5. EPR Spectroscopy. In the previous section of this chapter on NMR spectroscopic studies, we often discussed the molecular structure of complexes with the $\{Mn_2O_2\}$ (III,IV) core using the convenient assumption that unpaired electrons between two manganese centers are distributed evenly at room temperature on the NMR time

scale. But in solid state, the X-ray crystal structures have revealed that these (III,IV) dimers are actually valence trapped, which is deduced by analysis of the bond lengths around each manganese center. For the Mn_2O_2 (III,IV) dimers reported in the literature, for example $[Mn_2O_2(bpy)_4]^{3+}$, are generally found to exhibit a '16-line' EPR signal centered at g = 2, which originates from a S = ½ ground state. Therefore, we expected that the EPR spectra for the dimeric manganese complexes studied in this work would reveal the characteristic 16-line pattern. The EPR spectroscopic results using the perpendicular mode instrument configuration for [**21**] and [**22**] are shown in Figs. 17 and 18. As expected, they both reveal a typical 16-line hyperfine pattern. This indicates that both complexes retain a (III,IV) oxidation state in solution phase when cooled down to low temperature.[22] Based on these EPR spectra, we suggest that the dimeric structural conformation of [**21**] and [**22**] remains intact in solution and that we can assume they are the same as the solid state X-ray crystal structures which were described in Section 3.3.2. Therefore, we conclude that no further structural decomposition or aggregation occurs for a short period of time in solution. If phenomena like disproportionation or redox-triggered aggregation took place, one would expect to obtain EPR spectral results different from the 16-line pattern. In addition, there was no evident 6-line signal corresponding to mononuclear Mn(II) species, which are often impurities generated during the synthesis.

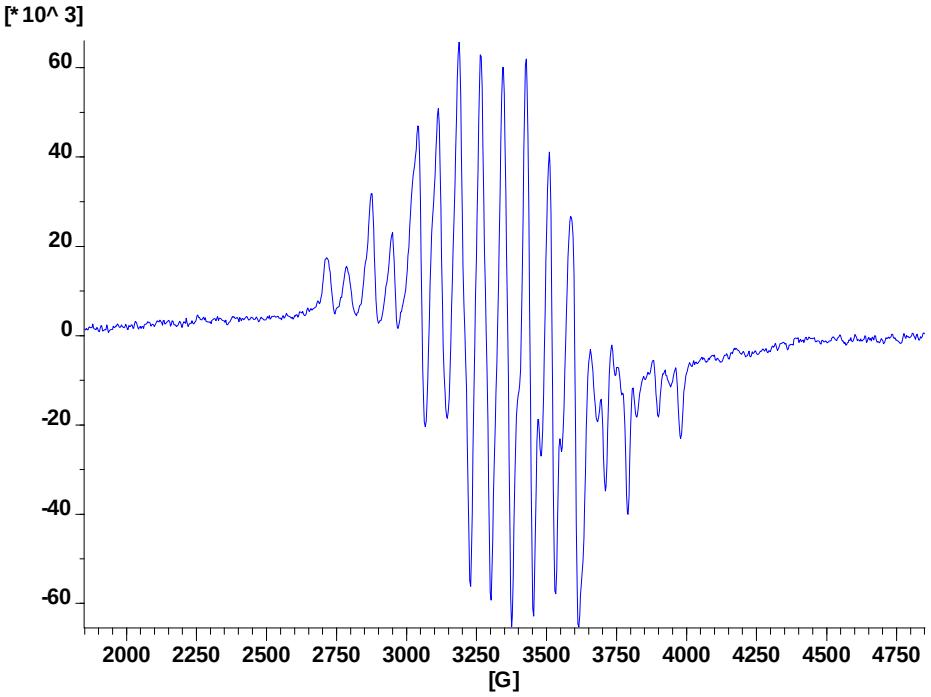

Figure 3.17. EPR specturm of $[Mn_2O_2(Ar^{Ph}COO)_2(bpy)_2](ClO_4)$ [**21**] in acetonitrile.

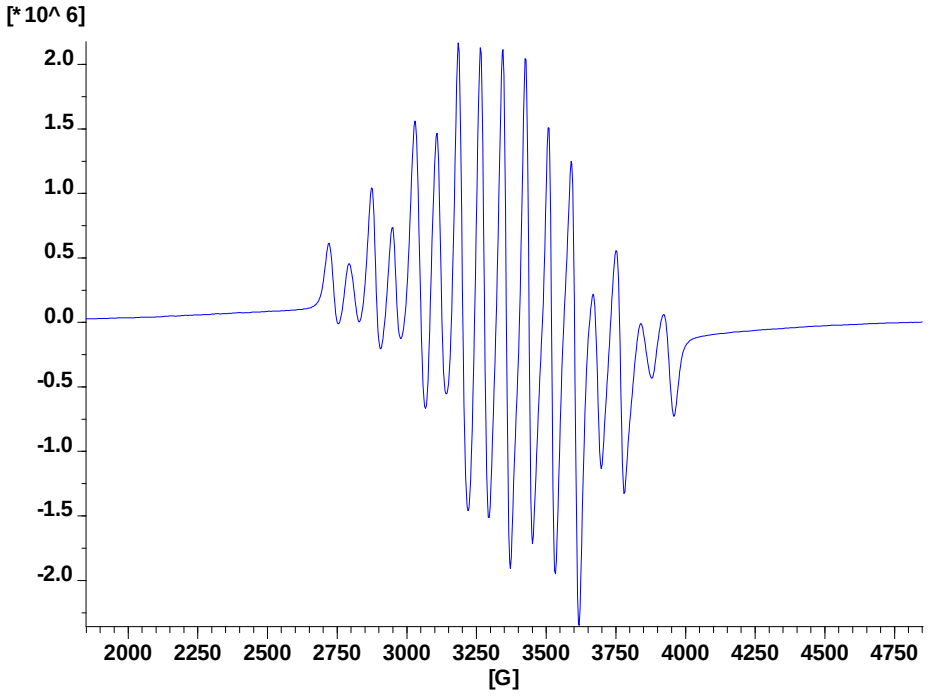

Figure 3.18. EPR spectrum of $[Mn_2O_2(Ar^{Tol}COO)_2(bpy)_2](ClO_4)$ [**22**] in CH_2Cl_2.

3.3.6. Electrochemical Study. The cyclic voltammetry (CV) result for an electrochemical study of [**24**] is shown in Figure 19. The diagram displays an irreversible oxidation wave at potential *ca.* +0.9 V. We assign this oxidation wave as the (III,III,IV,IV,IV,IV)→(III,IV,IV,IV,IV,IV) oxidation state change. This redox behavior indicates that when complex [**24**] is chemically oxidized, the higher oxidation state resulting compound could retain different physical properties and undergo a redox-triggered reaction process, such as structural rearrangement or complex disproportionation.[23] This may lead to a further reaction to possibly generate an entirely novel species. The related studies with regard to the aforementioned redox behavior are under investigation. In addition, the $\{Mn_2O_2\}$ core complexes [**21**] and [**22**] were observed to be redox inactive based on the CV measurements. We postulate that this character is owing to the sterically crowded carboxylate ligands coordinated to the dimanganese center and these hydrophobic ligands create an energy barrier, which makes it difficult for the electron transfer process to take place.

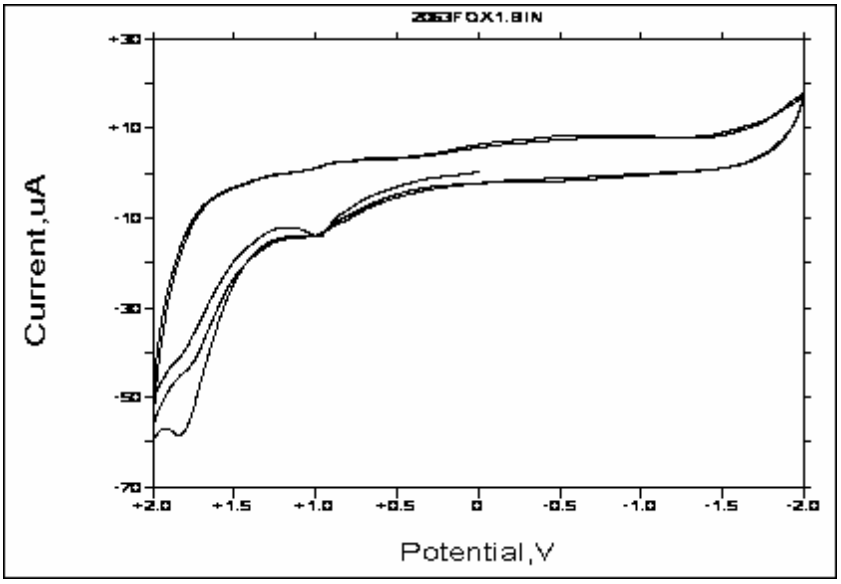

Figure 3.19. Cyclic voltammetry of [**24**] in acetonitrile and 0.1 M TBAP as the electrolyte.

3.3.7. Magnetism. Based on the X-ray crystal structures of [**21**] and [**22**] as described in Section 3.3.2 and the magnetic behavior observed for related compounds, one would predict a strong antiferromagnetic coupling between manganese centers within each dinuclear structure. The $\{Mn_2O_2\}$ cores of both clusters were found to be planar, whereas all other carboxylate-bridged species have a single carboxylate and as a result their $\{Mn_2O_2\}^{3+}$ core are puckered. We were interested to find out whether the puckering would influence the magnetic coupling. The magnetic susceptibility studies of two microcrystalline samples of [**19**] and [**22**] were measured and the corresponding results are shown in the following figures. The complex of $[Mn_2O_2(bpy)_4](ClO_4)_3$ [**19**] was first examined in order to set standard experimental protocols as a reference procedure while carrying out the measurements for the other compounds of interest. The plots of χ_m *vs.* temperature and χ_m*T *vs.* temperature for [**19**] are illustrated in Figs. 20 and 21, respectively. In Fig. 22, the plot is for μ_{eff} *vs.* temperature, which was utilized in order to find the best fit of the data for magnetic exchange with respect to the coupled Mn(III) and Mn(IV) ion centers of [**19**]. The spin Hamiltonian for the magnetic exchange couple between Mn(III) and Mn(IV) centers is given by the equation: $\hat{H} = -2J\cdot\hat{S}_1\cdot\hat{S}_2$ and we used the Van Vleck equation and a nonlinear least-squares technique, to obtain the best fit for the *J* value. Table 3.2 shows the calculated results from our measurement, $J = -169.4 \pm 1.5$ cm^{-1}, $g = 2.000$ (constrained), diamagnetic correction = -357.46×10^{-6} emu/mole, with a temperature-independent paramagnetism term, TIP = 0.1194 cm^{-1}. These results are comparable to the reported *J* values from the literature. Stoufer et al reported $J = -147$ cm^{-1} with $g = 2.003$ and TIP = 60×10^{-5} cgs emu;[24] Cooper and coworkers had $J = -150 \pm 7$ cm^{-1} with $g = 2.0$ and TIP = 120×10^{-6} cgs emu.[25]

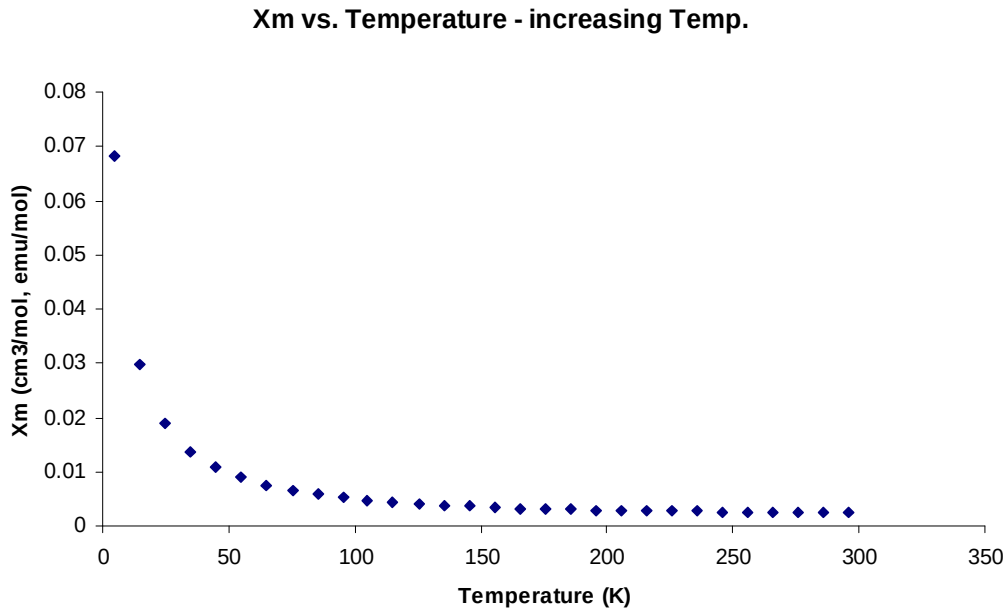

Figure 3.20. The χ_m *vs.* temperature plot for $[Mn_2O_2(bpy)_4](ClO_4)_3$ [**19**].

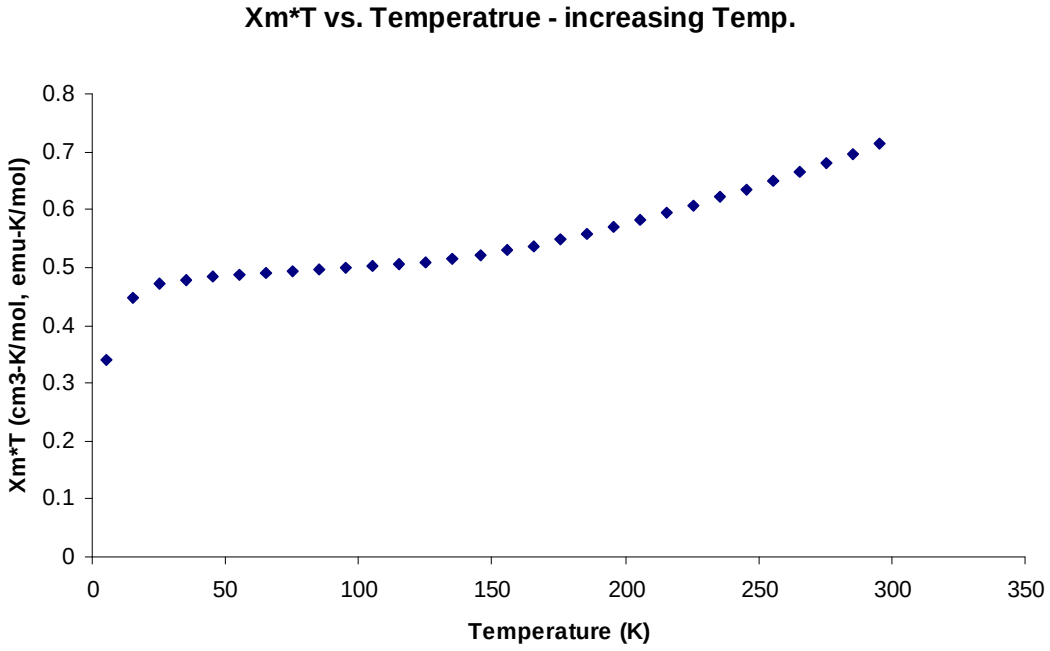

Figure 3.21. The $\chi_m T$ *vs.* temperature plot for $[Mn_2O_2(bpy)_4](ClO_4)_3$ [**19**].

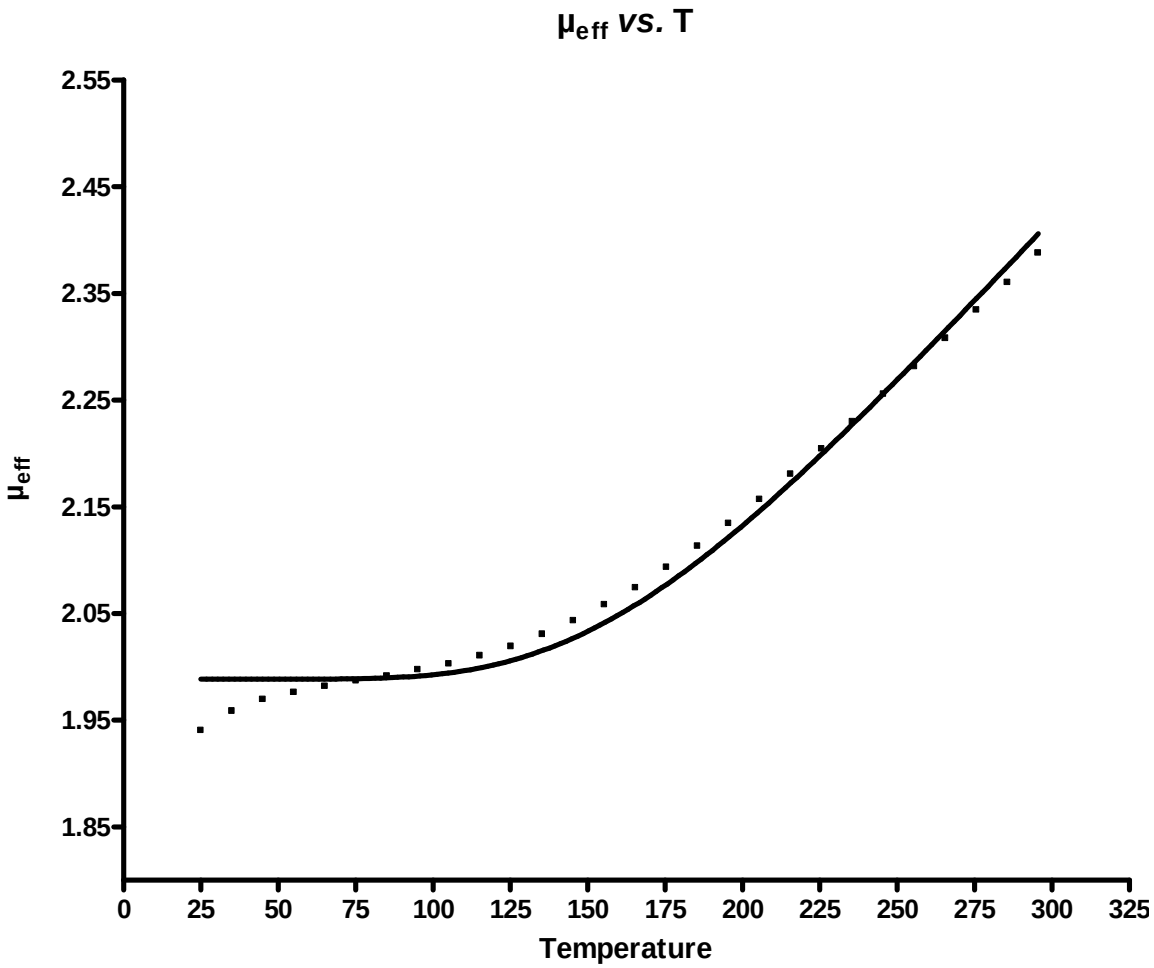

Figure 3.22. The plot of μ_{eff} *vs.* temperature for $[Mn_2O_2(bpy)_4](ClO_4)_3$ [**19**]. The theoretical best fit is show in solid line.

Table 3.2. The results from nonlinear least-squares calculation for best fit of the data.

Best-fit values	J = -169.4	G 2.000	TIP 0.1194
Std. Error	1.537	Constrained	TIP 0.002224
95% Confidence Intervals	J = -172.5 to -166.2	Constrained	TIP 0.1148 to 0.1240
Goodness of Fit Degrees of Freedom: 26 R^2 0.9864 Absolute Sum of Squares 0.006858			

The plots of χ_m *vs.* temperature and χ_m*T *vs.* temperature for [**22**] are shown in Figs. 23 and 24, respectively. In Fig. 25, the plot is for μ_{eff} *vs.* temperature was utilized in order to find the best fit of the data for magnetic exchange with respect to the coupled Mn(III) and Mn(IV) ion centers of [**22**]. As described above, the spin Hamiltonian equation: $\hat{H} = -2J\cdot\hat{S}_1\cdot\hat{S}_2$ and Van Vleck equation were used to find the best fit for magnetic exchange couple *J* value. Table 3.3 shows the calculated results from our measurement, $J = -179.0 \pm 0.879$ cm^{-1}, $g = 2.000$ (constrained), diamagnetic correction = -536.61×10^{-6} emu/mole, which is calculated based on the result of elemental analysis, which shows that 1.75 CH_2Cl_2 was retained in the crystal lattice, and with a temperature-independent paramagnetism term, TIP = 201×10^{-5} cgs emu.

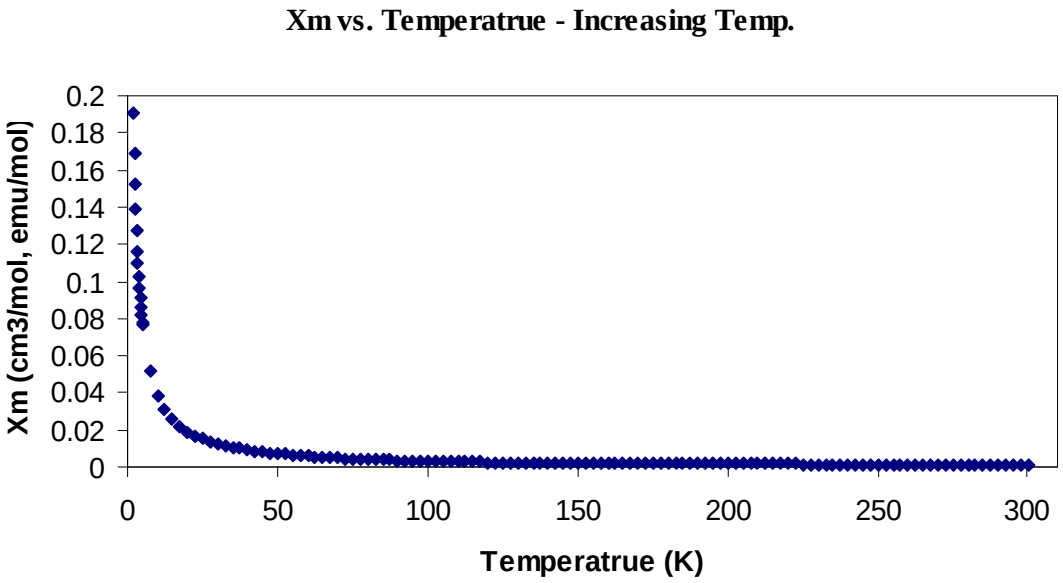

Figure 3.23. The χ_m *vs.* temperature plot for $[Mn_2O_2(Ar^{Tol}COO)_2(bpy)_2](ClO_4)$ [**22**].

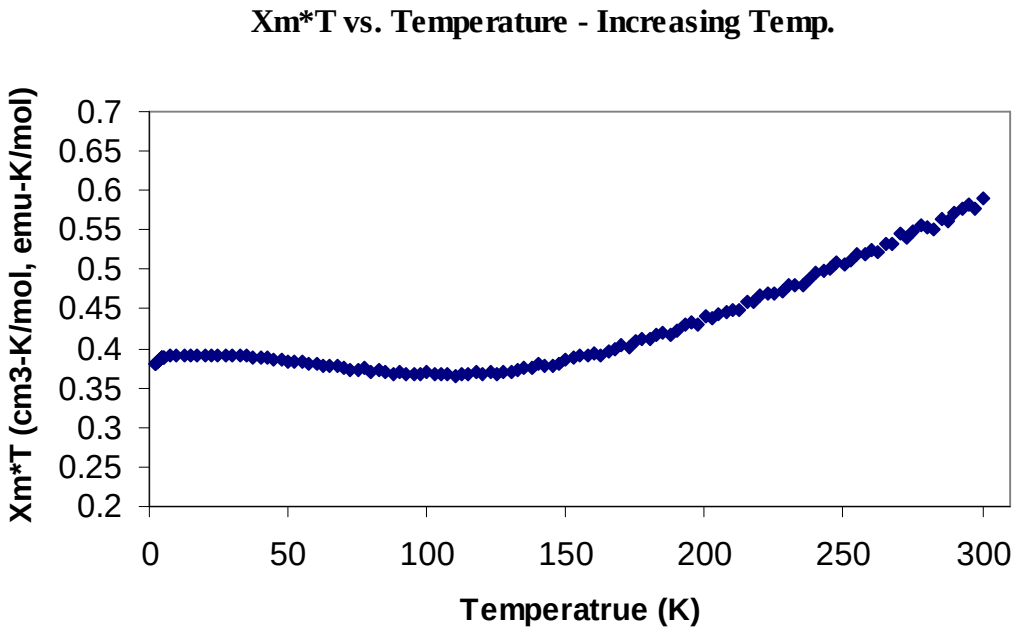

Figure 3.24. The $\chi_m T$ *vs.* temperature plot for $[Mn_2O_2(Ar^{Tol}COO)_2(bpy)_2](ClO_4)$ [**22**].

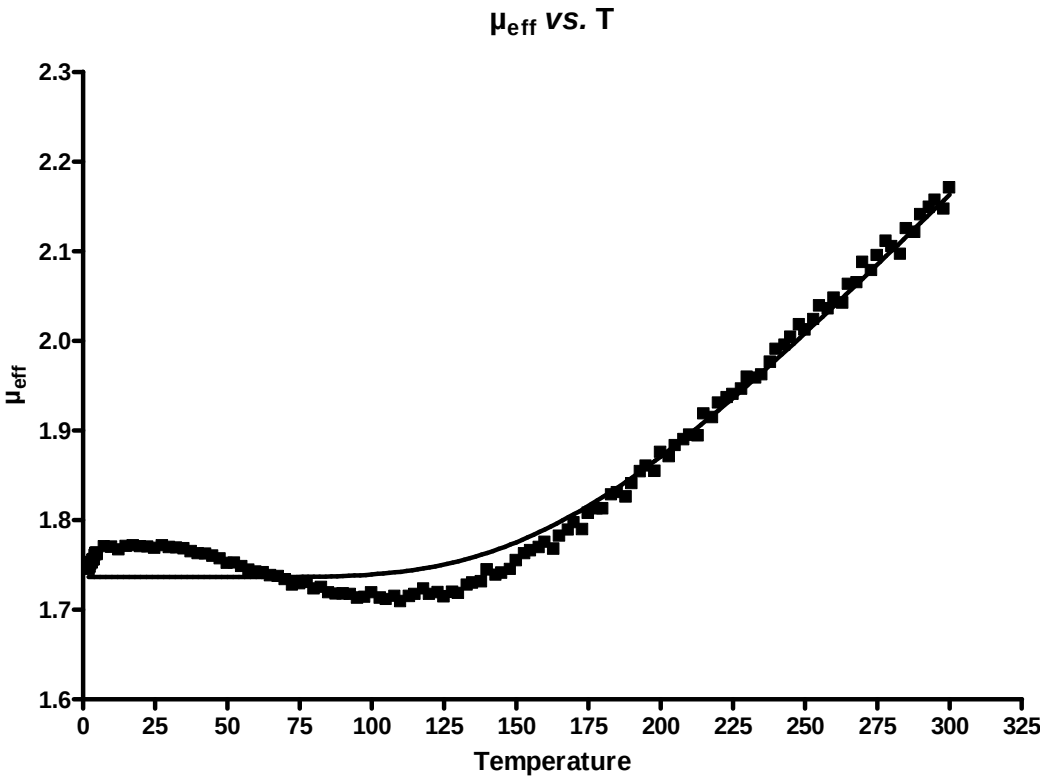

Figure 3.25. The plot of μ_{eff} *vs.* temperature for $[Mn_2O_2(Ar^{Tol}COO)_2(bpy)_2](ClO_4)$ [**22**]. The theoretical best fit is show in solid line.

Table 3.3. The results from nonlinear least-squares calculation for best fit of the data.

Best-fit values	J = –179.0	G 2.000	TIP 0.002013
Std. Error	0.8794	Constrained	TIP 0.0009866
95% Confidence Intervals	J = –180.7 to –177.2	Constrained	TIP $7.875e^{-5}$ to 0.003946
Goodness of Fit Degrees of Freedom: 130 R^2 0.9789 Absolute Sum of Squares 0.04968			

3.4. Conclusion

The alteration of ligand steric and electronic properties provides a degree of control over the resulting cluster size and shape as well as certain physical and chemical properties. When using various types of carboxylates for the ligand exchange reactions that we have employed different kinds of reaction products were obtained. For the dimanganese starting materials, we were able to make larger aggregates such as hexanuclear clusters, which however are less biologically relevant with regard to the PSII OEC. The substituted benzoate ligand types favored of the formation of dinuclear manganese complexes except some high nuclearity aggregates, such as $\{Mn_4O_4\}$, $\{Mn_6O_8\}$ or $\{Mn_8O_{12}\}$ complexes based on mass spectra results, were also formed unexpectedly along with $\{Mn_2O_2\}$ core cluster as impurities during the syntheses. Even though the steric effect of carboxylates is not the only factor that determines product distribution, efforts are being directed toward obtaining more structural and mechanistic information about photosynthetic water oxidation. We believe that the synthetic modeling approach taken here by us and by other research groups holds much promise in revealing more insight into Photosystem II water oxidation chemistry.

3.5. Acknowledgement

We thank Mr. Marek Domin and Dr. John Boylan for the valuable assistance with Mass Spectroscopy and NMR training. We also thank Dr. Richard J. Staples for the training in resolving crystal structures. Dr. Ralph Weber (Bruker Bio-Spin EPR, Billerica, MA) is extremely thankful for his great guidance for the EPR measurements. Dr. Shaoyan Chu and Mr. Patrick Boisvert at MIT CMSE center deserve special thanks for their fabulous helps with magnetism measurements on the SQUID magnetometer. We are particularly grateful for Dr. Chu for his in-depth assistance with magnetism experimental design, data calculations and training for data fittings.

3.6. References

1. Larson, E. J.; Pecoraro, V. L. In *Manganese Redox Enzyme*; Pecoraro, V. L. Ed.; VCH: New York, **1992**, pp. 1-28.
2. Cotton, F. A.; Wilkinson, G. *Advanced Inorganic Chemistry, 5th Ed.*; John Wiley & Sons: New York, **1988**, pp. 697-709
3. (a) Suib, S. L. *Acc. Chem. Res.* **2008**, *41(4)*, 479-487 and references therein.

   (b) Corà, F.; Sankar, G.; Catlow, C. R. A.; Thomas, J. M. *J. Chem. Soc. Chem. Comm.* **2002**, 734-735.

   (c) Chen, X.; Shen, Y.-F.; Suib, S. L., O'Young, C. L. *Chemistry of Materials* **2002**, 940-948.
4. (a) Autret, C.; Gervais, M.; Gervais, F.; Raimboux, N.; Simon, P. *Solid State Sci.* **2004**, *6*, 815-824.

(b) Ju, H. L.; Kown, C.; Li, Q.; Greene, R. L.; Vekatesan, T. *Appl. Phys. Lett.* **1994**, *65*, 2108-2110.

(b) Kucherenko, S. S.; Pashchenko, V. P.; Polyakov, P. I.; Shtaba, V. A.; Shemyakov, A. A. *Low Temperature Physics*, **2001**, *27*, 559-562.

5. (a) Milios, C. J.; Inglis, R.; Vinslava, A.; Bagai, R., Wernsdorfer, W.; Parsons, S.; Perlepes, S. P.; Christou, G.; Brechin, E. K. *J. Am. Chem. Soc.* **2007**, *129*, 12505-12511.

   (b) Murugesu, M.; Wernsdorfer, W.; Abboud, K. A.; Brechin, E. K.; Christou, G. *J. Chem. Soc. Dalton Trans.* **2006**, 2285-2287.

   (c) Christou, G. *Polyhedron* **2005**, *24*, 2065-2075.

6. Cotton, F. A.; Wilkinson, G. *Advanced Inorganic Chemistry, 5th Ed.*; John Wiley & Sons: New York, **1988**, pp. 697, 18-D-1.

7. Debus, R. J. *Biochim. Biophys. Acta* **2001**, *1053*, 164-186.

8. Tasiopoulos, A. J.; Vinslava, A.; Wernsdorfer, W.; Abboud, K. A.; Christou, G. *Angew. Chem. Int. Ed.* **2004**, *43*, 2117-2121.

9. An example for this type of complex formation with regard to a structural dimerization or aggregation can be seen in Chapter 4 work of this dissertation, which demonstrates that by using a manganese-oxo dimer under a suitable condition, a tetranuclear adamantane shape of Mn_4O_6 complex was formed.

10. (a) Cooper, S. R.; Calvin, M. *J. Am. Chem. Soc.* **1977**, *99*, 6623-6630.

    (b) Dave, B. C.; Czernuszewicz, R. S. *New J. Chem.* **1994**, *18*, 149-155.

11. Yu, Z.; Liu, K.; Tao, J. Q.; Zhong, Z. J.; You, X. Z.; Siu, G. G. *Appl. Phys. Lett.* **1999**, *74(26)*, 4029-4031.

12. Connelly, N. G.; Geiger, W. E. *Chem. Rev.* **1996**, *96*, 877-910.

13. (a) Du, C. -J. F.; Hart, H.; Ng, K. -K. D. *J. Org. Chem.* **1986**, *51*, 3162-3165.

(b) Hart, H.; Rajakumar, P. *Tetrahedron* **1995**, *51(5)*, 1313-1336.

(c) Saednya, A.; Hart, H. *Synthesis* **1996**, 1455-1458.

14. Mukhopadhyay, S. *Ph.D. Dissertation*, Boston College, **2002**.

15. Mukhopadhyay, S.; Gandhi, B. A.; Kirk, M. L.; Armstrong, W. H. *Inorg. Chem.* **2003**, *42*, 8171-8180.

16. Mukhopadhyay, S.; Armstrong, W. H. *J. Am. Chem. Soc.* **2003**, *125*, 13010-13011.

17. Wang, S.; Folting, K.; Streib, W. E.; Schmitt, E. A.; McCusker, J. K.; Hendrickson, D. N.; Christou, G. *Angew. Chem. Int. Ed. Engl.* **1991**, *30(3)*, 305-306.

18. Petrie, S.; Stranger, R. *Inorg. Chem.* **2004**, *43(17)*, 5237-5244.

19. (a) Bashkin, J. S.; Schake, A. R.; Vincent, J. B.; Chang, H.-R.; Li, Q.; Huffman, J. C.; Christou, G.; Hendrickson, D. N. *J. Chem. Soc., Chem. Commun.* **1988**, 700-702.

(b) Dave, B. C.; Czernuszewicz, R. S.; Bond, M. R.; Carrano, C. J. *Inorg. Chem.* **1993**, *32*, 3593-3594.

(c) Reddy, K. R.; Rajasekharan, M. V.; Padhye, S.; Dahan, F.; Tuchagues, J.-P. *Inorg. Chem.* **1994**, *33*, 428-433.

(d) Collomb, M.-N.; Deronzier, A.; Richardot, A.; Pécaut, J. *New J. Chem.* **1999**, *23*, 351-353.

20. (a) Li, C.-S.; Xue, L.; Che, Y.-X.; Luo, F.; Zheng, J.-M.; Mak. T. C. W. *Inorg. Chim. Acta* **2007**, *360*, 3569-3574.

(b) Godbole, M. D.; Roubeau, O.; Clérac, R.; Kooijman, H.; Spek, A. L.; Bouwman, E. *Chem. Commun.* **2005**, 3715-3717.

21. (a) Colton, R.; D'Agostino, A.; Traeger, J. C. *Mass Spec. Rev.* **1995**, *14*, 79-106.

(b) Sam, J. W.; Tang, X.-J.; Peisach, J. *J. Am. Chem. Soc.* **1994**, *116*, 5250-5256.

(c) Katta, V.; Chowdhury, S. K.; Chait, B. T. *J. Am. Chem. Soc.* **1990**, *112*, 5348-5349.

22. Teutloff, C.; Schäfer, K.-O.; Sinnecker, S.; Barynin, V.; Bittl, R.; Wieghardt, K.; Lendzian, F.; Lubitz, W. *Magn. Reson. Chem.* **2005**, *43*, S51-S61.

23. Baffert, C.; Romain, S.; Richardot, A.; Leprêtre, J.-C.; Lefebvre, B.; Deronzier, A.; Collomb, M.-N. *J. Am. Chem. Soc.* **2005**, *127*, 13694-13704.

24. Plaksin, P. M.; Stoufer, R. C.; Mathew, M.; Palenik, G. J. *J. Am. Chme. Soc.* **1977**, *94(6)*, 2121-2122.

25. Cooper, S. R.; Dismukes, G. C.; Klein, M. P.; Calvin, M. *J. Am. Chem. Soc.* **1978**, *100(23)*, 7248-7252.

Chapter 4

Synthesis, Structure, Spectroscopic and Electrochemical Study of a Novel Mixed-Ligand Manganese Cluster: $[Mn_4(\mu\text{-}O_6)(bpy)_4(py)_4](ClO_4)_4$

4.1. Background

For the water oxidase (WO) enzyme in photosystem II, it is generally accepted that a tetranuclear manganese-oxo complex is responsible for the redox activity in the oxygen evolution catalytic cycle. The intrinsic polypeptides surrounding this manganese complex have also drawn great attention by numerous research groups for many years. Based on the spectroscopic results from various research groups, several geometric structural types for the tetranuclear manganese-oxo aggregate have been proposed (Chapter 1, Figure 7).[1] It is also believed that the OEC $CaMn_4$ cluster is ligated by polypeptide amino acid residues, primarily carboxylate and histidine residues.[2] The synthetic model clusters reported to date usually contain multidendate ligands, which serve as amino acids analogues.[3]

We and others have been heavily involved in using N-donor tridentate ligands (Figure 1), such as tacn, tame, dien, Me_3dien, bpxa, tach, and the bidentate ligand, 2,2'-bipyridyl, the nitrogens of which loosely resemble the nitrogen atoms in imidazole, the coordinating histidine (His) side chain residue.[4] For example, we have used the ligands[5] bpma, bpea, and bpta to synthesize a number of tetranuclear manganese-oxo aggregates in initial attempts to mimic the OEC.[6] Also, the bipyridyl ligand has long been utilized for the preparation of dinuclear Mn complexes.[7] In this work we will focus on the adamantane core type $\{Mn_4O_6\}^{4+}$ clusters.

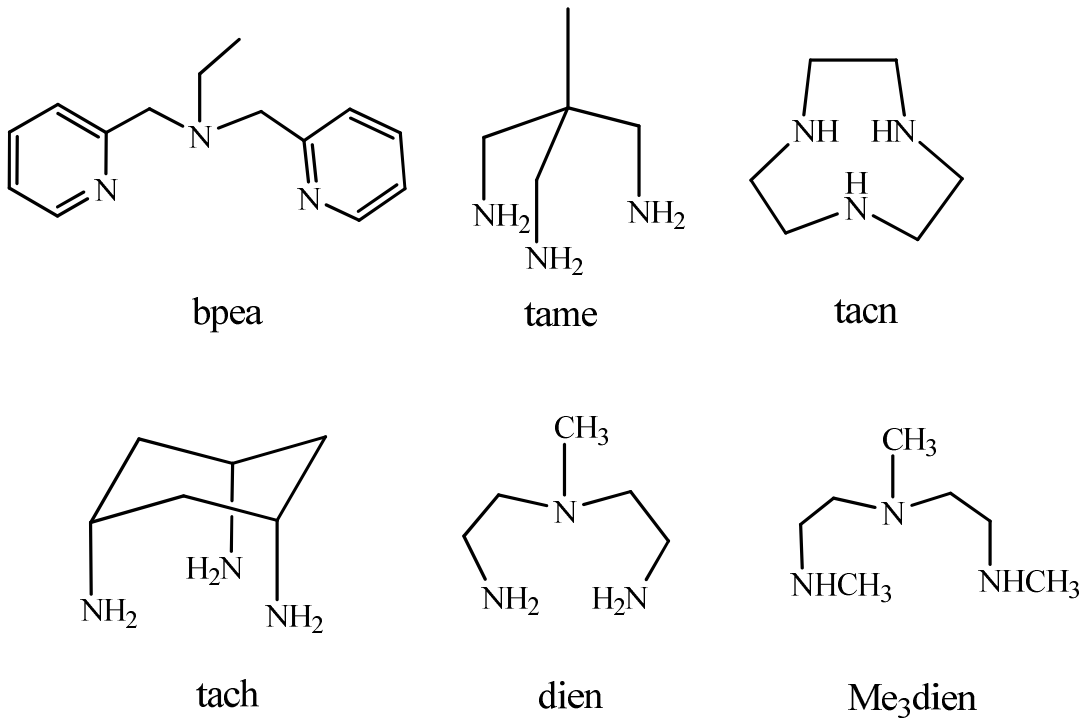

Figure 4.1. Structural drawings of various tridentate ligands.

For bpea-ligated adamantane-shaped tetramanganese complexes, our group has done extensive studies of their structure, physical properties, and reactivity characteristics.[8] The bpea ligand is capable of adopting both meridional and facial coordination to manganese atoms in contrast to tacn, tame and dien type of ligands, which bind in a facial configuration for the compounds of interest. Also, we have incorporated carboxylate donors into the ligand system in order to more closely mimic the environment of PSII. For instance, we have prepared the mixed-ligand adamantane complex $[Mn_4O_6(bpea)_2(R\text{-}ida)_2]$ via ligand exchange reactions between $[Mn_4O_6(bpea)_4]^{4+}$ and R-ida (iminodicarboxylate, a tridentate ligand). However, because the ligands mentioned above are tridentate and sterically crowding around the Mn centers, it is difficult to obtain an open site on the manganese centers for binding water molecules, an important initial step in attempts to mimic the PSII water oxidase activity. This goal prompted us to find a

synthetic method to replace the tridentate ligands that were discussed above with either three monodentate ligands on each manganese atom or a dissociable monodentate ligand along with a bidentate ligand. In this work, we chose to employ pyridine (py) and *N*,*N*-dimethylformamide (DMF) as the monodentate ligands. We have succeeded in preparing a mixed bidentate/monodentate ligand coordinated adamantane core complex, {[Mn_4(μ-O)$_6$(bpy)$_4$(py)$_4$](ClO_4)$_4$} [**36**]. Herein we report the synthesis, spectroscopic characterization and crystal structure of this novel oxo-bridged tetramanganese cluster.

4.2. Experimental Section

4.2.1. Materials. Acetonitrile used for synthesis and spectroscopic studies was distilled over CaH_2 under nitrogen and stored over 3 Å molecular sieves prior to use. Deuterated acetonitrile (Cambridge Isotope Laboratories, Inc.) was dried in oven-dried glassware over activated 3 Å molecular sieves. All other reagents were purchased from commercial sources and used as received. The supporting electrolytes TBAP, tetrabutylammonium perchlorate, and TEAP, tetraethylammonium perchlorate, were electrochemical grade and used as received. Paratone-N oil was obtained from Hampton Research Corp.. All chemicals used in this work were reagent grade.

4.2.2. Physical Methods. ^{1}H NMR spectra data were collected on Varian Unity 300 MHz and 400 MHz spectrometers with a 60-100 kHz sweep width. A first-order correction function provided with the spectrometer software was used for baseline correction wherever needed. Chemical shifts are quoted on the δ scale with shifts downfield being positive. Values for chemical shifts (ppm) are the observed shifts referenced to resonances for residual protic protons in the various deuterated solvents: CHD_2CN, 1.94 ppm; $CHCl_3$, 7.26 ppm; and $CHDCl_2$, 5.32 ppm. Electrospray ionization

mass spectrometry (ESI-MS) was performed in the Boston College Mass Spectrometry Facility and recorded by using a Waters LCT classic instrument (Milford, MA). All samples were dissolved in LC/MS CHROMASOLV® grade solvents (≥ 99.9%) such as acetonitrile, methanol and filtered prior to analysis. Mass spectra were measured for 10-100 μM sample solutions in positive ion mode, and samples were infused using a Harvard syringe pump operating at a flow rate of 10μL per minute. Typical instrument conditions: 3.5 kV capillary voltage, 5 V cone voltage, and desolvation temperature at 120 °C, data were recorded using electrospray method. Electronic spectra were collected by using a Hewlett Packard 8453 diode array spectrophotometer and a Varian Cary 50 Bio spectrophotometer. Infrared spectra were recorded by using a Nicolet 360 FTIR spectrometer on samples prepared as either KBr pellets or as acetonitrile solutions or in some cases untreated when using diamond ATR analysis. Elemental analyses were performed by Robertson Microlit Laboratories, Inc. Madison, NJ.

4.2.3. EPR Spectroscopic Study. X-band EPR spectra were collected with a Bruker 500 CW-EPR spectrometer of the ELEXSYS series (at Bruker Instruments, Inc., Billerica, MA) in the temperature range 4-77 K with an Oxford Instruments ESR 900 continuous-flow cryostat interfaced with an Oxford Instruments ITC4 temperature controller. The tested samples were first cooled down to 77 K, liquid nitrogen temperature, in order to freeze the solution prior placing into the spectrometer. Final results were recorded at 4 K, liquid helium temperature.

4.2.4. Electrochemistry. A BAS-100A Electrochemical Analyzer was used for electrochemical measurements. A conventional three-electrode cell was used for the study employing a platinum disk working electrode, a platinum wire auxiliary electrode

and $Ag/AgClO_4$ was used as the reference electrode. The measurements were performed in distilled acetonitrile solution in the presence of a supporting electrolyte (generally 0.1 M TBAP or 0.1 M TEAP) and under a dry, purified argon atmosphere. Under these conditions the $E_{1/2}$ value for the Fc/Fc^+ couple was +79 mV. Potentials are reported versus SCE by correcting the $E_{1/2}$ value for the Fc/Fc^+ couple in acetonitrile versus a SCE reference (0.36V). The potentials reported in this work were uncorrected for a junction contribution.

4.2.5. X-ray Crystallography. Data were collected using a Bruker SMART CCD (charge coupled device) based diffractometer equipped with an LT-3 low-temperature apparatus operating at 193K or 100K. Suitable single crystals were chosen and mounted on a glass fiber or glass loop by using APIEZON-T grease mixed with Paratone-N oil. Data were measured using omega scans of 0.3° per frame for 20 or 30 seconds, such that a hemisphere was collected. A total of 1271 frames at the sample-detector distance of 5.00 cm or 2412 frames at 6.00 cm were collected to a maximum resolution of 0.75 Å. The first 50 frames were recollected at the end of data acquisition to monitor for decay. The crystals used for the X-ray diffraction studies showed no decomposition during the data collection. Cell parameters were determined by using SMART software and data reduction was performed and refined by using SAINT software, which corrects for Lp and decay on all observed reflections. Absorption corrections were performed with the program SADABS as supplied by George Sheldick. The structures were solved by the direct or Patterson method using the SHELXS-97 program and refined by least squares methods on F^2 in SHELXL-97, incorporated in SHELXTL-PC V 5.10. All non-hydrogen atoms were refined with anisotropic thermal parameters. Hydrogen atom positions were

calculated by geometrical methods and refined by using a riding model. All ORTEP drawings are made using 50% probability thermal ellipsoids.

4.2.6. Preparation of Compounds.

Synthesis of Complexes.

$[Mn(CF_3SO_3)_2]\cdot 2CH_3CN$. This compound was synthesized as reported.[9]

$[Mn_2O_2(L)_4](X)_3$ (where, L = bpy [**19**], dmb [**20**] and phen [**30**]; X = ClO_4 and OTf). The complexes were synthesized and purified according to the same procedures as described in Chapter 3, Section 3.2.7. $[Mn_2O_2(bpy)_4](ClO_4)_3$ [**19**] was prepared according to the literature procedure[10] (see Ch.3, page XX for details). Instead of using the analogous preparative method used for [**19**], an alternative synthetic route reported by our group was applied to make all of the listed complexes. This method utilizes *tert*-butyl-hydroperoxide as the oxidant as opposed to permanganate (MnO_4^-). The procedures for each complex are described in the following section.

To a clear acetonitrile solution (20 mL) of $Mn(ClO_4)_2\cdot 6H_2O$ (0.200 g, 0.552 mmole) or $Mn(CF_3SO_3)_2\cdot 2CH_3CN$ (0.217 g, 0.552 mmole) was added the ligand 2,2'-bipyridyl (bpy) (0.174 g, 1.113 mmole) or 4,4'-dimethyl-2,2'-bipyridyl (dmb) (0.205g, 1.113 mmole) or 1,10-phenanthroline (phen) (0.200 g, 1.113 mmole) to give a light yellow solution. Then 3.86 mL of 70% *t*-BuOOH (27 mmole) was added dropwise over 15 min with continuous stirring and the color immediately turned to dark green as a gas evolved from the reaction mixture. The solution was then stirred for an additional 30 min, filtered, and evaporated to dryness. The crude product was redissolved in acetonitrile, filtered, and kept for recrystallization by ACN/Et_2O vapor diffusion at –20 °C. A dark green crystalline product was formed after 1d and the crystals were collected by filtration, washed with

diethyl ether and dried under vacuum. Yield: **19**, 95.7 mg (bpy, 32.6%); **20**, 0.217 g (dmb, 66.8%); **30**, 6.3 mg (phen, 1.97%). The percent yield calculation for all the products is based on Mn. The crystal structure of $[Mn_2O_2(phen)_4](ClO_4)_3$ [**30**] is shown in Appendix E.

$[Mn_2O_2(L)_3(py\text{-}d_5)_2](X)_3$ (where, L = bpy [**31**] and dmb [**32**]; X = ClO_4 and OTf). The starting material $[Mn_2O_2(L)_4](X)_3$ (**19,** 106.4 mg; **20**, 117.7 mg, 0.1 mmole) was dissolved in 1 g of pyridine-d_5 (99.5 atom % D). The color of the solution changed from dark green to dark brownish after all of the starting material had dissolved. The identity of the resulting complex, $[Mn_2O_2(L)_3(py\text{-}d_5)_2](X)_3$, was established by NMR spectroscopy (Figure 3(b)) and verified by the use of mass spectroscopy. The isolated yield of this type of complex is poor (see Section 4.3 for detailed discussion) for this work but based on the NMR results, we deduce that the quantitative yields of [**31**] and [**32**] in solution were obtained.

$[Mn_2O_2(L)_3(dmf\text{-}d_7)_2](X)_3$ (where, L = bpy [**33**] and dmb [**34**]; X = ClO_4 and OTf). A procedure analogous to the one described for [**31**] and [**32**] was used except that N,N-dimethylformamide-d_7 replaces pyridine. The identity of the resulting complex, $[Mn_2O_2(L)_3(dmf\text{-}d_7)_2](X)_3$, was established by NMR spectroscopy (Figure 3(c)) and verified by the use of mass spectroscopy. The isolated yield of this type complex is poor, as it is for the aforementioned complexes [**31**] and [**32**] (see Section 4.3 for detailed discussion). However, based on the NMR results, we speculated that the quantitative yields of [**33**] and [**34**] in solution were obtained.

$[Mn_4O_6(bpy)_4(py\text{-}d_5)_4](ClO_4)_4$ [**35**]. The pyridine-d_5 solution of $[Mn_2O_2(bpy)_4](ClO_4)_3$ (0.1 mmole in 1g of pyridine-d_5) was left undisturbed under

ambient conditions. After 6 h the dark precipitate that formed was collected by filtration. The dark filtrate was again left undisturbed for 1 d, and a second crop of precipitate was collected by filtration. The two crops of precipitate were combined and dissolved in acetonitrile. Vapor diffusion of diethyl ether into the acetonitrile solution at –20 °C gave dark crystals suitable for X-ray crystallography. The yield after recrystallization was 36.5 mg (45.9%). A synthetic summary is provided in Scheme 4.1.

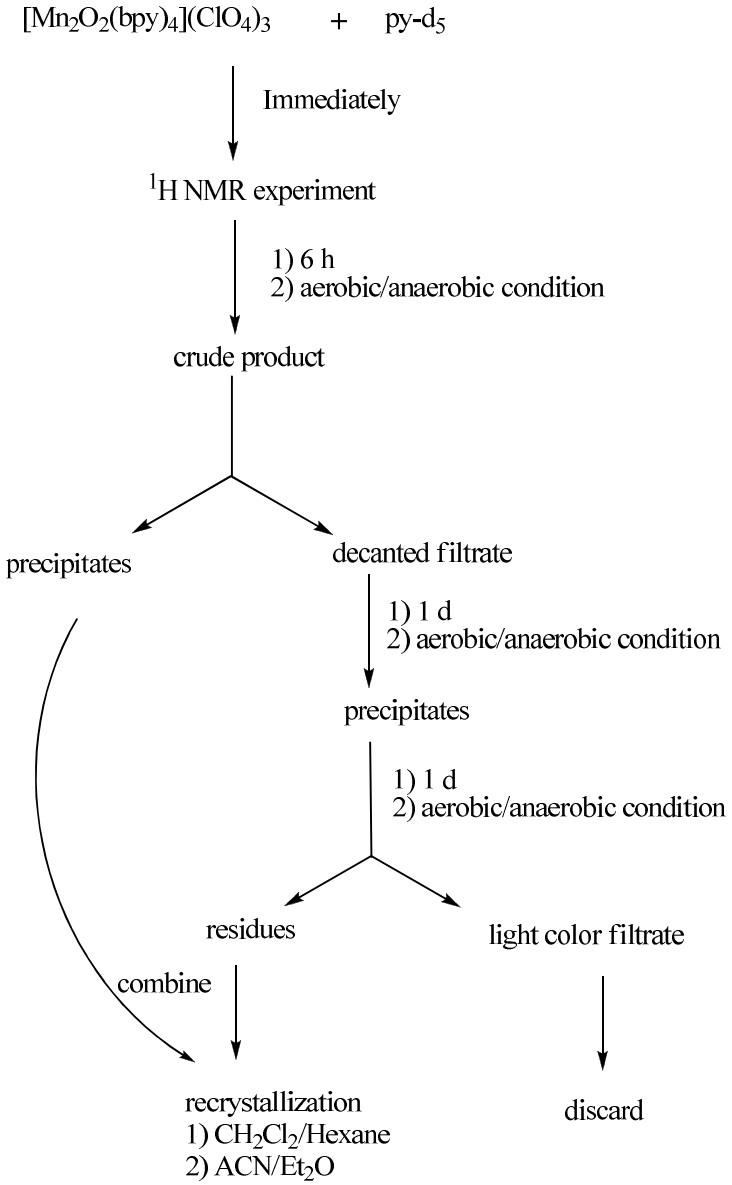

Scheme 4.1. Summary of the synthetic preparation of [**35**].

$[Mn_4O_6(bpy)_4(py)_4](ClO_4)_4$ [**36**]. We followed the identical procedure as described above for pyridine-d_5 system except that pyridine (C_6H_5N) was used as the solvent in the synthesis. The solid product that accumulated after 5 d was recrystallized from acetonitrile/Et_2O at –20 °C. The yield after recrystallization was 35.9 mg (43.4%).

4.3. Results and Discussion

4.3.1. Synthesis. The origin of the work described came from our research group's longstanding interest in the application of paramagnetic ^{1}H NMR spectroscopy to the study of manganese-oxo clusters.[11] The species we frequently employ as an NMR standard is $[Mn_2O_2(bpy)_4](ClO_4)_3$ [**19**], which we also use as a fundamental synthetic building block for OEC modeling applications. Complexes with the formulation $[Mn_2O_2(L)_4](ClO_4)_3$ (where L = bpy and phen) were first reported in 1960 and for many years thereafter their ^{1}H NMR spectra were not reported.[12,13] Our group has measured the distinctive ^{1}H NMR spectrum of $[Mn_2O_2(bpy)_4](ClO_4)_3$ in deuterated acetonitrile solution (also shown here in Fig. 5d).[14] In addition to this dimeric complex, we have measured the paramagnetic ^{1}H NMR spectra of many Mn-oxo complexes initially as a convenient tool in the identification of products from various reaction mixtures.[11] Unlike the organic or biochemical molecules for which NMR techniques are commonly used for reaction product identification, there is no well-established NMR spectral database for inorganic complexes, especially paramagnetic ones, which would assist in the same. In order to use NMR spectroscopy to determine the structures of products in our systems, we must establish a database. Therefore, we are continuing to accumulate ^{1}H NMR data for a large set of paramagnetic Mn-oxo clusters of interest. We believe this spectral

database will be valuable for analysis of the outcome of various reactions, and of course we are particularly interested in detection of unexplored/unknown species.

Guided by the most recently reported PSII OEC X-ray crystal structure and XAS studies (see Chapter 1), we have been involved in searching for synthetic paths to different high-valent Mn_4 model complexes in order to learn by comparison more about the PSII active site complex. Previous workers proposed that $[Mn_2O_2(L)_4](ClO_4)_3$ (where L = bpy, phen) were converted to $[Mn_2O_2(L)_3(py)_2](ClO_4)_3$ or $[Mn_2O_2(L)_3(dmf)_2](ClO_4)_3$ in pyridine or *N*,*N*-dimethylformamide, respectively.[15] These complexes would arguably have labile monodentate ligands on a manganese center (Scheme 4.2).

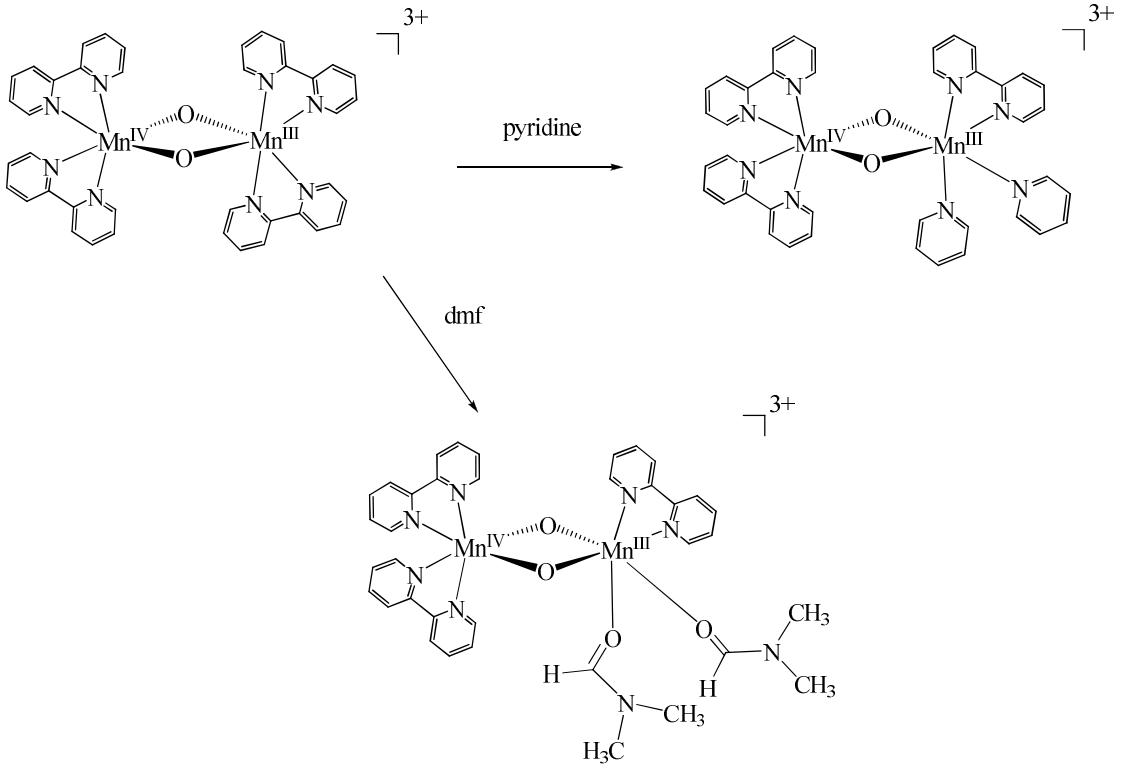

Scheme 4.2. Ligand exchange reactions of interest in this Chapter.

As mentioned above, we see these complexes as desirable with regard to opening up a site on a Mn center for substrate water binding. We also wish to use these modified dimers as synthetic precursors for higher nuclearity Mn clusters. The intriguing reactions

shown in Scheme 4.2 have provoked us to study this system in more depth. First, we decided to utilize the NMR to investigate the products formed when $[Mn_2O_2(L)_4]^{3+}$ was exposed to the coordinating solvents, py and DMF, as described in the literature. Based on the ^1H NMR spectra of the ligand substituted complexes, we found the new dimeric Mn_2O_2 clusters have very distinctive NMR signatures. Such observations provide us helpful information with regard to the nature of reaction products in the solution state; especially since there was no X-ray crystal structure reported for the complexes under study. The ^1H NMR spectra of [**19**] and [**20**] in solution are shown in Section 4.3.3. Subsequently, we performed EPR measurements so as to assess whether or not the di-μ-oxo-bridged dinuclear (III, IV) cores remained intact. Our results indicate that the bridged cores do indeed retain their structures after ligand substitution reactions occur (Section 4.3.2).

More surprisingly, the product we isolated from one ligand exchange reaction described above was not the expected binuclear species but instead an interesting and perhaps more useful novel tetranuclear Mn complex, $[Mn_4O_6(bpy)_4(py\text{-}d_5)_4](ClO_4)_4$ [**35**]. Our first observation of this product came when it precipitated out at the bottom of an NMR tube. At that time, we assumed it was the binuclear species suggested by Rajasekharan et al.[15] But after a careful study of this material, it was identified as a tetranuclear mixed-ligand adamantane cluster, which features monodentate and bidentate ligands coordinated to each manganese site. The synthesis of [**35**] was accomplished by simply dissolving $[Mn_2O_2(bpy)_4](ClO_4)_3$ [**19**] in deuterated pyridine under aerobic atmosphere. We speculated that O_2 may play a role in the conversion of binuclear to tetranuclear species. Therefore, a variety of other reaction conditions were explored in a

search for a logical explanation with respect to the formation of this complex, and also for an alternative synthetic method which would be more rational and higher yielding. For example, we examined the reaction between [**19**] with varying amounts of pyridine in a less coordinating solvent, CH_3CN, in the presence of strong oxidants such as H_2O_2 or *t*-BuOOH. The oxidants were thought to be required for the reason that the starting material is in the Mn_2 (III, IV) redox state, however for the product [**35**], all Mn atoms are in the +4 oxidation state. In addition, the oxidants were chosen because they have the potential to provide O atoms. According to NMR studies, the reaction with H_2O_2 did not produce [**35**]. On the other hand, the reaction containing the oxidant *t*-BuOOH shows formation of the targeted adamantane complex (spectrum not shown). To reach any conclusive statement about the involvement of O_2, we have also carried out the reaction of [**19**] in deuterated pyridine solvent under anaerobic conditions by using an inert, pure dinitrogen (N_2) atmosphere box. We observed that a precipitate of [**35**] formed even without O_2 present. This was confirmed by using NMR and mass spectroscopy. The conclusion we draw from these results is that dioxygen is not involved in the reaction that produces [**35**]. Furthermore, we carried out an experiment, monitored by NMR spectroscopy, in which [**19**] was titrated with pyridine in order to investigate the concentration dependence of ligand substitution. This was performed by dissolving [**19**] in CD_3CN and then various equivalents of pyridine (C_5H_5N) were added to the solution. The formation of tetranuclear Mn complex [**35**] was observed according to the corresponding NMR spectral results (Section 4.3.3, Figure 5). As mentioned before, we often use $[Mn_2O_2(bpy)_4]^{3+}$ a building block for the synthesis of higher nuclearity Mn complexes (also see Chapter 3) and obtaining [**35**] from it provides a solid example for

such an application. Moreover, we proposed the formation of this tetranuclear complex could be from a self-aggregation pathway that has been shown, for example, by the observation that thiolate complexes $[Fe_2S_2(SR)_4]^{3-}$ core are unstable and react further undergoing a '2 plus 2' aggregation to give a tetrameric product.[16] Or another possible pathway would involve initial formation of the known open chain complex $[Mn_4O_6(bpy)_4]^{4+}$,[17] followed by a structural rearrangement induced by pyridine ligand substitution. Such proposals are presented in Scheme 4.3. The idea that $[Mn_4O_6(bpy)_6]^{4+}$ could be an intermediate in the formation of [**35**] has been studied by using ^{1}H NMR. In fact the spectral results support this proposal. We observed the initial formation of [**31**] followed by precipitation of [**35**]. However, the driving force and detailed reaction process for this proposed mechanistic route remains unclear. Lastly, since the $\{Mn_2O_2\}$ (III, IV) core starting material [**19**] has long been considered as a structural subunit in a tetranuclear Mn-oxo complex which is referred to the "Berkeley OEC model" (details see Chapter 1), we are very excited about this observation with regard to the unforeseen formation of complex [**35**] from [**19**]. We think that the associated redox reaction with this formation can be viewed as (III,IV) + (III,IV) $\rightarrow$ (IV,IV,IV,IV), which is related to the $2e^-$ oxidation process of $S_1 \rightarrow S_2 \rightarrow S_3$ transition in the OEC cycle, given the proposed "Berkeley model" complex designation for the S_1 state.

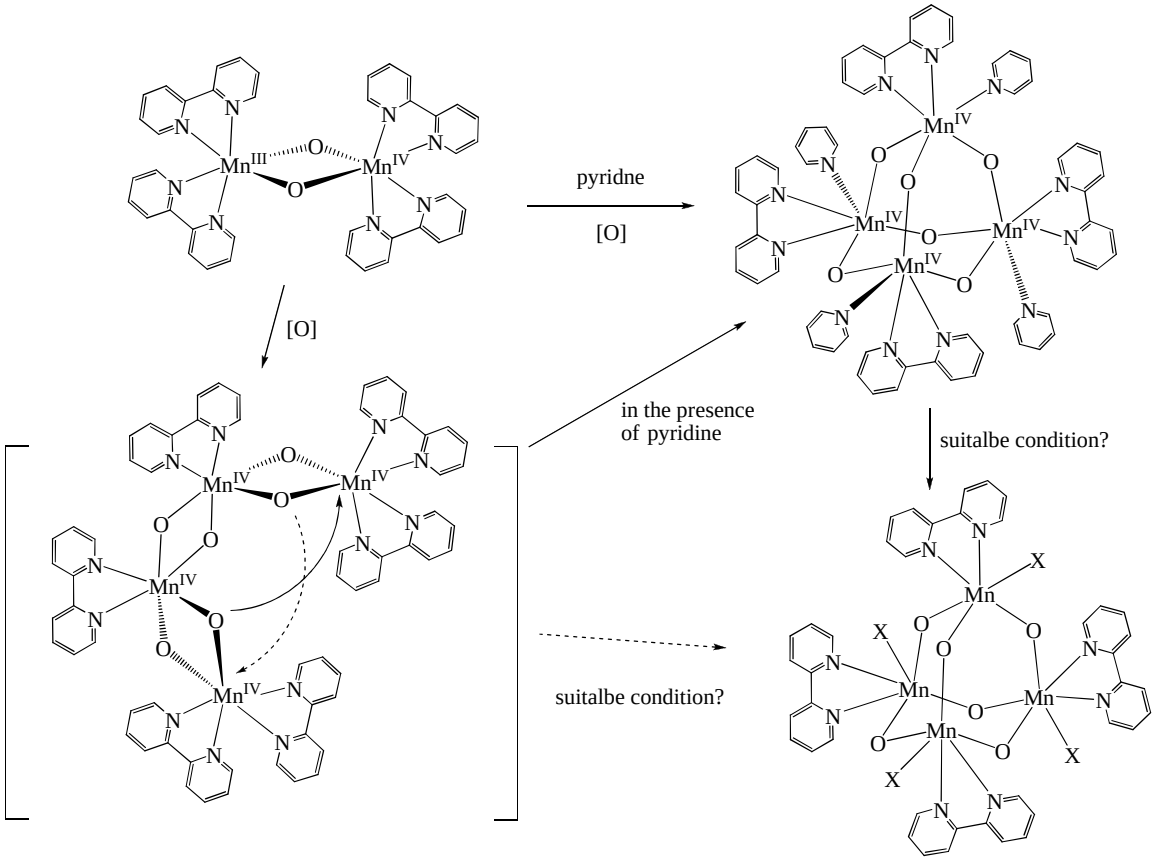

Scheme 4.3. Hypothesis of the mechanism in the formation process of [**35**].

4.3.2. EPR Spectroscopy. We attempted to utilize the EPR spectroscopy to examine whether or not the Mn_2O_2 unit remains intact immediately after the bpy ligand of [**19**] is displaced either by py or DMF. The selected ligand substitution reaction we measured was that of [**19**] in *N*,*N*-dimethylformamide-d_7 (dmf-d_7) which, according to NMR results, does not proceeded on to give the Mn_4O_6 type of aggregate over a longer period of time as occurs for the pyridine case. As shown in Figure 2, the EPR spectrum at 4 K of this proposed $[Mn_2O_2(bpy)_3(dmf\text{-}d_7)_2](ClO_4)_3$ [**33**] complex, shows a 16-line hyperfine pattern characteristic of the $\{Mn_2O_2\}^{3+}$ core in addition to other lines which are attributed to an impurity. Even though the actual structure of [**33**] is not determined by solid state X-ray crystallography yet, the observed EPR and corresponding NMR results lead us to

believe that the {Mn_2O_2 (III,IV)} core was not disturbed by the ligand substitution process. Since the dimeric core of [**33**] remains intact in solution, our proposed structure $[Mn_2O_2(bpy)_3(dmf\text{-}d_7)_2](ClO_4)_3$ is considered the best fit tentatively based on these spectroscopic results. Further studies are under investigation, especially toward the crystallization of proposed complexes $[Mn_2O_2(L)_3(py)_2]^{3+}$ and $[Mn_2O_2(L)_3(dmf)_2]^{3+}$ (where L = bpy or dmb) in order to determine their structures in solid state. We also anticipate that the bpy ligand-substituted complex, $[Mn_2O_2(bpy)_3(py\text{-}d_5)_2]^{3+}$ [**31**], will be a very desirable starting material for the further ligand substitution and '2 + 2' aggregation studies.

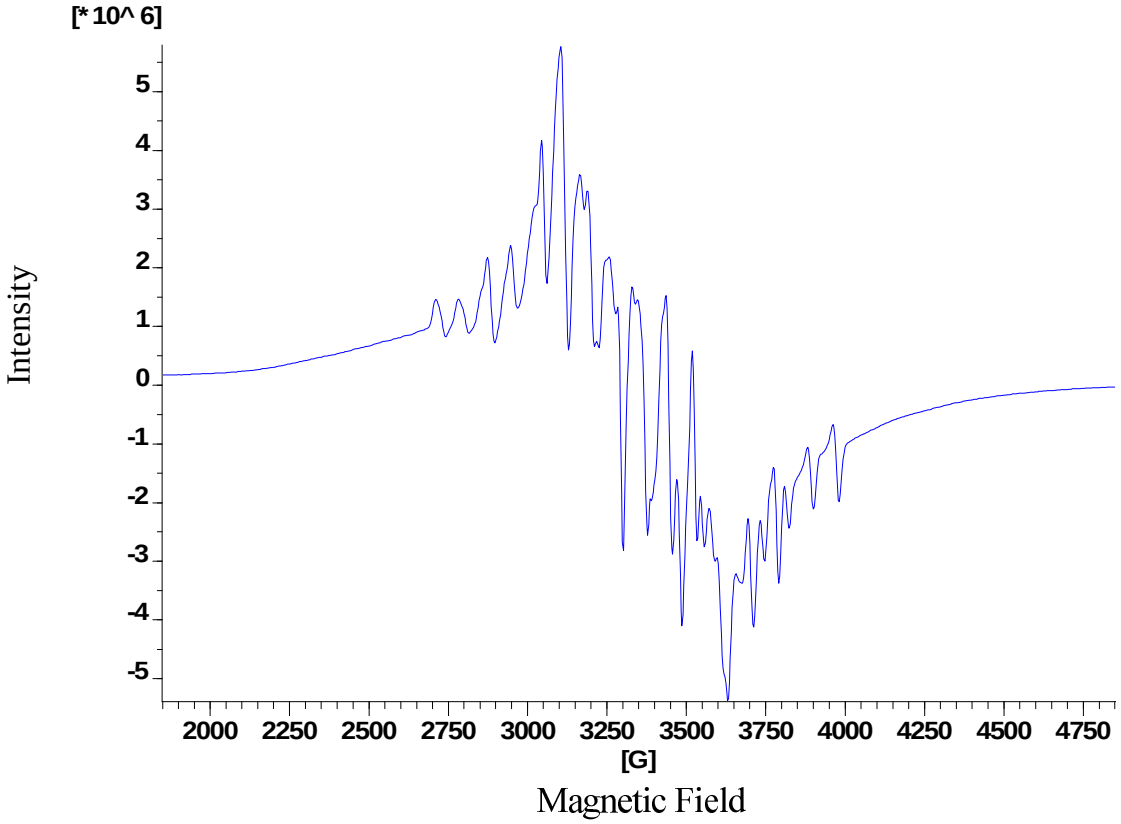

Figure 4.2. X-band EPR Spectrum of $[Mn_2O_2(bpy)_3(dmf\text{-}d_7)_2](ClO_4)_3$ [**33**] in DMF-d_7 solvent. Conditions: modulation frequency 100 kHz, modulation amplitude 0.5 mT, frequency 9.478 GHz, microwave power 0.2 mW, T = 4K.

4.3.3. ^{1}H NMR Spectroscopic Study. A comparison of the ^{1}H NMR spectra for [**19**] in various deuterated solvents is shown in Figure 3. The dissimilarity of the series of spectra was very surprising to us because the only difference among them was the deuterated solvent used for each measurement. These results indicate that new complexes are formed by reaction of the solvent with $[Mn_2O_2(bpy)_4]^{3+}$. As described in Section 4.3.1 and 4.3.2, the proposed solution state structure for the reaction products in various deuterated solvents retain a dimeric core, $\{Mn_2O_2\}$, analogous to [**19**] but with different ligand configurations (Scheme 4.2). The ^{1}H NMR spectrum of [**19**] in CD_3CN is shown in Fig. 3d and the isotropic shifts are between +3 ~ +26 ppm. When [**19**] was dissolved in py-d_5 or dmf-d_7 and then ^{1}H NMR spectroscopic measurements were carried out immediately, the resulting spectra revealed dramatically different patterns of isotropic shifts relative to the shifts found for the complex dissolved in CD_3CN. The py-d_5 and dmf-d_7 NMR spectra are displayed in Figs. 3b and 3c, and the proposed formulations for the corresponding complexes are $[Mn_2O_2(bpy)_3(py\text{-}d_5)_2]^{3+}$ [**31**] and $[Mn_2O_2(bpy)_3(dmf\text{-}d_7)_2]^{3+}$ [**33**], respectively. These proposed structures, generated by ligand substitution reactions, are assigned tentatively and we will need further evidence such as X-ray crystal structures to verify these formulations. We believe that the difference in the pyridine and DMF spectra compared to acetonitrile and DMSO can be explained by the different molecular symmetries and perhaps varying ligand exchange rates.

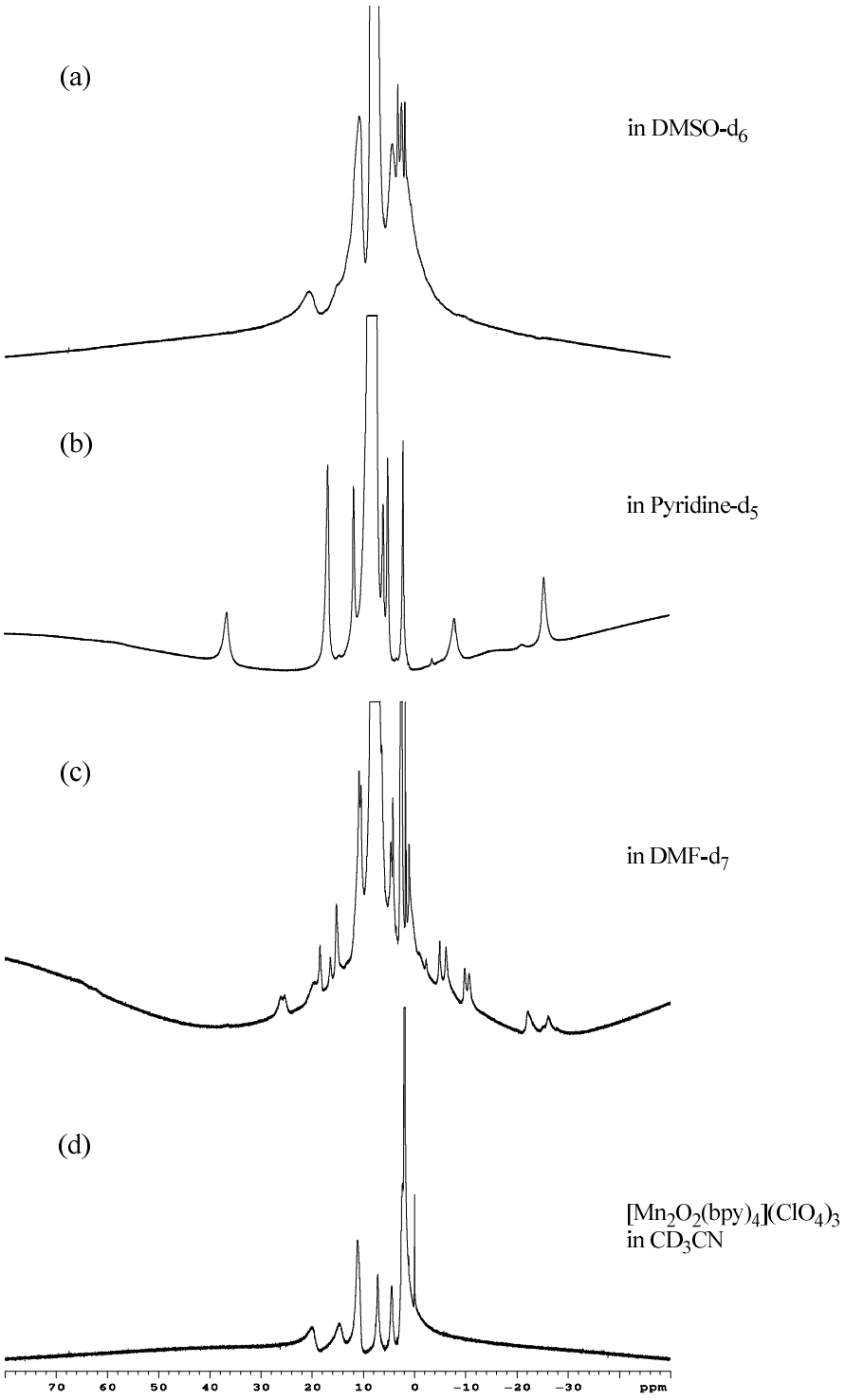

Figure 4.3. ^{1}H NMR spectroscopic study for $[Mn_2O_2(bpy)_4](ClO_4)_3$ in various deuterated solvent systems: (a) DMSO-d_6; (b) Pyridine-d_5; (c) DMF-d_7; (d) Acetonitrile-d_3.

For the greater majority of the paramagnetic complexes we study, distinctive ^{1}H NMR spectra are observed despite the fact that unpaired electrons in metal *d* orbitals can greatly broaden resonances. So, we can distinguish different species in solution even though their solid state structures have not been determined by using X-ray crystallography. According to the suggested structural conformations of [**31**] and [**33**], we believe that one of the bpy ligands on the Mn(III) site of [**19**] is replaced by two solvent molecules. We choose the Mn(III) because it is expected to exhibit much more labile ligand exchange processes due to its lower charge and the Jahn-Teller effect associated with an octahedrally coordinated $3d^4$ transition metal ion. These proposed products possess different molecular symmetries and in turn dissimilar ^{1}H NMR isotropic shifts. An examination of point group symmetry for the complexes of [**19**], [**31**] and [**33**] provides a rationale for the observed spectra. For complex [**19**], the molecular structure retains a relatively high-symmetry point group of D_{2h} assuming that the dimanganese (III,IV) centers of Mn_2O_2 are equivalent, each with an effective +3.5 charge, on the NMR time scale. Its ^{1}H NMR spectrum reveals five prominent isotropic shifts which all reside in the downfield spectral region between +3 to +25 ppm (Fig. 3d), while we predict there should be six resonances in theory. However, the protons at the 6,6'-positions are expected to be broad and difficult to observe. For [**31**], the point symmetry reduces down to a lower symmetry point group of C_{2h}, given the coordinating solvent ligands py-d_5 are not freely rotating in solution to affect the molecular symmetry determination and also assuming that dimanganese (III,IV) center are equivalent on the NMR timescale as described above. The observed ^{1}H NMR spectrum shows a different pattern of isotropic shifts as compared to [**19**]. There remain relatively few peaks between –35 to +45 ppm,

approximately eight observed which is close to the predicted resonances of nine in theory, the protons at the 6,6'-positions are expected to be broad and difficult to observe, and the key difference is that [**31**] has two prominent upfield chemical shifted resonances (Fig. 3b). Whilst the molecular symmetry of [**33**] has possibly an even lower point symmetry, such as pseudo-C_{2h} or C_2 since the DMF-d_7 molecules are not as symmetric as pyridine given that both of the ligands are not freely rotating in solution for the simplicity of molecular symmetry elucidation, which would lead to symmetry reduction and thus a somewhat more complicated ^{1}H NMR spectrum was obtained (Fig. 3c). The isotropic shifts were found between –40 to +40 ppm and approximately 17 resonances were observed in the spectrum as we predicted there should be 18 resonances in theory according to its molecular point symmetry discussed above and the protons at the 6,6'-positions are expected to be broad and difficult to observe. All of the ^{1}H NMR resonances are of course all from the bpy ligands since the coordinated pyridine is deuterated. In view of the fact that the structural conformation of [**31**] and [**33**] was suggested as having one bpy ligand substituted with two solvent molecules, there are overall 24 protons reside in the compound formulation. There are more resonances for complexes with a lower molecular symmetry as described above and when the symmetry is higher there are fewer resonances expected. The results revealed in this section demonstrate the utility of ^{1}H NMR in detecting paramagnetic products and even intermediates from syntheses of inorganic complexes. However, the proposals for solution structures discussed above need to be compared to solid state X-ray crystal structures, which will be a priority for future work. In addition, we also used DMSO-d_6 as another solvent for further investigation (Fig. 3a). The ^{1}H NMR spectrum displays a

similarity to the spectrum of [**19**] in CD_3CN with some minor changes. The structural postulation based on this result is unclear and it could be that there is no ligand substitution or a very slow ligand exchange in this system. The observed analogous ^1H NMR isotropic shifts indicate that the structural conformation in DMSO would be similar to that in acetonitrile solution.

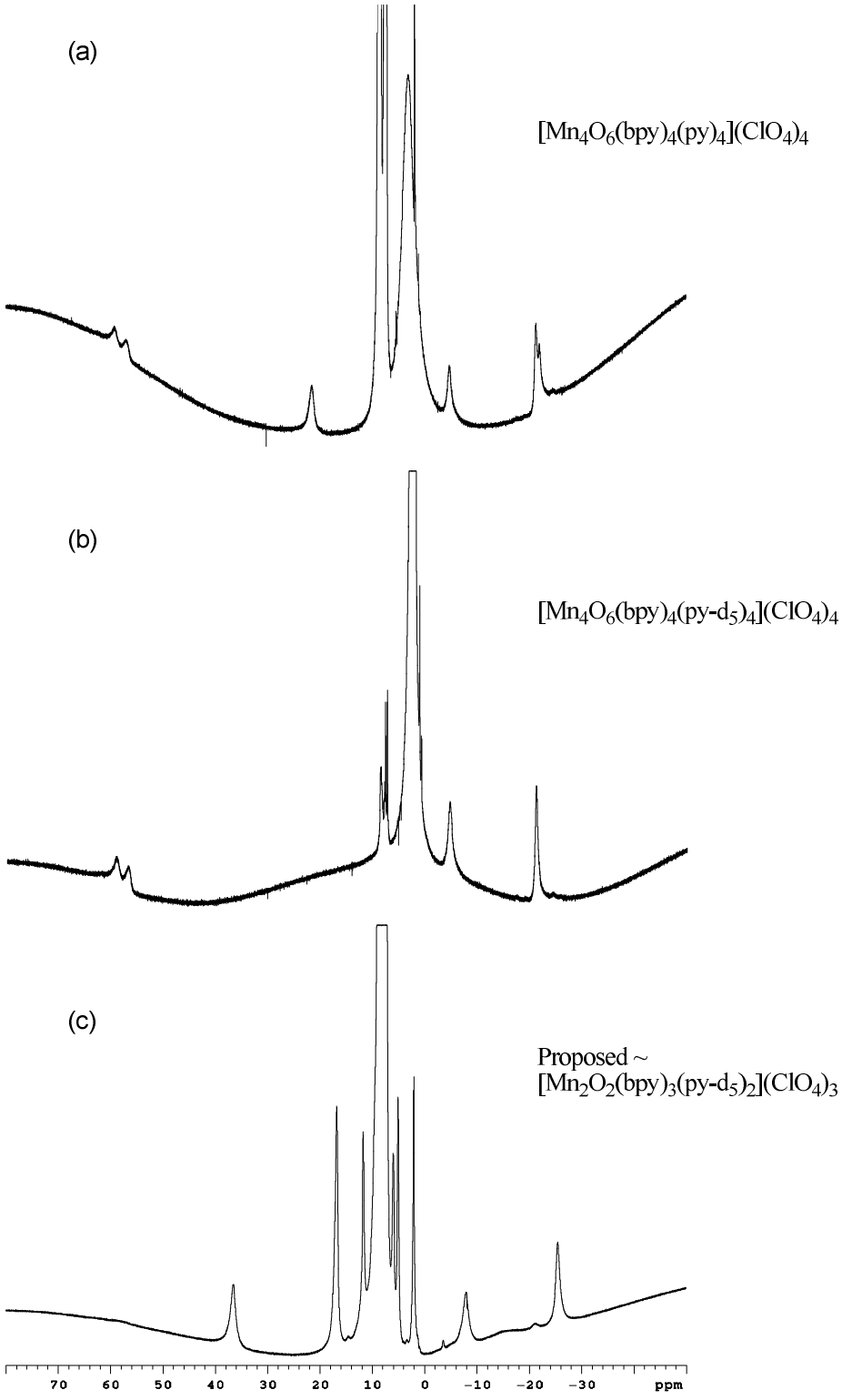

Figure 4.4. ^{1}H NMR spectra in CD_3CN of (a) $[Mn_2O_2(bpy)_4](ClO_4)_3$; (b) $[Mn_4O_6(bpy)_4(py\text{-}d_5)_4](ClO_4)_3$; (c) $[Mn_4O_6(bpy)_4(py)_4](ClO_4)_3$.

Several attempts were carried out in order to obtain the solid state structures as indicated by the aforementioned ^{1}H NMR results in the solution state but no products of the proposed complexes have yet been isolated or structurally identified. However, in the pyridine-d_5 system, an unexpected product, [**35**], was discovered and its solid state structure was determined by the X-ray crystallography (Section 4.3.4). When dissolving the isolated complex, [**35**], in CD_3CN solvent for ^{1}H NMR measurements, the resulting spectrum was found to give a different isotropic shift pattern as compared to the pattern for [**31**]. The spectra of [**35**] and [**31**] are shown in Fig. 4b and 4c, respectively. According to the X-ray crystal structure discussed in the next section, this novel mixed-ligand adamantane $\{Mn_4O_6\}$ cluster was considered to retain the high-symmetry point group of S_4 which explains the relatively simple ^{1}H NMR spectrum. The observed NMR results provide strengthened evidence for the hypothetic mechanism shown in Scheme 4.3 but this mixed-ligand type of $\{Mn_4O_6\}$ adamantane complex has only been isolated and structurally determined in the pyridine-d_5 solvent system up to now. Moreover, the upfield isotropic shifts of Fig. 4b and 4c show a great level of similarity and from this observation, we cannot rule out the other structural possibilities for the corresponding ^{1}H NMR of [**33**], which was tentatively proposed as a dimeric complex. The other possible structures, for instance, could be a structural isomer of a tetramanganese cluster, such as $[Mn_4O_6(bpy)_6]^{4+}$ or $[Mn_4O_6(bpy)_4(py)_4]^{4+}$ with high molecular point symmetry. Or a high oxidation state of $\{Mn_2O_2\}$ core (IV,IV) dimer, $[Mn_2O_2(bpy)_4]^{4+}$, may be involved with the formation of the observed adamantane complex, [**35**].

For this adamantane-type of tetramanganese complex, we were not only able to isolate [**35**], which contained deuterated pyridine as monodentate ligands, but also [**36**], which

had regular pyridine (C_5H_5N) as the coordinating monodentate ligand. Such a product is useful for making ^1H NMR assignments (see Figs, 4a and 4b). The only difference between [**36**] and [**35**] is that one has C_5H_5N as the monodentate ligand and the other has C_5D_5N. In Fig. 4(a), the peak at +23 ppm is assigned as the pyridine protons at 5-position and there is an overlapping resonance at –25 ppm which is corresponding to the 4-position pyridine protons. This is because these two resonances are not present in the deuterated complex of [**35**].[18] This observation is extremely valuable for the purpose of identification when we decided to run a ^1H NMR titration experiment in order to examine how pyridine behaves as a reactant during the formation of such a tetramanganese complex in MeCN solution. The corresponding titration results were shown in Figure 5 and the representative arrows indicate the observed isotropic shifts of [**36**] in Fig. 4a. During the titration experiment (in CD_3CN), the average time span between each ^1H NMR measurement was *ca.* 30 min and the equivalent molar ratio was compared to the quantity of complex [**19**]. The results have shown that after 1 equivalent of pyridine was added, the characteristic isotropic shifts started to appear but in a small intensity. With more addition of pyridine, the related intensities increased.

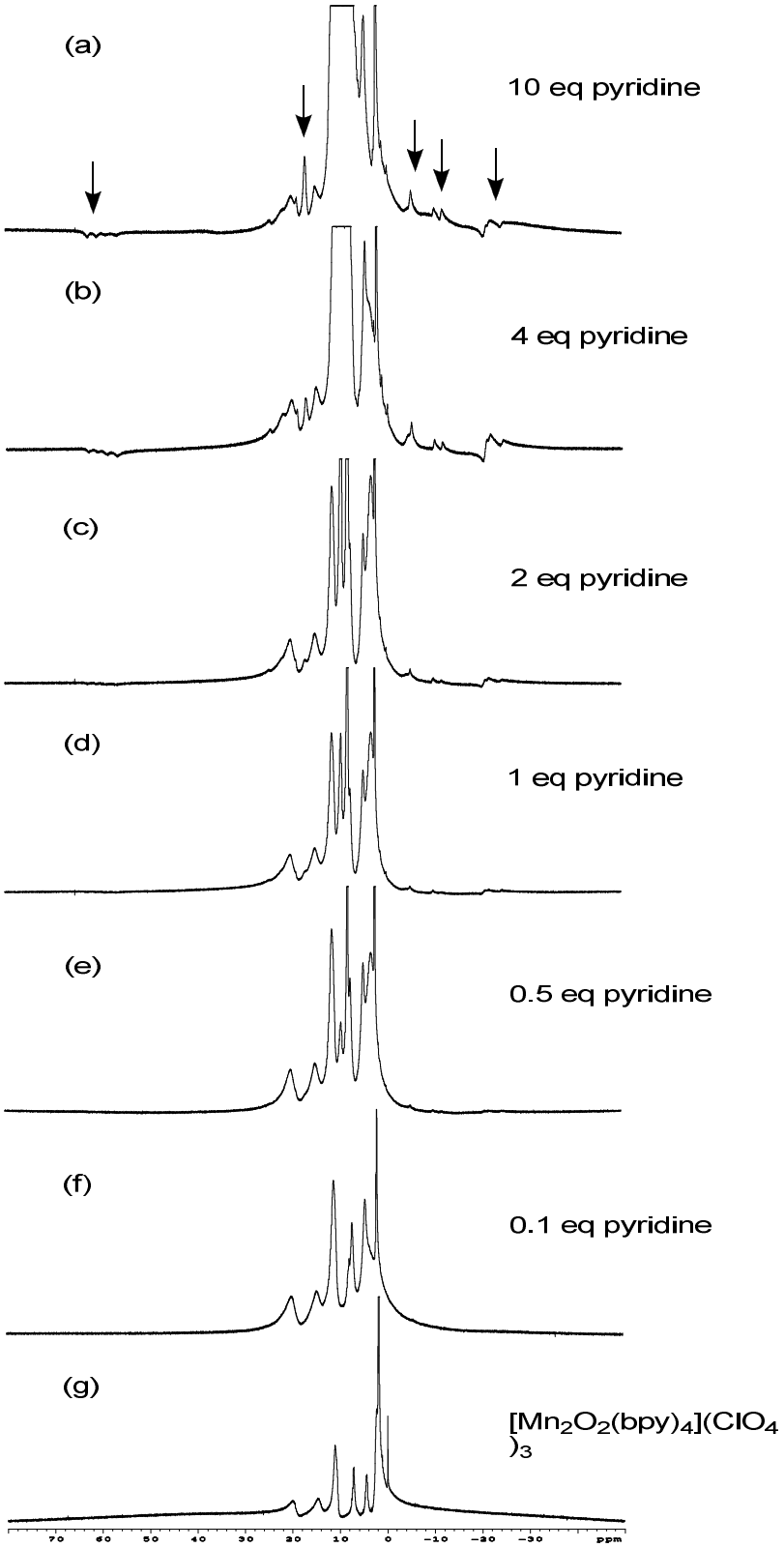

Figure 4.5. Titration of [**19**] with pyridine in CD_3CN followed by ^1H NMR spectroscopy.

Furthermore, we extended the ligand-exchange reactions by first using a different type of bidentate ligand such as 4,4'-dimethylbipydine (dmb) along with varying counterions (ClO_4^- and $CF_3SO_3^-$) as the starting material. All of the systems with different combinations in terms of the ligands and counterions gave comparable spectral results by dissolving them in the different deuterated solvent systems, and which were similar to those observed ^{1}H NMR spectra shown in the complex [**19**] as the starting material that were discussed above. The resulting ^{1}H NMR spectra of these varied ligands with different counterions in various deuterated solvents were listed in Appendix B.

As described in Section 4.3.1, it is essential to construct an informative database of synthetically prepared paramagnetic complexes so that products of other reactions may be easily identified. Table 4.1 presents a comparison of a related set of tetranuclear manganese (IV) complexes, including [**35**] and [**36**]. Another complex which may be related to mechanism of the formation of [**35**], $[Mn_4O_6(bpy)_6]^{4+}$, is included in Table 4.1 as well. Even though the ^{1}H NMR spectra do not absolutely prove that the solution state structures are consistent with the solid state structures, we still assume that in the absence of other data, the solution and solid structures are the same. Therefore, the characteristic NMR isotropic shifting patterns will be an asset to help the potential structural determination/verification when the solid state X-ray crystal structures are unattainable.

Table 4.1. Paramagnetic Proton NMR Spectroscopic Data Comparison (numbers in parentheses stand for FWHM).

$[Mn_4O_6(bpy)_4(py)_4]^{4+}$	$[Mn_4O_6(bpy)_4(py\text{-}d_5)_4]^{4+}$	$[Mn_4O_6(tacn)_4]^{4+}$	$[Mn_4O_6(bpea)_4]^{4+}$	$Mn_4O_6(bpea)_2(m\text{-}ida)_2$	Assigned Protons
61.8 (114)	58.9 (212)		54.9 (470)		5,5'-H
58.7 (112)	56.8 (189)		46.1 (420)	52.0 (529)	5,5'-H
			29.4 (520)	27.7 (733)	N-$CH_2C\mathbf{H}_3$ (bpea)
21.6 (422)					4,4'-H (py)
			4.6 (360)		3,3'-H(bpea)
			2.5 (330)		
–4.2 (438)	–4.2 (445)			–1.6 (1630)	3,3'-H(bpy)
				–17.0 (1864)	
–21.9 (637)	–21.9 (682)		–18.5 (200)	–17.3 (1723)	4,4'-H (bpy, bpea)
–23.0 (410)			–20.1 (210)		4,4'-H (py, bpea)
			–24.2(ND)		
		–41.4 (2900)	–46.0 (VB)	–59.2 (ND)	
		–56.7 (1640)	–73.0 (VB)	–69.3 (ND)	N-$C\mathbf{H}_2CH_3$ (bpea)
				–76.8 (ND)	
			–82.0 (VB)	–88.8 (ND)	
			–113.5 (1200)	–95.2 (ND)	

4.3.4. Crystal Structure. The X-ray crystal structure of [**35**] is shown in Figure 6. Four Mn and six bridging O atoms form an adamantane shaped core. The Mn atoms reside at the apices of a tetrahedron while each O atom bridges two Mn atoms and occupy the apices of an octahedron.[19] All of the Mn atoms are six-coordinate in a

pseudooctahedral geometry. Each Mn atom is ligated with three bridging O atoms and three N atoms, with two of the N atoms contributed from the bipyridine (bpy) ligand and the third one from a pyridine (py). To our knowledge, this mixed-ligand bidentate combined with monodentate ligand set in coordinating configuration on a Mn center has not previously been observed among oxo-bridged multinuclear manganese complexes. The novel complexes $[Mn_4O_6(bpy)_4(py\text{-}d_5)_4]^{4+}$ [**35**] and $[Mn_4O_6(bpy)_4(py)_4]^{4+}$ [**36**] both crystallize in the tetragonal space group I_4. The intrinsic molecular point symmetry of [**35**] and [**36**] is observed as S_4. The $[Mn_4O_6(bpxa)_4]^{4+}$ type clusters have point symmetry S_4 and complexes such as $[Mn_4O_6(tacn)_4]^{4+}$ and $[Mn_4O_6(tach)_4]^{4+}$ are nearly T_d point symmetric. The assigned molecular point symmetries for these aforementioned compounds, which have the same $\{Mn_4O_6\}$ adamantane-shaped core, are distinguished by different ligand coordination. Ligands of the tacn and tach type are more sterically rigid and are nearly three-fold symmetric and thus will not reduce the molecular symmetry. In the bpxa type ligands, where x is the abbreviation for an *N*-alkyl substituent, the alkyl groups reduce the overall molecular point symmetry of $\{Mn_4O_6\}$ adamantane-shaped complexes, except the bpma (m = methyl) type ligand. The mixed-ligand configuration {bpy + py} is considered to be analogous to the bpxa type ligands in terms of it symmetry properties. The compounds with molecular point symmetry of S_4 or T_d show a relatively simple pattern of isotropically shifted ^{1}H NMR resonances (Section 4.3.3 and reference X). This is mainly because of the high molecular symmetry observed and in each case all four manganese atoms are magnetically equivalent. For the higher molecular symmetry T_d, $[Mn_4O_6(tacn)_4]^{4+}$ and $[Mn_4O_6(tach)_4]^{4+}$ complexes were found to have the fewest isotropic shifts in their ^{1}H NMR spectra among these adamantane-shaped

complexes. $[Mn_4O_6(tacn)_4]^{4+}$ has two prominent resonances between –20 and –80 ppm and $[Mn_4O_6(tach)_4]^{4+}$ also reveals two peaks between +5 and +30 ppm.[19a] Even though one cannot assume that the solid state X-ray crystal structures are identical to those in solution, we have shown that in general they do match according to NMR results. In some cases, we have observed molecules that retain their solid state structures upon dissolution only to undergo rearrangements after some time[20] but this kind of behavior was not observed in the complex systems we studied here. As mentioned above, the crystal structure of [**35**] reveals its molecular point symmetry to be S_4, which makes the corresponding ^1H NMR isotropic shifts analogous to the ones observed for $[Mn_4O_6(bpxa)_4]^{4+}$ complexes (see Table 4.1 for the corresponding assignments). The eight protons on each bipyridine ligand are expected to be detected by ^1H NMR spectroscopy. According to the molecular symmetry, we expected to find that all four bpy ligands are in the same magnetic environment so there should be total of 8 proton resonances not 32. However, the protons at the 6,6'-positions are expected to be broad and difficult to observe in the ^1H NMR spectrum. So in the spectrum of [**35**] in CD_3CN, we found only six isotropically shifted resonances. We also examined pyridine analogue, [**36**]. The major differences, as described in previous section are the resonances at +23 and –25 ppm, which we assign as the 5- and 4-position protons for four symmetry-related pyridine rings, respectively. Our interpretation is that the 2- and 6-position protons on the pyridine ligands are difficult to detect and the 3-position protons reside in the diamagnetic region of ^1H NMR spectrum.

It is noteworthy that the bond lengths between Mn and N atoms of the mixed-ligand complex differ from the Mn-N bond distances in the $[Mn_4O_6(bpxa)_4]^{4+}$ adamantane

complexes. For complex [**35**], Mn-$N_{pyridine}$ and Mn-$N_{bipyridine}$ are 2.113 Å and 2.088 (average) Å, respectively, while for $[Mn_4O_6(bpea)_4]^{4+}$ the distances for Mn-N_{alkyl} and Mn-$N_{pyridyl}$ are 2.193 Å and 2.080 (average) Å, respectively. The longer bond length of Mn-$N_{pyridine}$ in [**35**] as compared to Mn-$N_{bipyridine}$ indicates that the monodentate pyridine ligands are more labile than the bipyridine ligands in the solution phase,[21] which is supported by the mass spectral results that show characteristic signals corresponding to a loss of each py ligand (Section 4.3.5). In a comparison, in $[Mn_4O_6(bpea)_4]^{4+}$, Mn-N_{alkyl} is longer than Mn-$N_{pyridyl}$, which leads one to believe that the $N_{pyridyl}$ nitrogen atom is a stronger donor atom than N_{alkyl} nitrogen atom. This may be caused by the steric effect from methylene groups of the bpea ligand along with the electron-donating property from the *N*-ethyl substituent which causes Mn-N_{alkyl} to be a longer metal–ligand bond. This observation is considered as the main reason that $[Mn_4O_6(bpea)_4]^{4+}$ can undergo ligand substitution reactions as reported by our group previously and we think this newly discovered mixed-ligand complex type, [**35**] and [**36**] will undergo analogous substitution reactions. Furthermore, the mixed-ligand coordination environment features a labile monodentate ligand at each manganese center unlike the bpxa ligand, which is tridentate and blocks all of the terminal coordination sites. Substitution of various ligands at the pyridine site, which we assume will be facile, will be advantageous for various applications such as incorporating biologically relevant amino acids analogues of carboxylates, water molecules binding on the metal center of high valent tetramanganese clusters, even introducing strong O-atom transfer reagent in attempts to generate a manganyl species on a tetranuclear Mn adamantane motif to mimic the S_4 state of the OEC catalytic cycle.

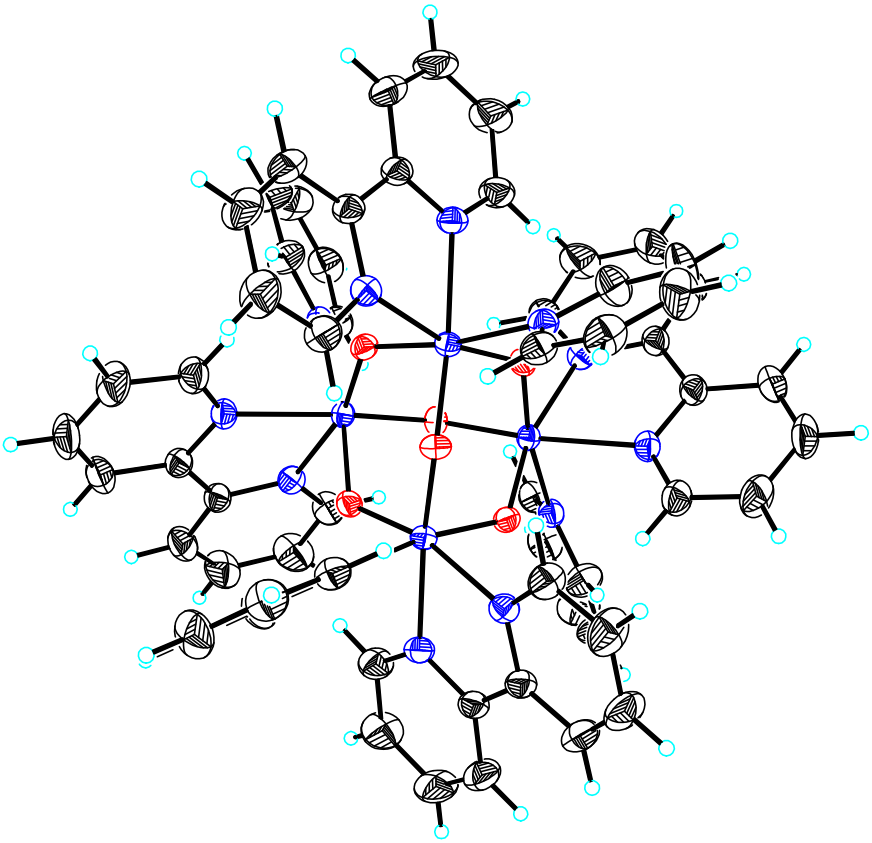

Figure 4.6. ORTEP diagram of $[Mn_4O_6(bpy)_4(py)_4]^{4+}$ [**36**].

4.3.5. **Mass Spectroscopy.** As described in Section 3.3.4, we frequently use mass spectrometry as a tool for assessing the relative purity of the reaction products in our studies. Electrospray ionization mss spectrometry (ESI-MS) data of complexes [**35**] and [**36**] are presented in this section. Positive ion ESI-MS spectra of complex [**35**] are shown in the following figures and the same observations were found for complex [**36**] as well (data were not shown). Assignments for the major signals in the mass spectra are consistent with fragmentation of the structures established by X-ray crystallography (data are summarized in Table 4.2). We also generated simulated mass spectra, showing the

isotope pattern of each major peak. The solid state structures can be fragmented in different ways in order to rationalize the observed peaks. The isotope fits support the formulations we provide for each peak in the mass spectrum. It is noteworthy that in the mass spectral results of [**35**], the monodentate pyridine ligands were observed to be relatively labile in the ESI-MS experimental conditions as shown in Fig. 8. The corresponding structural formulations are represented for the loss of each pyridine ligand from [**35**] at higher m/z signal region and isotope patterns of these assignments match very well as shown in Fig. 9.

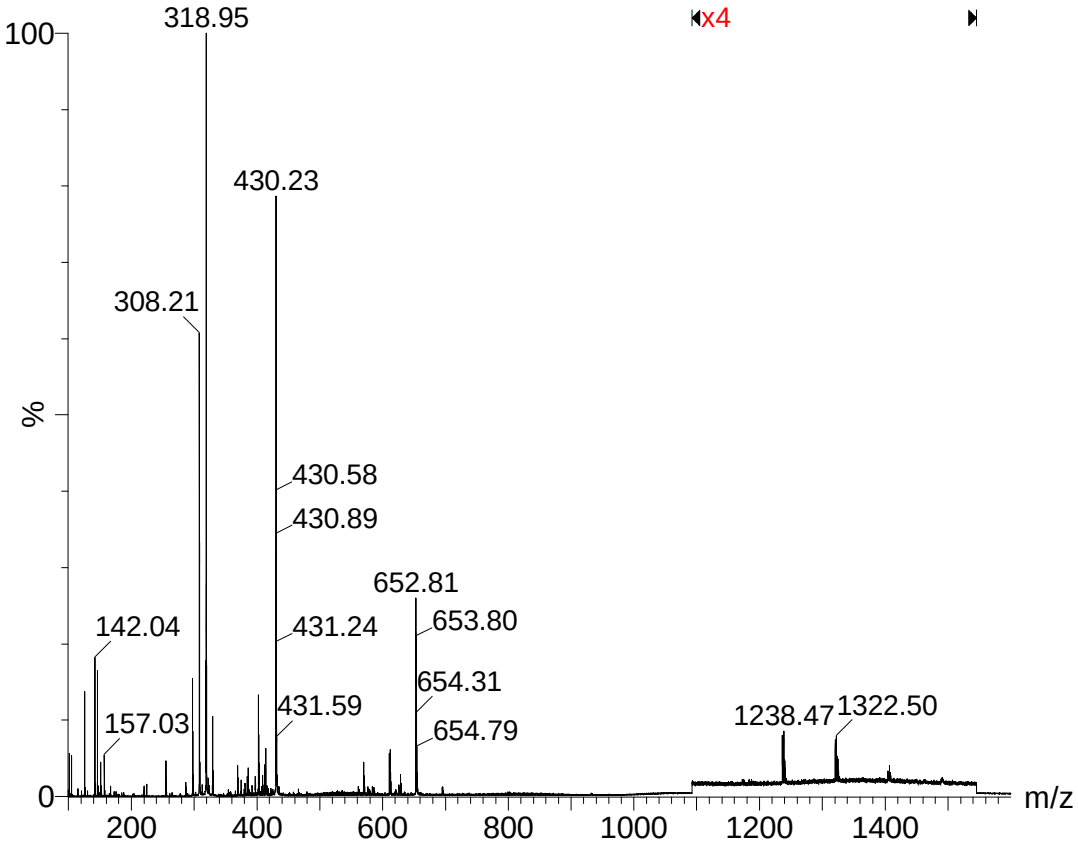

Figure 4.7. Positive ion electrospray ionization mass spectrum of [**35**] in acetonitrile.

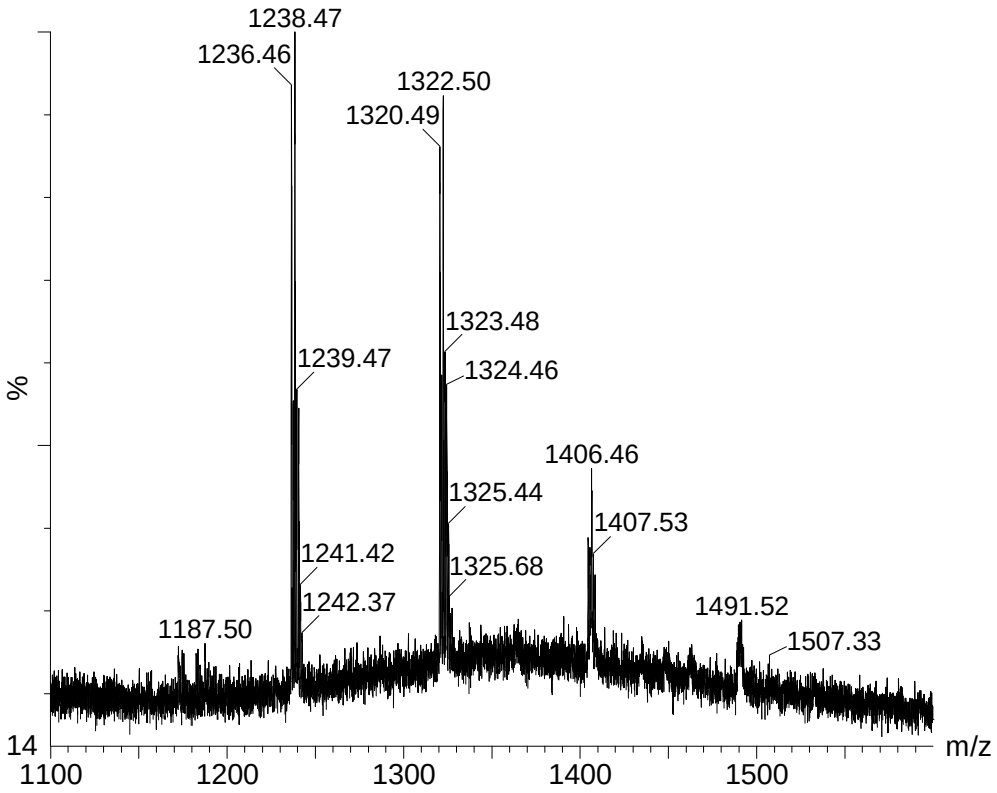

Figure 4.8. The expanded region between m/z 1100 and 1600.

Table 4.2. Summary of the observed positive mode ESI-MS spectral results of [**35**].

m/z	Corresponding structural formula	Charged species and isotope pattern for representative figure
1491.52	$\{[Mn_4O_6(bpy)_4(py\text{-}d_5)_3](ClO_4)_3\}^+$	+1 charge, $[M - ClO_4]^+$
1406.46	$\{[Mn_4O_6(bpy)_4(py\text{-}d_5)_2](ClO_4)_3\}^+$	+1 charge, Fig. 9
1322.50	$\{[Mn_4O_6(bpy)_4(py\text{-}d_5)](ClO_4)_3\}^+$	+1 charge, Fig. 9
1236.46	$\{[Mn_4O_6(bpy)_4](ClO_4)_3\}^+$	+1 charge, Fig. 9
652.81	$\{[Mn_4O_6(bpy)_4(py\text{-}d_5)_2](ClO_4)_2\}^{2+}$	+2 charge, $[M - 2ClO_4]^{2+}$, Fig. 10
430.23	$\{[Mn_4O_6(bpy)_4(py\text{-}d_5)_3](ClO_4)\}^{3+}$	+3 charge, $[M - 3ClO_4]^{3+}$, Fig. 10
318.95	$[Mn_4O_6(bpy)_4(py\text{-}d_5)_4]^{4+}$	+4 charge, $[M - 4ClO_4]^+$, Fig. 10
308.21	Unknown	+4 charge
157.03	$[bpy + H]^+$	$[Ligand + H]^+$

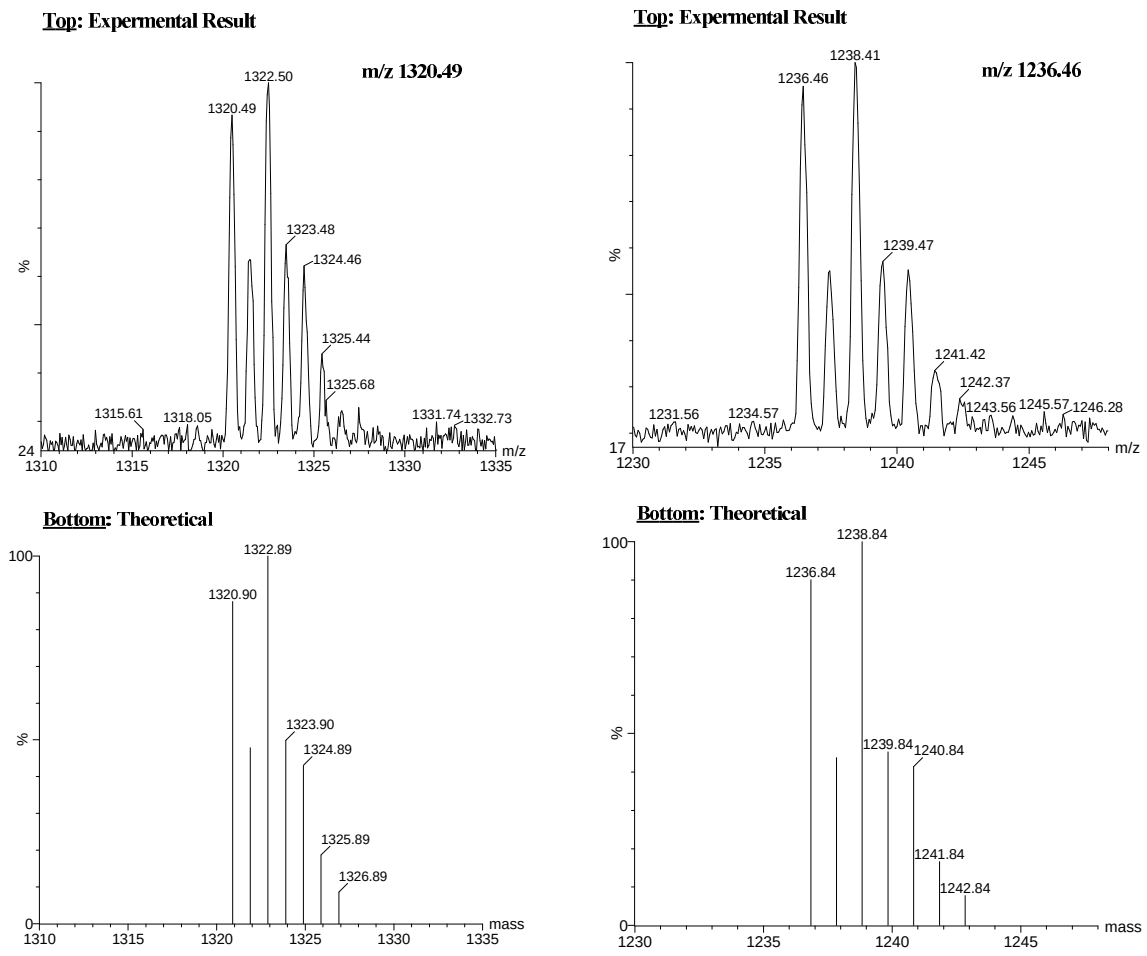

Figure 4.9. Isotope patterns for m/z 1320.49 and 1236.46 which corresponding to $\{[Mn_4O_6(bpy)_4(py\text{-}d_5)](ClO_4)_3\}^+$ and $\{[Mn_4O_6(bpy)_4](ClO_4)_3\}^+$.

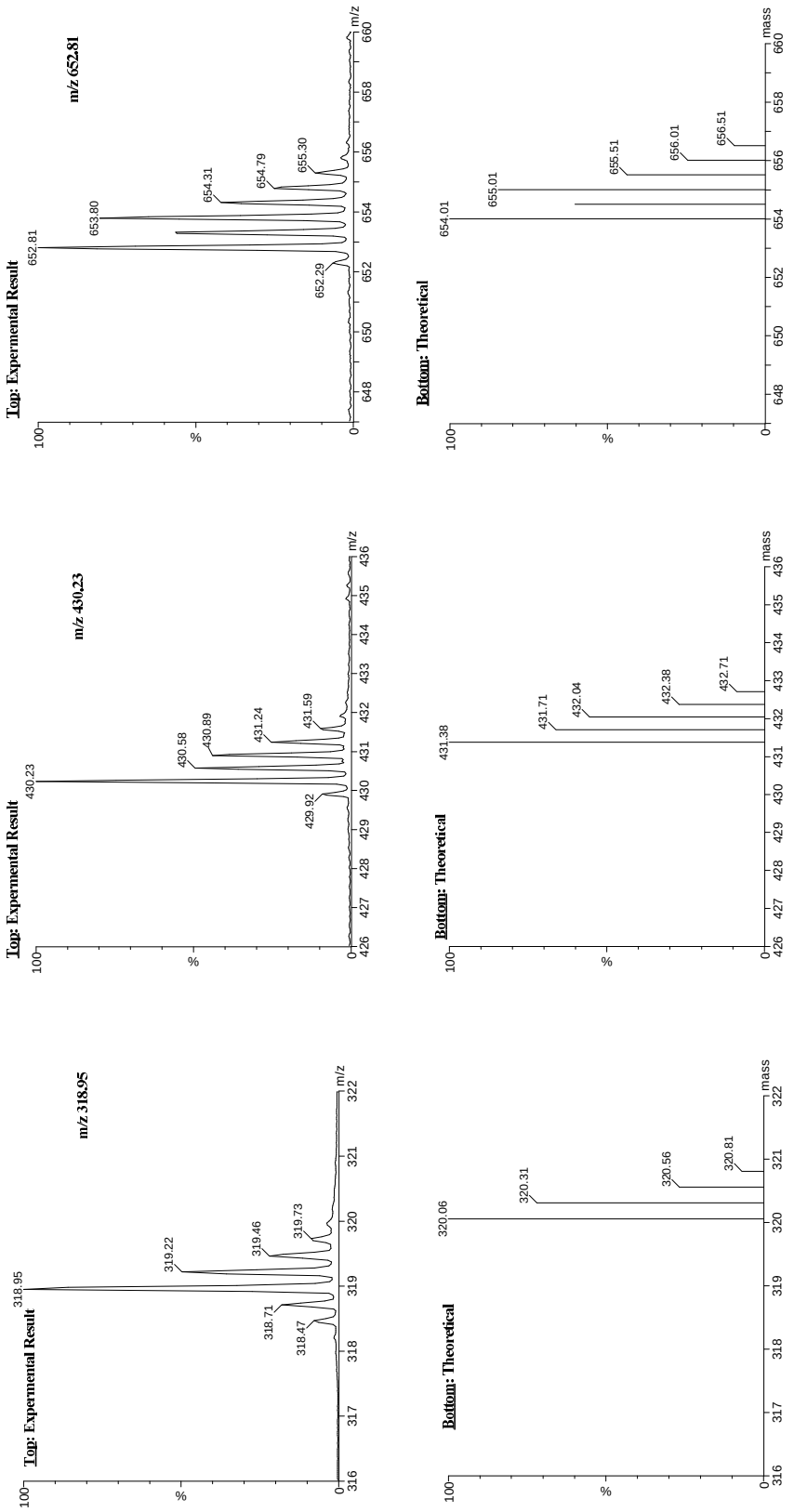

Figure 4.10. Isotope patterns for $[Mn_4O_6(bpy)_4(py\text{-}d_5)_4](ClO_4)_4$ [**35**], +2, +3, and +4 charged fragments.

4.3.6. **Electrochemistry study (Cyclic Voltammetry/CV, Differential Pulse Polarogram/DPP).** The electrochemical study of this high valent tetramanganese adamantane-shaped complex, $[Mn_4O_6(bpy)_4(py\text{-}d_5)_4]^{4+}$ [**35**], has revealed unique redox properties based on the experimental results shown in this section. We have utilized cyclic voltammetry and differential pulse polarography methods to illustrate the unusual redox behavior. The results obtained by using these two methods are described below.

Cyclic Voltammetry/CV. Electrochemical analysis of [**35**] by cyclic voltammetry is shown in Fig. 8. It reveals a quasi-reversible oxidation wave at *ca.* +0.6 V to +0.9 V, which is not well resolved in the initial scan. We assign this oxidation wave as the (IV,IV,IV,IV)→(IV,IV,IV,V) oxidation state change. The quasi-reversible redox couple was found having its potential for oxidation at $E_{½}$ = +0.82 V. This is comparable to other adamantane core type tetramanganese complexes which possess a similar quasi-reversible redox behavior.[8] The (IV,IV,IV,IV)/(IV,IV,IV,V) redox couples ($E_{½}$) for these reported complexes are $[Mn_4O_6(tacn)_4]^{4+}$ (0.978 V); $[Mn_4O_6(tach)_4]^{4+}$ (0.942 V); $[Mn_4O_6(bpea)_2(bz\text{-}ida)_2]$ (0.775 V); $[Mn_4O_6(bpea)_2(^t\text{Bu-ida})_2]$ (0.718 V); $[Mn_4O_6(bpea)_2(^c\text{penta-ida})_2]$ (0.641 V), where all of these potentials are referenced against Fc/Fc^+. Complex [**35**] differs from the others in that they all incorporate tridentate ligands coordinated to each manganese atom. We postulate that the redox potentials listed above are a function of the particular ligand set in each case. In [**35**], we believe that labile monodentate pyridines facilitate access to the higher oxidation states that are probably needed for these complexes to function as water oxidizers. The $\{Mn_4O_6\}^{4+}$ complexes that incorporate anionic iminocarboxylate (R-ida) ligands are found to have lower potential for oxidation as compared to the complexes with only

tridentate tacn or tach donors. We think that the negative charge contributed from carboxylates assist to stabilize the higher oxidation state of $Mn^{(V)}$. The cyclic voltammogram shown in Fig. 8 also reveals an irreversible reduction wave between +0.2 V to –0.4 V during the first scan. This wave corresponds to the (IV,IV,IV,IV)→(IV,IV,IV,III) oxidation state change. The reduction potential of the irreversible wave was estimated at *ca.* E_p = +0.05 V, which shows that complex [**35**] is relatively easy to reduce, comparable to $\{Mn_4O_6\}$ adamantane core complexes with tridentate ligand configurations mentioned above. For example, the (IV,IV,IV,IV)/(IV,IV,IV,III) reduction potentials for $[Mn_4O_6(bpea)_4]^{4+}$ and $[Mn_4O_6(bpea)_2(bz\text{-}ida)_2]$ are $E_{½}$ = –0.28 V and $E_{½}$ = –1.03 V, respectively. This comparison shows the special reducing character of [**35**], which indicates the idea of labile monodentate pyridines in the ligand configuration make the electron transfer access toward the Mn center easier for the CV electrochemical process. Based on the analysis of these CV results, we concluded that the ligand configuration of complexes plays the crucial role in affecting the redox properties intrinsically. The characteristic redox behaviors found in [**35**], which were influenced by the ligand configuration of monodentate pyridines, give an exquisite example.

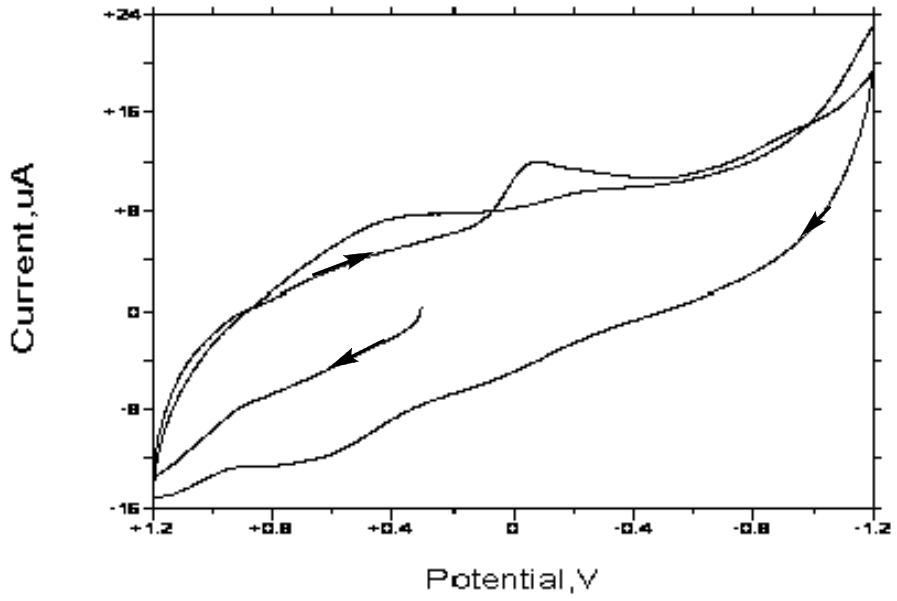

Figure 4.11. The cyclic voltammogram of $[Mn_4O_6(bpy)_4(py)_4]^{4+}$ [**35**].

Differential Pulse Polarogram/DPP. This method was carried out for the purpose of obtaining a complementary analysis to the CV studies. Below, the differential pulse voltammograms are shown separately for oxidation and reduction behavior. The results are presented as current response as function of applied voltage as the CVs, however in DPP measurements there is a slower scan rate (2 mV/sec) as compared to the scan rate (50 or 100 mV/sec) for CV experiments. The DPP results for [**35**] are shown in Figs. 9 and 10. The oxidative scan is shown in Fig. 9. The data reveal that there are at several current responses at the following potentials E_{ox1} = +0.48 V, E_{ox2} = +0.74 V, E_{ox3} = +0.96 V, E_{ox4} = +1.19 V. The most prominent peak is for E_{ox3}, which we believe corresponds to the poorly resolved CV wave mentioned above. We think that the smaller peaks for E_{ox1} and E_{ox2} may result from some reduction that occurs prior to the beginning of the scan, which starts at +0.24 V. The higher potential E_{ox4} is proposed to be associated with a

species that is created after the E_{ox3} process takes place, perhaps due to an unstable $Mn^{(V)}$ center. Further experimentation is underway to test this hypothesis.

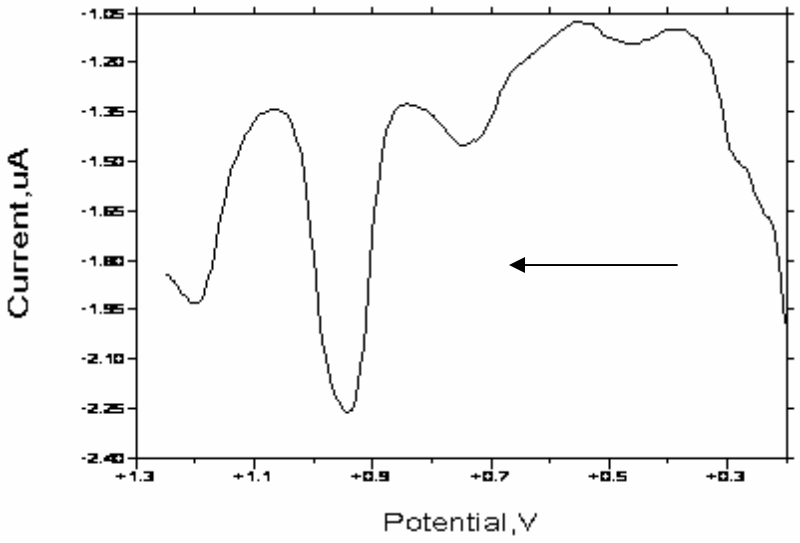

Figure 4.12. Differential pulse polarogram for $[Mn_4O_6(bpy)_4(py\text{-}d_5)_4]^{4+}$ [**35**] in the oxidation scan mode. Scan rate: 2mV/sec.

For the reduction scan as shown in Fig. 10, there are four reduction potentials with notable current signals as well. E_{re1} = +0.09 V corresponds to the irreversible reduction wave shown in the CV result. We speculated that the peaks at E_{re2} = –0.87 V, E_{re3} = –1.16 V, and E_{re3} = –1.48 V correspond either to successive reduction processes, including (IV,IV,IV,III)→(IV,III,III,III), (IV,III,III,III)→(III,III,III,III) and (III,III,III,III)→-(III,III,III,II), or to species that are chemically produced subsequent to the initial reduction. In sum, the DPP measurements provided an excellent way to bring out the redox waves that are poorly resolved and even difficult to observe at all by using cyclic voltammetry analysis.

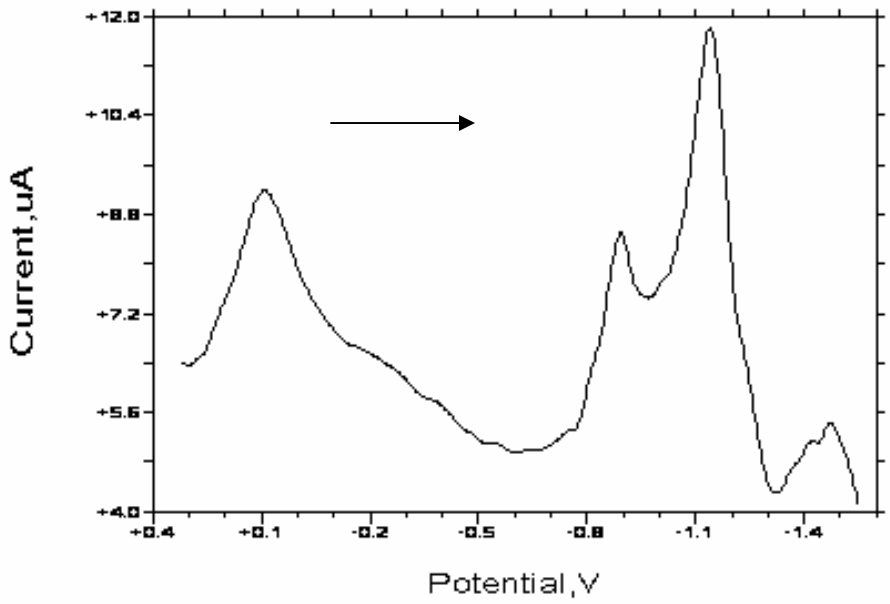

Figure 4.13. Differential pulse polarogram of $[Mn_4O_6(bpy)_4(py\text{-}d_5)_4]^{4+}$ [**35**] in the reduction scan mode. Scan rate: 2mV/sec.

4.4. Conclusion

We suggest that $[Mn_4O_6(bpy)_4(py)_4]^{4+}$ will be an interesting starting point for the material science applications. We envision it being used for the synthesis of framework structures where adamantane cluster would be linked together after a bridging ligand displaces the labile monodentate py ligand. As for the PSII OEC structural modeling, since determination of the actual active site structural arrangement of the tetranuclear manganese complex is still an ongoing project, one should not exclude the possibility of any type of aggregate being involved during the catalytic water oxidation, especially at the S_4 state. Occasionally structural transformations can be interpreted in the sense of functional properties, which provides certain insightful looks at the structural modeling given that the actual biological system is related. Although the EXAFS analysis for the

active site of PSII suggests that highly symmetric adamantane- or cubane-shaped Mn-oxo cores are likely not accurate structural models for the OEC in S_0, S_1, S_2 states, we speculate that core rearrangement upon further S state advancement, under some conditions, to S_3 and S_4, may produce a structure more akin to the adamantane-type structure and the discovery of complex [**35**] indicates that such speculation should be taken into serious consideration when studying the O_2 evolution mechanism of the PSII water oxidase. Furthermore, with this new ligands arrangement, the undesired ligand oxidation found by Dubé for bpxa type of ligand with their alkyl amine in $\{Mn_4O_6\}$ core type of adamantane complexes and which were observed leading to the formation of impurities can be avoided due to the aromaticity of pyridine and bipyridine ligands. The aromatic ring character makes the ligands resistant to oxidation as compared to the bpxa type of ligand. Possible carboxylate ligand exchange reactions where pyridine ligands would be replaced by various numbers of carboxylate anions ($RCOO^-$), will undoubtedly supply a new host of interesting mixed-ligand products for further investigation.

4.5. Acknowledgement

Mr. Marek Domin, Dr. John Boylan, Dr. Richard J. Staples for their assistance with Mass Spectroscopy, NMR and X-ray crystallography training. We also thank Dr. Peter Müller (MIT) and Dr. Jianfeng Jiang (Harvard University) for the pivotal role they played in solving crystal structures. We are grateful for Dr. Ralph Weber (Brüker Bio-Spin EPR, Billerica, MA) for his great guidance for EPR measurements.

4.6. References

1. Mukhopadhyay, S.; Mandal, S. K.; Bhaduri, S.; Armstrong W. H. *Chem. Rev.* **2004**, *104(9)*, 3981-4026.
2. Debus, R. J. *Biochim. Biophys. Acta* **2001**, *1503*, 164-186 and references therein.
3. McEvoy, J. P.; Brudvig, G. W. *Chem. Rev.* **2006**, *106(11)*, 4455-4483.
4. (a) Limburg, J.; Vrettos, J. S.; Liable-Sands, L. M.; Rheingold, A. L.; Crabtree, R. H.; Brudvig, G, W. *Science* **1999**, *Vol. 283*, 1524-1527.

   (b) Wieghardt, K.; Bossek, U.; Gebert, W. *Angew. Chem., Int. Ed. Engl.* **1983**, *22*, 328-329.

   (c) Wieghardt, K.; Bossek, U.; Nuber, B.; Weiss, J.; Bonvoisin, J.; Corbella, M.; Vitols, S. E.; Girerd, J.-J. *J. Am. Chem. Soc.* **1988**, *110*, 7398-7411.

   (d) Hagen, K. S.; Westmoreland, T. D.; Scott, M. J.; Armstrong, W. H. *J. Am. Chem. Soc.* **1989**, *111*, 1907-1909.
5. Abbreviations used: bpma = *N*,*N*-bis(2-pyridylmethyl)methylamine; bpea = *N*,*N*-bis(2-pyridylmethyl)ethylamine; bpta = *N*,*N*-bis(2-pyridylmethyl)*tert*-butylamine.
6. Pal, S.; Chan, M. K.; Armstrong, W. H. *J. Am. Chem. Soc.* **1992**, *114*, 6398-6404.
7. Cooper, S. R.; Calvin, M. *J. Am. Chem. Soc.* **1977**, *99*, 6623-6630.
8. Dubé, C. E.; Mukhopadhyay, S.; Bonitatebus, P. J., Jr.; Staples, R. J.; Armstrong, W. H. *Inorg. Chem.* **2005**, *44*, 5161-5175.
9. Bryan, P. S.; Dabrowick, J. C. *Inorg. Chem.* **1975**, *14*, 296-299.
10. Dubé, C. E.; Wright, D. W.; Pal, S.; Bonitatebus, P. J. Jr.; Armstrong, W. H. *J. Am. Chem. Soc.* **1998**, *120*, 3504-3516.
11. Wright, D. W.; Mok, H. J.; Dubé, C. E.; Armstrong, W. H. *Inorg. Chem.* **1998**, *35*, 3514-3518.

12. Nyholm, R. S.; Turco, A. *Chem. Ind.* **1960**, 74.

13. Cooper, S.; Calvin, M. *J. Am. Chem. Soc.* **1977**, *99(20)*, 6623-6630.

14. Mukhopadhay, S.; Armstrong, W. H. *J. Am. Chem. Soc.* **2003**, *125*, 13010-13011.

15. Swarnabala, G.; Rajasekharan, M. V. *Proc. Indian Acad. Sci. (Chem. Sci.)* **1990**, *102(2)*, 87-98.

16. (a) Mascharak, P. K.; Papaefthymiou, G. C.; Frankel, R. B.; Holm, R. H. *J. Am. Chem. Soc.* **1981**, *103*, 6110-6116.

    (b) Cambray, J.; Lane, R. W.; Wedd, A. G.; Johnson, R. W.; Holm, R. H. *Inorg. Chem.* **1977**, *16*, 2565-2571.

17. Philouze, C.; Bolondin, G.; Girerd, J.-J.; Guilhem, J.; Pascard, C.; Lexa, D. *J. Am. Chem. Soc.* **1994**, *116*, 8557-8565.

18. The paramagnetic isotropic shifts are: –25 ppm, –23 ppm –4 ppm, +58 ppm and +62 ppm; the diamagnetic isotropic shits are: +9 ppm, +8 ppm and + 6 ppm.

19. (a) Dubé, C. E. *Ph. D dissertation*, **1998**, Boston College.

    (b) Wieghardt, K.; Bossek, U.; Gebert, W. *Angew. Chem. Int. Ed. Engl.* **1983**, *22(4)*, 328-329.

20. Mukhopadhyay, S.; Mok, H. J.; Staples, R. J.; Armstrong, W. H. *J. Am. Chem. Soc.* **2004**, *126*, 9202-9204.

21. The chelate effect from the bidentate bipyridine ligands is also expected to make the bpy ligands much less labile.

Appendix A

Size Exclusion/Gel Permeation Chromatography (SEC/GPC) Applied to the Separation of Manganese Cluster Complexes

A.1. Introduction

A variety of problems are encountered when carrying out the synthesis of manganese-oxo complexes. For instance, purification by recrystallization is not always successful because in a number of cases the solubilities of the desired compound and impurities are very similar. We sought an alternative method and were successful on an analytical scale using chromatographic methods. This was not a trivial exercise because procedures had not been developed for this type of complex and therefore a new set of parameters had to be established.

Among the various available chromatographic separation methods, high-performance liquid chromatography (HPLC) has been extensively applied to organic and biochemical-related compounds extensively. Other methods such as gas chromatography (GC), thin-layer chromatography (TLC), classical gravity feed column chromatography (CCC)[1] will not be discussed here. Most HPLC separations today are performed using reversed-phase columns. In reversed-phase chromatography (RPC), the separation (retention time difference) is determined by interactions between the bonded phase, sample molecules, the mobile phase and the other chromatographic parameters such as elution solvent flow rate.[2] Standard reversed-phase chromatographic separation methods proved not to be suitable separation techniques for our synthetic products primarily owing to the charge-balanced anions residing in our complexes. These negative charge counterions usually coordinate loosely to the manganese center complexes and when applying standard

reversed-phase chromatography, the stationary phase of RPC would possibly interact with the ionic bonded counterions. This may result in changes of manganese ion center oxidation state and could lead to a possible structural rearrangement, or even clusters degradation. To avoid these issues, we successfully utilized size exclusion chromatography (SEC) for separations and thus were able to assess purity, which is difficult using methods such as NMR spectroscopy. In SEC (also know as molecular exclusion chromatography, gel filtration, or gel permeation chromatography), molecules are separated in accordance with their sizes, which are roughly proportional to molecular weights.[3] Therefore, the renowned nature of this method is a great advantage for our complexes because the analytes in SEC are principally determined by the physical interaction between the compounds and packing pores of the chromatography column,[4] and there is no chemical reaction that could occur using RPC. Here we illustrate the results for HPLC analysis by using an SEC column in examining a group of synthetic complexes within our research projects which were encountered as was described in Chapter 2 – 4. The chromatographic results are shown below in UV-vis absorbance signal *vs*. retention time.

A.2. Experimental Section

A.2.1. Materials. Acetonitrile used for spectroscopic studies was distilled over CaH_2 under nitrogen and stored over 3 Å molecular sieves prior to use. The solvents used for HPLC mobile phases were LC/MS grade such as acetonitrile and methanol. All other reagents were purchased from commercial sources and used as received and all chemicals used in this work were reagent grade.

A.2.2. Specification of GPC/SEC Column. Size-Exclusion Column consists of the styrene-divinylbenzene copolymer (SDVB) shown in Figure 1 as the packing material. The representative chemical structure diagram shown below was adapted from Sigma-Aldrich catalog. The column that we used for the chromatography measurements is a 5 µm narrow bore (NB) PHENOGEL™ GPC/SEC column with 50 Å pore size. The corresponding molecular range for this analytical column is between 100 – 3000 g/mole.

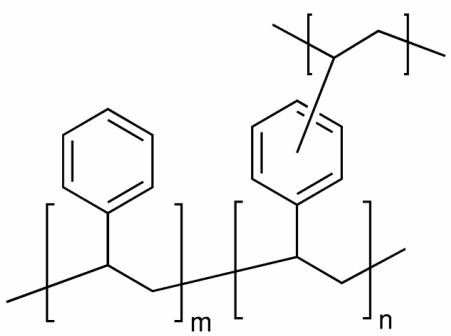

Figure A1. Styrene-divinylbenzene copolymer.

A.3. Results and discussion

The following diagrams are all represented in the same time scale between 0.01 – 100 min. The chromatographic results are shown on a scale of absorbance for the UV detector *vs.* retention time in minutes.

(a) We first measured the 2,2'-bipyridine ligand that we utilized for many synthetic complexes in order to attain a reasonable time range for further analytical applications. The resulting chromatogram is shown in Fig. 2. We observed a peak with a retention time of 25.77 min.

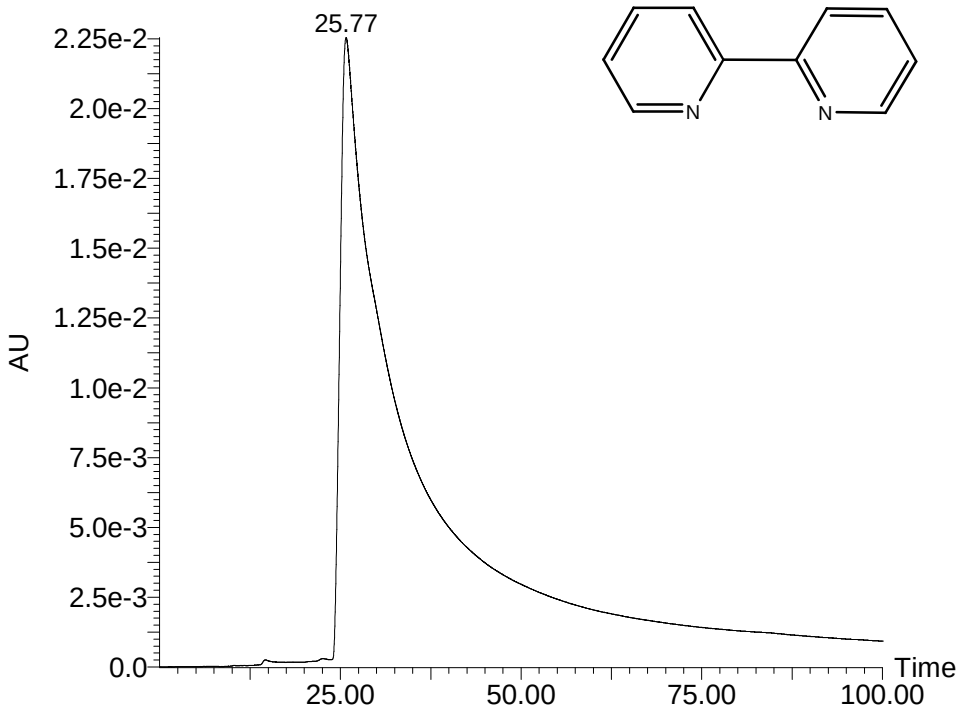

Figure A2. SEC/GPC Chromatogram of 2,2'-bipyridine shown as a plot of absorbance *vs.* retention time (0.01 – 100 min)

(b) The second sample that we tested was the complex, $[Mn_4(\mu\text{-}O_6)(bpy)_4(py)_4](ClO_4)_4$ [**38**], which is shown in Fig. 3. Based on the retention time observed for the 2,2'-bipyridine case described above, we assigned the peak at 35.65 min as pyridine. Complex [**38**] was eluted from the column first with a retention time of 8.89 min., the peak for which is indicated by the red asterisk in Fig. 3 below.

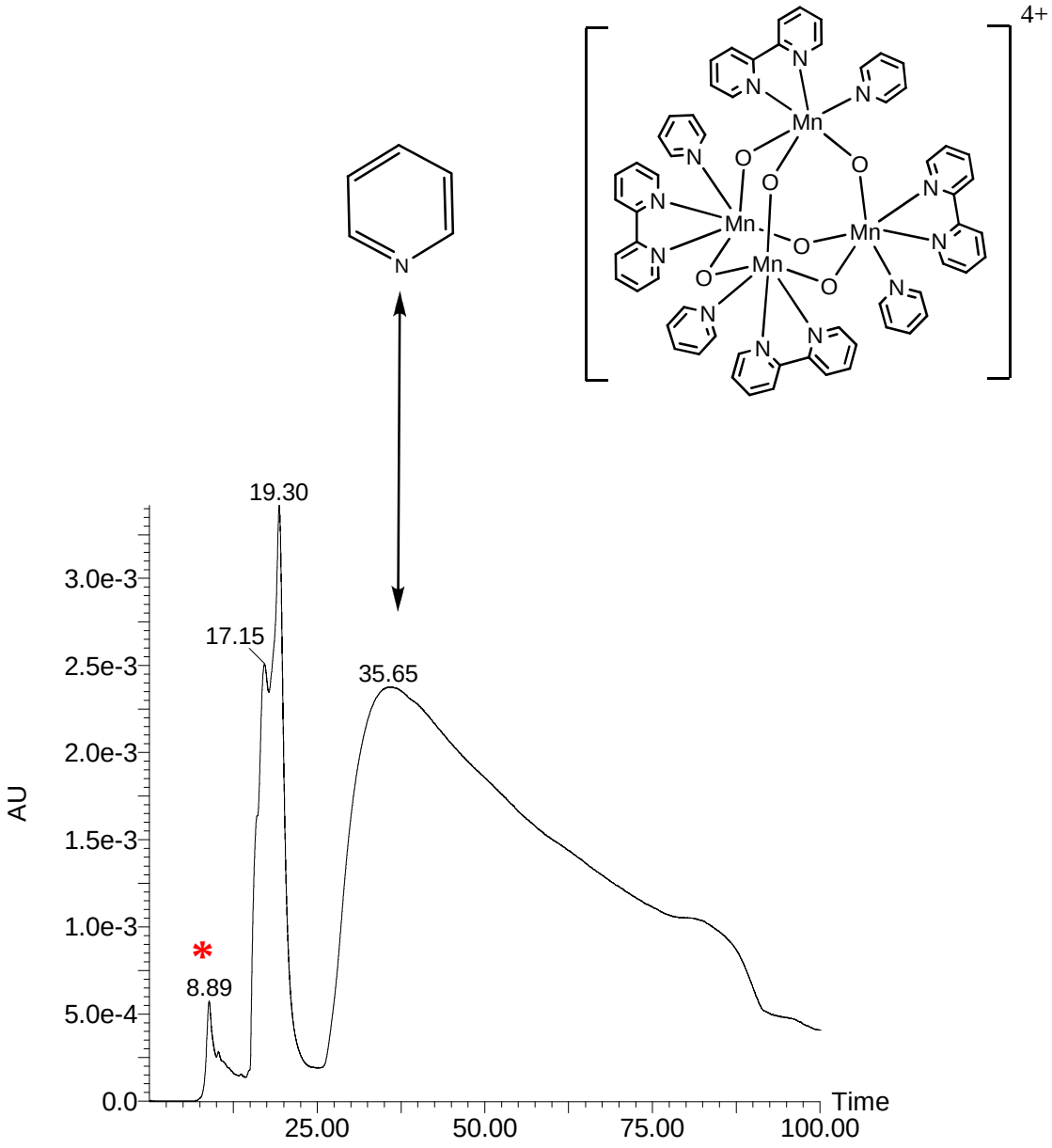

Figure A3. SEC/GPC Chromatogram of $[Mn_4(\mu\text{-}O_6)(bpy)_4(py)_4](ClO_4)_4$ [**38**] shown in scale of absorbance *vs.* retention time (0.01 – 100 min)

(c) The original impetus to use this chromatography technique was to solve a difficult purification problem that we encountered during the synthetic preparation of Mn^{III}(*N*-Et-3-NO_2-Sal)$_2$Cl [**14**], which was utilized for the manganyl intermediate formation kinetic study. As described in Chapter 2, we found that reactions products MnL_2Cl [**14**] and

Mn^{III}(*N*-Et-3-NO_2-Sal)$_3$ (MnL_3) [**14a**] was cocrystallized. So the SEC/GPC HPLC method seemed very promising for the purpose of separating this type of cocrystallized material. We have tried two sets of this type of mixture of complexes and both showed intriguing separation results. The first one we examined was [**14**] and [**14a**], the result for which is illustrated in Fig. 4. Another mixture we investigated was Mn^{III}(*N*-Et-3-NO_2-Sal)$_2$(OAc)(MeOH) and Mn^{III}(*N*-Et-3-NO_2-Sal)$_3$, the results for which is shown in Fig. 5. Tentatively, we have assigned the MnL_3 complex was separated at t = 13.14 and 13.24 min. We also assign the peaks at t =14.70 and 15.02 min as MnL_2Cl and MnL_2(OAc)(MeOH) species, respectively.

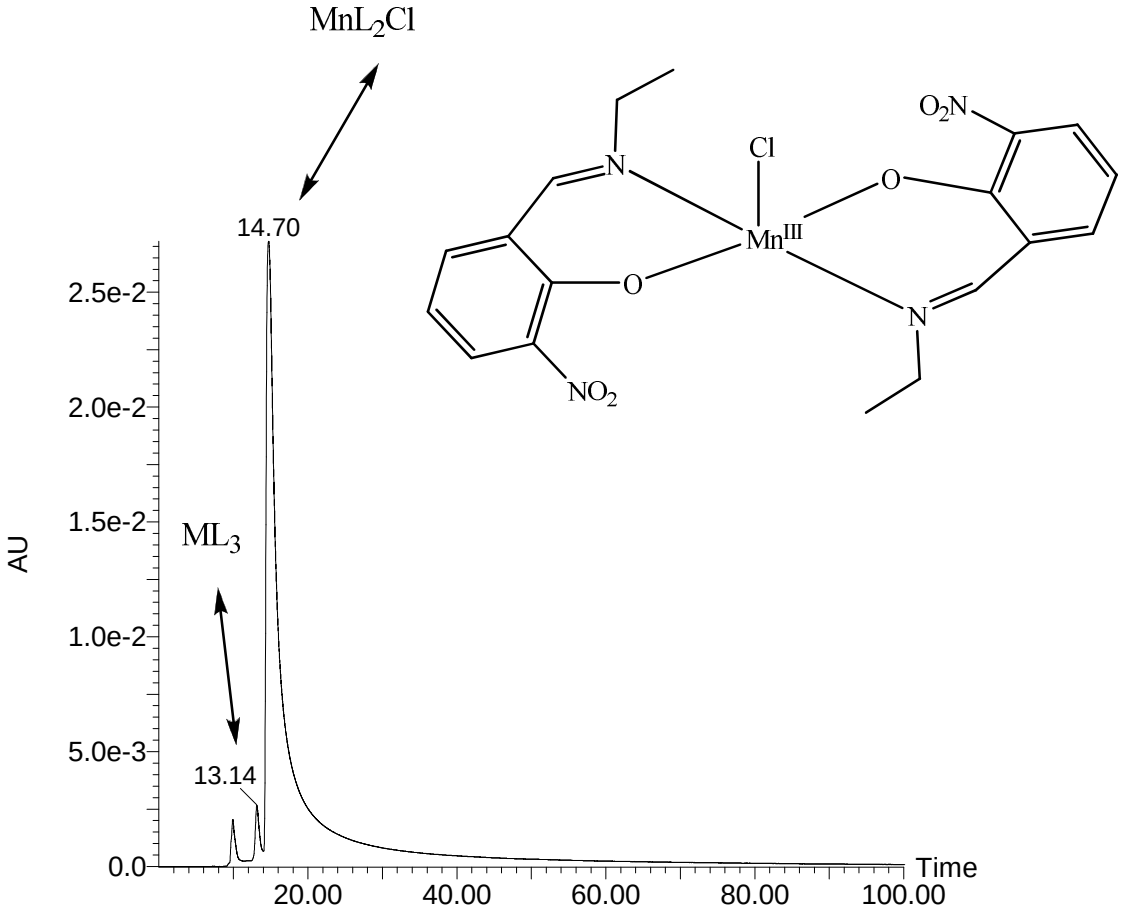

Figure A4. SEC/GPC Chromatogram of Mn^{III}(*N*-Et-3-NO_2-Sal)$_2$Cl [**14**] and Mn^{III}(*N*-Et-3-NO_2-Sal)$_3$ [**14a**] shown in scale of absorbance *vs.* retention time (0.01 – 100 min)

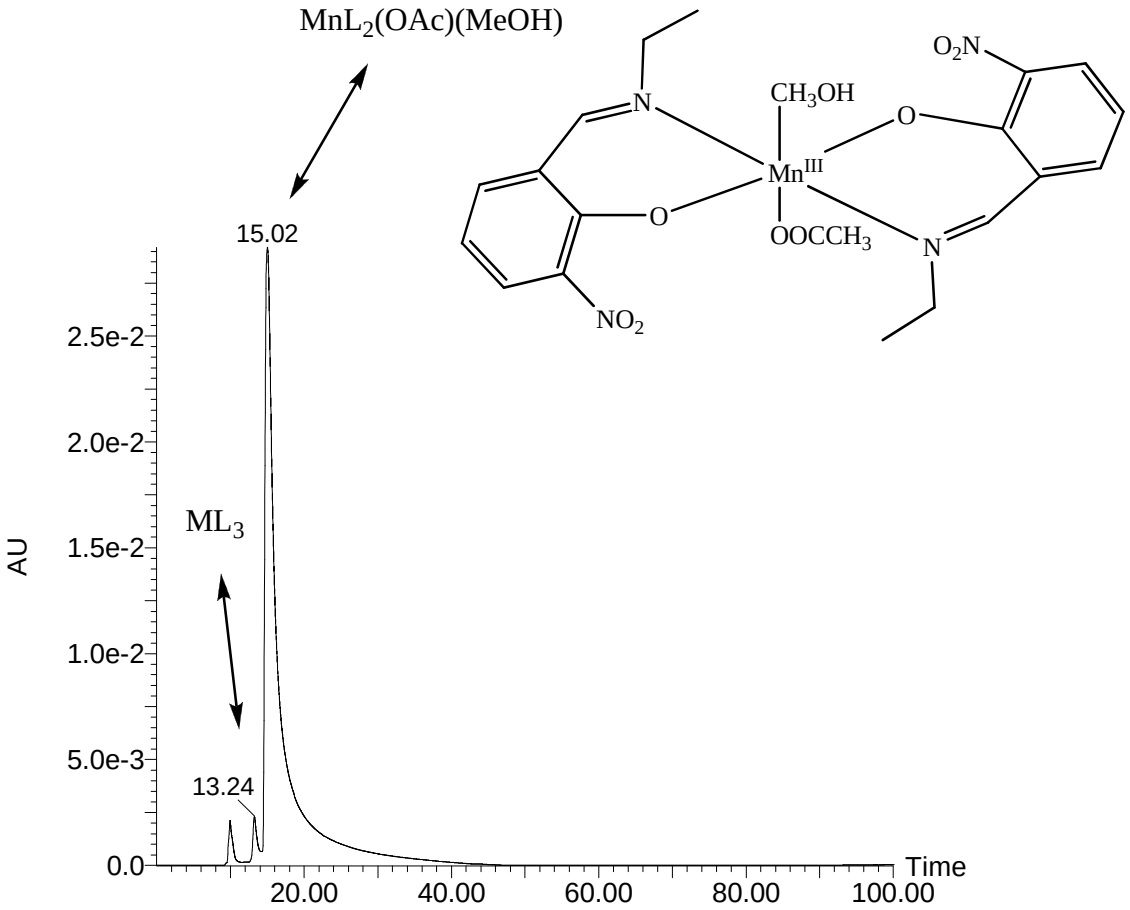

Figure A5. SEC/GPC Chromatogram of Mn^{III}(*N*-Et-3-NO_2-Sal)$_2$(OAc)(MeOH) and Mn^{III}(*N*-Et-3-NO_2-Sal)$_3$ shown in scale of absorbance *vs.* retention time (0.01 – 100 min)

We believe that the order of elution can be predicted based on molecular weights in this chromatographic analysis. We found this method provides a promising sample purification technique for the further work. Improved purification will likely make our task of complex crystallization less daunting. Thus structural elucidation should come more readily.

Conclusion. Our studies have shown that inorganic cluster mixtures can be separated readily by GPC/SEC chromatography. The major factor which affects the separation using this technique is the molecular size and it is important that the stationary phase does not cause decomposition of our complexes. Therefore, in our opinion, for the

inorganic complexes that we study, this technique will be of great assistance for the purpose of purification of complex reaction product mixtures.

A.4. Acknowledgement

We are greatly indebted to Mr. Marek Domin for the pivotal role that he has, especially in running all the chromatography experiments. His great guidance for the HPLC techniques, chromatography theories and special column selections become a valuable asset for me in the future and myself, personally. I am in an extreme appreciation for him with respect to all the scientific knowledge that he passes out.

A.5. References

1. Willeford, P. R.; Veening, H. *Journal of Chromatogr., Chromatogr. Rev.* **1982**, *251*, 61-88.
2. Majors, R. E.; LC, *Liq. Chromatogr. HPLC Mag.*, **1985**, *Vol. 3*, p.774.
3. Wu, C.-S. *Handbook of Size Exclusion Chromatography, Chromatographic Science Series*, **1995**, *Vol. 69*, pp. 1-453.
4. Phenomenex, Inc. *A User's Guide to Gel Permeation Chromatography*, **July, 2000**, technical note 3.

Appendix B

Library of ^{1}H NMR Spectroscopic Data

B.1. ^{1}H NMR Spectra.

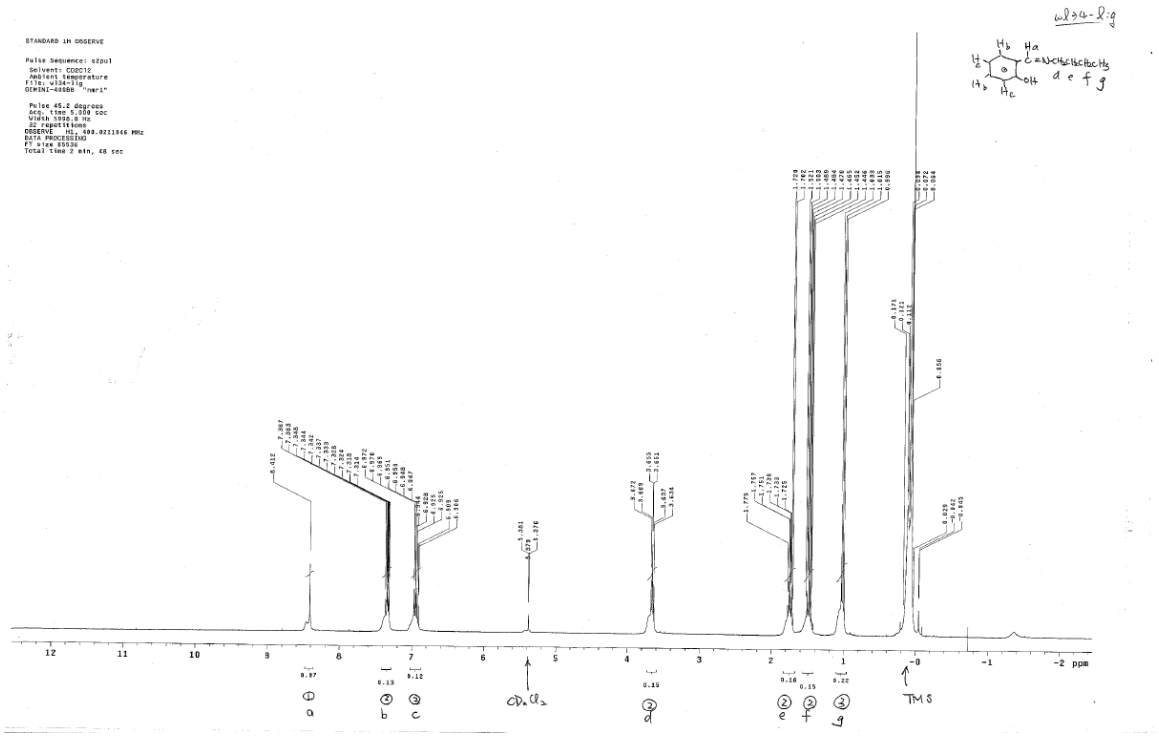

Figure B1. The ^{1}H NMR spectrum of *N*-*n*-butyl-salicylideneamine ligand.

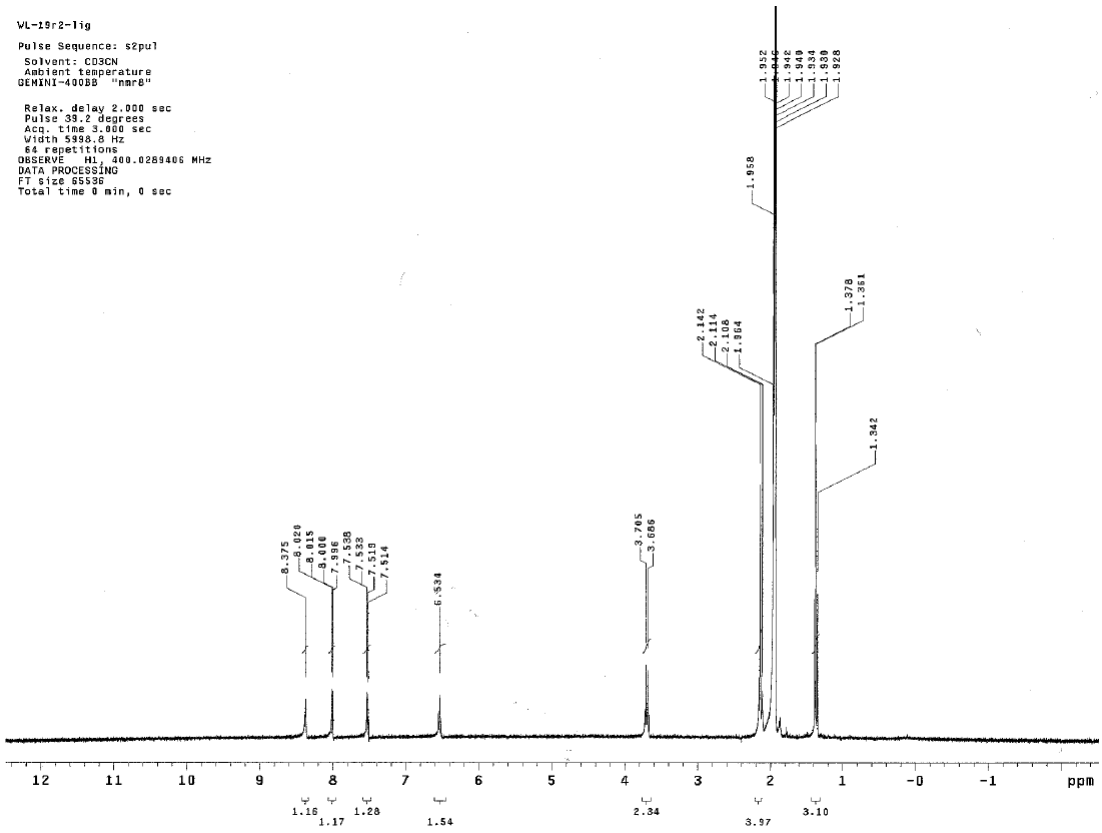

Figure B.2. The ^{1}H NMR spectrum of *N*-ethyl-3-nitro-salicylideneamine ligand.

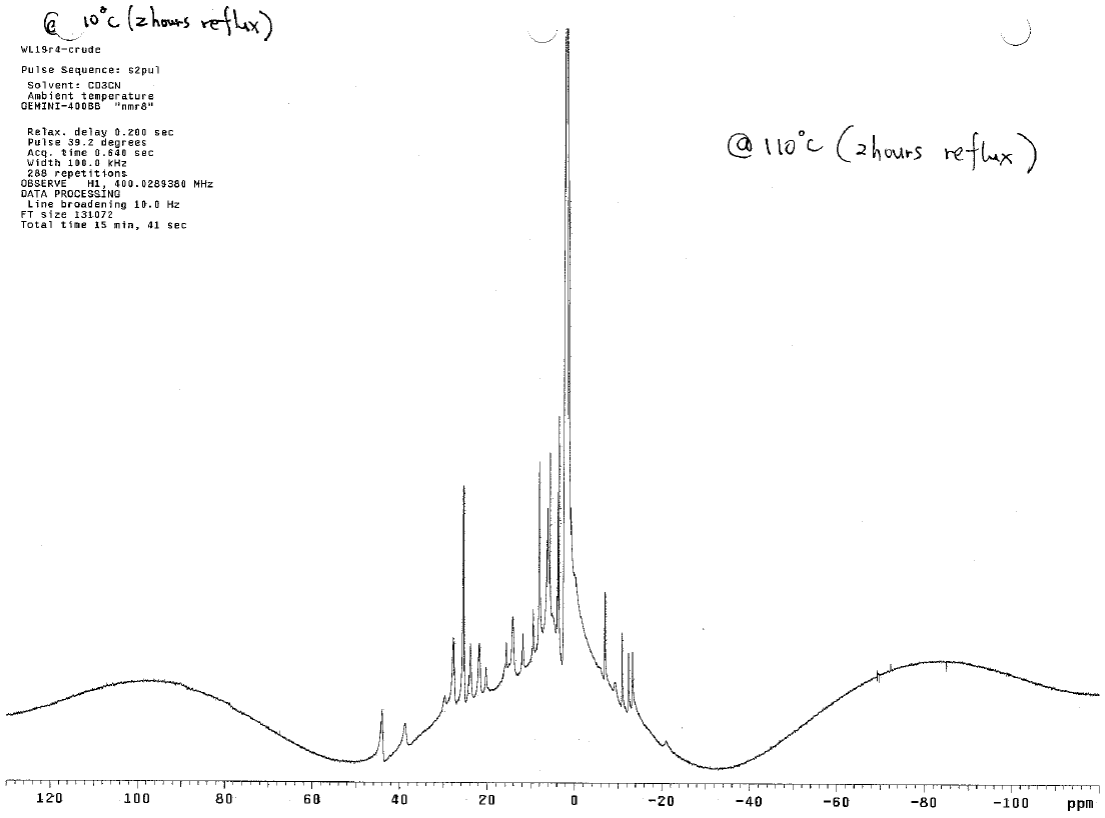

Figure B3. The ^{1}H NMR spectrum of the unknown product for the reaction discussed in Chapter 2, page 35, [1 $Mn(acac)_3$: 2 L, refluxed at 110 °C for 2 h, where L = *N*-ethyl-3-nitro-salicylideneamine].

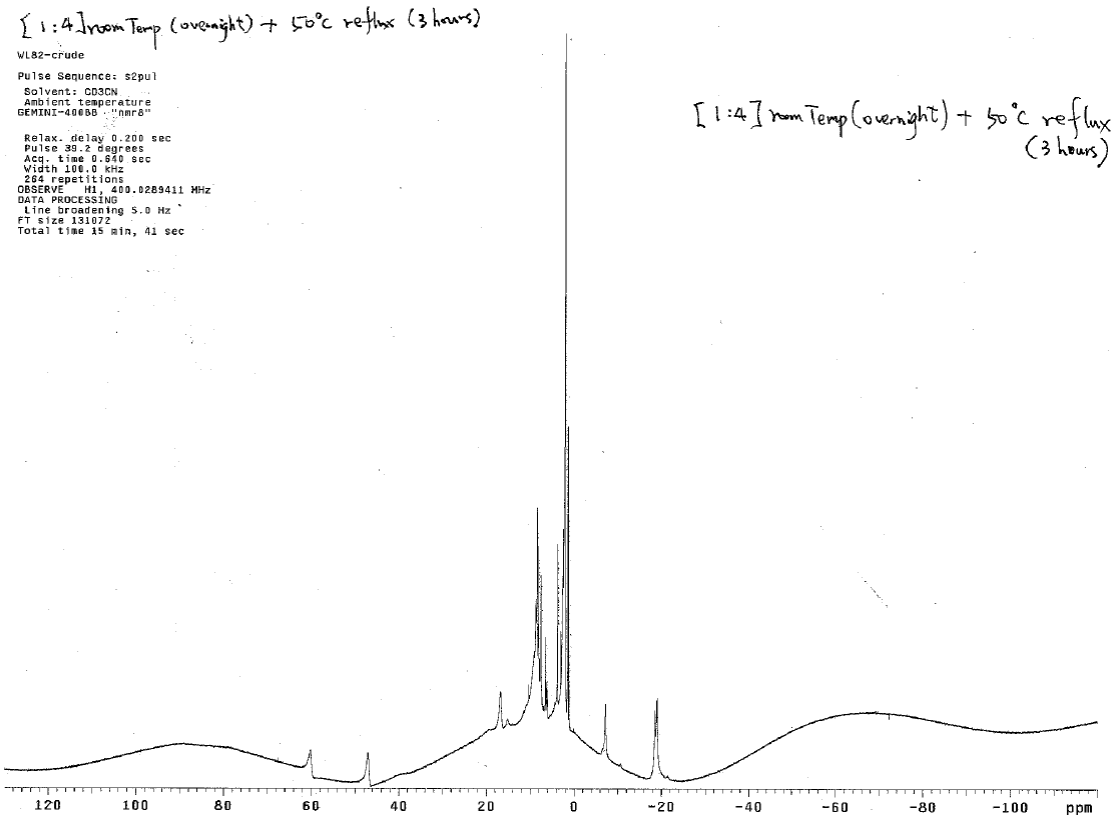

Figure B4. The ^{1}H NMR spectrum of the unknown product for the reaction discussed in Chapter 2, page 35, [1 $Mn(OAc)_3 \cdot 2H_2O$: 4 L, overnight stirring at room temperature and then heating at 50 °C for 3 h, where L = *N*-ethyl-3-nitro-salicylideneamine].

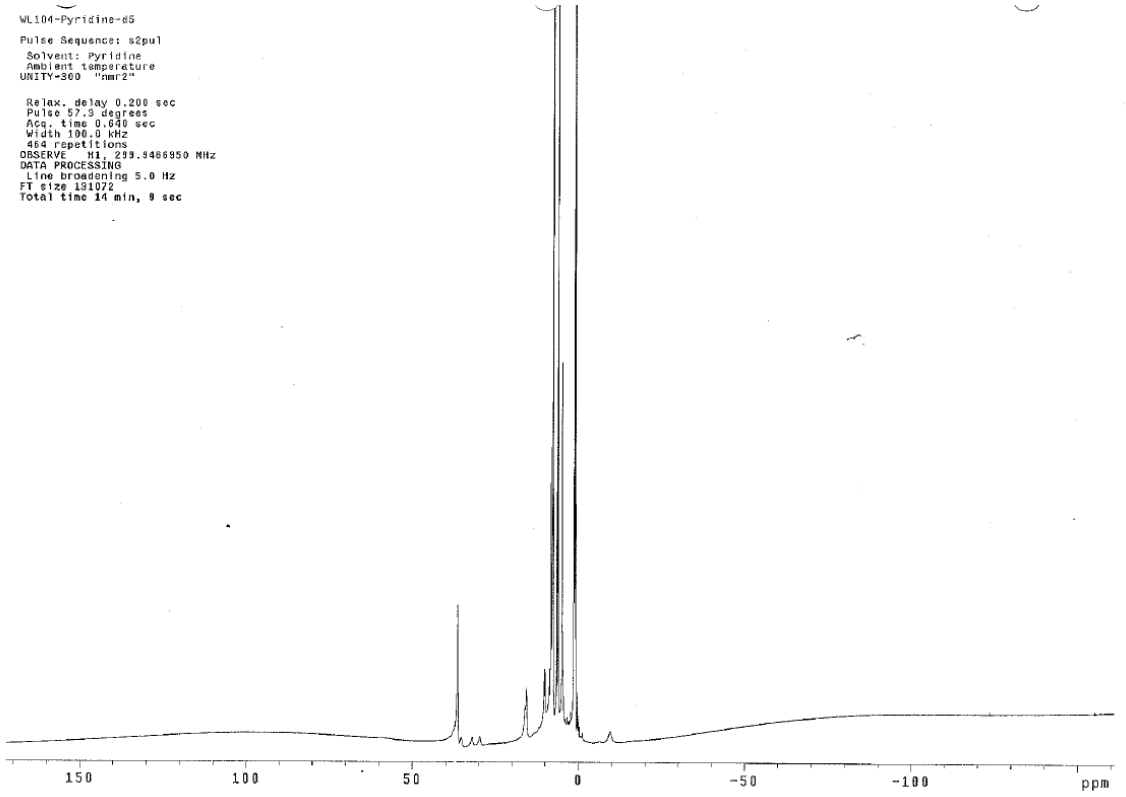

Figure B5. The ^{1}H NMR spectrum of the speculated product $[Mn_2O_2(dmb)_3(py\text{-}d_5)_2](ClO_4)_3$, which was discussed in Chapter 4, page 139. Measurement was taken immediately after dissolved the material in pyridine-d_5 solution.

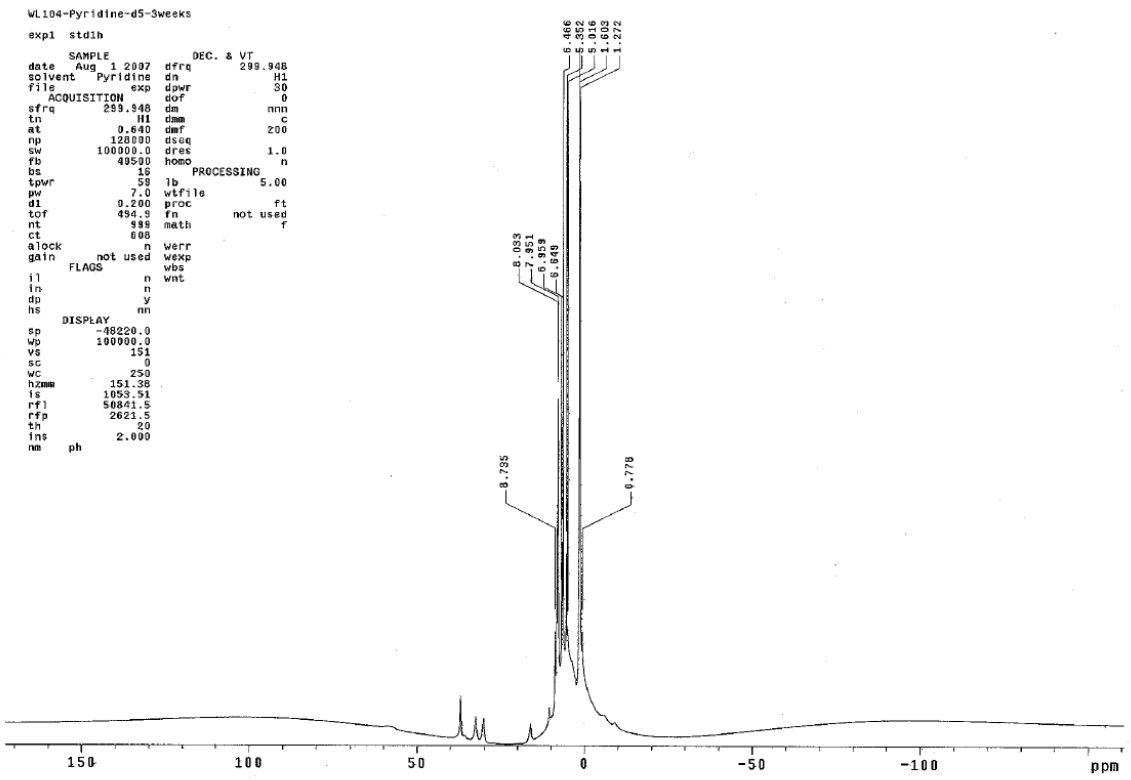

Figure B6. The ^{1}H NMR spectrum of the speculated product $[Mn_2O_2(dmb)_3(py\text{-}d_5)_2](ClO_4)_3$, which was discussed in Chapter 4, page 139. Measurement was taken 3 weeks later after Fig. B5, the pyridine-d_5 solution was left undisturbed.

Appendix C

EPR Spectroscopic Data for Compounds $Mn_2O_2(bpy)_4$ and Mn3

C.1. Dimanganese Complexes.

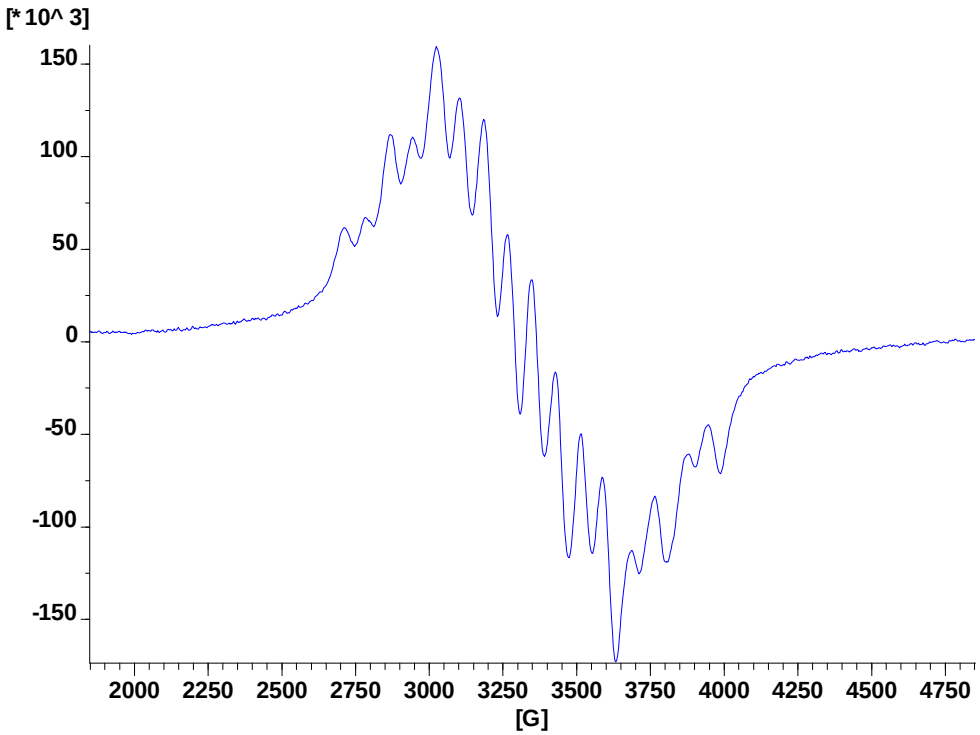

Figure C1. $[Mn_2O_2(bpy)_4](ClO_4)_3$ – crude product in acetonitrile solution.

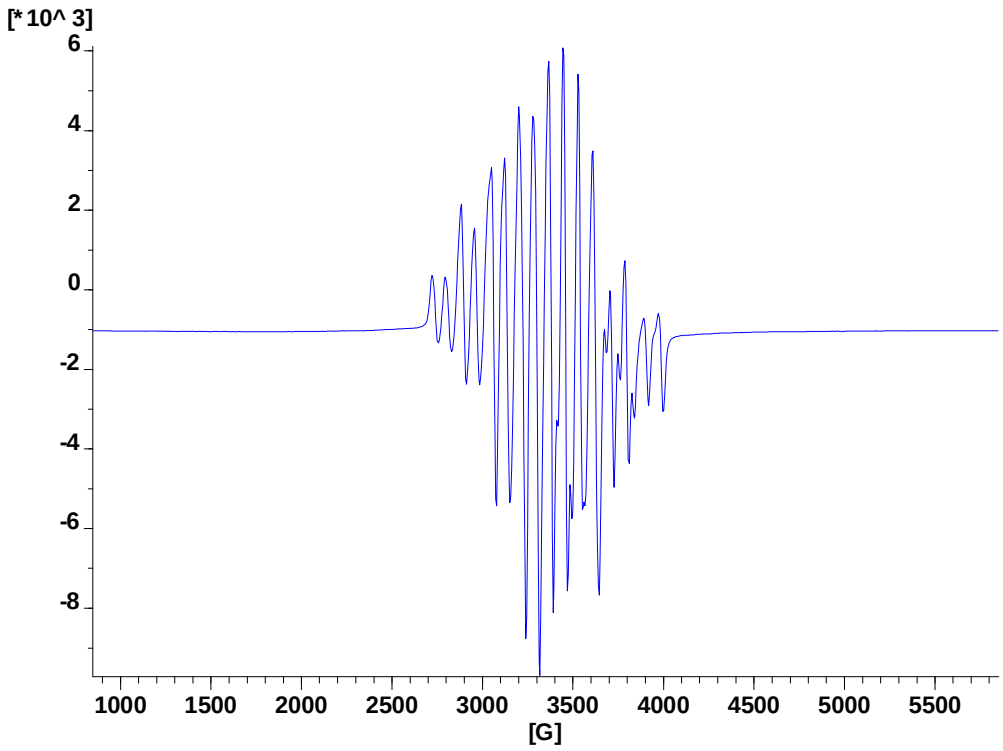

Figure C2. $[Mn_2O_2(bpy)_4](ClO_4)_3$ – recrystallized material in acetonitrile solution.

C.2. Trimanganese Complex.

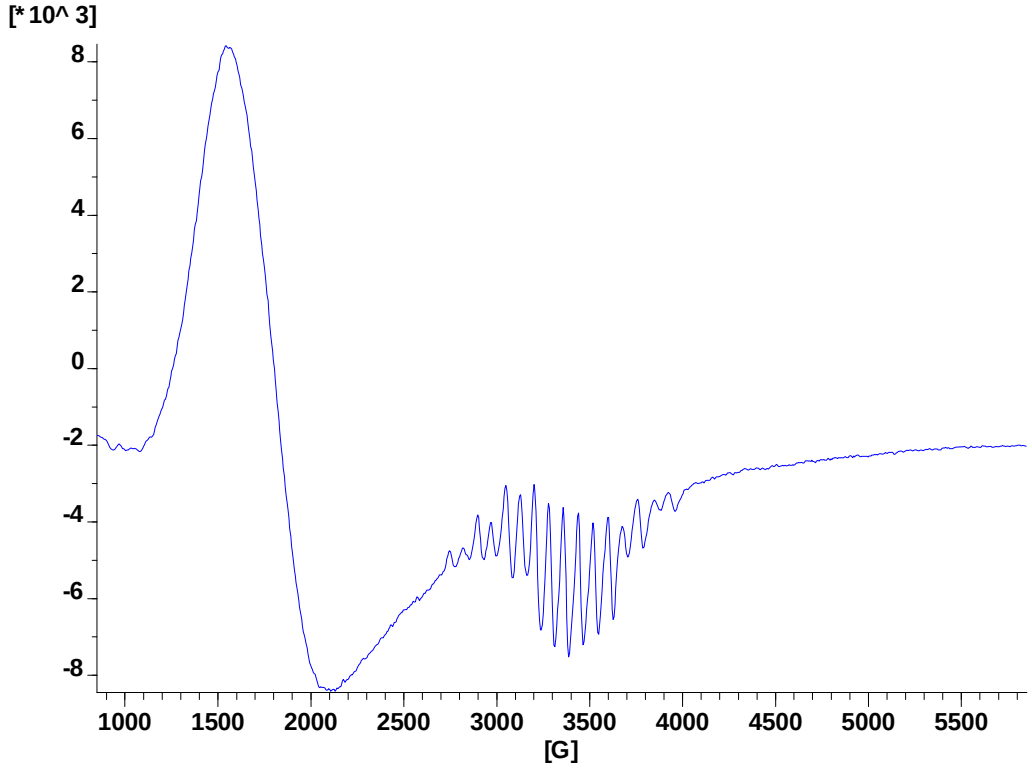

Figure C3. $Mn_3^{(IV,IV,IV)}(OH)(bpea)_3(ClO_4)_4$ in acetonitrile solution.

Appendix D

Library of Electrospray Ionization Mass Spectrometry Data

D.1. Mass Spectra for Ligands.

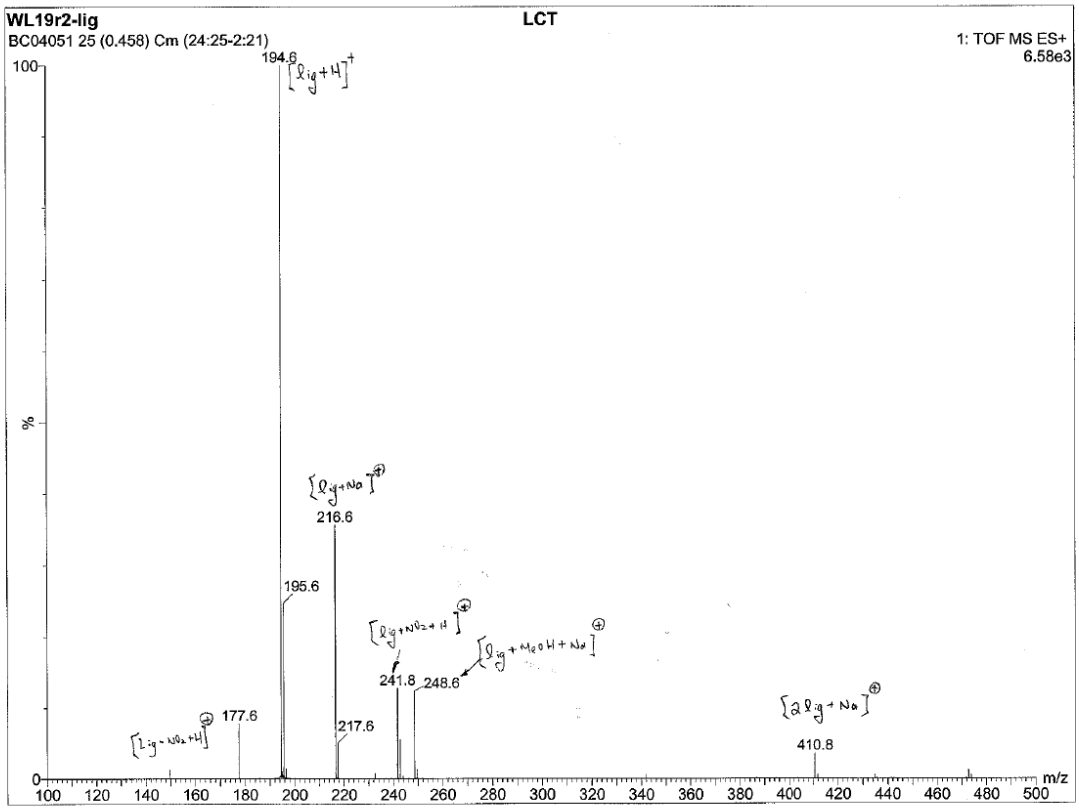

Figure D1. Mass **spectrum of** *N*-ethyl-3-nitro-salicylideneamine ligand.

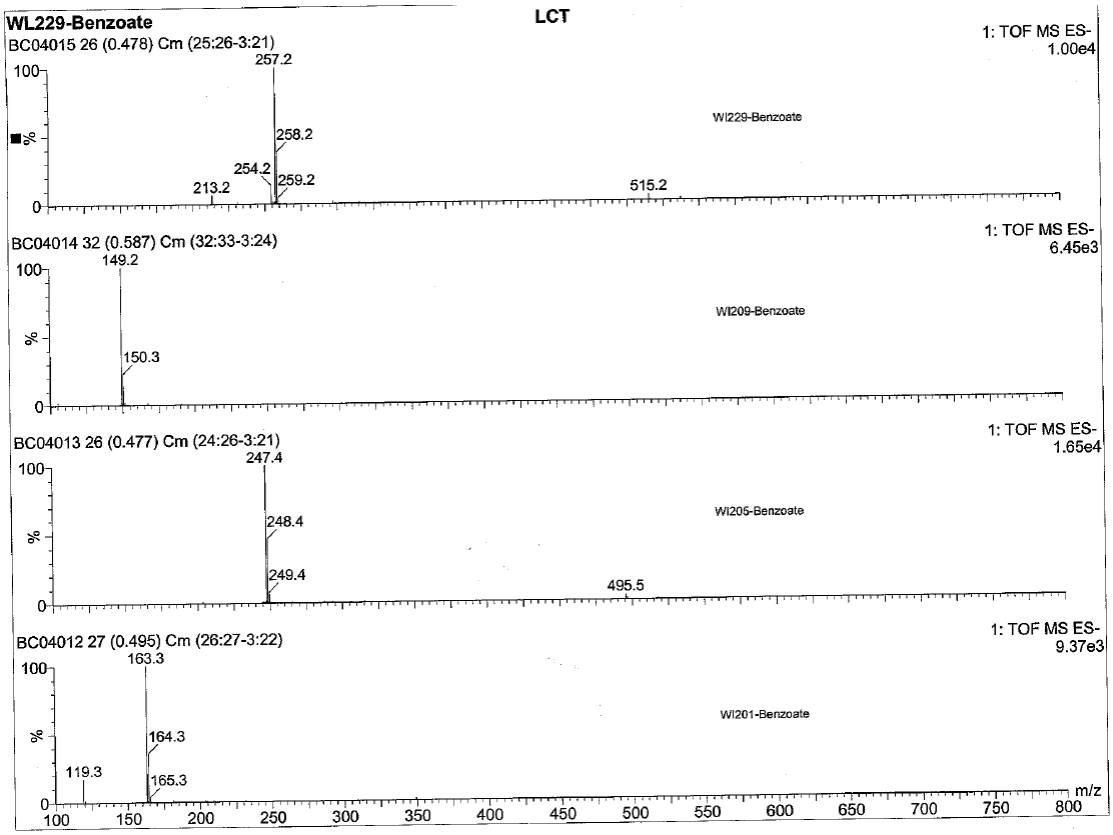

Figure D2. Mass spectral results for various carboxylate ligands. The p**urity of the products was assessed by the mass spectrometry.**

D.2. Mass Spectra for Mn Complexes.

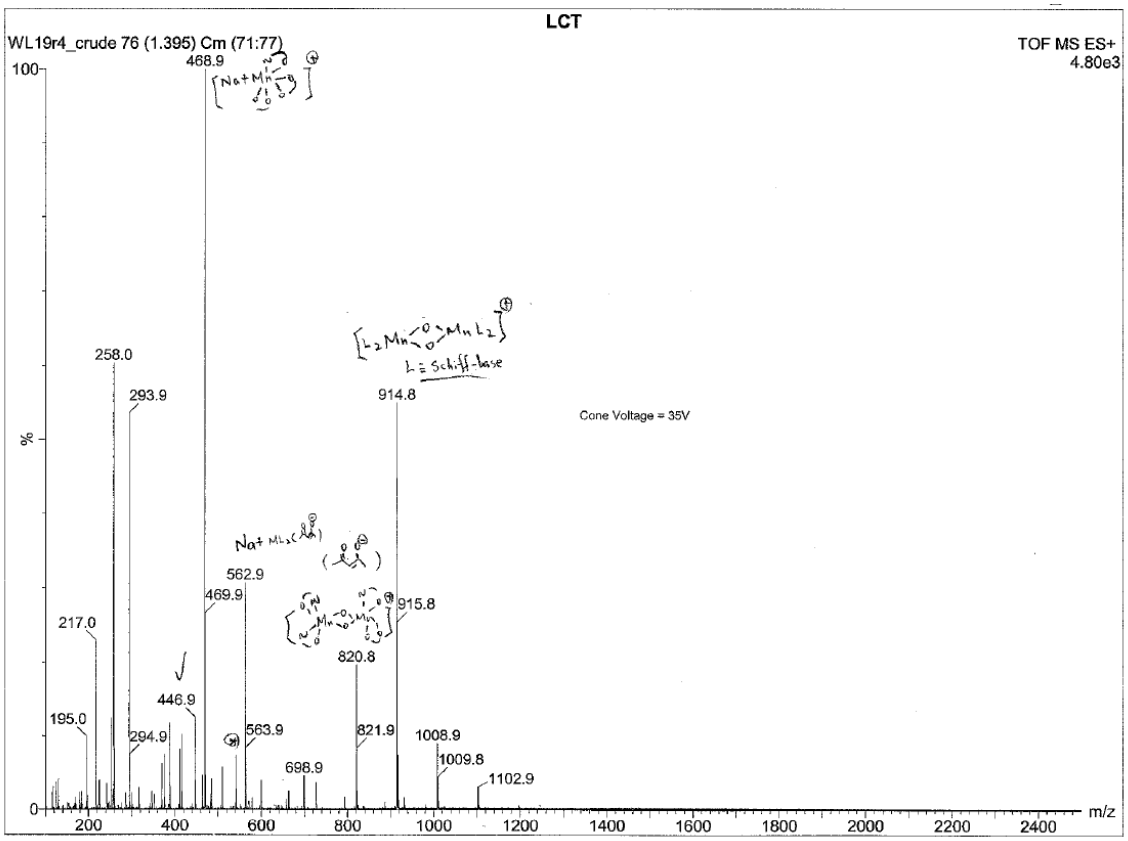

Figure D3. The mass spectrum of the unknown product for the reaction discussed in Chapter 2, page 35, [1 $Mn(acac)_3$: 2 L, refluxed at 110 °C for 2 h, where L = *N*-ethyl-3-nitro-salicylideneamine]. The corresponding ^1H NMR spectrum was shown in Figure B3.

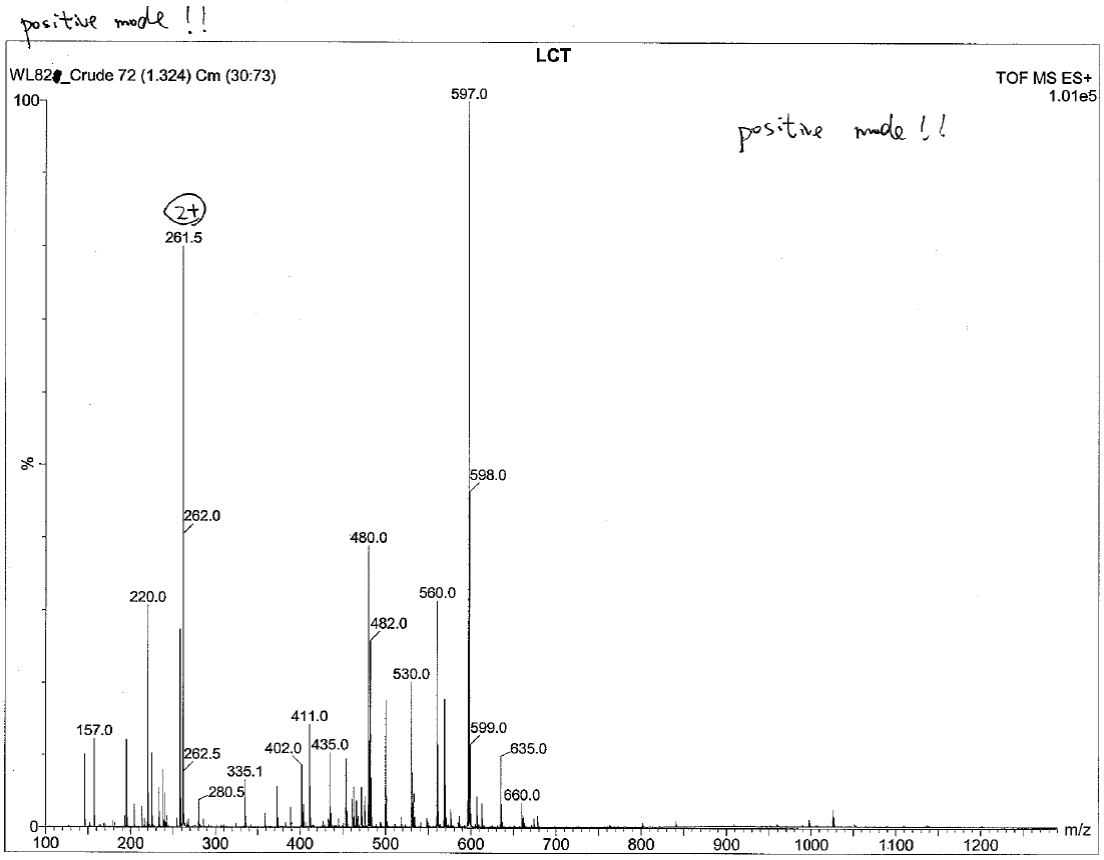

Figure D4. The ^{1}H NMR spectrum of the unknown product for the reaction discussed in Chapter 2, page 35, [1 $Mn(OAc)_3 \cdot 2H_2O$: 4 L, overnight stirring at room temperature and then heating at 50 °C for 3 h, where L = *N*-ethyl-3-nitro-salicylideneamine]. The corresponding ^{1}H NMR spectrum was shown in Figure B4.

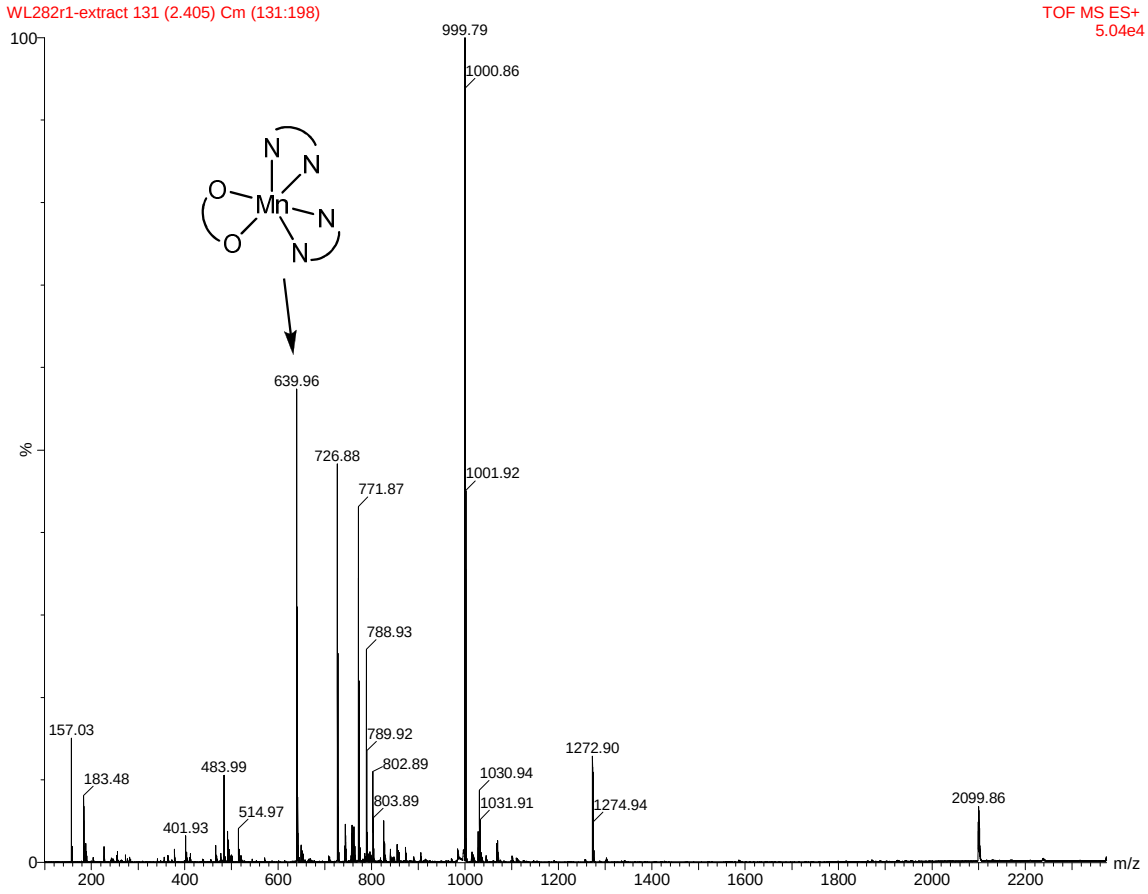

Figure D5. Mass spectrum of $[Mn_2O_2(bpy)_2(Ar^{Ph}CO_2)_2](ClO_4)$ [**21**] in CH_2Cl_2 solution.

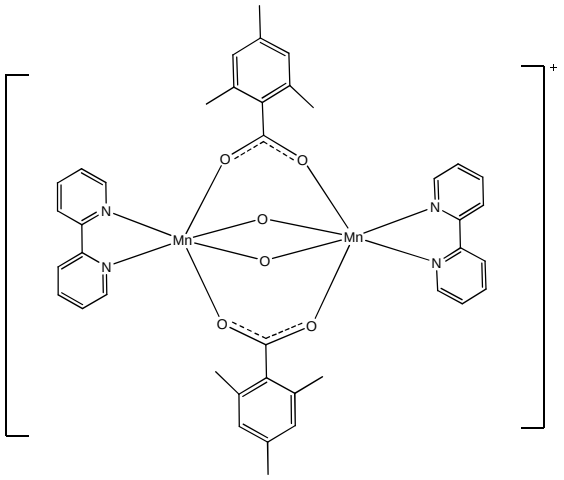

Chemical Formula: $C_{40}H_{38}Mn_2N_4O_6^+$
Exact Mass: 780.15
Molecular Weight: 780.63
m/z: 780.16 (100.0%), 781.16 (43.9%), 782.16 (11.3%), 781.15 (1.5%), 783.17 (1.3%)
Elemental Analysis: C, 61.54; H, 4.91; Mn, 14.08; N, 7.18; O, 12.30

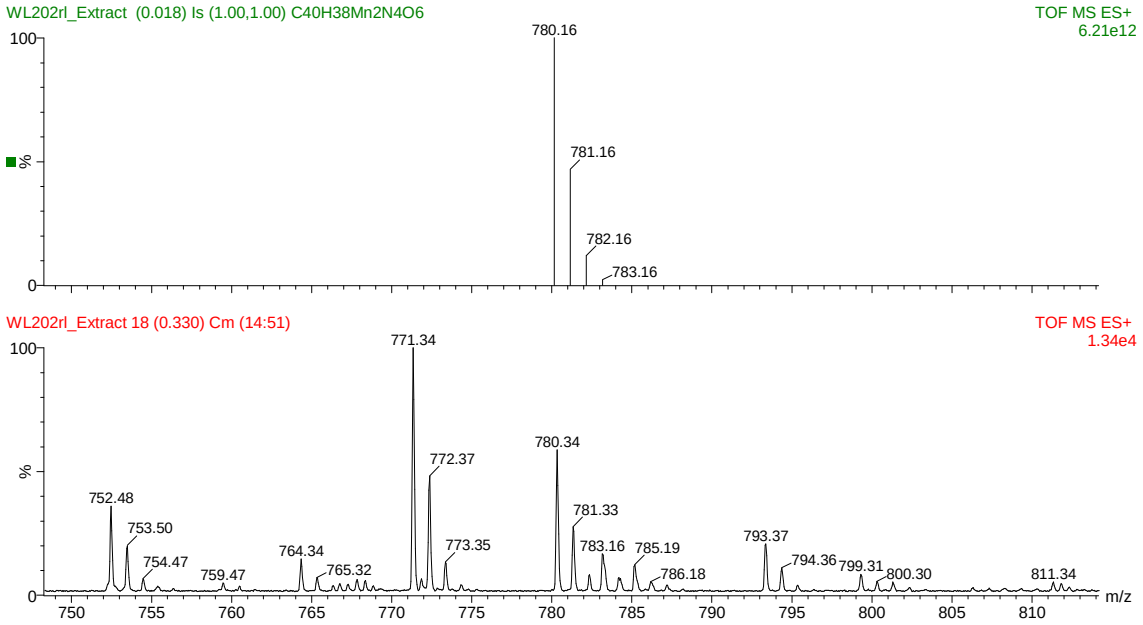

Figure D6. Mass spectrum of $[Mn_2O_2(bpy)_2(Ar^{tri\text{-}methyl}CO_2)_2](ClO_4)$ in CH_2Cl_2 solution.

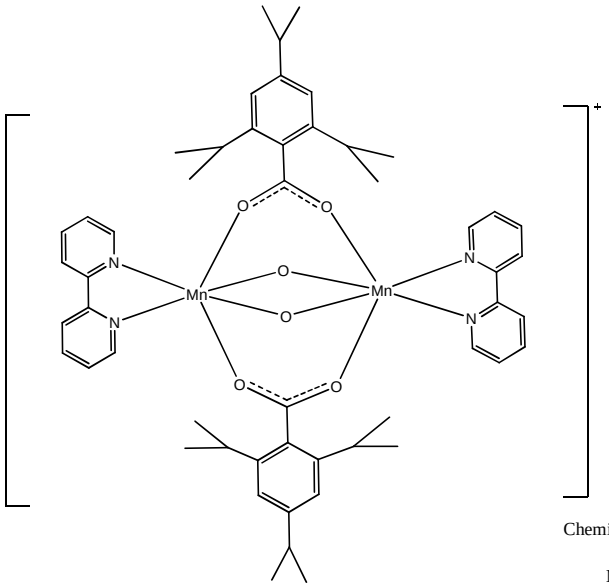

Chemical Formula: $C_{52}H_{62}Mn_2N_4O_6^+$
Exact Mass: 948.34
Molecular Weight: 948.95
m/z: 948.34 (100.0%), 949.35 (57.2%), 950.35 (17.3%), 951.35 (3.8%), 949.34 (1.5%)
Elemental Analysis: C, 65.82; H, 6.59; Mn, 11.58; N, 5.90; O, 10.12

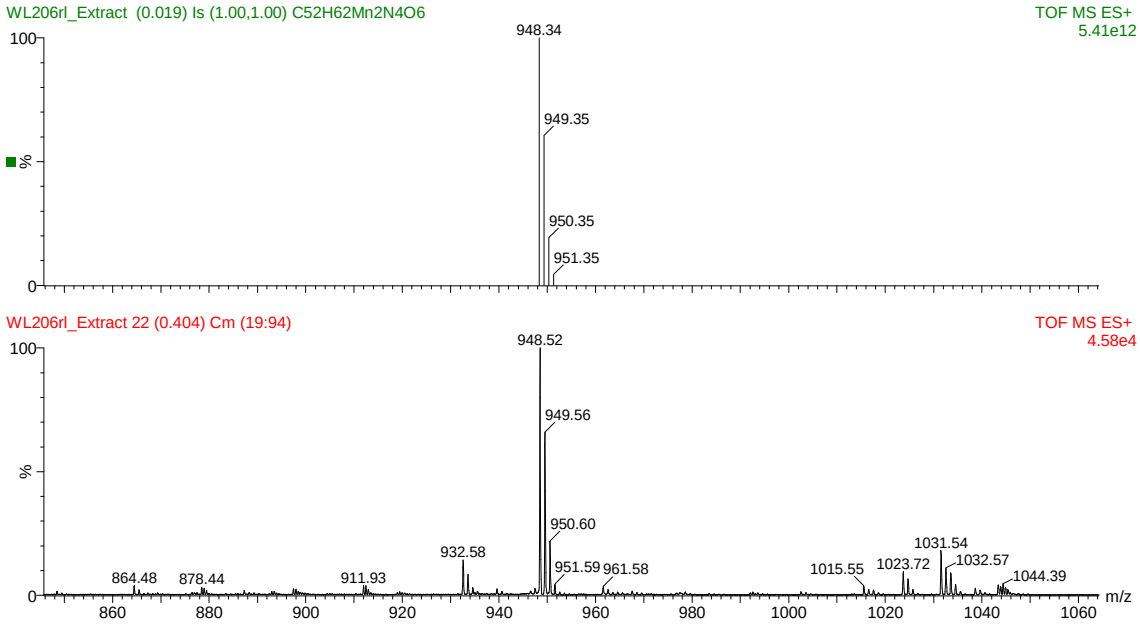

Figure D7. Mass spectrum of $[Mn_2O_2(bpy)_2(Ar^{2,4,6\text{-}tri\text{-}i\text{-}Pr}CO_2)_2](ClO_4)$ in CH_2Cl_2 solution.

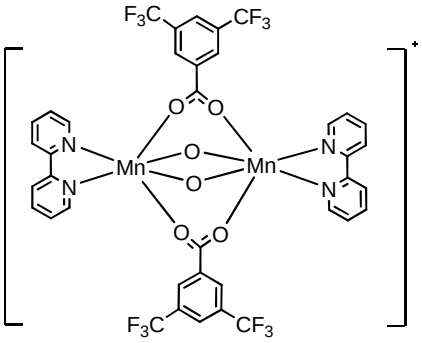

Chemical Formula: $C_{38}H_{22}F_{12}Mn_2N_4O_6^+$
Exact Mass: 968.01
Molecular Weight: 968.46
m/z: 968.01 (100.0%), 969.01 (42.6%), 970.02 (9.7%), 971.02 (1.6%)
Elemental Analysis: C, 47.13; H, 2.29; F, 23.54; Mn, 11.35; N, 5.79; O, 9.91

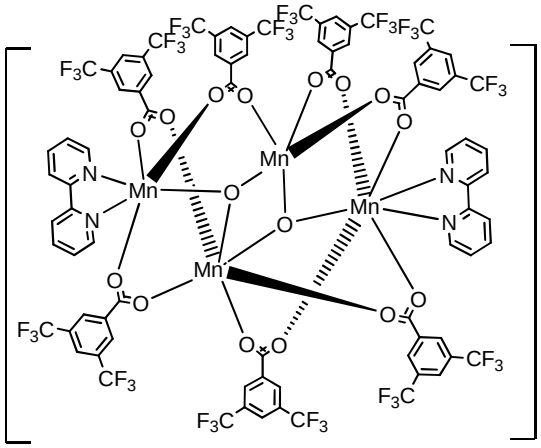

Chemical Formula: $C_{83}H_{37}F_{42}Mn_4N_4O_{16}$
Exact Mass: 2362.91
Molecular Weight: 2363.88
m/z: 2362.91 (100.0%), 2363.91 (90.8%), 2364.91 (45.0%), 2365.92 (12.1%), 2366.92 (4.0%), 2365.91 (3.6%), 2363.90 (1.5%)
Elemental Analysis: C, 42.17; H, 1.58; F, 33.76; Mn, 9.30; N, 2.37; O, 10.83

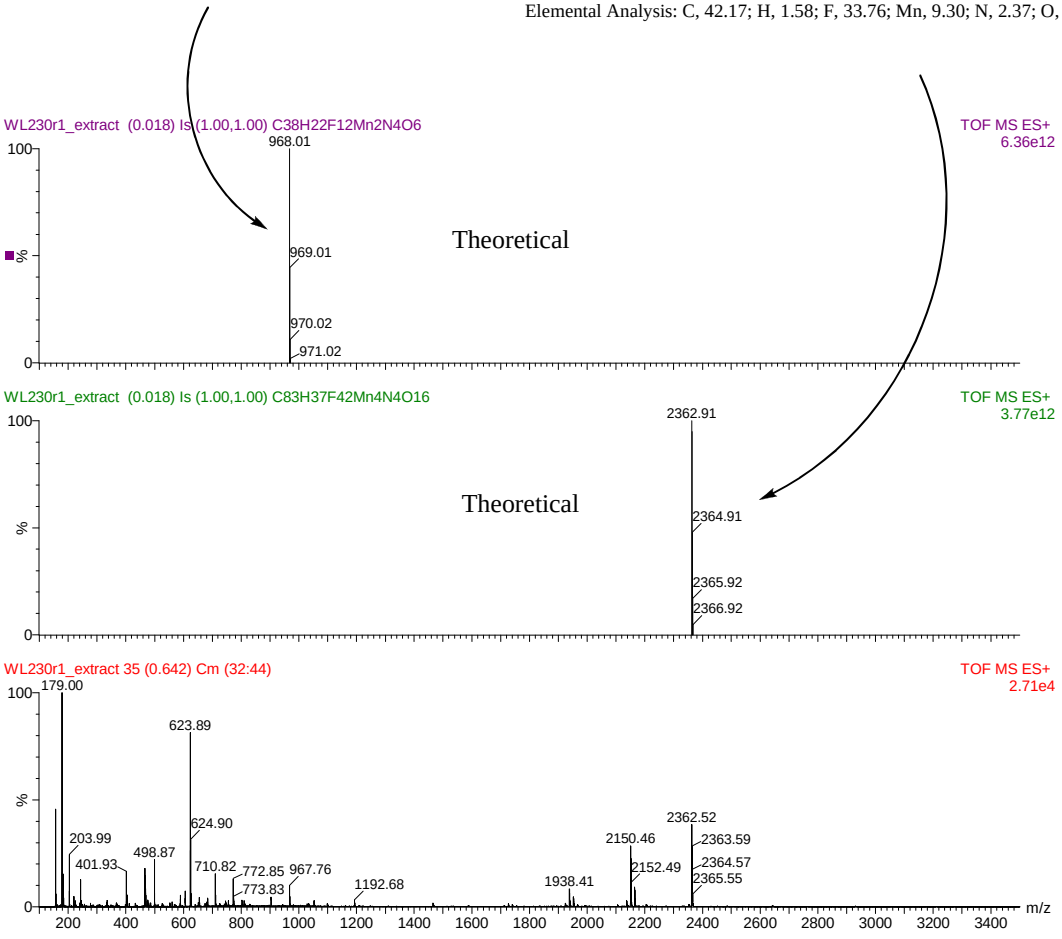

Figure D8. Mass spectrum of $[Mn_4O_2(bpy)_6(Ar^RCO_2)_7](ClO_4)$ [**26**] in CH_2Cl_2 solution.

Appendix E

X-ray crystallographic Data Tables for Some Compounds in This Dissertation

E.1. Ligands.

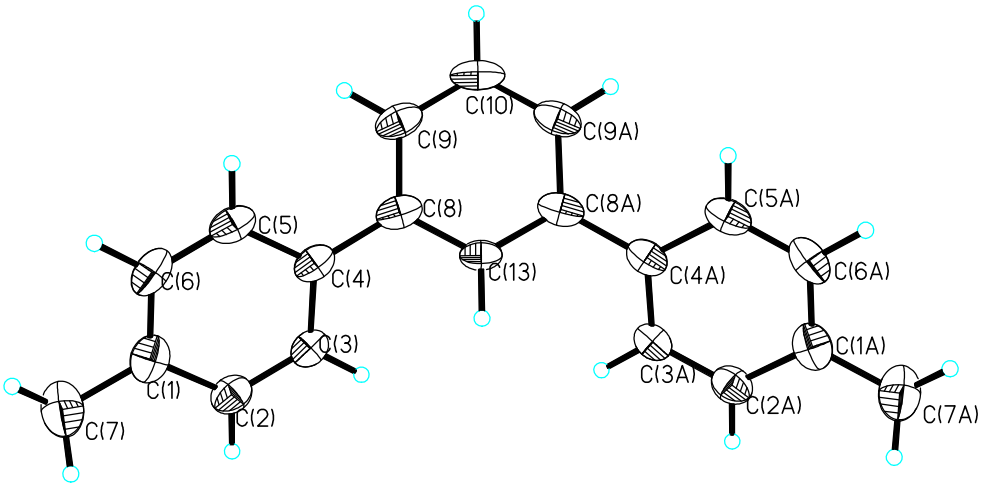

Figure E1. Di-tolylbenzene.

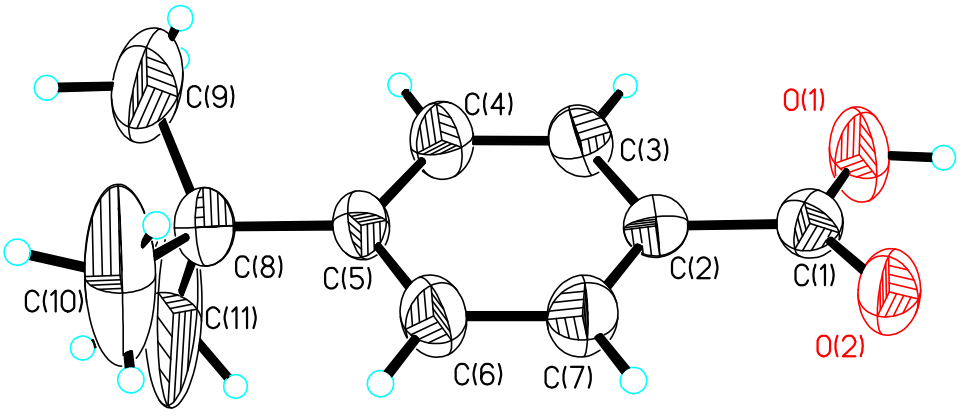

Figure E2. *tert*-butylbenzoic acid.

E.2. Manganese Complexes.

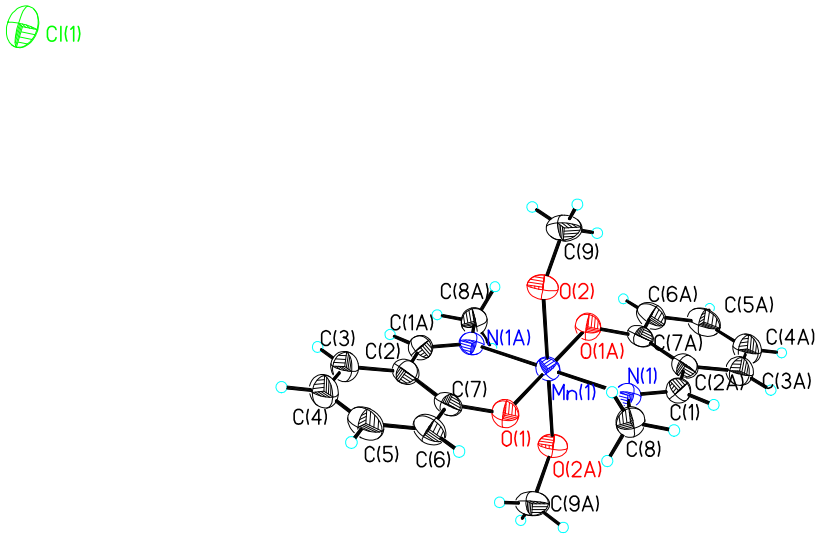

Figure E3. $[Mn_1^{(III)}(N\text{-Me-Sal})_2(OMe)_2](Cl)$

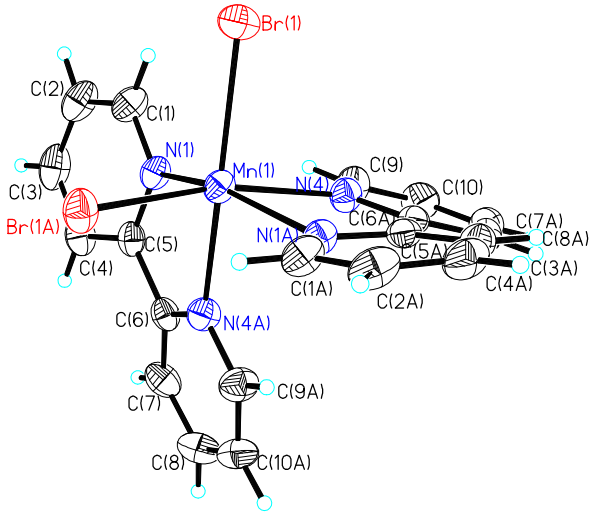

Figure E4. $Mn^{II}(bpy)_2Br_2$

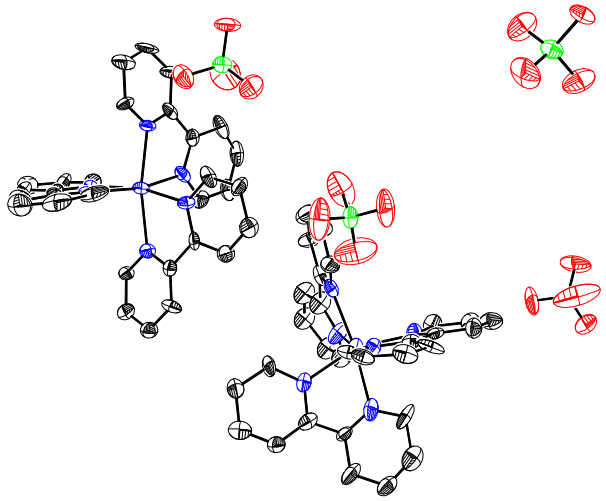

Figure 5. $[Mn^{II}(bpy)_3](ClO_4)_2$